UNIVERSITÀ DEGLI STUDI DI UDINE
hic sunt futura

www.uniud.it

Doctoral course in

Biomedical Sciences and Biotechnology

35th CYCLE

Thesis title

‘’Transcriptional Networks in Adipogenic and Thermogenic Programming’’

Ph.D. student
Dr. Uzair Ali

Supervisor
Prof. Monica Colitti

Co-Supervisor
Prof. Egeria Scoditii

Year 2023

Acknowledgments

I am grateful to Allah Almighty for bestowing His grace and blessings upon me, enabling me to successfully complete my Ph.D. study. Throughout this journey, despite facing challenges, I had the privilege of interacting with wonderful individuals who made the entire experience smoother and more delightful.

First, I express my deep gratitude to my supervisor Professor Monica Colitti for her unwavering support during the entire Ph.D. duration. Her expertise, insightful feedback, and dedication to my academic growth have been instrumental in shaping the outcome of this thesis. I am also thankful to my co-supervisor Egeria Scoditti for providing valuable feedback on the progress of my research and offering insightful suggestions for further enhancements. I would like to extend my appreciation to the Ph.D. coordinator Professor Alessandra Corazza and Professor Claudio Brancolini (Ex) for their administrative support and guidance throughout the doctoral program. Their consistent updates on courses, seminars, and other learning opportunities, contributed to a smooth and enriching academic experience.

I am grateful to Professor Martin Wabitsch and Dr. Daniel Tews at the Medical Faculty of Ulm University in Germany for their collaboration and valuable input in my research. I am also immensely thankful to my fellow researchers Dr. Tommaso Montanari, Dr. Giulia Polacchini, and Dr. Francesca D'Este for their support, enriched discussions, and willingness to lend a helping hand whenever needed.

In addition, I would like to extend my deep gratitude to Professor Jan Nedergaard and Professor Barbara Cannon for providing me with the invaluable opportunity to gain research experience in their esteemed laboratory at the Department of Molecular Biosciences, The Wenner-Gren Institute at Stockholm University. I am thankful for their continuous support, encouragement, and the opportunities they have provided me to expand my horizons and thrive in the academic realm. Their guidance, expertise, and dedication to advancing scientific knowledge have been truly inspiring. I would like to express my gratitude for the assistance and guidance provided by the esteemed group members, Dr. Irina Shabalina, Dr. Natasa Petrovic, and Dr. Ruda Glauber Braz. The engaging discussion, brainstorming sessions, and constructive feedback from these researchers and others have been instrumental in shaping my research ideas and refining my methodologies. I am truly fortunate to have had the privilege of working in the

research group, as the research experience has not only deepened my understanding of the subject matter but has also instilled in me a passion for research and a strong work ethic. The stimulating and inclusive atmosphere within the lab has fostered a strong sense of fellowship, making my time as a visiting researcher truly memorable.

I would like to express my gratitude to the technical and administrative staff of both the University of Udine and Stockholm University for their support whenever needed.

Last, but certainly not least, in this remarkable moment, I would like to take a moment to express my heartfelt gratitude to my parents and siblings. Their enduring support, prayers, and encouragement have been invaluable throughout my journey. I am truly grateful for the love, understanding, and sacrifices made by my parents, who have stood by me every step of the way. Their unwavering belief in my abilities and their constant encouragement has been a source of strength and inspiration. I extend my appreciation to my brother Dr. Kamran Khan whose support and companionship have been a constant source of motivation. His presence and wise guidance have provided the necessary encouragement, especially during challenging times.

Table of Contents

Abstract

The efforts to prevent or reduce obesity, which is a serious health problem also associated with numerous diseases, include the use of natural substances to promote the change from white adipocytes toward a brown type. Brown adipose tissue is of interest because it can dissipate energy in the form of heat and regulate triglyceride and glucose metabolism through expression of uncoupling protein 1 (UCP1). High-throughput RNA sequencing was used to investigate transcriptomic changes and to identify key patterns involved in adipogenesis and browning during the development of Simpson-Golabi Behmel Syndrome (SGBS) human cells, which gradually acquire browning function and were used for following study.

Allicin, a bioactive component of garlic, was used to study its possible browning effect in human SGBS cells after six days of differentiation in terms of lipid droplet and mitochondrial dynamics, and transcriptomic changes. Allicin promoted the reduction of the size and surface area of lipid droplets, leading to the development of multilocular adipocytes, and a shift in mitochondrial dynamic toward fission. Increased expression of genes related to beige adipocytes, was observed. In addition, allicin was also tested on mouse iWAT cells and the expression of UCP1 was stimulated. The results discussed support the modulatory role of allicin in stimulating the brown phenotype of SGBS cells, which is associated with adynamic modulation of mitochondria and lipid droplets

I. Introduction

1. Obesity a major health concern

Obesity is a complex disease characterized by an increased mass of adipose tissue and associated with various metabolic disorders such as insulin resistance, dyslipidemia, coagulopathies, hepatosteatosis, and hypertension[1]. The main cause of obesity is an imbalance between energy intake and energy expenditure. The energy imbalance causes excess energy to be stored in the form of triglycerides in white adipose tissue (WAT). Several environmental factors, such as high-calorie food intake and low physical activity, contribute to fat accumulation. In addition, a sedentary lifestyle, and abnormal sleep habits may also contribute to the development of obesity[2]. Genetic factors also play an important role in the development of obesity. Mutations in the genes that regulate hunger and metabolism, such as leptin, can lead to a hormonal imbalance that results in more hunger and less energy expenditure, which ultimately promotes fat accumulation[3].The World Health Organization (WHO) has provided alarming statistics on the rising prevalence of obesity and overweight among children and adults worldwide (WHO, https://www.who.int/, accessed on 14 February 2023). In 2016, more than 1.9 billion adults were overweight, with more than 650 million of them with obesity. The global prevalence of obesity nearly tripled between 1975 and 2016, affecting not only high-income countries, but also low and middle income countries, particularly in urban areas. The prevalence of overweight and obesity among children and adolescents aged 5 to19 years has also increased substantially from 4% in 1975 to over 18% in 2016. Overweight and obesity are associated with more deaths worldwide than underweight, with obesity prevalent in all regions except parts of sub-Saharan Africa and Asia. Due to high the prevalence of obesity in recent decades obesity has become an interesting area of research aimed at understanding the physiological mechanisms and developing therapeutic strategies to treat obesity and its associated metabolic complications.

2. Adipose tissue

Adipose tissue is a connective tissue composed mainly of adipocytes and plays an important role in energy homeostasis in the body. It has also endocrine functions by the secretion adipokines that influence various physiological and pathophysiological

processes[4]. Adipokines include cytokines, hormones, growth factors, vascular factors, and extracellular matrix proteins. It is an essential component of the body's energy storage system and plays a critical role in metabolism and overall health[5]. The goal of adipose tissue research is to understand the mechanisms that control the formation, storage, and breakdown of fat in the body, as well as the effects of adipose tissue on overall health. Adipose tissue grows by hypertrophy, enlargement of existing fat cells and/or hyperplasia, formation of new fat cells through differentiation of resident progenitors' cells known as preadipocytes. Differentiated adipocytes have incredible hypertrophy potential and can grow up to several hundred micrometers in diameter. The number of adipocytes in each depot is established early in the human development and remains relatively constant throughout adulthood[6]. Lineage-tracing models in mouse have shown that with continued caloric excess, new adipocytes can arise from preadipocyte differentiation and contribute to the accumulation of adipose tissue[7].

There are three main types of adipose tissue in the body: white adipose tissue (WAT) brown adipose tissue (BAT), and beige or brite (brown-in-white).

2.1 White adipose tissue

White adipose tissue is an areolar connective tissue formed by the accumulation of large, lipid-accumulating fat cells with few mitochondria. WAT is divided into two main compartments i.e., subcutaneous adipose tissue (scWAT), and visceral adipose tissue (vWAT), which is particularly important as it is associated with metabolic disorders. It is mainly the site of energy storage and plays a key role in regulating overall health[8]. However, WAT also affects the immune system and can cause inflammation, in fact it is rich in immune cells such as macrophages, which can contribute to inflammation. This is known as "metaflammation" and is considered one of the mechanisms of diseases associated with obesity, such as type 2 diabetes and cardiovascular disease[9].

Visceral depots are in the gonadal, perirenal, retroperitoneal, omental, and pericardial areas.[10]. When the storage capacity of WAT reaches its limit, fatty acids accumulate in other internal organs, such as the liver and muscles, because they can no longer be safely removed from systemic circulation. This is ectopic lipid accumulation, which ultimately leads to insulin resistance causing type 2 diabetes and cardiovascular disease[11] (**Fig. 1**)

Preadipocytes from the stromal-vascular fraction (SVF) of WAT are recruited to differentiate into mature adipocytes through a process called adipogenesis[12]. Adipogenesis is a developmental process consists of two main steps. In the first step, the mesenchymal stem cells differentiate into preadipocytes. In the following step, the preadipocytes undergo major changes in cell morphology and gene expression and differentiate into mature adipocytes[13]. Adipogenic molecules include peroxisome proliferator receptor gamma (PPARγ) and CAAT enhancer binding proteins (C/EBP)[14]. Antiadipogenic preadipocyte factor 1 (PREF1) has been shown to be involved in direct regulation of the promoters of genes encoding CCAAT/enhancer-binding protein beta (C/EBPβ) and CCAAT/enhancer-binding protein delta (C/EBPδ) *via* the transcription factor SOX9. C/EBPα and PPARγ, the master regulators of adipogenesis, and sterol regulatory element binding protein 1 (SREBP1), a regulator of lipogenic genes, are the major targets of C/EBPβ and C/EBPδ. C/EBPα and PPARγ activate each other in a positive feedback loop[15]. In addition, PPARγ and C/EBPα induce the expression of genes involved in lipogenesis, insulin sensitivity, and lipolysis, including genes encoding glucose transporter type 4 (GLUT4), fatty acid binding protein 4 (FABP4), and lipoprotein lipase (LPL)[16].

2.2 Brown adipose tissue

Brown adipose tissue is a unique type of fat found in mammals. BAT is rich in mitochondria and has multilocular lipid droplets[17]. In addition, BAT has numerous blood vessels that provide high blood flow to the tissue allowing to respond quickly to temperature changes [18]. The main function of BAT is to release energy in the form of heat by uncoupling the electron transport chain, which results in energy released in the form of heat instead of producing ATP. This function of BAT is carried out by the uncoupling protein 1 (UCP1), which is in the inner mitochondrial membrane[19]. The expression of UCP1 in brown adipose tissue gives mammals an evolutionary advantage in being active and surviving the cold environments, especially during the neonatal period,[20]. The development of BAT involves precursor cells that express pro-myogenic factors such as Myf5 and Pax3, which are also expressed in myocytes. Two models have been proposed regarding the contribution of $Myf5^+$ cells to adipocyte development, with one suggesting that $Myf5^+$ and $Myf5^-$ precursors are spatially mixed, and the other suggesting that Myf5 expression occurs later during recruitment or differentiation[21]. PPARγ remains a key transcription factor for adipogenesis, with Peroxisome proliferator-activated receptor-

gamma coactivator (PPARGC1A) and PR/SET Domain 16 (PRDM16) as important brown-specific factors that positively induce mitochondrial biogenesis and oxidative metabolism, and upregulate many thermogenic genes, including UCP1. Bone Morphogenetic Protein 7 (BMP7) has been found to be involved in the regulation of PRDM16 induction and enhances brown adipogenesis[22].

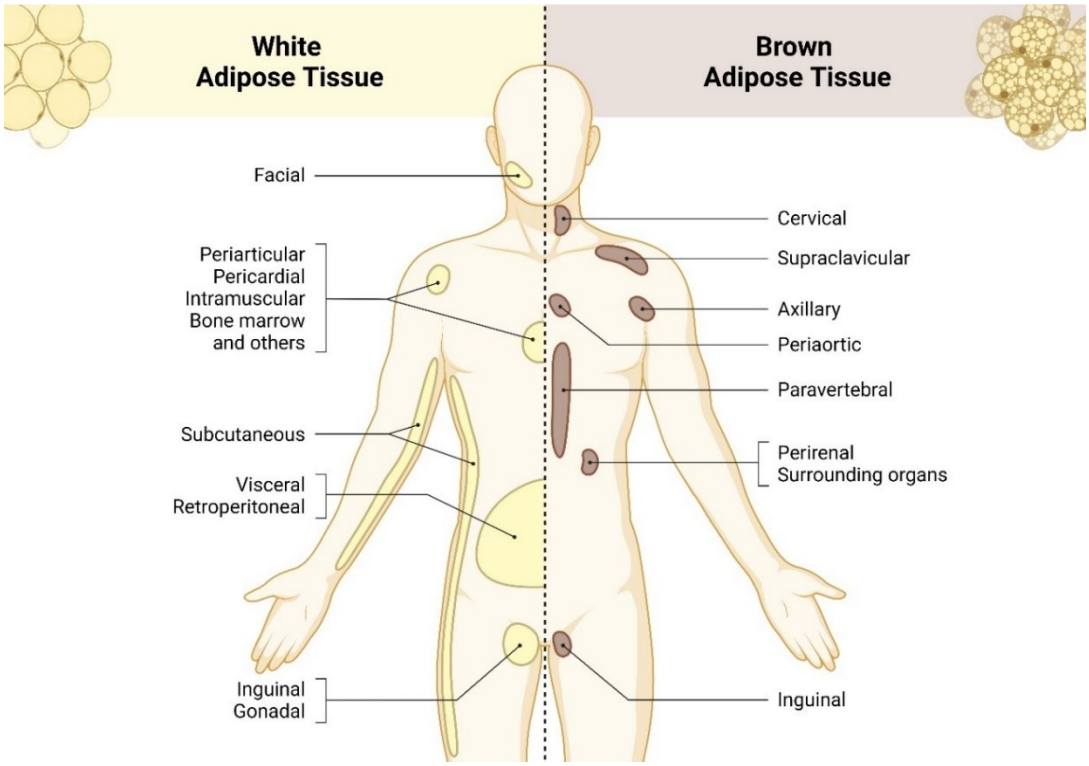

Figure 1. Distribution of WAT and BAT depots in the human body (modified from Rodrigruez et al)[23].

2.3 Beige adipocytes

A third type of adipocyte has been identified in the depots of WAT, termed beige or brite, with features intermediate between white and brown adipocytes, but unlike the classic BAT, these cells arise from Pax7/Myf5 precursors[24]. These adipocytes have a unicellular large lipid droplet and few mitochondrial contents, which is a typical morphological feature of WAT, but upon exposure to cold or adrenergic beta-3 stimulators, they transform into brown adipocytes with small multilocular lipid droplets and expression of the thermogenic protein UCP1. This inducible process is referred to as browning (**Fig. 2**). However, according to Wang et al. (2013) most beige adipocytes arise

from a precursor population rather than pre-existing adipocytes and/or mature white adipocytes, at least in the subcutaneous depot[25].

In recent decades, beige cells have become an important area of research in the field of metabolic sciences because they are unique cells that provide a more adaptive pathway for regulating body temperature and maintaining energy balance. Several factors have been identified that trigger browning in WAT. These include beta-aminobutyric acid (BAIBA), gamma-aminobutyric acid (GABA), PPARγ agonists, and Janus kinase (JAK) inhibition[26].

Brite adipocytes also expressed several brite specific genes that could serve as recognition markers. These markers include T-Box Transcription Factor 1 (TBX1), Transmembrane Protein 26 (TMEM26), and TNF Receptor Superfamily Member 9 (TNFRSF9 or CD137), which are over-expressed in subcutaneous white adipose tissue of mice[27]. However, the specificity of these markers for brite fat cells was found to be dependent on factors such as *in vivo* or *in vitro* models and adrenergic stimulation. Neuregulin 4 (NRG4) has been suggested as a potential brite marker in both mice and humans, whereas Fibroblast Growth Factor 21 (FGF21), Carbonic Anhydrase 4 (CAH4), and Cbp/P300 Interacting Trans activator with Glu/Asp Rich Carboxy-Terminal Domain 1 (CITED1) are validated brite markers. TBX1 and TMEM26 are highly expressed in adipocyte progenitors compared with mature adipocytes. These results suggest that the accuracy of putative brite markers depends on multiple factors and validated brite biomarkers are limited[28].

2.4 Transcriptional regulation of adipose tissue browning.

Adipose tissue browning is a complex process that involves the transcriptional regulation of multiple genes and pathways. The browning of WAT is regulated by several transcriptional factors, co-factors, and epigenetic regulators, which act in a coordinated manner to activate the thermogenic program in adipocytes.

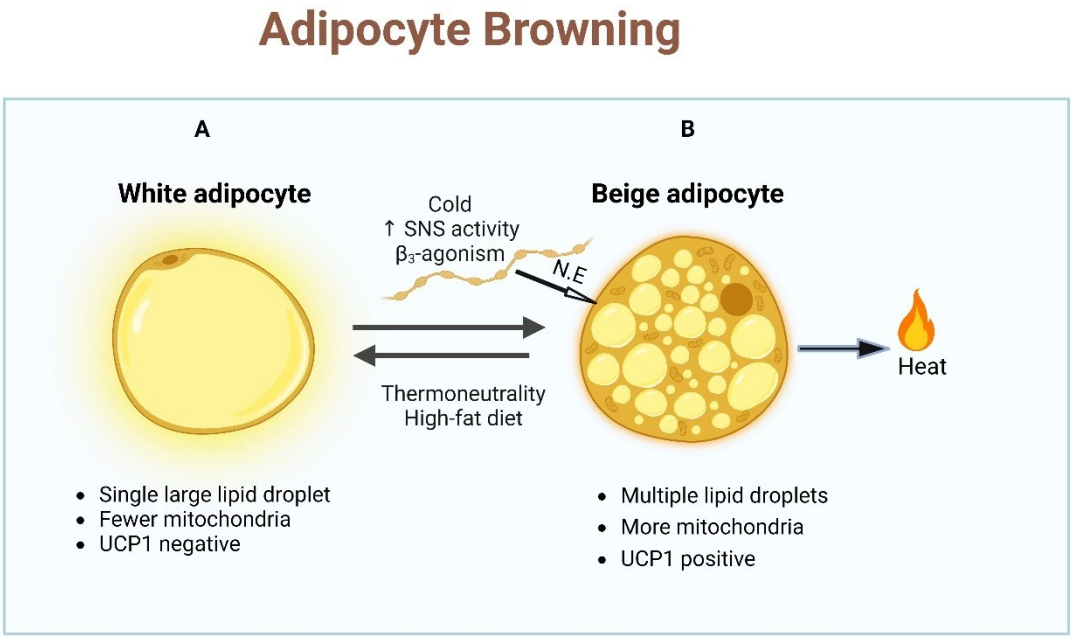

Figure 2. Schematic representation of adipocyte browning. (A) Under thermoneutral conditions, the white adipocyte is composed of a single large lipid droplet with few mitochondria and no UCP1 expression. (B) Upon cold stimulus, the sympathetic nervous system is activated releasing β3 agonist norepinephrine (NE) that activates the UCP1 in the adipocytes releasing heat to maintain homeostasis (modified from Ma, et al., 2022) [29].

Some of the master regulators of brown adipocyte includes UCP1, which is the hallmark gene of brown adipocytes, and is responsible for uncoupling oxidative phosphorylation, thereby dissipating energy as heat[30]. PPARγ is a transcription factor that is also involved in regulating the differentiation and activation of brown adipocytes. PPARγ and C/EBP transcription factors are key components of the transcriptional cascade that precedes the formation of mature, fully differentiated adipocytes. These transcription factors play a role in both brown and white adipocyte differentiation.

Another key transcriptional regulator of adipose tissue browning is PPARGC1A. PPARGC1A is a co-activator that interacts with several transcriptional factors, including PPARγ, promote mitochondrial biogenesis, oxidative metabolism, and thermogenesis. PPARGC1A is induced by cold exposure, exercise, and other stimuli that activate the thermogenic program in adipocytes, and it has been shown to be essential for the browning of WAT[31]. In mouse model, *Ppargc1a* has been identified as the target of BMP signaling, required for beige cells changes in WAT[32]. PPARGC1Ais activated by Mitogen-Activated Protein Kinase 14 (p38 or MAPK14) and activating transcription factor 2 (ATF2) and the transcription factor PDRM16, which interacts with C/EBP [33].

PRDM16 plays a crucial role in brown and beige adipocyte differentiation[34] because it is essential for the maintenance of the beige adipocyte phenotype, and when its expression is low, beige adipocytes can convert to white adipocytes[35]. Among the genes that have been shown to be regulated by PRDM16 are PPARGC1A, UCP1, Cell Death Inducing DFFA Like Effector A (CIDEA), Cytochrome C Oxidase Subunit 7A1 (COX7A1), and Iodothyronine Deiodinase 2 (DIO2).

Several PPARγ binding regulators could also influence differentiation to brown. These include sirtuin 1 (SIRT1, the NAD-dependent deacetylase), which deacetylates PPAR, allowing recruitment of PRDM16 and initiation of the brown fat-specific program[36]. The transcription factor Early B-cell Factor 2 (EBF2) is responsible for the recruitment of genes involved in brown adipogenic processes[37]. CIDEA is highly expressed in brown adipose tissue and promotes the formation of lipid droplets, and COX7A1 is a subunit of the mitochondrial respiratory chain that is involved in oxidative phosphorylation.

Adrenergic stimulation is responsible for the rapid responses of BAT to external stimuli, but triiodothyronine (T3) plays an important role in controlling thermogenesis by enhancing the ability of cells to respond to catecholamines. Type 2 5′-DIO2 in BAT is activated by cold induced noradrenergic stimulation and facilitates the conversion of tetraiodothyronine (T4) to T3. T3 promotes the expression of genes that activate UCP1 and together, these genes are regulated by PRDM16. These are essential for the function and maintenance of brown adipocytes and are crucial for energy metabolism and thermogenesis in mammals[38]. PRDM16-specific control of BAT-specific genes is regulated by the zinc finger transcription factor (ZFP516) and lysin-specific demethylase-1 (LSD1)[39]. In addition to PPARGC1A and PRDM16, other transcription factors have been shown to regulate adipose tissue browning, including C/EBPβ, interferon regulatory factor 4 (IRF4), and Kruppel-like factor 11 (KLF11), which interact with PPARγ, PPARGC1A, and PRDM16 to activate the expression of thermogenic genes, including UCP1, and to promote the browning of WAT[40].

Moreover, AMP-activated protein kinase (AMPK) is also required for sympathetic activation of WAT browning and BAT thermogenesis. In response to negative energy balance, AMPK directs intracellular activities toward ATP synthesis. Because sympathetic AMPK inactivation increases WAT browning and BAT thermogenesis, AMPK is a potential target for obesity therapy.[41].

Fox head P1 (FOXP1), instead is a negative regulator of brown/beige adipogenic differentiation by directly repressing ADRB3 transcription. FOXP1 deletion in adipose tissue increases the activity of BAT and browning of the WAT. In contrast, overexpression of FOXP1 in adipocytes, hinders adaptive thermogenesis and increases diet-induced obesity[42].

Significantly, human obesity is associated with lower expression of thermogenesis-related genes in WAT, which may impair sensitivity to hormonal and adrenergic stimuli involved in thermogenesis activation[43].

Many other mechanisms involved in the formation of BAT formation and control of thermogenesis have been found during the last decades such as Atrial natriuretic peptide (ANP) and brain natriuretic peptide (BNP). Both play critical roles in fluid balance and control of hemodynamic by activating natriuretic peptide receptors (NPRs) and downstream mediators such as cyclic guanosine monophosphate (cGMP), protein kinase G (PKG), and mammalian target of rapamycin complex 1 (mTORC1)[44,45]. The discovery of the expression of NPRs in adipose tissue provided new insight into the importance of ANP/BNP signaling pathways for whole body homeostasis[46]. Subsequently, it was discovered that ANP activates lipolysis in white adipocytes and thermogenesis in BAT, whereas both NPs can increase UCP1 expression and mitochondrial content *via* the cGMP-PKG-mTORC1 pathway[47].

2.5 Adipokines

A prominent function of WAT is the production and release of adipose derived hormones and cytokines called adipokines[48]. One of the most important adipokines is leptin, which correlates positively with body mass index (BMI) and regulates energy intake by reducing appetite and increasing energy intake. The concentration of leptin in the blood and WAT mass depends on energy balance and stored fat in the body. Leptin is a pro-inflammatory cytokine and belongs to the IL-6 family of cytokines. It is encoded by the gene OB, which is expressed by adipocytes[49]. The main function of leptin is to regulate energy intake by activating of its receptors (ObR) in the central nervous system. However, the receptors of leptin are also expressed in peripheral tissues, suggesting its role in other processes such as immunity, brain development, metabolism, reproduction, and cardiovascular function[50]. Leptin synthesis is higher in scWAT than in vWAT, and it

is also inhibited by androgens and stimulated by estrogen. For these two reasons, leptin levels are higher in women than men[51].

The protein adiponectin is primarily recognized for its anti-inflammatory and insulin-sensitizing properties, but it also influences several metabolic processes. Plasma adiponectin level is inversely correlated with fat mass. Adiponectin binds two receptors, ADIPOR1 and ADIPOR2, which are located together with ObR in the hypothalamus. Here, adiponectin regulates energy expenditure by regulating the AMPK signalling pathway[52]. Aadiponectin negative (*Adipoq*-/-) mice, for example, showed increased leptin sensitivity, demonstrating that these two hormones likely act reciprocally by suppressing and stimulating appetite and energy expenditure, respectively, providing a homeostatic mechanism to maintain fat levels and energy stores in the body[53].

In addition, resistin is a cysteine rich peptide with 108 amino acids. It has a striking structural similarity to adiponectin. In addition to adipocytes, a considerable number of particularly immunocompetent cells also secrete resistin[54]. Diet-induced mice and patients with obesity have higher resistin blood concentrations in the blood[55]. Administration of the anti-diabetic drug rosiglitazone and an anti resistin antibody has been shown to lower resistin concentrations in the blood and improve blood glucose levels and insulin action[56]. Moreover, inflammation, lipopolysaccharides (LPS), estrogen, testosterone (gonadal hormones), IL-6, and hyperglycaemia stimulate the secretion of resistin[57]. When resistin is released from adipose tissue, it induces insulin resistance by acting on fat cells and promoting hepatic gluconeogenesis. It has also been observed that preadipocytes have a 3-fold higher expression of resistin compared to mature adipocytes, highlighting its potential role in the process of adipogenesis[58].

3. Thermogenesis

Thermogenesis is the process by which the body generates heat. It occurs in all living organisms but is particularly important in mammals as it helps to maintain body temperature in cold environments[59]. The different ways in which the body can generate heat include metabolism, shivering, and non-shivering thermogenesis. In the mammalian cell, thermogenesis is supported by the oxidation of food, particularly glucose, fatty acids within the inner mitochondrial membrane and amino acids. The mitochondrial uncoupling proteins allow to identify mechanisms that control the ratio between energy accumulated as ATP and energy dissipated as heat[60].

There are two main categories of thermogenesis called obligatory thermogenesis and facultative thermogenesis. Facultative thermogenesis is further divided into shivering and non-shivering thermogenesis.

3.1 Obligatory thermogenesis

Obligatory thermogenesis refers to the minimum amount of energy required to maintain the basic metabolic processes of the body, such as respiration, circulation, and temperature regulation. It can be influenced by several factors, including basal metabolic rate (BMR), body size, and ambient temperature[61]. The energy required for these functions is supplied by the oxidation of glucose and fatty acids in the mitochondria of cells. Obligatory thermogenesis also contributes to the regulation of body temperature by generating heat. This heat is generated as a byproduct of cellular metabolism and helps maintain stable body temperature in response to environmental changes[62].

3.2 Facultative thermogenesis

Facultative thermogenesis refers to energy expenditure that is not required for basic physiological functions but is used to regulate body temperature in response to changes in the environment. This is also called adaptive thermogenesis and is a metabolic adaptation in mammals[63] in response to chronic or repeated cold exposure. Other factors that influence facultative thermogenesis include diet, exercise, and circadian rhythm. A high-fat diet leads to an increase in facultative thermogenesis, while exercise triggers thermogenesis in muscle tissue[64].

3.2.1 Shivering thermogenesis

This is a form of facultative thermogenesis that occurs in response to cold exposure and is mediated by activation of the sympathetic nervous system. The sympathetic nervous system releases NE in response to cold, which triggers skeletal muscles contraction. This leads to the development of heat, which contributes to the regulation of body temperature and ultimately to thermal homeostasis[65]. Shivering thermogenesis is inhibited by low glucose levels and enhanced by elevated levels of leptin[66]. In humans, shivering thermogenesis is less efficient compared to non-shivering thermogenesis. Nevertheless, it plays an important role in energy metabolism and contributes to the regulation of body temperature in response to cold exposure[67].

3.2.2 Non shivering thermogenesis

Non-shivering thermogenesis is a process in which mammals, including humans, generate heat through metabolic processes. This process primarily occurs in BAT,[68]. When UCP1 is activated, BAT can generate heat by burning stored triglycerides, which can help to maintain body temperature and increase energy expenditure[69]. This process is mainly controlled by the sympathetic nervous system, which activates BAT by releasing norepinephrine in response to cold or other stimuli. The signal is transmitted to the individual adipocytes that initiate the breakdown of triglycerides mainly through the β3-adrenergic receptor (β3-AR). Free fatty acids regulate the activity of UCP1 and are an acute substrate of thermogenesis[70,71]. For instance, in humans, stimulation of BAT thermogenesis has been proposed to improve metabolic health. However, previous attempts using a β3-AR agonist in clinical trials were not successful. Recent research has found that, unlike in rodents, human BAT thermogenesis is not mediated by β3-AR stimulation. Oral administration of the β3-AR agonist mirabegron only induced increased BAT thermogenesis at the maximal allowable dose, which also resulted in off-target binding to β1-AR and β2-AR, leading to cardiovascular responses and white adipose tissue lipolysis. The study showed that β2-AR, mediates BAT lipolysis and thermogenesis in humans through co-expression of ADRB2 and UCP1 in human brown adipocytes[72].

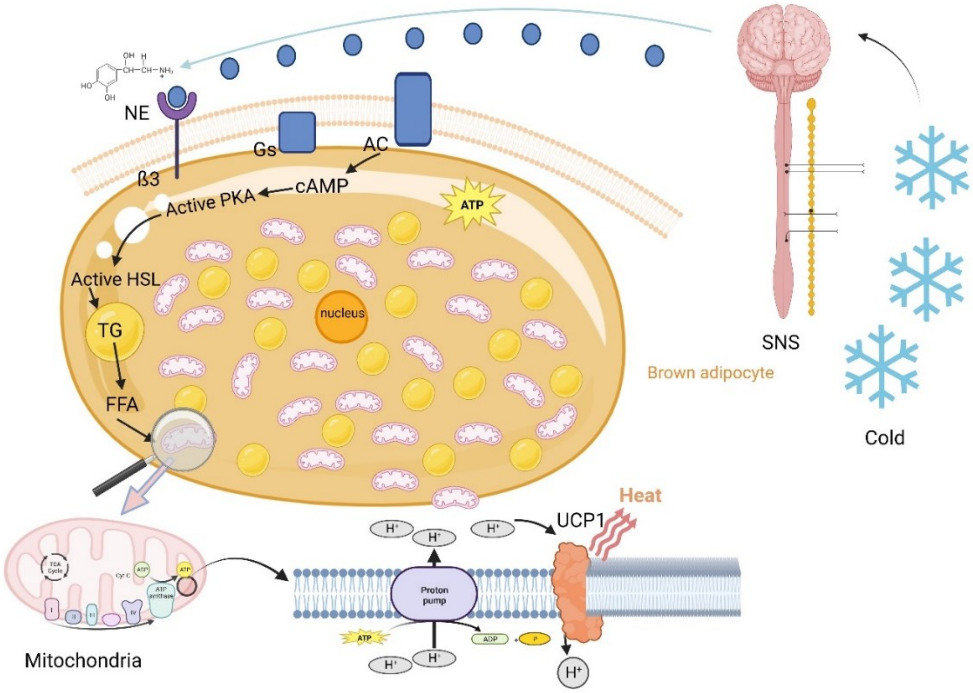

Figure 3. Mechanism of heat production in brown adipocytes. Sympathetic nerve fibers releases NE that interacts with the β-3 receptor. This system includes a GTP-binding, stimulatory protein

(Gs) that activates adenylyl cyclase (AC), leading to an increase in cycle adenosine monophosphate (cAMP). Protein kinase A (PKA) is then activated and phosphorylates hormones-sensitive lipase (HSL), which hydrolyses triacylglycerols, increasing intracellular free fatty acid (FFA) concentration. The mitochondria of brown adipose tissue are characterized by tightly packed cristae and the ability to produce heat through uncoupled respiration. This is achieved through the action of the UCP1, which dissipates the proton electrochemical gradient built up by the electron transport chain. In brown adipose tissue subjected to chronic cold stress, endogenous triacylglycerols are rapidly consumed, and fatty acids are taken up from the blood by lipoprotein lipase to maintain a constant supply of substrate (modified from Mc Neill et al., 2021)[73].

4. *In vitro* cell models to study adipose tissue

In vitro cell models have largely been used in adipose tissue research.[74] . They have allowed researchers to understand the molecular processes that control adipose tissue development, differentiation, and functions [75]. These models have been useful to study the effects of drugs, hormones, and diet on adipocyte activity and metabolism of adipose tissue, as well as they contributed to elucidate key pathways that contribute to the development of obesity and associated metabolic diseases such as type 2 diabetes[76].

The murine 3T3-L1 cell line, which can develop into mature adipocytes *in vitro*, is one of the most widely used cell models to study adipose tissue. This cell line provides a reliable and repeatable system for exploring the molecular mechanisms of adipogenesis, lipogenesis, lipolysis, and browning[77].

The 3T3-F442A cell line is another cell line derived from murine Swiss 3T3 cells which accumulates more fat than 3T3-L1 cells without being exposed to glucocorticoids for differentiation[78]. Although less frequently used compared to 3T3-L1 cells, this cell line has been used to study adipogenic differentiation under the influence of various drugs[79]. Additionally, gene silencing studies have been performed using this cell line to investigate the effect of alkaline phosphatase on lipid metabolism, gene expression, and the secretion of adipokines[80].

The OP9 mouse cell line is another *in vitro* adipocyte model derived from mouse bone marrow. These cells accumulate large lipid droplets filled with triacylglycerol after exposure to acute adipogenic stimuli[81]. This cell line has been studied for the antiadipogenic and antilipolytic effect of various compound such as quercetin and ascorbic acid[82,83]. Xiao et al. (2011) demonstrated the formation of reactive oxygen species (ROX) in OP9 cells after lipid uptake that were significantly suppressed with fullerene treatment[84].

In addition, primary adipocytes can also be used *in vitro* to study various aspects of adipose tissue biology which can be obtained from human or animal tissues[85]. For instance, murine primary brown adipocytes from the interscapular region have been a useful tool to study brown adipogenesis under the treatment of various compounds[86]. Adipose derived stem cells (ADSCs) are derived from SVF of adipose tissue, and they present characteristics of actual adipocytes once differentiated[87]. They are multipotent and has the potential to differentiate to other cells such as chondrocytes, osteocytes, and myocytes. They have high expansion ability and can be passaged numerous times and cryopreserved for long time period. Differentiation can be induced in these cells using 3-isobutyl-1-methylxanthine (IBMX), indomethacin and dexamethasone (DEX)[88].

Some other cell lines that I have used in my study are discussed below.

4.1 Simpson-Golabi-Behmel Syndrome (SGBS) cells strain

Simpson-Golabi-Behmel Syndrome (SGBS) cells are recognized as a representative *in vitro* model more suitable than mouse models for studying the biology of human white subcutaneous preadipocytes. Indeed, the SGBS model has been widely used to analyse key signalling pathways, networks, and regulators[89]. This strain was established in 2001 by Wabitsch and colleagues, who isolated preadipocytes from the subcutaneous adipose tissue of pediatric patients with SGBS[90]. This syndrome is X-linked and characterized by pre and postnatal overgrowth, developmental delay, macrocephaly, polydactyly, and many other malformations[91].

Although SGBS cells are neither immortalized nor transformed, they retain the ability to expand and differentiate into mature adipocytes over a high number of generations. However, this ability has not been shown to be related to mutations in the X-lineage gene Glypican 3 (GPC3)[92]. Moreover, SGBS cells are the only fully inducible human pre-adipocyte cell line[93] and for these reasons, these cells are an excellent model for obesity research and have been used extensively in recent years[94].

During differentiation, these adipocytes exhibit a transient brown phenotype[95,96], due to a sharp increase in the expression of canonical BAT markers, such as UCP1, around the 14th day of differentiation. However, this feature can be due to the action of rosiglitazone in the medium[97]. At later time points in adipogenesis, morphological changes in lipid droplets and mitochondria, and a decrease in the expression of BAT markers indicate the induction of a white adipocyte differentiation program.

Morphological dynamics of lipid droplets and mitochondria, consistent with energy expenditure, have been observed in SGBS cells during 21 days of differentiation. The expression of genes involved in adipocyte differentiation was upregulated at different stages, and the highest expression of hormone sensitive lipase (LIPE), UCP1 and PPARGC1A was observed after 14 and 21 days of differentiation. The mitochondrial morphology changed during differentiation and reflected an increase in fragmentation at day 21 to support uncoupled fatty acid oxidation overall, and the transient phenotype of SGBS cells[98].

Additionally, Klusóczki, et al. (2019) investigated SGBS cells in response to prolonged PPARγ ligand stimulation or irisin administration. It was reported that the SGBS cells can transform into beige adipocytes with multilocular lipid droplets, elevated UCP1 levels, and the expression of browning genes such as CIDEA and elongation of very long fatty acid protein 3 (ELOVL3), PPARGC1A and TBX1[99]. However, the expression level of these genes was dependent on the presence or absence and the exposure time to PPARγ ligand or irisin. The expression of CEBP and PPARγ was unaffected by the different treatment. According to the study the beige phenotype can be sustained over time, though it can be partially reversed by removing the PPAR ligand[100]. Therefore, the SGBS cells can be used as a cellular model to investigate the differentiation and function of white and sustainable beige adipocytes.

4.2. Mice inguinal white adipose tissue cells

In mice, the inguinal white adipose tissue (iWAT) is a subcutaneous depot that runs from the pelvis dorsally and extends ventrally down the hindlimb to the thigh. This is the largest subcutaneous depot, weighing approximately 500mg. Other names of this depot include flank subcutaneous WAT or posterior subcutaneous fat. It is comprised of the dorsolumbar and inguinal portions, which cannot be visually distinguished except tin cold acclimated mice when the dorsolumbar portion acquires a brown colour[101](**Fig. 4**).

iWAT has received considerable attention in recent years because of its importance in energy metabolism and its potential role in the development of metabolic diseases such as obesity[102]. Unlike other forms of WAT, iWAT has a unique gene expression profile and is more metabolically active, releasing more lipids into the bloodstream compared to other forms of WAT[103]. This makes it a critical component of energy balance and metabolism and it has been implicated in the development of obesity and related metabolic disorders.

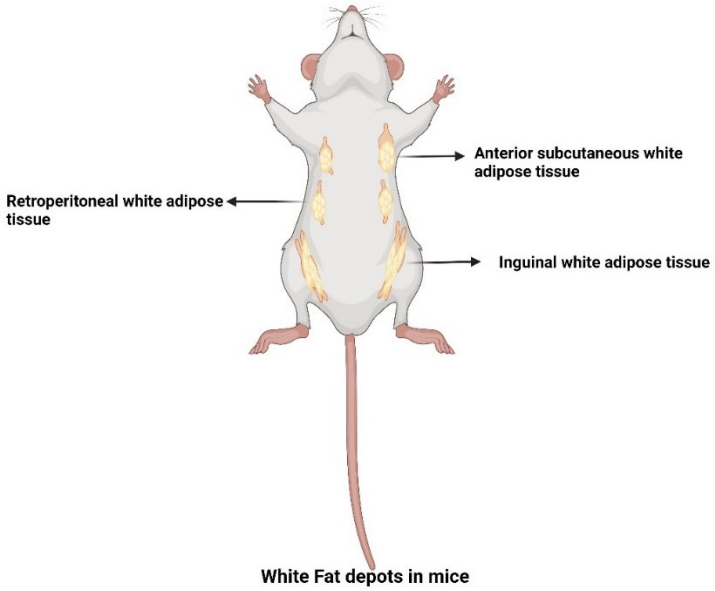

Figure 4. Distribution of WAT depots in mice (created in Bio Render according to Zhang et al., 2018) [104].

4.2.1 Browning potential of iWAT

iWAT has a high browning potential, making it an attractive target for research. Studies have shown that the activation of browning in this region can lead to increased energy expenditure and improved glucose metabolism[105]. In addition, the activation of browning in the inguinal region has been associated with a reduction in body weight and fat mass[106], making it a promising target for the treatment of obesity. Several factors can impact the browning potential: for example, age, genetics, and diet[107]. In addition, hormonal factors, such as changes in leptin levels, can also impact the browning potential of iWAT [108]. Despite the promising results of studies on the browning potential of iWAT, further research is needed to fully understand the underlying mechanisms and to develop effective strategies for promoting browning in this area. This may involve the use of drugs, lifestyle interventions, or other interventions to enhance the activation of brown adipose tissue in the inguinal region.

Moreover, the process of browning in iWAT through β-adrenergic agonists relies on autocrine FGF21 signalling. The FGF21 and co-receptor β-Klotho plays a crucial role in this process, as adipose specific deletion of β-Klotho leads to a lack of response to β-adrenergic stimulation. However, liver specific ablation of FGF21, which eliminates circulating FGF21, does not affect the response of iWAT to β-adrenergic browning [109]. The β-adrenergic dependent increase in circulating FGF21 happens indirectly, where fatty acids released by adipocyte lipolysis activate hepatic PPARα to increase FGF21

expression revealing FGF21 as a cell autonomous autocrine regulator of adipose tissue function[110].

5. Induction of adipose tissue browning as a strategy to treat obesity

The development of BAT oriented techniques to increase energy expenditure and combat obesity could be aided by understanding the molecular mechanisms that control brown adipocyte activity and differentiation[111]. Because of its ability to burn calories and produce heat, BAT has attracted considerable interest in recent years. This makes it an attractive target for the treatment of obesity and related metabolic diseases. Promoting beiging, or browning of white adipose tissue, is therefore a viable method for improving metabolic health[112]. Various strategies have been explored for this purpose, including the use of drugs, genetic engineering, and dietary modifications[113,114].

The use of β-adrenergic agonists, such as isoproterenol and clenbuterol, is one of the most promising drug methods. These drugs promote the expression of genes involved in the development and activation of BAT and the sympathetic nervous system. However, long term use of β-adrenergic agonists is discouraged because of their potential side effects, including heart palpitations, tachycardia, and tremors,[115]. In addition to drug methods, genetic methods have also been developed to achieve browning of white adipose tissue. One of these methods is overexpression of UCP1 in target tissue such as in fatty liver[116]. In addition, certain transcription factors such as PRDM16, which are important for controlling differentiation and activation of BAT can also be over expressed by genetic engineering[117]. Another strategy is to alter the expression of microRNAs that can control target genes involved in the activation of BAT[118].

5.1 Dietary factors promoting browning and thermogenesis.

Natural compounds, or nutraceuticals could be a potential strategy for developing safe and effective drugs for obesity treatment. A more promising field for obesity therapeutics could be the activation of molecular pathways involved in energy expenditure. There is evidence that compounds that affect white adipose tissue browning or increase energy expenditure may be effective in treating obesity[119]. Nutraceuticals are compounds found in foods or dietary supplements that are potentially beneficial to health. Some nutraceuticals, such as curcumin, resveratrol, and capsaicin, have been shown to

have the potential to stimulate the browning of WAT, resulting in increased energy expenditure and improved insulin sensitivity[120,121].

In addition, numerous natural substances have also anti adipogenic properties. By understanding the mechanism of action of these supplements we can identify potential health benefits and better tailor treatment according to patient needs [122]. Some of the nutraceuticals that are studied for their anti adipogenic, and browning effect compounds are discussed below.

Coffee (CF), oleuropein (OLE), docosahexaenoic acid (DHA), *Silybum marianum*, *Citrus aurantium*, *Taraxacum officinale* (TO), resveratrol (RE), *Curcuma longa*, and *Citrus aurantium* was investigated for their anti adipogenic effects. The finding demonstrated that DHA, RE, and CF were the most potent adipogenesis inhibitor[123]. Adipogenesis inhibiting genes including GATA2, GATA3, wingless related integration site 1 (WNT1), WNT3A, soluble frizzled related proteins (SFRP5), and delta like Non-Canonical Notch Ligand 1 (DLK1) were significantly upregulated by CF therapy, whereas adipogenesis promoting genes like CCND1, CEBPB, and SREBF1 were significantly downregulated. Apoptosis was most effectively induced by TO, triglyceride build up by DHA, CF, and RE was reduced, and lipolysis was suitably raised by CF, DHA, and OLE[124].

The exact mechanism by which dietary supplements induce the WAT browning is still under investigation. It is thought to be related to the activation of specific signalling pathways, such as AMPK and PPARγ[125]. These signalling pathways have been shown to play a key role in regulating the differentiation and activation of BAT. Nutraceuticals have been shown to increase their activity and promote the conversion of WAT into BAT like cells[126].

Curcumin is a polyphenolic compound extracted from *Curcuma longa*, an active ingredient in turmeric that activates AMPK which is a modulator of adipocyte differentiation and WAT browning. It increases mitochondrial biogenesis, down regulates the expression of WAT associated genes such as *Ppar, C/ebpα*, and upregulates the expression of BAT related genes such as UCP1 in iWAT by promoting the secretion of NE from the sympathetic nervous system that ultimately activates the β3 AR pathway[127]. Similarly, curcumin significantly increased basic mitochondrial respiration, ATP production, and uncoupling capacity of mature adipocytes in high fat diet obese mice by regulating *Pparγ* signalling pathways[128]. In addition, it remarkably increased the mRNA level of *Ucp1, Ppargc1a*, positive regulate *Prdm16*, and *Pparγ* in vivo and in vitro[129].

Resveratrol is a polyphenol that is commonly found in skin grapes (*Vitis vinifera* L.), berries, and red wine. It stimulates the expression of *Ucp1* by promoting the expression and activity of SIRT1, a histone deacetylase class III, which has been shown to play a role in regulating metabolic processes and inducing browning in WAT. SIRT1 interacts with promoters of genes involved in fatty acid oxidation, thermogenesis, and energy metabolism[130]. In addition, resveratrol has been shown to promote the expression of browning associated genes by activating AMPK through increasing its phosphorylation. Activation of AMPK induce the expression of PGC1α, which in turn induces the expression of UCP1 through direct interaction with its promoter region and stimulates the expression of other thermogenic genes[131],[132].

Capsaicin an active ingredient found in the fruit of *Capsicum* spp. (hot pepper), which increases the oxidation of fatty acids and promotes the browning of WAT by increasing the expression of key brown fat markers such as UCP1[133]. Capsaicin at a concentration of 1μM had the greatest effect on 3T3-L1 cells after 8 days of differentiation, leading to increased expression of brown adipocyte markers and upregulation of the TRPV1 receptor. This was confirmed by the detection of Ca^{2+} flux caused by TRPV1 activation and the expression of *Ucp1*[134] Capsaicin also triggered a beige phenotype by increasing the expression of *Ucp1, Tbx1, Prdm16, and Pgc1α* in 3T3-L1 cells. Treatment with NE alone or in combination with capsaicin resulted in a reduction in lipid droplet size and surface area in both 3T3-L1 and X9 cells[135]. Moreover, another study reported that capsaicin induces activation of AMPK and the stimulation of SIRT1 expression and activity. This activation of AMPK has been found to play an important role in regulating energy metabolism by increasing fat oxidation and decreasing *de novo* lipogenesis.[136].

Quercetin, a flavonoid commonly found in fruits and vegetables, has been shown to have a browning effect on white adipose tissue[137]. In mice, a high-fat diet (HFD) containing 1% quercetin lowered blood cholesterol levels and promoted weight loss compared to mice fed only high-fat diet. Quercetin was found to activate several signalling pathways involved in regulating energy metabolism and browning of WAT, including activation of AMPK and stimulation of SIRT1 expression and activation[138]. Phosphorylated AMPK increased the expression of *Pgc1α, Ucp1, Adrb3, and Cidea* in BAT compared to HFD[139]. In addition, quercetin was found to reduce oxidative stress and inflammation in WAT, which is believed to be a result of its antioxidant and anti-inflammatory properties.[140].

Theobromine (TB, 3,7dimethylxanthine) is the principal alkaloid of *Theobroma cacao*, abundant in cocoa beans and dark chocolate. The effect of this compound on cell cycle, adipogenesis, and cytokine release was studied using SGBS cell line as a model for human adipocytes[141]. It was found that TB significantly inhibited cell proliferation at a concentration of 200µg/ml. Quantitative analysis of the effect of TB on SGBS cell differentiation showed partial but significant inhibition of adipocyte differentiation from day 8 to day 14[142]. TB also decreased the levels of proinflammatory cytokines such as MCP1 and IL1β. The antiadipogenic effect of TB involves the suppression of adenosine receptor 1 signalling, which is associated with adipogenesis[143]. In addition, TB treatment in mouse derived primary adipocytes led to an increase in the expression of UCP1 protein and mitochondrial content dependent on the activation of *Pparγ* ligand. It also stimulated the phosphorylation of *Pgc1α* and increased its interaction with *Pparγ* in adipose derived stem cells (ASCs)[144]. TB treatment at a concentration of 0.1% increased the expression of *Ucp1, Elovel3, Cidea, Cox7a1, Cox8b,* and *Cpt1b*, in mouse derived iWAT cells[145] suggesting its browning ability and a potential drug for the treatment of obesity.

Cocoa tea (*Camellia ptilophylla*) is a source of antioxidants that have been shown to have therapeutic effects against inflammation, hypertension, endothelial dysfunction, and oxidative stress[146]. Instead of caffeine, cocoa tea contains theobromine and the main catechin is gallocatechin gallate (GCG). The anti-obesity effect of cocoa tea has already been studied in 3T3-L1 mouse cell lines. It was found that cocoa tea significantly inhibited the accumulation of triglycerides in mature adipocytes[147]. Cocoa tea downregulated the expression of *Pparγ* and *C/Ebpα*, consequently, the expression of adipogenic genes was downregulated demonstrating the anti-obesity effect of cocoa tea in mouse 3T3-L1 cells[148].

Oleuropein, a natural polyphenol extracted from olive leaves, exerts beneficial effects such as antioxidant, anti-cancer, and anti-obesity[149]. *In vivo* studies have shown their biochemical and pharmacological properties in improving insulin resistance in high fat diet induced diabetes in rats by reducing tumour necrosis factor-alpha (*Tnf-α*), and interleukin-6 (*Il-6*)[150]. In rats, a high-fat diet significantly decreased the expression of *Ucp1* and the beige fat marker *Cd137* in adipose tissue by 70.4% and 97.2%, respectively. In contrast, physical exercise, oleuropein administration, and a combination of both simultaneously with a high-fat diet increased *Ucp1* expression by 2.13-, 1.71-, and 2.04-fold respectively, and *Cd137* expression by 25.71-, 21.75-, and 26.59-fold, respectively as compared with the HFD group[151].

Allicin is the main bioactive ingredient in garlic[152], with multiple pharmacological functions, such as anti-oxidative stress, anti-tumour and cholesterol lowering effects, anti-platelet aggregation, prevention of cardiovascular disease, and anti-inflammatory capacity[153,154]. Allicin treatment was found to reduce the size of lipid droplets and enhance the expression of UCP1 and OXPHOS-related protein in BAT[155]. In HFD mice, the administration of allicin led to a significant increase in the expression of genes associated with thermogenesis and energy expenditure. These genes include *Ucp1, Prdm16*, *Ppargc1a*/B, Carnitine palmitoyl transferase 1A (*Cpt1*α), and medium-chain acyl coenzyme A dehydrogenase (*MCAD*), in the BAT. It activates BAT through Sirt1-PGC1α-Tfam pathway, and it may increase the succinylation of Ucp1 by inhibiting Sirt5. Allicin treatment upregulate the expression of downstream proteins of Sirt1, including PGC1α, nuclear respiratory factor 1 (NRF1), and Tfam, which are involved in the PGC1α Tfam signaling pathway. It increases SIRT1 activity by increasing its phosphorylation levels, and this leads to the deacetylation of PGC1α, ultimately resulting in the generation of mitochondria in BATs. These results suggest that allicin can stimulate whole body energy expenditure and reduce adiposity by activating BAT in mice[156]. In addition, allicin was found to increase the expression of brown adipocyte markers, such as *Ucp1* in 3T3-L1 and differentiated iWAT from SVF.

In another study allicin was shown to increase of KLF15 protein expression and its interaction with the UCP1 promoter region. This effect was absent in cells lacking KLF15, indicating the crucial role of KLF15 in the action of allicin. Thus, allicin was found to induce brown like adipogenesis *in vivo*, associated with the appearance of multilocular adipocytes, increased UCP1 expression, and increased lipid oxidation. Collectively, these results suggest that allicin has the potential to prevent obesity and related metabolic disorders, such as type 2 diabetes mellitus, by increasing the expression of brown adipocyte specific genes, including UCP1, *via* the KLF15 pathway[157].

Taurine is a sulfur containing amino acid commonly found in animal tissues, including heart and skeletal muscle[158]. In recent years, the possible role of taurine in the regulation of metabolism has been investigated, particularly in the process of white adipose tissue browning. Studies have shown that taurine supplementation increases the expression of *Ucp1* in the inguinal fat pads of mice. This increase in *Ucp1* expression leads to an increase in energy expenditure, and a decrease in iWAT mass. In addition, taurine has been shown to regulate the activation of several signalling pathways involved in the browning process, including activation of the AMPK pathway and the regulation

of the PGC1-α pathway[159]. Taurine-mediated browning also occurs through a mechanism involving activation of the Transient Receptor Potential Channel Melastatin Subfamily Member 8 (TRPM8), which stimulates the expression of genes involved in thermogenesis s and oxidative metabolism. The effects of taurine contribute to an overall increase in energy expenditure, leading to a reduction in body fat and an improvement in metabolic health[160].

Secretin is a hormone produced mainly in the small intestine that regulates digestive processes. It induces meal related BAT thermogenesis and causes satiety in mice[161]. Secretin receptors are significantly expressed in BAT. Increased circulating secretin levels initiate lipolysis by binding to secretin receptors on the surface of BAT and induce the *Ucp1* expression thereby initiating UCP1-dependent thermogenesis[162]. Recent studies suggest that secretin may play a role in the activation of BAT by increasing the release of NE, a neurotransmitter that has been shown to stimulate thermogenesis from BAT. Secretin may also modulate the activity of certain signalling pathways in BAT, such as the MAPK/ERK pathway, which is involved in the regulation of cellular metabolism and energy homeostasis[163].

6. Pharmacophore screening and Network Pharmacology

Network pharmacology is a new field of research that aims to predict the potential targets and active ingredients of bio compounds or drugs. As a comprehensive and systematic analytical approach, network pharmacology was applied to understand the mechanism of complex potentially bioactive constituents[164] and to develop better therapeutic strategies[165]. A key advantage of network pharmacology is that it can address the multiple and interrelated targets of drugs and could be applied to a variety of diseases, including cancer, neurological disorders, and cardiovascular disease. Researchers have used network pharmacology to identify new targets for the treatment of breast cancer and to understand the underlying mechanism of Alzheimer's disease. This approach has also been used to develop personalized medicine, in which drugs are tailored to the specific genetic and molecular profiles of individual patients.

PubChem (https://pubchem.ncbi.nlm.nih.gov/) is a publicly accessible database maintained by the National Centre for Biotechnology Information (NCBI) that provides information on the biological activities of millions of chemical substances. It provides access to a vast amount of data on the biological activities and properties of chemical

substances, which can be used as a starting point for network pharmacology studies. PubChem contains information on the structures, properties, and activities of chemical substances and provides access to a large collection of scientific data including over 150 million compounds. The database enables researchers to identify potential targets involved in the molecular mechanisms of drug action and to perform *in silico* studies to predict the potential efficacy and side effect of drugs[166]. By integrating and analysing data from PubChem with other sources, researchers can gain a deeper understanding of the complex relationships between drugs and their targets, which can help to guide the development of more effective and safer drugs (**Fig. 5**).

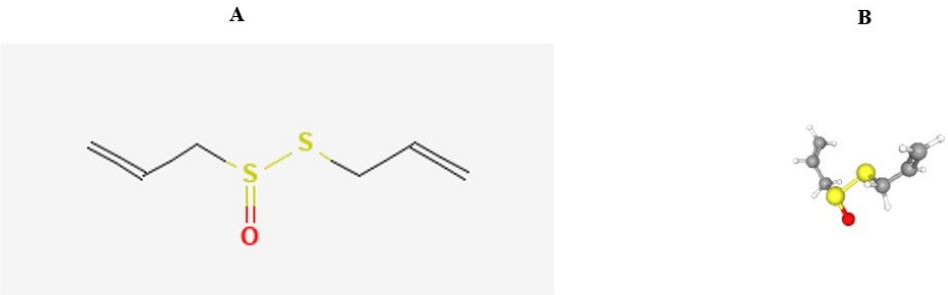

Figure 5. Structure of allicin. (**A**) 2D structure, (**B**) 3D structure (source: pubchem.ncbi.nlm.nih.gov).

A variety of software and online services for predicting the protein targets of small molecules have been developed such as, Pharm Mapper[167], INVDOCK[168], similarity ensemble approach (SEA) [169], tool for interactions of chemicals (STITCH) [170] and Gene Card[171] which are among the earliest tools for shape screening, pharmacophore screening and reverse docking, respectively.

Pharmacophore modelling is a computer aided drug design approach that implies that when the ligand interacts with the macromolecular target, the active conformation should be generated in geometric and energetic agreement with the target. The pharmacophore is considered as the greatest common denominator of the molecular interaction properties of a group of active molecules. Any type of atom or group in the ligand that exhibits certain properties related to molecular recognition can be assigned to pharmacophore features, e.g., hydrophobic regions, hydrogen bonding acceptors/donors, aromatic ring systems, negatively ionizable groups, positively ionizable groups, and any

possible combination[172]. The biological activity of a compound can be evaluated when the compound binds to a specific macromolecule and elicits a specific response.

PharmMapper is a web server that allows researchers to identify potential targets of a molecule such as natural compounds or drug using pharmacophore modelling[173]. The targets are predicted based on the chemical and structural similarities between the test molecule and proteins in the database. The database is freely accessible with a simple user interface where the 2D or 3D structure of the target molecular is uploaded, the parameters are set, and the query is submitted. The output result is a list of potential target proteins organized in descending order based on fit score which is the predicted binding affinity for the test molecule. The chemical structures of the molecules can be used to predict the biological activities of the compounds using computational method such as SEA. The structure is compared to other reference compounds whose biological activities are known. The tool then calculates a score which is based on structural similarities among the target compound and references compounds[174]. Based on the chemical structure the interaction between the target molecules and proteins can be predicted using STITCH[175]. Importantly, this tool can also provide information about the tissue where the interaction has more chances to occur as well as the strength of interaction. Overall, the database is a powerful computational tool to predict the molecular mechanisms of a biological process and assist researchers in identifying potential targets of a drug. The GeneCards database provides a detailed information about all annotated and predicted human genes integrating data from more than 150 data sources such as NCBI and Ensembl. In addition to basic information of each gene such as sequence and location, it also provides other useful information about gene expression, regulation, protein interaction and associated disorders. The information can help to increase understanding of the genetic basis of health and disease conditions. To predict the potential target of bioactive compounds in humans an online tool known as swiss target prediction (STP) is available[176]. The tool provides useful information in understanding the underlying molecular mechanism of a compound and to predict its non-target effects.

Once the gene targets are selected, GeneMANIA (https://genemania.org) is used to predict the function of a gene and identify genes with similar function and their interaction with other proteins[177]. The tool integrates data from various dataset that include protein-protein, protein-DNA and genetic interactions, pathways, reactions, gene and protein expression data, protein domains and phenotypic screening profiles.

7. Aim of the thesis

The aims of the Ph.D. project are:

1) To investigate transcriptomic changes during differentiation of SGBS cells to identify changes in the gene expression and pathways involved during transient phenotype.
2) To investigate the browning effect of allicin on mitochondrial morphology, lipid droplet dynamics, and gene expression changes by evaluating its ability to activate genes involved in beige adipocyte development and thermogenesis using transcriptomic data and a network pharmacology approach.

II. Materials and methods

8. Chemicals and Culture Media

The chemicals and culture media used in the experiments of the research project, as well as the buffers and solvents are listed in the Tables 1 and 2. Kits and chemicals for RNA extraction, cDNA synthesis and amplification are listed in Table 3. Table 4 contains the list of products and dies used in structural analysis, immunofluorescence, and Western blotting.

Table 1 Reagents and media for cell culture and buffer preparation

Product	Identifier	Source
DMEM/F12 (1:1)	31330038	Thermo Fisher Scientific
High glucose DMEM, GlutaMAX™ supplement	10566016	Thermo Fisher Scientific
Low glucose DMEM, GlutaMax ™ supplement	10567014	Thermo Fisher Scientific
Biotin	B4639	Sigma-Aldrich
D-pantothenic acid hemi calcium salt	P5155	Sigma-Aldrich
Penicillin-streptomycin	15140122	Thermo Fish Scientific
Fetal bovine serum	10270106	Thermo Fisher Scientific
Human apo-Transferrin	T2252	Sigma-Aldrich
Human insulin	I1507	Sigma-Aldrich
Hydrocortisone	H0888	Sigma-Aldrich
3,3',5-Triiodo-L-thyronine sodium salt	T6397	Sigma-Aldrich
Dexamethasone	D1756	Sigma-Aldrich
3-Isobutyl-1-methylxanthine	5879	Sigma-Aldrich
Rosiglitazone	71740	Cayman Chemical
Thiazolyl blue tetrazolium bromide (MTT)	M5655	Sigma-Aldrich
Allicin	IA1100	Solarbio® Life Sciences

Table 2 Salts, buffer, and solvents

Reagent	Identifier	Source
Sodium chloride	S7653	Sigma-Aldrich
Potassium chloride	P9333	Sigma-Aldrich
Sodium Phosphate dibasic	S7907	Sigma-Aldrich
Potassium phosphate monobasic	P5655	Sigma-Aldrich
Hank's balanced salt solution	ECM0507L	Euroclone S.p. A
HEPES buffer	ECM0180D	Euroclone S.p. A
Tween 20	P7949	Sigma-Aldrich
Absolute ethanol	3096052	Carlo Erba reagents S.r.l
2-propanol	I9516	Sigma-Aldrich
Dimethyl sulfoxide	D2650	Sigma-Aldrich
Buffer neutral 10% formalin	05-01004F	Bio-Optica S.p.A

Table 3 Reagents and kits used for RNA extraction and analyses.

Product	Code	Source
TRIzol™ reagent	15596026	Thermo Fisher Scientific
Chloroform	C2432	Sigma-Aldrich
PureLink™ RNA Mini Kit	12183018A	Thermo Fisher Scientific
SuperScript™ III one-step RT-PCR system	12574026	Thermo Fisher Scientific
Agarose	EMR010001	Euroclone S.p.A.
GelRed®	41003	Biotium
1 kb DNA ladder	31022	Biotium
Tris-borate-EDTA (TBE)	AM9863	Thermo Fisher Scientific
ImProm-II™ Reverse Transcription System	A3800	Promega Corporation
Transcription High-Fidelity cDNA Synthesis Kit	5091284001	Roche Diagnostics
Platinum™ SYBR™ Green qPCR SuperMix-UDG	11733046	Thermo Fisher Scientific

Table 4 Reagents for Immunofluorescence and Western blotting

Reagents	Identifier	Source
Fluorescent dyes		
BODIPY™	D3922	Thermofisher Scientific
Mitotracker Orange CMTMRos	M7510	Thermofischer Scientific
Fluoroshield mounting medium with DAPI	ab104139	Abcam
Protein Expression analysis		
TritonTM X 100	T9284	Sigma-Aldrich
Glycine	G8898	Sigma-Aldrich
Ammonium chloride	A9434	Sigma-Aldrich
Normal goat	S-1000	Vector Laboratories
Bovin Serum Albumine (BSA)	A7906	Sigma-Aldrich
Fat free milk powder	-	Semper, Sweden
ECL detection reagent	RPN2232	Amersham Biosciences
12% polyacrylamide gel (acrylamide/bis-acrylamide, 37.5:1)	1610159	Bio-Rad
Polyvinylidene difluoride (PVDF) membranes	IPVH0001	Millipore Corporation
Antibodies		
Anti-rabbit Alexa FluorR 555	ab150078	Abcam
Anti-rabbit fluorescein IgG	FI-1000	Vector Laboratories
Anti-mouse fluorescein IgM	FI-2020	Vector Laboratories
Anti-rabbit IRdyeR 800 CW	925-32211	LI-COR Inc.
Anti UCP1	AB10983	Abcam
Anti-rabbit IgG	7074	Cell Signaling

9. Cell Culture

The experiments are mainly performed on human SGBS cells strain. In addition, experiments were also performed on iWAT cells isolated from C57BL/6 mice.

The human liver cell line HepG2 was used to study the expression capacity and functional effects of different mutant variants of the thermogenic protein UCP1 (Appendix).

9.1 SGBS cell culture

Human SGBS cells were kindly provided by Prof. M. Wabitsch (University of Ulm, Germany). Cells were grown in DMEM/F-12 supplemented with 10% FBS, 3.3 mM biotin, 1.7 mM pantothenate, and 1% penicillin/streptomycin solution, at 37°C with 5% CO_2 and 95% relative humidity. Differentiation was induced on confluent cells after washing the cells 2 times with phosphate buffer saline (PBS). Differentiation medium consisted of serum-free growth medium supplemented with 10 µg/ml transferrin, 0.2 nM triiodothyronine (T_3), 250 nM hydrocortisone, 20 nM human insulin, 25 nM dexamethasone, 250 µM (IBMX) and 2 µM rosiglitazone (day 0 of differentiation). After 4 days, the differentiation medium was replaced with a maintenance medium composed of a serum-free growth medium supplemented with 10 µg/ml transferrin, 0.2 nM T_3, 250 nM hydrocortisone, and 20 nM human insulin. Fresh maintenance medium was added every 4 days. The protocol for cell proliferation, differentiation, and maintenance was developed elsewhere[178]. A complete list of mediums and reagents is listed below (Table 5).

Table 5 Formulation of SGBS cells culture media as reported by Wabitsch et al., 2001[179].

Reagents	Growth medium	Differentiation medium	Maintenance medium
Basal Medium	DMEM/F12	DMEM/F12	DMEM/F12
FBS	10%	-	-
P/S	1%	1%	1%
Biotin	33µM	33µM	33µM
Pantothenic acid	17µM	17µM	17µM
Human transferrin	-	10µg/ml	10ug/ml
Triiodothyronine	-	0.2nM	0.2nM

Hydrocortisone	-	100nM	100nM
Human Insulin	-	20nM	20nM
Dexamethasone	-	25nM	-
IBMX	-	250µM	-
Rosiglitazone	-	2µM	-

9.2 Primary inguinal white adipose tissue cell culture

Mice were kept in a thermoneutral condition for 3-4 weeks after birth. On the day of the experiment, HEPES buffer solution was prepared for tissue digestion prior to entering the animal facility. Table 7 contains the reagents that constitute the HEPES buffer solution.

The protocol of harvesting adipose tissue from mice and subsequent cell culture involves first euthanizing the mice with CO_2 and disinfecting the skin around the inguinal area. Using sterile scissor and forceps, the inguinal adipose tissue was then excised and placed in a sterile dish containing fresh DMEM. The tissue was then digested into small pieces using a digestion buffer containing HEPES buffer and collagenase and incubated at 37°C for 30 minutes with constant shaking. After the incubation period, the digested tissue was filtered through a 250µm nylon filter to remove any remaining tissue debris. The filtered tissue was then put on ice for 20 minutes to allow the mature fat cells and lipid droplets to float on the surface. The cell suspension was filtered again through a 25µm nylon filter and centrifuged to pellet the cells, which were then resuspended in DMEM and centrifuged again to wash the cells. The cells were then resuspended in DMEM and centrifuged again to wash the cells. The cells were then resuspended in a growth medium consisting of DMEM supplemented with 10% fetal calf serum, antibiotics, glutamine, sodium ascorbate, and insulin. Finally, the cells were plated onto a tissue culture dish and incubated at 37°C with 8% CO_2 (**Fig. 6**). Daily checks were performed to monitor cell confluency.

The next day the growth medium was refreshed. After a few days, the growth medium is replaced with a differentiation medium, which promotes the differentiation of preadipocytes into mature adipocytes. The differentiation medium developed by Guo et al. typically consists of DMEM supplemented with 10% FCS, insulin, dexamethasone, IBMX, rosiglitazone, and T3[180]. After day four of differentiation the cells were maintained in a maintenance medium. The medium was changed every two to three days, and after 7-10 days, mature adipocytes with visible LDs were visible under microscope.

Table 6 Formulation of medium for primary iWAT cells.

Reagents	Growth medium	Differentiation medium	Maintenance medium
Basal Medium	DMEM/F12 High Glucose	DMEM/F12High Glucose	DMEM/F12 High Glucose
Newborn Calf serum	10%	10%	10%
Insulin	4nM	85nM	85nM
HEPES	10mM	10mM	10mM
Glutamine	4mM	4mM	4mM
Penicillin	50IU	50IU	50IU
Streptomycin	50µg	50µg	50µg
Sodium ascorbate	25µg	25µg	25µg
Dexamethasone	-	1Mm	-
IBMX	-	250µM	-
Rosiglitazone	-	2µM	1µM

Table 7 Formulation of HEPES tissue digestion buffer developed by Cannon and Nedergaard, 2001[181].

Reagents	Concentration
NaCl	123mM
KCL	5mM
$CaCl_2$	1.3mM
Glucose	5mM
Crud serum albumin	1.5%
***N*-2-hydroxyethyl piperazine-*N'*-2-ethane sulfonic acid (HEPES)**	100mM

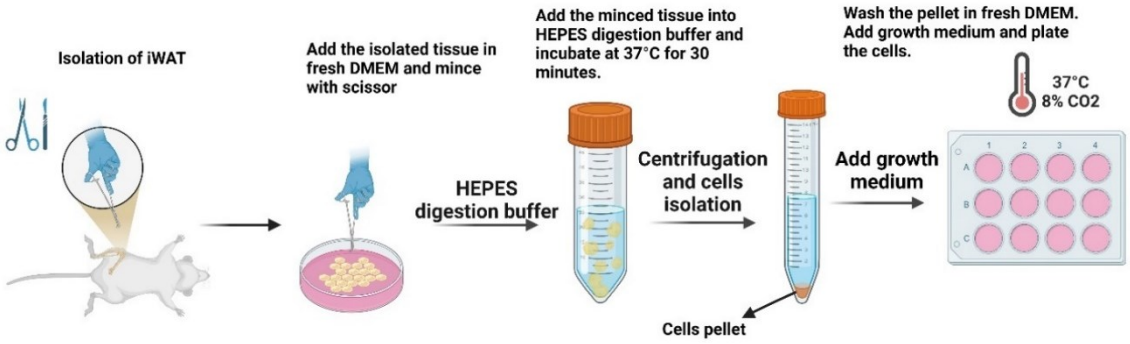

Figure 6. Steps of iWAT isolation and subsequent primary cell culture. (Image created in Bio Render).

10. Structural Analyses

10.1 BODIPY™ staining

BODIPY™, also known as 4,4-difluoro-1,2,5,7,8-pentamethly-4-bora-3a,4a-diaza-s-indacene, is a fluore1scent dye utilized for staining neutral lipids in biological samples. Cells for BODIPY™ staining and subsequent confocal imaging were cultured on ibiTreat 8-wells µ slides. On experiment day slides were fixed for 15 minutes at room temperature using a 2% formalin solution diluted in PBS 1X. Following fixing, the cells

were washed with PBS 1X and treated in the dark for 45 minutes at room temperature with 1mg/mL BODIPY™. After washing the stained cells three times with PBS 1X, they were mounted using a Fluor shield mounting media containing 4',6-diamidino-2-phenylindole (DAPI). Fluorescent images were obtained using either the epifluorescence Axio Observer Z1 microscope (Carl Zeiss GmbH) or the SP8 confocal microscope (Leica Microsystems GmbH) equipped with LAS X software, version 3.1.5.16308. Slides were observed with HC PL APO CS2 40X/1.10 WATER objective lens. BODIPY™ fluorescence was detected by white light laser (503/588nm). The images were acquired by a photomultiplier tube (PMT), which allowed point-by-point scanning of the region of interest (ROI) with the selected laser and produced 1024 X 1024 px images (**Fig 7**).

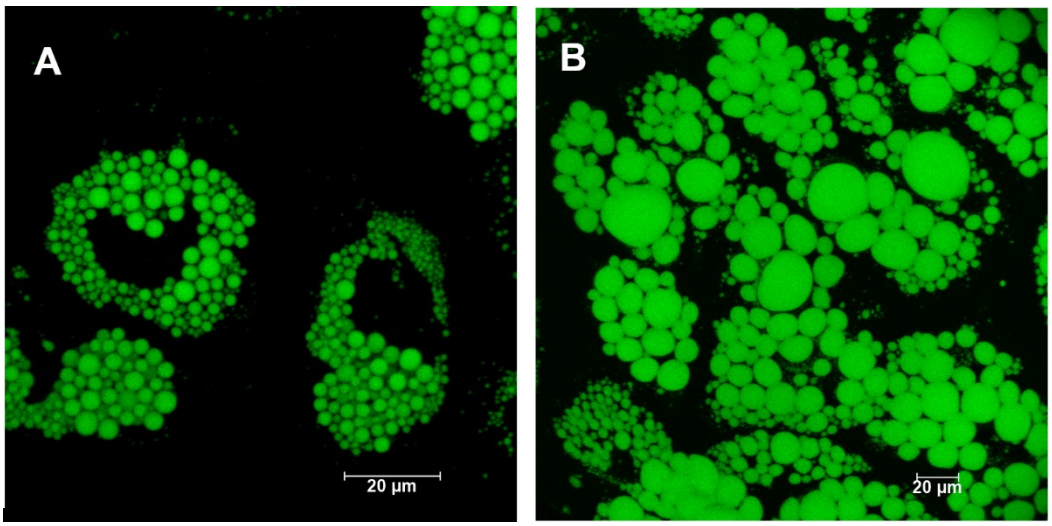

Figure 7. Detection of lipid droplets by BODIPY™ of SGBS adipocytes during differentiation. Confocal microscopy, scale bar = 20 µm. **A.** SGBS cells at 6 days of differentiation; **B.** SGBS cells at 10 days of differentiation.

10. 2 Lipid droplet (LD) dynamic analysis

Adipocyte browning process involves dynamic changes in lipid droplet, that can be analyzed using the MRI Lipid Droplets macro (http://dev.mri.cnrs.fr/projects/imagej-macros/wiki/LipidDroplets_Tool), for ImageJ software (http://rsb.info.nih.gov/ij/)[182]. The macro applied a bandpass filter and an automatic threshold to the BODIPY™ stained adipocyte images, producing a mask that removed artefacts. Contacting lipid droplets were separated by a binary watershed transformation and individual LDs were enclosed in single regions of interest (ROI) for which the software measured the area surface. The macro provided several data, including the number of LDs, their area surface, maximum ferret diameter (MFD), and integrate optical density (IOD). There is no theoretical

connection between the size and integrated optical density (IOD) of LDs, which are frequently employed to quantify the amount of lipid in cultured cells. To establish a mathematical relationship between size and IOD, a straightforward model was developed [183]. It is based on the spherical form of LDs and the Lambert-Beer law, which explains light absorption by an optical thick material. The model can be used to determine LDs subpopulations and calculate the absorption coefficient in the LDs population, which may be helpful for understanding cellular lipid related disorders[184]. MFD estimated the diameter of irregularly shaped objects, while IOD indicated the triglyceride content.

10.3 MitoTracker Staining

MitoTracker® Orange CMTMRos is a fluorescent dye commonly used to selectively label and visualize mitochondria in live cells. The accumulation of this in the mitochondria is dependent on their membrane potential, making it a useful tool for studying mitochondrial function and dynamics. According to a study by Chazotti (2011)[185], MitoTracker® Orange CMTMRos has been shown to selectively label mitochondria in a range of cell types, including various primary cells[186].

The MitoTracker® stock solution is diluted in cell growth medium to a final concentration of 100nM. The live cells are then incubated with the working solution for 30 minutes prior to fixation with 4% formalin. After fixation, cells were rinsed three times with PBS 1X, mounted in a DAPI containing mounting medium, and imaged using a Leica SP8 confocal microscope (Leica Microsystems, Germany) and LAS X 3.1.5.16308 software. Slides were viewed with the HCX PL APO lambda blue 63x/1.40 OIL objective. DAPI fluorescence was detected using a 405-diode laser (410/480 nm), while MitoTracker® fluorescence was detected using a white light laser (550/605 nm). Images were acquired using a photomultiplier tube (PMT) that allowed point by point scanning of the region of interest (ROI) with the selected laser and produced images with a resolution of 1024 x 1024 px.

10.4 Mitochondrial morphology analysis

The Mitochondrial Analyzer, an adaptive thresholding based tool in the open source ImageJ/Fiji image analysis platform, was utilized for quantifying mitochondrial morphology[187]. To optimize the image analysis, a block size of 1,350 µm and a C-value of 5 were applied for thresholding after 2D optimization. Other tools like MiNa[188] and

Micro2P[189] were also used for processing the images (**Fig. 8**). These tools provided a comprehensive analysis of mitochondrial morphology and connectivity, which can help in understanding the functional implications of mitochondrial changes during browning.

The Mitochondrial Analyzer provided various parameters including counts (number of mitochondria in the image), total area (sum of the area of all mitochondria in the image), mean area (total area/mitochondria number), total perimeter (sum of perimeter of all mitochondria in the image), mean perimeter (total perimeter/mitochondria number), mean aspect ratio (shape descriptor measuring elongation), and mean form factor (shape descriptor measuring round to filamentous shape). Morphological features of the mitochondrial network were also calculated, such as the number of branches, the total length of branches, the mean length of branches, the branch junctions, the endpoints of branches and the mean diameter of branches.

These features were also expressed as normalization to either the number of mitochondria or total area The MiNa tool, which is a macro of the ImageJ1.53o program (http://rsb.info.nih.gov/ij/), was used to quantify mitochondrial morphology. Threshold images were processed using the MiNa interface and the Top hat option. The macro recognized "individual" mitochondrial structures in a skeletonized image, such as punctate, rod-shaped, big, spherical structures without branches, and "networks," which were recognized as mitochondrial structures with a single node and three branches. The discriminant analysis made use of every parameter. The number of individuals (punctate, rod-shaped, and large/round mitochondria), the number of networks (items with at least one branch), and the mean rod/branch length, which is the average length of all mitochondrial rods/branches, were all taken into consideration in the study. The followed discriminant analysis also considered other factors, such as the mean number of branches per network (i.e., the mean number of mitochondrial branches per network), the mean length of branches, and the mitochondrial footprint (i.e., the total area of mitochondria).

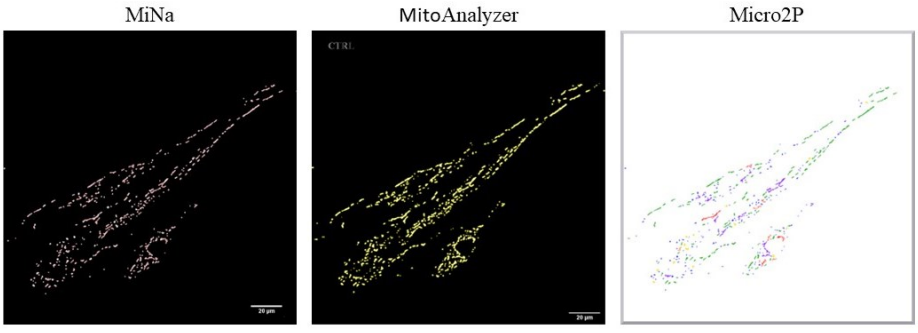

Figure 8. Mitochondrial morphology analysed with the three different tools.

MicroP software was utilized to classify six morphological types of mitochondria in SGBS cells, which included small globules, round-shaped mitochondria, large globules, simple tubules, twisted tubules, donuts, and branched tubules[190]. The total number of mitochondria and their area for each subtype were calculated for the different treatments of SGBS cells, and the data were used for discriminant analysis.

11. Cell viability assay

The MTT assay is a commonly used colorimetric assay for evaluating cell viability and metabolic activity. It is based on the ability of mitochondrial reductases in viable cells to convert the water soluble MTT reagent into an insoluble formazan product, which can be quantified by measuring the absorbance at 550nm. The MTT assay has been used to evaluate the cytotoxicity of a wide range of bioactive compounds, including natural products, synthetic chemicals, and nanoparticles, in various cell types[191,192]. However, it should be noted that the MTT assay measures metabolic activity rather than cell proliferation or cell death, and thus may not be an accurate indicator of cell viability under all conditions. Cells were treated with four different doses of allicin to examine the cytotoxic its effect on the cells. Based on cell viability assay 12.5µM dose allicin was chosen as safe for cells treatment (**Fig. 9**).

12. RNA extraction and Gene expression analysis

Purified RNA obtained from cell culture was used for all gene expression experiments. The experiments were set up with at least 2 biological replicates for the different experimental conditions. RNA was isolated by lysing cells with 1mL/10 cm^2 TRIzol reagent, which caused severe breakdown of cellular structures and preserved nucleic acid integrity when stored at -80°C. The isolated RNA was purified using the PureLink™ RNA Mini Kit according to the manufacturer's instructions.

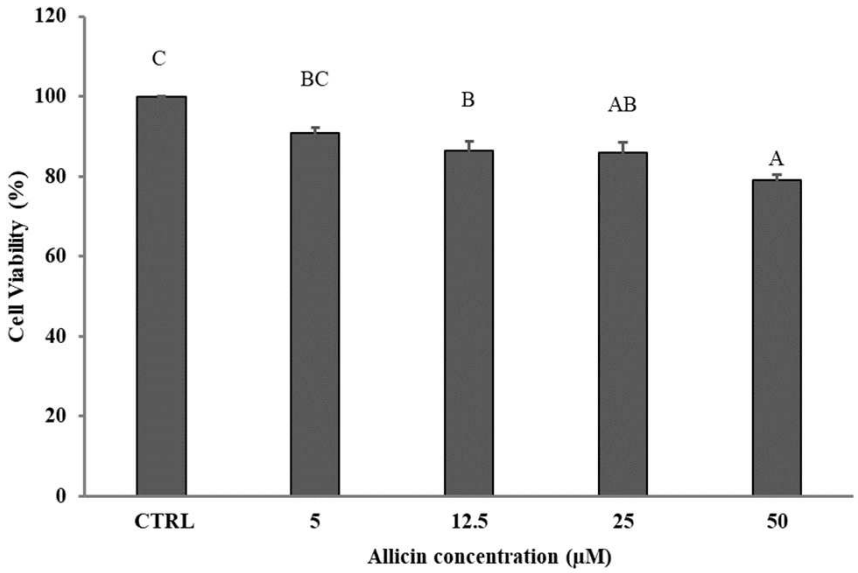

Figure 9. Cell viability assay performed on SGBS cells with different doses of allicin.

The concentration and quality of RNA were measured using either a NanoDrop 1000 spectrophotometer (ThermoScientific, Wilmington, Delaware), or the Spark multi plate reader (Tecan, CH). The purity of the RNA samples ranged from 1.8 to 1.9; RNA integrity was assessed by observing the 18S and 28S ribosomal bands after electrophoresis on 1% agarose gel, in the presence of GelRed. beta-actin expression was used as an internal control and confirmed the complete integrity of the RNA.

12.1 RT-PCR

Total RNA from each sample was reverse transcribed and amplified using an MJ thermal cycler (PT-100; MJ Research, Inc., Waltham, MA, USA).

The required primers for PCR amplification were designed using the Primer3 Input web tool[193]. In Table 8 the list of primers is reported. Among the various housekeeping genes, β-actin, and ribosomal protein lateral stalk subunit 0 (RPLP0) was selected as they were found to be more Stable in human adipocytes during preliminary trials.

RT-PCR cycle conditions were as follows: cDNA synthesis: 50 °C, 30 min; SuperScript III RT inactivation: 94 °C, 2 min; cDNA amplification: [94 °C (30 s), primers annealing at different temperatures according to Table 8 (30 s), 72 °C (30 s) 40 cycles]; ending of reaction: 72 °C (5 min).

PCR reactions carried out without reverse transcription of the RNA samples, using the same sets of primers, did not give any amplification product, ruling out the possibility that the observed bands may be due to the presence of contaminant genomic DNA. The expression of target genes was normalized using the geometric means between RPLP0 ribosomal protein (36b4) and β-actin mRNAs and analysed using ΔΔCt method[194].

For iWAT specific experiment, RNA was extracted using the chloroform isopropanol extraction protocol. 500ng RNA was reverse transcribed using the High Capacity cDNA kit from Life Technologies, in a 20µl reaction volume. The primers were mixed with SYBR Green JumpStartTM Taq Ready MixTM from Sigma-Aldrich, and 11ul aliquots were dispensed into a MultiplateTM Low Profile 96-well PCR plate from Bio-Rad. The cDNA was diluted 1:10, and 2µl aliquots were added in triplicate. The Bio-Rad CFX Connect TM Real-Time system was used to perform thermal cycling, with the following conditions: 2 minutes at 50°C, 10 minutes at 95°C, and 40 cycles of 15 seconds at 95°C and 1 minute at 60°C.

13. RNA sequencing (RNA seq)

The purified RNA was then subjected to deep sequencing analysis. Before sequencing with the Illumina Genome Analyzer (GA), RNA was quantified with the Agilent Bioanalyzer 2100, and only RNA with an RNA integrity number (RIN) greater than 8.0 was used. Typically, 2-4µg total RNA were used in library construction. Total RNA was reverse transcribed to double-stranded cDNA, digested with NIaIII, and ligated to an Illumina-specific adapter containing a recognition site of Mmel. Following Mmel digestion, a second Illumina adapter, containing a 2-dp degenerate 3′ overhang, was ligated. The obtained sequences were aligned to the GRCh38 human genome (https://www.ncbi.nlm.nih.gov/assembly/GCF_000001405.39) using STAR software. Then, data were uploaded in the NCBI Sequence Read Archive (SRA), bioproject ID PRJNA783150.

13.1 Data processing

The raw counts were analyzed using the iDEP95 R package (v0.92), a web-based tool available at http://ge-lab.org/idep[195,196]. In the pre-processing step, genes with low expression levels across samples were filtered out, and genes expressed with a minimum of 0.2 or 0.5 counts per million (CPM) in one library were further analyzed. To reduce

variability, the normalized count data was transformed using the EdgeR log2(CPM+c) method. Heatmaps, principal component analysis (PCA), k-means cluster analysis, and enrichment analyses, were also performed in iDEP95. DESeq2 package in the R language was used to identify differentially expressed genes (DEG) between different experimental conditions using a false discovery rate (FDR) < 0.05 and log_2fold-change > 1.0.

To investigate the function of the DEGs, GO term enrichment analysis was performed. The DEGs were significantly enriched in biological processes (BP), molecular functions (MF), cellular components (CC), Kyoto Encyclopaedia of Genes and Genomes (KEGG) and TF. target. TRED analyses were completed[197]. Venn diagrams were created by web too available at http://bioinformatics.psb.ugent.be/webtools/Venn/.

13.2 RNA-seq validation by Real-time PCR

To validate the results obtained by RNA seq the expression analysis of some genes was measured by Real-time PCR and compared with converted counts obtained by iDEP95 analysis. The Real-time PCR was performed in triplicate with the Platinum SYBR® Green qPCR SuperMix-UDG w/ROX (Invitrogen, Milan, Italy) on CFX96 Real-Time PCR Detection System (Bio-Rad). Master mix reactions were prepared as the manufacturer's instructions with each primer pair and the cDNA added last. Figures were prepared by http://www.bioinformatics.com.cn/srplot.

Table 8. List of primers used for qPCR validation.

Gene symbol	GenBank accession number	Sequence	Amplicon length (bp)	T_m (°C)
ACTB	JN038572.1	F: 5'-CTCTTCCAGCCTTCCTTCCT-3'	**116**	**59.4**
		R: 5'-AGCACTGTGTTGGCGTACAG-3'		
PPARG1	NM_138712.3	F: 5'-GCCGCCAGATTTGAAAGAAGC-3'	**110**	**57.3**
		R: 5'-TGGCATCTCTGTGTCAACCA-3'		
PPARG2	NM_015869.4	F: 5'-TACAGCAAACCCCTATTCCA-3'	**240**	**55.6**
		R: 5'-GAGAAGTCAACAGTAGTGAAG-3'		
PPARA	NM_005036.4	F: 5-TCTGTCGGGATGTCACACAA-3'	**191**	**57.3**
		R: 5'-CGGGCTTTGACCTTGTTCAT-3'		
PRDM16	AF294478.1	F: 5-GAGGAGGACGATGAGGACAG-3'	**103**	**61.4**
		R: 5'-GCTCCTCATCCTCCTCATCC-3'		
PPARGC1A	NM_001330751	F: 5'-GCCCAGGTACAGTGAGTCTT-3'	**105**	**59.4**
		R: 5'-GTGAGGACTGAGGACTTGCT-3'		
UCP1	NM_021833.4	F: 5'-GCGGATGAAACTCTACAGCG-3'	**117**	**59.4**
		R: 5'-GTTTCTTTCCCTGCGGTGAG-3'		

LEP	D63519.2	F: 5'-ACCAAGGTCTTCAGCCATCA-3'	**108**	**58.4**
		R: 5'-CCCTCTGCCCTCTCTGAAAT-3'		
ADIPOQ	EU420013.1	F: 5'-CCTAAGGGAGACATCGGTGA-3'	**173**	**57.4**
		R: 5'-GTAAAGCGAATGGGCATGTT-3'		
LIPE	NM_005357.3	F: 5'-CTCTGGTCTACTACGCCCAG-3'	**121**	**60.4**
		R: 5'-CATCCCTTATGCAGCGTGAC-3'		

14. Protein expression

14.1 Western blotting

On the sixth day of treatment of SGBS cells with allicin, the cells were harvested. The medium was removed, the wells were rinsed with PBS, and then the cells were lysed directly in 200 µl ice-cold RIPA buffer with protease inhibitor cocktail (Complete Mini, Roche). Cell lysates were transferred to 2ml Eppendorf tubes and homogenized at 30 Hz for 30 seconds using a Tissue Lyzer. The lysates were centrifuged at 14 000 rpm for 2 minutes, and the supernatant was collected on ice. Protein concentration was determined according to the method of Lowry[198].

Each sample was boiled with an equal amount of sample buffer, and proteins were separated by SDS-PAGE in a 12% polyacrylamide gel at 80 V for 2 hours. Proteins were then transferred to a PVDF membrane in a transfer buffer using a semi dry Trans Blot TurboTM Transfer System (Bio-Rad) at 2.5 A and 25 V for 10 minutes. The membrane was blocked with 4% non-fat milk powder in Tris buffered saline containing 0.1% Tween 20 (TBS/T) for 1 hour at room temperature and then incubated overnight at 4°C with the specific antibodies diluted in TBS/T with 5% BSA. Membranes were then washed 3 x 15 minutes in TBS/T and incubated for one hour at room temperature with horseradish peroxidase conjugated secondary antibodies diluted in 2.5% non-fat milk powder in TBS/T. Membranes were washed 3 x 15 minutes in TBS/T before detection reagents (ECL Plus Kit, Amersham Biosciences) were added. The chemiluminescence signal was measured using a ChemiDoc XRS+ Imaging System with Image Lab software (BioRad).

Table 9 Buffers used for western blot protein analysis.

Reagent	Composition
Phosphate-buffer (PBS) pH 7.4	137 mM NaCl, 2.7 mM KCl, 10 mM Na_2HPO_4, 1.8 mM KH_2PO_4,
RIPA buffer	50 mM Tris HCl, 1% Triton X-100, 150 mM NaCl and 1 mM EDTA) containing Protease Inhibitor Cocktail (Complete Mini, Roche, Cat No. 0469312408
Sample Buffer	62.5 mM TrisHCl, pH 6.8, 2% (wt/vol) SDS, 10% (v/v) glycerol, 100 mM dithiothreitol, and 0.1% (w/v) bromophenol blue
Running Buffer	47mM Tris, 38mM Glycine, 0,04 w/v (%) SDS
Transfer Buffer	48 mM Tris-HCl, 39 mM glycine, 0.037 (wt/vol) SDS and 15% (vol/vol)
Tris-buffer + Tween (TBS/T)	20 mM Tris, 150 mM NaCl with 0.1% Tween 20

Antibodies: Anti UCP1 antibody was diluted 1:5000 and the secondary antibody conjugated with horseradish peroxidase (HRP) was diluted 1:20000.

15. Protein-protein interaction, Network construction and hub genes analysis

Using the online Search Tool for the Retrieval Interacting Genes (STRING; https://string-db.org/), protein-protein interaction (PPI) networks for the upregulated and downregulated DEGs in each comparison were generated with a confidence level of at least 0.4. The resulting PPI network was visualized using Cytoscape software (version 3.9.0 and 3.9.1, https://cytoscape.org/). To identify significant modules in the PPI network, the Molecular Complex Detection (MCODE) plugin within the Cytoscape suite was used. The plugin was configured with degree cut off = 6 and 2, K-core = 2, and node Score Cut off = 0.2. Subsequently an enrichment analysis of DEGs in modules with a score ≥ 5 was performed.

To gain a better understanding of the variation between DEG targets in TF networks, specific subnetworks were created using the Maximal Clique Centrality (MCC) algorithm in CytoHubba plugin of Cytoscape, focusing on the overlapping genes between

comparisons. To further analyze these subnetworks, an enrichment analysis was conducted on the top 10 genes based on their MCC scores[199].

16. BATLAS and PROFAT webtool analysis

BAT estimated content, of adipose tissue was measured using two computational techniques. Both tools, BATLAS[200] and PROFAT[201], use RNAseq data to estimate the proportion of brown adipocytes in human or mouse tissue. BATLAS webtool (https://fgcz-shiny.uzh.ch/tnb_ethz_BATLAS_app/), uses a Digital Sorting Algorithm from the Cell Mix package in combination with the brown and white markers to estimate the percentage of brown adipocytes of human or mouse tissues. Using normalized read counts, this program examined the assessment of the fraction of brown adipocytes for each sample at various phases of development. The second tool, PROFAT, from RNAseq dataset automatically estimates browning capacity using hierarchical clustering methodology.

17. Target prediction of allicin, dially sulphide (DAS), diallyl disulfide (DADS), diallyl trisulfide (DATS)

Because allicin is rapidly converted *in vitro* to its related fat soluble organosulfur compounds such as diallyl sulphide (CID 11617, DAS), diallyl disulphide (CID 16590, DADS), diallyl trisulfide (CID 16315, DATS) the potential targets of these compounds and of allicin (CID 65036) were screened by Pharm Mapper, SEA, STITCH database, Swiss Target Prediction and Gene Card. SDF files of 2D structure and canonical SMILES of the compounds were obtained from PubChem database and 2D structure of the compounds were uploaded to the PharmMapper. The search was started using the maximum generated conformations of 300 by selecting the option 'Human Protein Targets only (v2010, 2241)' and the default value of 300 for the number of reserved matching targets. For the other parameters, the 'default mode' was selected. Canonical SMILES were uploaded to the other tools.

The predicted targets were entered into the UniProt database (https://www.uniprot.org/) with the species set to *Homo sapiens* to identify their gene IDs. To find shared targets among all the allicin compounds, a Venn diagram was creating. Gene Card was accessed to download genes associated with adipocyte, browning, non-shivering thermogenesis, cold induced thermogenesis, brown adipose

thermogenesis and adaptive thermogenesis and the intersection of the targets was determined using the Venn tool. Again, a Venn diagram was created by merging the shared potential targets of allicin with the common genes related to browning and adipocytes. GeneMANIA was then used to perform functional gene analysis on the overlapped targets and generate a PPI network[202] (**Fig. 10**). CytoNCA, another Cytoscape plugin, was applied to the network to perform topological analysis evaluating the centrality measures of the network[203]. Then, the Cytoscape intersectional merge function was used to isolate the PPI subnetworks. Key node functions were determined by analyzing GO terms, KEGG and Reactome pathways. By entering the screened key nodes into the online tool Var Elect, the correlation between nodes and 'cold induced thermogenesis' was investigated[204].

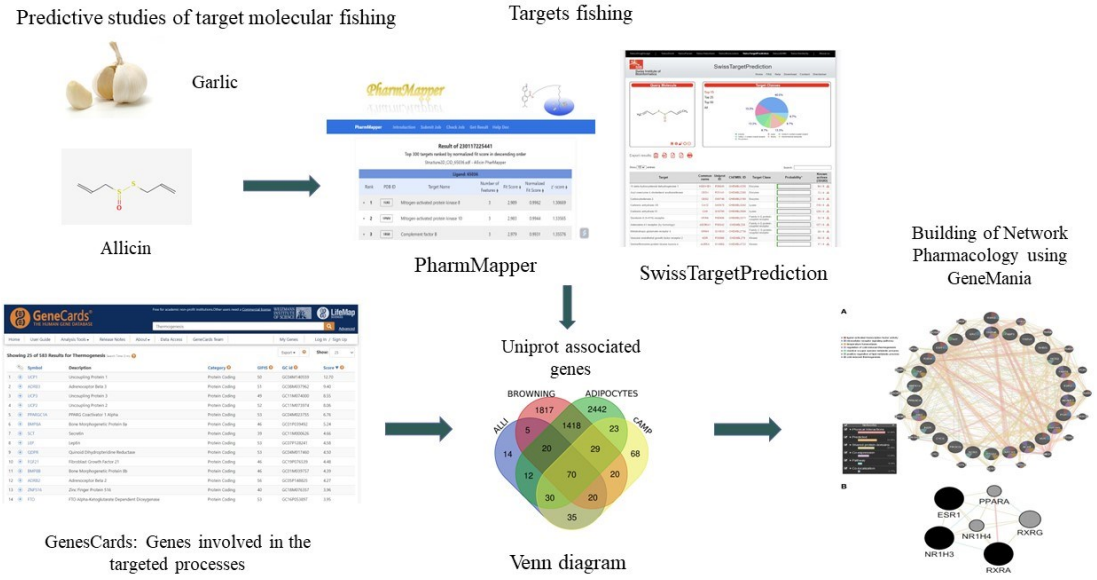

Figure 10. The workflow for the network-pharmacology approach (modified from Huang et al., 2017)[205]

18. Statistical analysis

The Kolmogorov Smirnov statistical test was used to compare Real time and RNA-seq gene expression data. This test allows the similarity of distributions to be assessed together with their form and location.

All measurement results are given as means ± SD analysed in XLSTAT[206]. The surface occupied by LDs in each input image was calculated as the sum of single LD area.

Morphological data were produced for a least 15 images per experimental condition and were analyzed as non-parametric data using Kruskal-Wallis followed by pairwise comparisons using the Mann-Whitney approach with post hoc Bonferroni correction of significance. The average area surface of a single LD was calculated by dividing the area surface of LDs/cells by the number of LDs per cell.

Mitochondrial Analyzer, MiNa, and Micro2P data were compared between treatments using the Kruskal-Wallis statistical test, followed by pairwise comparisons the Mann-Whitney approach with Bonferroni correction. All Mitochondrial Analyzer and MiNa parameters, as well as ratios of parameters obtained with the Micro2P tool, were used together to perform a canonical discriminant analysis (DA) that integrates morphological mitochondrial parameters into a single multivariate model with the aim of maximizing differences between treatments an calculating the best discriminant components between treatments.

III. Results and Discussion

19. SGBS cells exhibit BAT like function

Several studies have suggested that adaptive thermogenesis may be used to treat obesity and its associated diseases. Brown adipocytes are typically induced by activating PPAR with thiazolidinediones[207], which can boost energy expenditure and regulate cholesterol and glucose levels[208]. Other molecules like C/EBPs, RAR, ATF2, PPAR, and cAMP can also upregulate UCP1 expression at the transcriptional level[209]. Adipose tissue can transform white cells into beige cells in response to a variety of stimuli, including exposure to cold, hormones, and natural chemicals[210].

SGBS cells are considered a good model for studying the biology of human white subcutaneous preadipocytes, but they gradually acquire BAT like function during differentiation. To identify key transcriptomic changes, involved in adipogenesis and browning, during differentiation of SGBS cells, RNA sequencing was performed.

Cells were cultured as described above in the materials and method section. Cells were analyzed during differentiation at day 4 (D04), day 6 (D06), and at day 8 (D08) and 10 (D10), respectively. Two biological replicates for four different days of cell differentiation were used (**Fig. 11A**). The DEGs were identified at D06, D08, D10 in comparison to D04. Principal component analysis showed that early differentiated cells (D04) were significantly separated on the first component, which is consistent with the unsupervised hierarchical clustering (**Fig. 11B**).

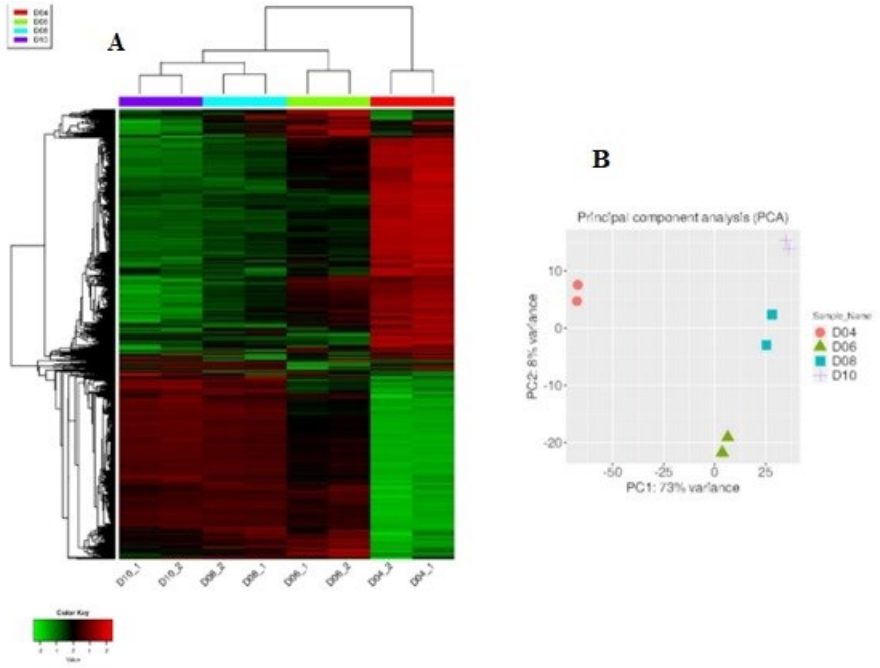

Figure 11. Two thousand genes expressed in SGBS cells at various stages of development are shown in **(A)** heatmap created using hierarchical clustering of two biological replicates. The differentiation stage is indicated by the colored bars above the heatmap. The color key represents the relative expression levels and the z-score: green denotes the lowest expression; black, the middle expression; and red, the highest expression. **(B)** Principal component analysis was performed on SGBS samples at various differentiation ages. Because duplicate samples are grouped together based on differentiation, the results show that the transcriptome data are of high quality. Early differentiated cells (D04) were significantly separated on the first component, which is consistent with the unsupervised hierarchical clustering.

The results of this research have been published in Tissue and Cell, in 2022. This study identified a group of upregulated DEGs that were enriched in GO terms related to energy production, oxidoreductase activity, and mitochondrial organization. KEGG pathways enrichment confirmed that oxidative phosphorylation, PPARG signaling, thermogenesis, and amino acid metabolism were the most significantly upregulated pathways at later days of differentiation in comparison to D04 of differentiation (**Fig 12**). However, PRDM16, a brown fat switch[211], was not listed among the clustered and hub upregulated genes enriched in 'Brown fat cell differentiation' or 'cold-induced thermogenesis,' suggesting that PRDM16 is an early transcription marker needed for early determination of differentiation as reported previously[212,213]. The study also found that the nuclear protein ZNF423 was up regulated and blocked the expression of BMP7 and transcription factor EBF2 essential for PRDM16 activation and brown cells formation in the mature and intermediate adipocytes compared to early differentiated adipocytes. The study identified 384 down regulated genes associated with protein translation,

cellular connectivity, and focal adhesion. Adipocytes could adjust their size according to substrate availability, and during differentiation, there is cytoskeletal restructuring and actin reorganization[214]. In fact, SGBS cells showed a constant increase in lipid droplet surface during differentiation without any variation in the number of lipid droplets per cell[215]. In this study, a cluster of upregulated genes associated with extracellular matrix (ECM) organization was identified using molecular complex detection and MCC scores. Adipocytes are surrounded by a basement membrane composed mainly of collagen IV and VI, which allows anchorage, survival, and signaling across the plasma membrane critical for adipocyte expansion[216]. Recent research has found that the interaction of ECM with adipocytes is related to brown adipose formation and function through actomyosin mechanics and integrin ECM interactions[217]. The cluster also includes muscle specific type II myosin heavy chains MYH1 and MYH11, which promote intrinsic physical forces in cells.

The solute career family 25 member 44 (SLC25A44) gene, which codes for a mitochondrial transporter involved in the breakdown of branched-chain amino acids (BCCA), was found to be significantly upregulated in D08 and D10 differentiated cells compared to early differentiated cells. The breakdown of BCAAs produces intermediates that can be exported from the mitochondria and further elongated into monomethyl branched chain fatty acids (mmBCFAs) through the action of carnitine acyl transferase (CPT2)[218], which was also upregulated in D06, D08, and D10 differentiated cells. The study also analyzed the target genes of several transcription factors involved in adipogenesis and lipid metabolism. The upregulated genes were found to be enriched in target genes of AR, CEBPA, cMYC, E2F1, E2F4, PPARA, PPARG, and transcription factor AP2 alpha (TFAP2A). E2F1 promotes adipogenesis by inducing transcription of PPARG while E2F4 represses PPARG transcription through the association of pocket proteins RBL1 or RBL2[219]. Hub genes shared between the citric acid cycle, respiratory electron transport, oxidative phosphorylation, and thermogenesis were also identified. Transcriptional repressors of WAT, CTBP1, and CTBP2, were significantly downregulated in all differentiated days compared to D04, promoting WAT browning[220].

Earlier studies shown that treating SGBS cells with rosiglitazone and T3 result in the induction of a beige adipocyte differentiation program[221], like what has been observed in adipocytes derived from epididymal depot[222].

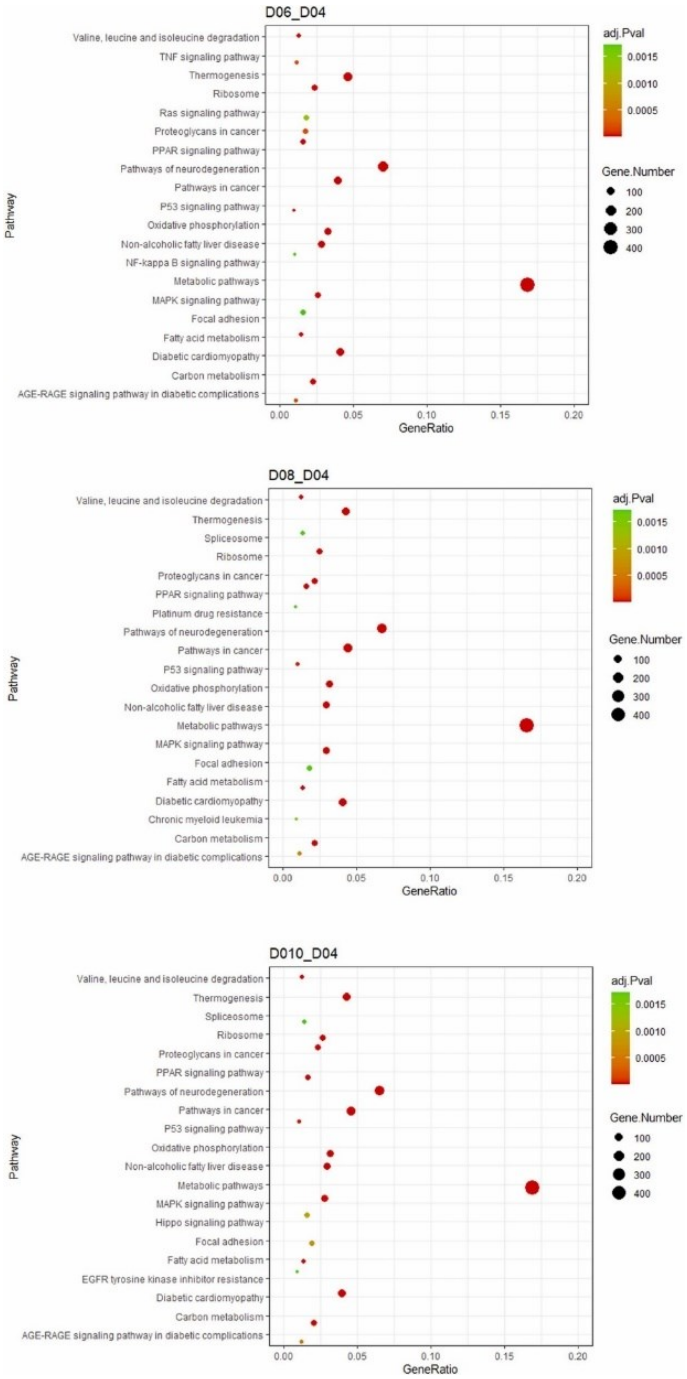

Figure 12. KEGG pathway enrichment analysis. Dot size represents the number of genes in each KEGG pathway; adj. Pval (adjusted *p*-value): Red < orange < green.

Rosiglitazone was also found to inhibit SMAD signalling in white adipose tissue *in vivo*[223], which supports the idea that SMAD$^{-/-}$ mice have increased brown adipocytes and mitochondrial biogenesis in their white adipose tissue[224]. In this study, it was observed that the expression of highly connected genes SMAD, TGFβ1, COL3A1, and COL6A1 decreased from D06 to D10 of differentiation, suggesting a decrease in excessive accumulation of ECM in adipose tissue associated with obesity. Collagen VI,

the major ECM protein in adipose tissues, along with TFGβ, have been identified as responsible factors for excessive ECM accumulation in adipose tissue of human with obesity[225].

The analysis of DEGs and candidate genes of brown and white cell molecular signature revealed an increase in the percentage of genes related to the brown phenotype during the differentiation of SGBS cells (**Fig. 13**).

RNA seq analysis identified genes involved in ECM organization and oxidative stress that may regulate thermogenesis. The present work provided helpful tools and sequencing data that will be very valuable for future studies on the browning process. A reference base to support experimental research, as well as the functional characterization of many unigenes involved in the identified biological processes, may promote future investigations into the molecular causes of adipose tissue browning.

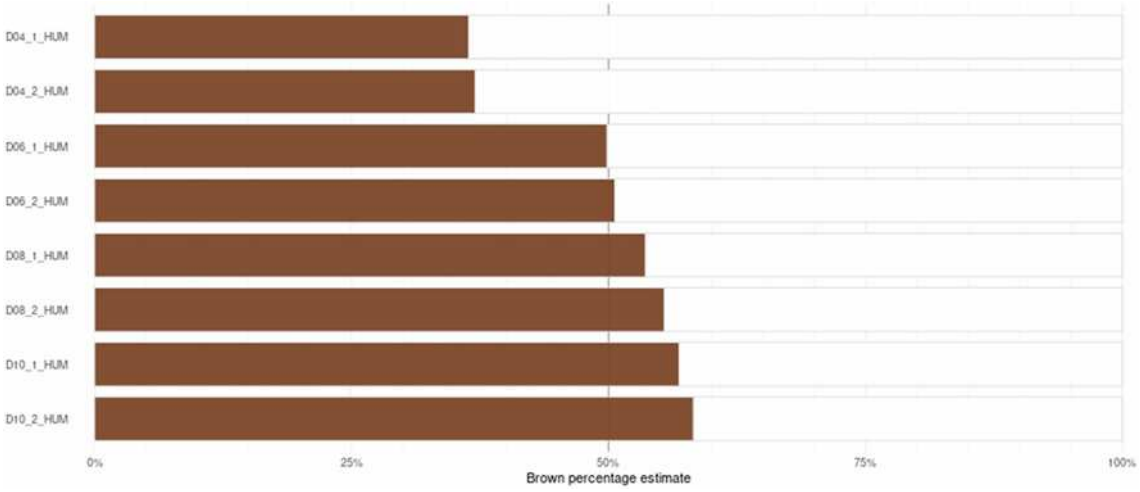

Figure 13. The BATLAS estimation of the percentage of brown phenotype at different days of differentiation in SGBS cells of two biological replicates. In accordance with the comparison of up and downregulated hub DEGs and the gene signature that distinguishes between brown and white adipocytes published by BATLAS (Perdikari et al., 2018)[226], six genes phosphoenolpyruvate carboxykinase (PCK1), UCP1, oxoglutarate dehydrogenase (OGDH), pyruvate dehydrogenase E1 subunit alpha 1 (PDHA1), acyl-CoA dehydrogenase short chain (ACADS), ECHS1, were linked to brown fat, and one gene LEP with white fat.

20. Transient phenotype of SGBS cells

Because SGBS cells are known to achieve a transient expression of classical brown markers, peaking at day 14 of differentiation, but decreasing thereafter[227], the characterization of genes involved in this process were studied by high throughput RNA sequencing in late differentiated cells (D20 and D28) and again in undifferentiated (D0), early differentiated (D02), differentiated (D14) cells.

Hierarchical clustering indicated the difference of genes during cell differentiation, showing that the transcriptome data was well clustered depending on the day of differentiation (**Fig. 14A**). PCA analysis revealed the overall variability in the expression profiles among the samples and treatments. Specifically, the first principal component accounted for 71% of the variance and clearly distinguished D14, D20 and D28, from the early differentiation day D0 and D02 while the second component accounted for only 15% of the differences (**Fig. 14B**).

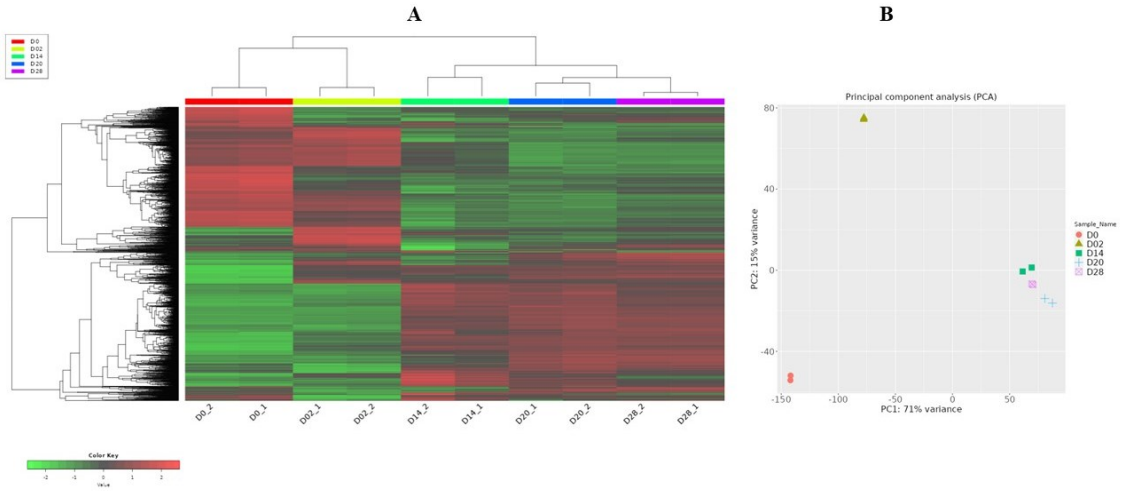

Figure 14. A) Heatmap generated through hierarchical clustering was used to display the relative expression levels of 2000 genes expressed in SGBS cells at different stages of differentiation of two biological replicates. Coloured bars above the heatmap indicated the differentiation stage, while the colour key showed the z-score and the corresponding expression levels: green for the lowest, black for intermediate, and red for the highest expression. **B)** PCA was performed on SGBS samples at different stages of differentiation, and the results showed that the transcriptome data were of high quality. Duplicate samples were clustered together based on differentiation, and early differentiated cells D0 and D2 were clearly separated on the first component from D14, D20 and D28.

20.1 Number of transcripts changed with the day of differentiation.

The DEGs between D02, D14, D20, and D28 were analyzed in comparison to D0, with a $\log_2$fold change of ≥ 2 and an FDR-adjusted p-value of ≤ 0.01.

The iDEP96 expression analysis revealed significant upregulation of 1608 genes at D02 *vs* D0, 3088 at D14 *vs* D0, 3243 at D20 *vs* D0, and 2985 at D28 *vs* D0. Moreover, a significant downregulation of 1281 genes at D02 *vs* D0, 2293 at D14 *vs* D0, 2675 at D20 *vs* D0, and 2629 D28 *vs* D0 was identified (**Fig. 15**).

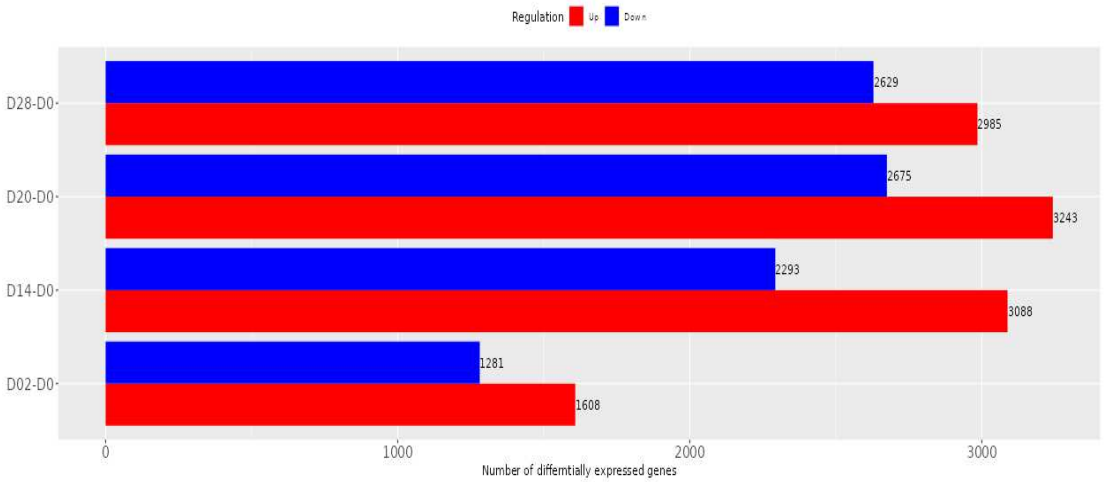

Figure 15. Number of total differentially expressed genes among each comparison.

A total of shared 883 and 790 DEGs were consistently up and downregulated, respectively, and were identified in the overlapping regions of the Venn diagrams (**Fig. 15**). Furthermore, a variable number of genes showed unique expression patterns for each of the four differentiated days when compared to day 0. Specifically, 443 genes were upregulated at D02, 361 at D14, 186 at D20, and 160 at D28 (**Fig. 16 A**), while 283 genes were downregulated at D02, 247 at D14, 194 at D20, and 264 at D28 (**Fig. 16B**). The greatest number of induced or suppressed transcripts was observed in the comparison D02_D0.

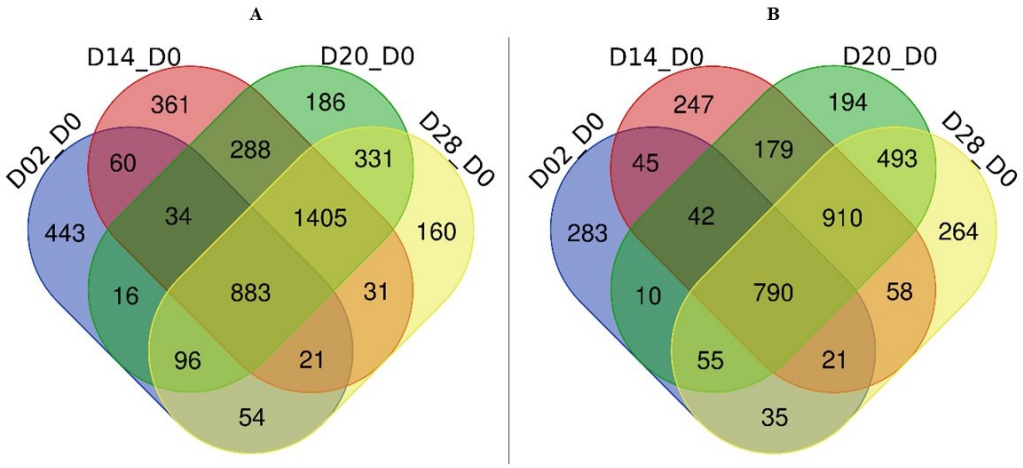

Figure 16. Venn diagrams showing **A)** the upregulated genes and **B)** the downregulated gene at each day of differentiation in comparison with D0, with an adjusted p value of ≤ 0.01 and a log_2fold change of ≥ 2. This analysis identified shared 883 and 790 DEGs upregulated or downregulated across all differentiation days.

20.2 Expression of thermogenic and adipogenic-associated genes

In Table 10 and 11 a list of genes extracted from the gene expression analysis of four comparisons D2, D14, D20, and D28 related to D0 are shown. The analysis provides the log_2 fold change (log_2FC) and adjusted p-value (adj. Pval) for each gene. The log_2FC value represents the magnitude of change in gene expression level between the two days of differentiation being compared. The genes listed in Table 10 are specifically involved in the process of adipogenesis and in Table 11 in adipocyte browning and thermogenesis.

In this study, the upregulation of several adipogenic genes such as ADIPOQ, CEBPA, Kruppel like factor 8 (KLF8), Kruppel like factor 13 (KLF13), fatty acid synthase (FASN), phosphoenolpyruvate carboxykinase (PCK1), glycerol 3 phosphate dehydrogenase 1 (GPD1), SREBF1, interferon regulatory factor 8 (IRF8), and PPARG was observed (**Table 10**). For instance, KLF8, KLF13, and FASN, which was significantly expressed only in D02_D0 comparison, regulate the expression of CEBPα and PPARγ by binding to their promoter regions[228]. PCK1 is a gluconeogenic enzyme involved in the synthesis of glucose from non-carbohydrate sources. Its knockdown in 3T3L1 cells inhibits adipogenesis as it influences the expression of PPARγ and C/EBPα necessary for adipocyte differentiation and the accumulation of lipid droplets during differentiation as reported previously[229]. Similarly, GPD1 catalyzes the synthesis of glycerol-3 phosphates and stimulates the expression of adipogenic genes and is upregulated during adipogenesis[230]. Expression of both PCK1 and GPD1 was particularly higher at D14_D0 ($log_2FC=16.68$), ($log_2FC=14.52$) respectively, demonstrating the formation of fully differentiated SGBS adipocytes at D14 of differentiation.

Table 10. List of adipogenic genes differentially expressed in all comparison.

Gene symbol	D02_D0 log2FC	D02_D0 adj.Pval	D14_D0 log2FC	D14_D0 adj.Pval	D20_D0 log2FC	D20_D0 adj.Pval	D28_D0 log2FC	D28_D0 adj.Pval
ADIPOQ	11,09	$3,17^{-13}$	19,60	$3,33^{-40}$	17,89	$9,87^{-34}$	17,14	$5,34^{-31}$
CEBPA	4,74	$1,86^{-61}$	9,78	$1,54^{-269}$	9,11	$6,26^{-234}$	8,31	$8,36^{-195}$
KLF8	2,43	$2,31^{-01}$	6,43	$4,95^{-05}$	7,41	$2,14^{-06}$	7,83	$5,16^{-07}$
KLF13	1,02	$2,21^{-12}$	2,16	$4,73^{-54}$	3,17	$2,95^{-116}$	2,95	$1,36^{-100}$
FASN	1,66	$1,05^{-55}$	5,83	$0,00^{+00}$	7,01	$0,00^{+00}$	6,95	$0,00^{+00}$
PCK1	4,87	$6,36^{-03}$	16,68	$1,28^{-27}$	13,87	$1,82^{-19}$	13,29	$6,42^{-18}$
GPD1	9,46	$1,56^{-86}$	14,52	$1,97^{-204}$	14,28	$1,11^{-197}$	14,00	$3,90^{-190}$
SLC36A2	-0,90	$7,50^{-01}$	4,40	$1,56^{-03}$	3,34	$2,01^{-02}$	2,91	$4,74^{-02}$
SREBF1	0,16	$3,36^{-01}$	3,89	$3,32^{-207}$	4,89	$0,00^{+00}$	4,54	$1,36^{-282}$
IRF8	0,00	$1,00^{+00}$	7,28	$6,30^{-06}$	7,50	$2,84^{-06}$	8,56	$6,86^{-08}$
PPARG	2,17	$1,38^{-72}$	3,85	$1,50^{-236}$	4,35	$1,83^{-303}$	4,66	$0,00^{+00}$

The results further showed that the expression of UCP1 was consistently upregulated until day 14 of differentiation ($log_2FC=11.30$) in comparison to D0, and then partially declined towards D28 ($log_2FC=9.43$) (Table 11). The expression of TRPM8 closely followed the expression pattern of UCP1 across different stages of differentiation. TRPM8 showed highest expression at D14 ($log_2FC=11.05$) that decline towards D28 ($log_2FC=9.59$). In a recent study, the cold sensing receptor TRPM8 was found in human white adipocytes and activation of this receptor with menthol led to an increase in intracellular calcium concentration, UCP1 expression, mitochondrial membrane potential, glucose uptake, and heat production[231]. In a similar study, the activation of TRPM8 in human progenitor cells led to increase UCP1 expression and uncouple respiration, indicating a shift towards a ‘’brown like’’ phenotype in the white adipocytes[232]. These findings suggest that TRPM8 may play a role in the control of adipose tissue metabolism and energy balance by inducing the ‘’browning’’ of white adipocytes[233]. However, PPARGC1A was consistently upregulated from D0 ($log_2FC=3.87$) to D28 ($log_2FC=11.0$). Additionally, the adipocyte differentiation marker gene, PPARG, was consistently up regulated from day 0 ($log_2FC=2.17$) to day 28 ($log_2FC=4.66$) of differentiation.

The data also showed a constant upregulation of FABP4 from D0 onwards. FABP4 is a cytoplasmic protein that encodes a fatty acid binding protein and is involved in the transport of fatty acids and is upregulated in all comparison *vs* D0. Solute Carrier Family 27 Member 1(SLC27A1) gene was upregulated at all timelines in present data.

Previous studies have demonstrated the role of SLC27A1 in fatty acid uptake and metabolism[234]. Moreover, TFAM encodes a mitochondrial transcription factor and is known to regulate mitochondrial replication and transcription[235]. TFAM was slightly downregulated at D0 but upregulated at later days of differentiation with the highest expression at D28 demonstrating mitochondrial stability and biogenesis in mature adipocytes. Moreover, Cytochrome c oxidase (CcO) is a component of the mitochondrial respiratory chain and is involved in oxidative phosphorylation[236]. It is encoded by COX7A1, which was slightly upregulated at D02 ($log_2FC=0.2$) and remarkably upregulated in later stages, especially at D20 ($log_2FC=1.27$) where it shows the highest expression, indicating enhanced mitochondrial activity in differentiated SGBS adipocytes.

DEGs which play a conceivable role in adipocyte browning (**Table 11**) were also involved. These data show a constant downregulation of lymphocyte cytosolic protein 1 (LCP1) from D0 ($log_2FC=2.60$) to D28 ($log_2FC= -1.78$) showing a shift towards brown phenotype. The knockdown of LCP1 has been shown recently to induce browning in white adipocytes *via* the β3-AR/ERK signaling pathway. Its deficiency promotes mitochondrial biogenesis and induces the expression of browning markers such as *Ucp*1, *Ppargc1α*, and *Prdm16*[237].

Table 11. List of genes that are identified to have a potential role in the process of browning.

Gene symbol	D02_D0 log2FC	D02_D0 adj.Pval	D14_D0 log2FC	D14_D0 adj.Pval	D20_D0 log2FC	D20_D0 adj.Pval	D28_D0 log2FC	D28_D0 adj.Pval
UCP1	0,00	$1,00^{+00}$	11,30	$6,53^{-14}$	10,96	$3,47^{-13}$	9,43	$5,37^{-10}$
PPARGC1A	3,87	$3,92^{-02}$	9,76	$1,36^{-10}$	10,28	$1,05^{-11}$	11,00	$3,17^{-13}$
PPARGC1B	2,31	$8,80^{-08}$	6,04	$1,96^{-57}$	6,25	$2,20^{-61}$	5,97	$5,68^{-56}$
TBX1	0,59	$6,45^{-01}$	0,11	$9,28^{-01}$	0,37	$7,48^{-01}$	-0,08	$9,49^{-01}$
DFFA	-0,07	$7,04^{-01}$	0,46	$6,95^{-04}$	0,26	$7,05^{-02}$	0,35	$1,11^{-02}$
TRPM8	3,13	$1,26^{-01}$	11,05	$2,31^{-13}$	10,74	$1,02^{-12}$	9,59	$2,61^{-10}$
COX7A1	0,20	$4,35^{-01}$	1,08	$3,26^{-08}$	1,27	$5,83^{-11}$	0,79	$7,72^{-05}$
PRDM16	-0,97	$6,35^{-02}$	-1,53	$1,72^{-03}$	-1,84	$2,24^{-04}$	-1,15	$1,58^{-02}$
TFAM	-0,19	$4,31^{-01}$	0,66	$5,04^{-04}$	0,31	$1,21^{-01}$	0,33	$1,00^{-01}$
PTGS1	1,54	$7,97^{-31}$	-1,04	$9,92^{-14}$	-0,94	$2,07^{-11}$	-1,25	$1,76^{-19}$
PTGS2	-4,64	$2,90^{-103}$	-4,80	$4,82^{-111}$	-6,17	$9,45^{-128}$	-5,83	$2,12^{-134}$

UCP2	0,07	$8{,}12^{-01}$	5,89	$2{,}44^{-293}$	6,34	$0{,}00^{+00}$	5,66	$1{,}72^{-270}$
UCP3	0,90	$2{,}35^{-01}$	1,81	$3{,}43^{-03}$	3,37	$3{,}35^{-09}$	2,84	$9{,}49^{-07}$
BMP4	3,77	$6{,}37^{-17}$	3,12	$5{,}78^{-12}$	2,99	$5{,}44^{-11}$	3,98	$2{,}42^{-19}$
SLC36A2	-0,90	$7{,}50^{-01}$	4,40	$1{,}56^{-03}$	3,34	$2{,}01^{-02}$	2,91	$4{,}74^{-02}$
ESR1	1,52	$2{,}70^{-01}$	4,31	$3{,}67^{-05}$	4,49	$1{,}55^{-05}$	4,70	$5{,}36^{-06}$
MGLL	0,46	$6{,}89^{-04}$	2,11	$8{,}34^{-66}$	2,41	$3{,}09^{-85}$	1,99	$9{,}97^{-59}$
PLIN1	10,57	$1{,}21^{-34}$	14,53	$1{,}81^{-65}$	13,92	$3{,}22^{-60}$	13,97	$1{,}40^{-60}$
PNPLA2	1,93	$3{,}34^{-72}$	4,13	$0{,}00^{+00}$	4,56	$0{,}00^{+00}$	4,53	$0{,}00^{+00}$
ALPL	2,63	$6{,}31^{-25}$	3,91	$5{,}19^{-58}$	4,39	$1{,}66^{-73}$	4,63	$2{,}78^{-82}$
LIPE	2,89	$9{,}66^{-48}$	9,26	$0{,}00^{+00}$	9,12	$0{,}00^{+00}$	8,92	$0{,}00^{+00}$
PLIN2	2,18	$2{,}13^{-79}$	3,10	$2{,}02^{-161}$	3,92	$9{,}27^{-258}$	3,43	$9{,}97^{-197}$
PLIN4	6,91	$0{,}00^{+00}$	10,30	$0{,}00^{+00}$	9,69	$0{,}00^{+00}$	9,14	$0{,}00^{+00}$
PLIN5	6,97	$1{,}34^{-05}$	11,79	$4{,}30^{-15}$	9,79	$9{,}80^{-11}$	8,75	$9{,}24^{-09}$
DGAT1	0,21	$2{,}54^{-01}$	3,03	$8{,}84^{-111}$	3,61	$2{,}62^{-157}$	2,89	$1{,}73^{-100}$
DGAT2	1,39	$1{,}80^{-12}$	8,20	$0{,}00^{+00}$	9,63	$0{,}00^{+00}$	9,84	$0{,}00^{+00}$
AQP7	10,70	$2{,}07^{-12}$	15,76	$2{,}00^{-26}$	15,34	$3{,}64^{-25}$	14,61	$7{,}02^{-23}$
PDE3B	6,34	$1{,}05^{-08}$	13,49	$1{,}57^{-37}$	13,68	$1{,}34^{-38}$	13,03	$4{,}51^{-35}$
NR1H3	2,92	$2{,}13^{-80}$	7,03	$0{,}00^{+00}$	6,91	$0{,}00^{+00}$	5,89	$0{,}00^{+00}$
NR1H4	-1,34	$6{,}58^{-01}$	5,07	$3{,}80^{-03}$	5,90	$5{,}83^{-04}$	4,11	$2{,}14^{-02}$
PREX1	0,44	$1{,}50^{-01}$	3,90	$4{,}69^{-68}$	3,62	$1{,}78^{-58}$	2,83	$1{,}50^{-35}$
SLC27A1	1,23	$1{,}01^{-20}$	2,71	$2{,}41^{-103}$	3,30	$1{,}44^{-153}$	2,84	$2{,}57^{-113}$
FABP4	11,10	$1{,}71^{-25}$	17,29	$2{,}33^{-61}$	15,69	$1{,}06^{-50}$	14,29	$3{,}15^{-42}$
LCP1	2,60	$2{,}18^{-01}$	-1,67	$5{,}31^{-01}$	-0,42	$8{,}68^{-01}$	-1,78	$4{,}97^{-01}$
GHR	1,01	$2{,}72^{-04}$	6,00	$5{,}80^{-159}$	6,93	$4{,}98^{-213}$	7,28	$7{,}19^{-235}$
ADRB1	1,54	$5{,}89^{-01}$	7,61	$1{,}11^{-06}$	9,47	$6{,}68^{-10}$	9,89	$1{,}09^{-10}$
ADRB2	1,10	$5{,}37^{-01}$	6,18	$7{,}85^{-08}$	5,50	$2{,}10^{-06}$	5,49	$2{,}17^{-06}$
QDPR	0,20	$2{,}35^{-01}$	1,94	$2{,}70^{-48}$	1,97	$1{,}26^{-49}$	1,88	$1{,}05^{-45}$
ACOT13	0,56	$3{,}28^{-04}$	1,33	$5{,}54^{-21}$	1,41	$2{,}02^{-23}$	1,23	$4{,}53^{-18}$
CPT2	0,44	$1{,}83^{-02}$	3,06	$1{,}95^{-85}$	2,78	$1{,}24^{-70}$	2,48	$4{,}49^{-56}$
LTF	0,52	$6{,}39^{-01}$	6,82	$2{,}28^{-28}$	8,35	$2{,}45^{-42}$	10,45	$7{,}44^{-66}$
SLC38A3	0,00	$1{,}00^{+00}$	7,42	$5{,}44^{-06}$	7,43	$4{,}85^{-06}$	7,12	$1{,}29^{-05}$

Additionally, a gradual upregulation of patatin like phospholipase domain containing protein 2 (PNPLA2) was observed from D0 ($log_2FC=1.93$) to D28 ($log_2FC=4.53$). It can be related to increase thermogenic activity in SGBS cells as previously, PNPLA2 was reported to be involved in the breakdown of triglycerides which aid in the formation of new lipid droplets. The breakdown of triglycerides by PNPLA2 in BAT helps in heat production through non-shivering thermogenesis[238]. A constant upregulation of diglyceride acyltransferase 1 (DGAT1) and DGAT2 from D0 to D28 was also showed, being DGAT1 the highest expression at D20 ($log_2FC=3.61$) and DGAT2 showed the highest expression at D28 ($log_2FC=9.84$). These enzymes are responsible for catalyzing TG synthesis. Mice lacking DGAT1 have partially decreased body fat and glucose intolerance when provided a high-fat diet, while mice lacking DGAT2 have normal TG storage and glucose metabolism on regular or high-fat diets, indicating that DGAT2 is not essential for fat storage[239]. A significant and constant upregulation of monoglyceride lipase (MGL) from D0 ($log_2FC=0.46$) to D20 ($log_2FC=2.41$) and a slight decline towards D28 ($log_2FC=1.99$) was observed indicating increased lipolytic activity in SGBS cells.[240]. Phosphodiesterase 3B (PDE3B) plays a role in the regulation of energy expenditure in BAT as its activity is required for the activation of the cAMP signaling pathway. PDE3B can directly interact with and regulate components of the cAMP signaling pathway such as PKA. Depending on the cellular environment it can either activate or inhibit cAMP activity which in turn activates PGC1α and UCP1[241]. SGBS cells showed a gradual upregulation of PDE3B from D0 ($log_2FC=6.34$) to D28 ($log_2FC=13.03$) that is known to increase intracellular cAMP and the downstream genes involved in lipolysis[242]. The upregulation of SLC38A3 from D0 ($log_2FC=0$) to D20 ($log_2FC=7.43$) and a slight decline towards D28 ($log_2FC=7.12$) could be related to the uptake of glutamine, a substrate for the TCA cycle, and oxidative phosphorylation in mitochondria acting as a fuel source of BAT. It has been linked with increased energy expenditure and improved glucose homeostasis[243].

20.3 GO term enrichment analysis.

DEGs were enriched in BP, MF, and cellular CC. Among the differential expression BP, the upregulated genes were involved in lipid metabolic processes and fatty acid metabolic processes among all the comparisons. The upregulation of genes involved in lipid biosynthesis such as FASN and SREBF1 was observed during differentiation with

the highest expression of SREBF1 (log_2FC=4.89), and FASN (log2FC=7.01) at D20. In particular, D02_D0 comparison showed the upregulated genes involved in lipid localization, in D14_D0 in energy derivation by oxidation, in D20_D0 in fatty acid oxidation, and in D28_D0 in lipid catabolic process, showing an increase in the metabolic activity of SGBS cells (**Fig. 17A**).

The downregulated DEGs among all comparisons were involved in the cell adhesion pathway. The downregulation of focal adhesion pathway in all comparison *vs* D0 support the round shape of mature adipocytes that is negatively associated with this pathway. It was previously reported that PPARγ facilitate the downregulation of focal adhesion pathway[244] which was upregulated in all comparison vs D0 in the current study. The downregulated DEGs enriched in cell mobility, cytoskeleton organization and movement of a cell or subcellular matrix components were reported in D02 *vs* D0 and D14 *vs* D0, respectively (**Fig. 17A**), supporting the static nature of lipid laden mature adipocytes[245].

Among the pathways enriched in CC, the upregulated DEGs were involved in the oxidoreductase complexes in all comparisons except D02_D0, supporting the metabolic activity in mature adipocytes. The mitochondrial matrix and mitochondrial inner membrane pathways were only upregulated in D20_D0 and D28_D0, demonstrating increased mitochondrial activity and mitochondrial respiration and biogenesis. Upregulated DEGs involved in the mitochondrial membrane and respiratory chain complex were specifically enriched in D14_D0 comparison, demonstrating mitochondrial function at the peak of thermogenic activity, while the upregulated genes in D02_D0 were enriched in the intrinsic component of the plasma membrane, an integral component of the plasma membrane and lipid droplets, showing adipocyte development at the early stages of differentiation (**Fig. 17B**).

Among the upregulated MF in all comparison oxidoreductase activity was observed. Transporter activity was found in all comparisons except D02_D0 and electron transport activity was enriched in D14_D0, this suggests a metabolic change observed at D14 of adipocyte differentiation. The downregulated DEGs were enriched in cell adhesion molecular binding in all comparisons likely facilitating the secretion and accumulation of extra cellular matrix molecules in mature adipocytes. Genes involved in structural molecular activity were enriched in D20_D0 and D28_D0, but cytoskeleton protein binding was found in D02_D0 and D14_D0 comparisons (**Fig. 17C**). This demonstrates the development of structural stability in SGBS adipocytes as they differentiate from preadipocytes to mature adipocytes accumulating large lipid droplets.

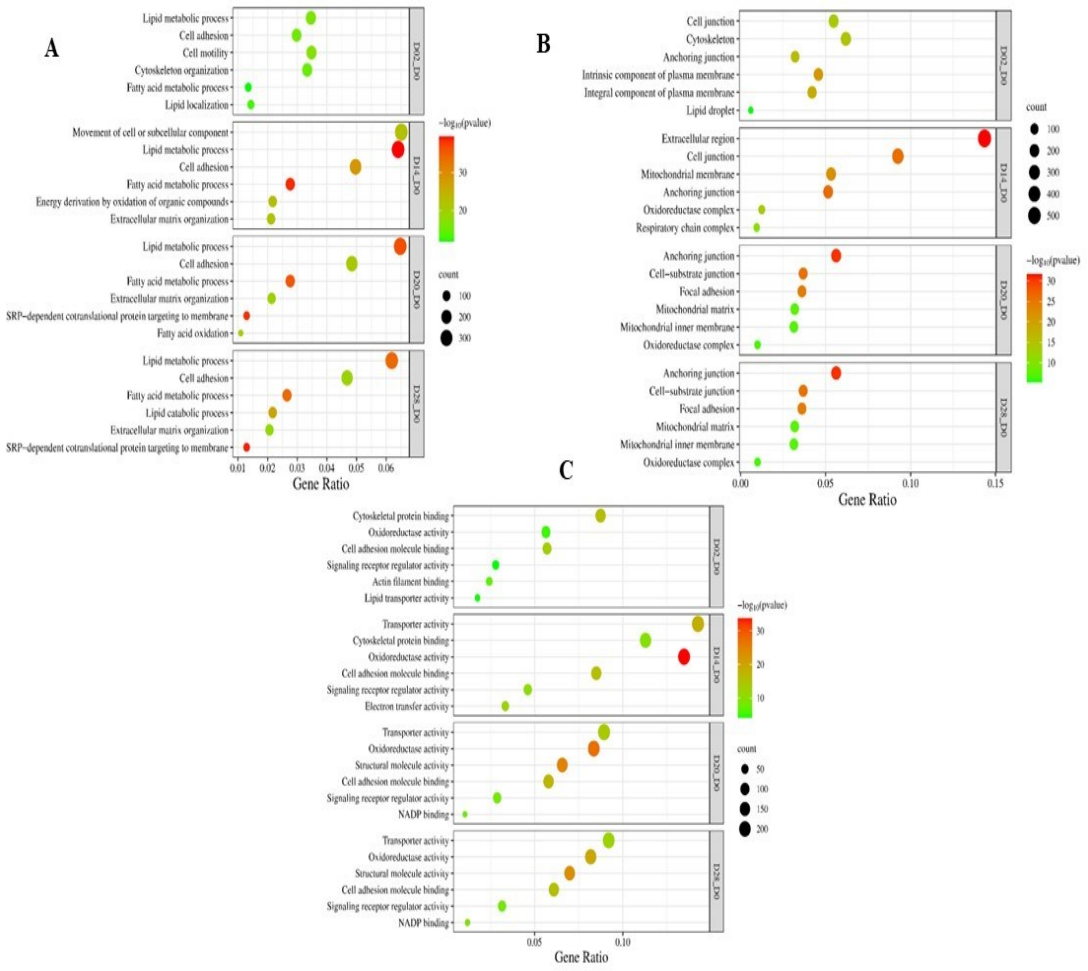

Figure 17. GO enrichment analysis in different comparison *vs* D0. The size of each dot indicates the number of genes in the corresponding pathway. The dot colors are arranged in order of significance, with red being the most significant, followed by orange and green. **A)** Biological processes. **B)** Cellular components. **C)** Molecular functions. Figures were plotted by http://www.bioinformatics.com.cn/srplot.

20.4 KEGG pathway analysis

The scatter plot in the **Figure 18** shows the results of KEGG analysis, depicting the enrichment of several pathways identified at the different time differentiation points in comparison to D0. Each plot includes the corresponding Gene Ratio, adjusted p-value, and the number of enriched genes in the pathway. The Gene Ratio calculates the proportion of enriched candidate genes to the total number of annotated genes in the pathway. A higher Gene Ratio indicates a more significant enrichment of candidate genes in the pathway, while the adjusted p-value represents the FDR used to measure variables in large datasets, such as gene expression levels from RNA sequencing data. Notably, the DEGs were mainly enriched in pathways related to the PPAR signaling pathway in all

comparisons and regulation of lipolysis except in D14_D0, while fatty acid metabolism, and thermogenesis were found only in D14_D0. Moreover, fatty acid degradation was upregulated in D14_D0 and D28_D0. Additionally, the ECM receptor interaction pathway was downregulated in D20_D0 and D28_D0. It can be inferred that SGBS cells attain a BAT phenotype upon complete maturation of the adipocytes around D14. This agrees with previous studies which reported the BAT phenotype of SGBS cells around D14 of differentiation[246, 247]. The upregulation of thermogenesis related genes in D14 *vs* D0 suggests that the cells are undergoing a browning process with enhanced mitochondrial activity and energy expenditure. This is evident by the increase in the expression of UCP1 from D0 to D14 and other thermogenic proteins such as PPARGC1A, PPARGC1B, and FABP4 from D0 to D28. However, the expression of UCP1 declines gradually from D14 to D28 indicating a shift towards the white phenotype. This is in partially in agreement with the previous study by Guennoun et al [248] who reported that SGBS cells at D14 show BAT characteristics by overexpressing UCP1 and PPARγ, while the oxidative capacity declines towards D28. PI3K-Akt pathway has been associated with the downregulation of PPARγ and UCP1, while PI3K-Akt inhibition has been shown to promote thermogenesis by increasing the expression of UCP1 and PPARγ[249]. Its downregulation for activation of BAT is necessary because it inhibits the activation of thermogenic genes by promoting the expression of adipogenic genes such as FASN and SREBP1c[250]. Moreover, studies have shown that cold exposure and β3 adrenergic stimulation can activate thermogenesis by inhibiting the PI3K-Akt signaling pathway[251]. Therefore, the downregulation of PI3K-Akt signaling in all comparison *vs* D0 could be attributed to the high adipogenic and thermogenic capacity of SGBS cells.

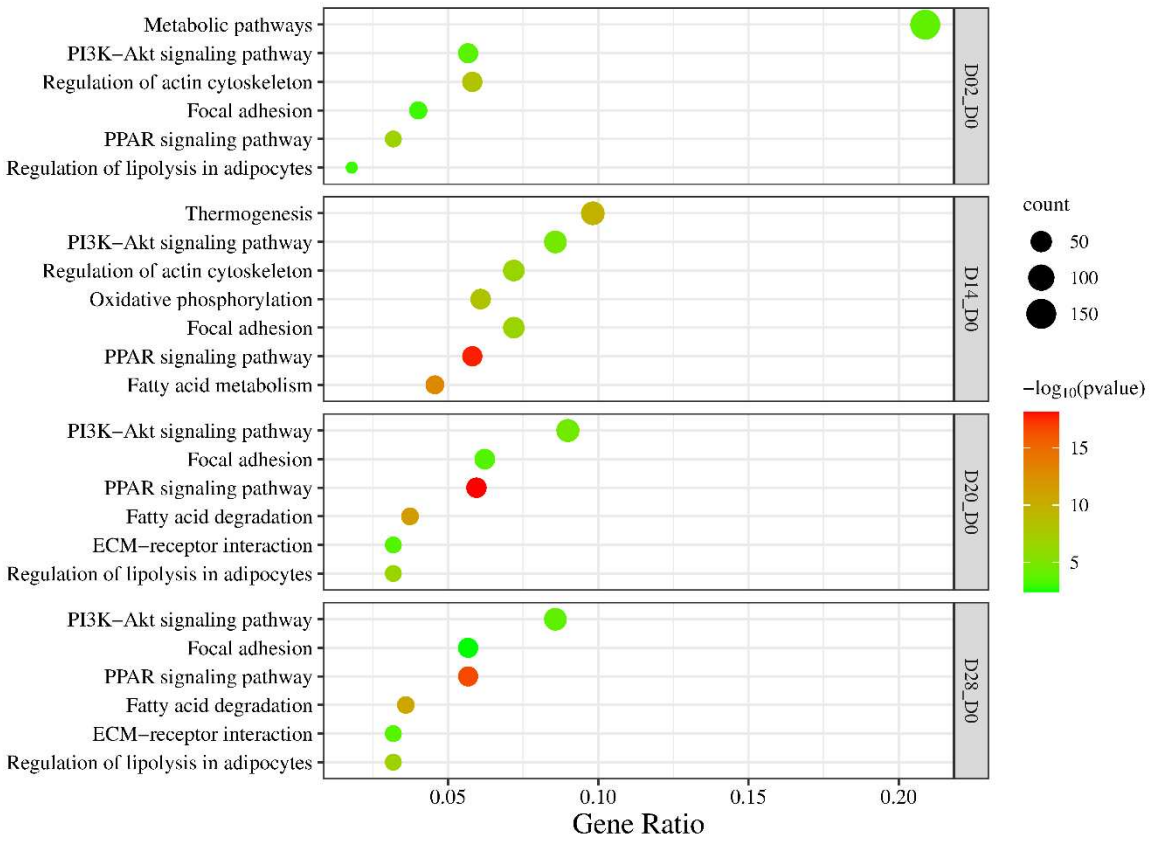

Figure 18. KEGG pathway enrichment analysis, dot size represents the number of genes in each KEGG pathway. The dot colours are arranged in order of significance, with red being the most significant, followed by orange and green. Figures were plotted using online tool available at http://www.bioinformatics.com.cn/srplot.

20.5 Construction of PPI networks and module analysis of DEGs

PPI networks were constructed with upregulated DEGs. Analysis in MCODE with a score ≥ 5 filtered 3 significant clusters (**Fig 19**). In cluster 1 the most significant pathways among others were enriched in the PPAR signaling pathway (FDR $2{,}32^{-20}$), AMPK signaling pathway (FDR 3.01^{-10}), thermogenesis (FDR $3{,}10^{-04}$), white fat cell differentiation (FDR $1{,}20^{-04}$), brown fat differentiation (FDR $1{,}23^{-05}$) regulation of lipid localization (FDR $1{,}61^{12}$), cellular lipid metabolic process ($7{,}05^{16}$), fatty acid metabolic process (FDR $6{,}55^{-16}$), fat cell differentiation (FDR 2.91^{-05}), regulation of lipid metabolic process (FDR $2{,}57^{-17}$), and lipid droplets (FDR $9{,}65^{-11}$) (**Fig. 19A**). Clusters 2 was enriched in positive regulation of protein kinase B signaling (FDR $2{,}54^{07}$), positive regulation of intracellular signal transduction (FDR $2{,}32^{-06}$), and PI3K-Akt signaling pathway (FDR $3{,}00^{-05}$) among others (**Fig. 19B**). Cluster 3 was enriched in oxidative phosphorylation (FDR $6{,}11^{-22}$), inner mitochondrial membrane protein complex (FDR

3,35^{-21}), mitochondrial respirasome (FDR 1,15^{-20}), thermogenesis (FDR 1,25^{-19}), electron transport chain: OXPHOS system in mitochondria (FDR 2,03^{-19}), mitochondrial respiratory chain complex I assembly (FDR 2,84^{-12}) and mitochondrial pathways (FDR 1,41^{-11}) (**Fig. 19C**).

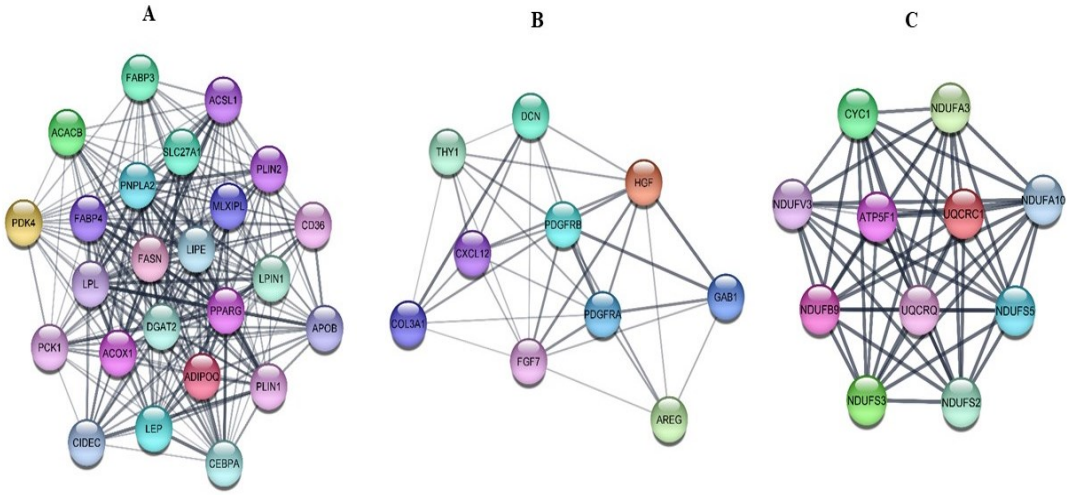

Figure 19. Clusters of DEGs among different comparisons with MCODE created in Cytoscape. **A**) Cluster of upregulated DEGs overlapping in all comparison's *vs* D0. **B**) Cluster of upregulated DEGs in D02 *vs* D0. **C**) Cluster of upregulated DEGs in D14 *vs* D0.

20.6 Validation of gene expression with Real-time PCR

Results of RNA sequencing analysis were confirmed by performing RT-PCR for UCP1, PPARGC1A, and ADIPOQ. The RT-PCR results, presented as $\log_2$(fold change), were in line with RNA seq analysis, and no considerable difference was observed among the two comparisons. (**Fig 20**).

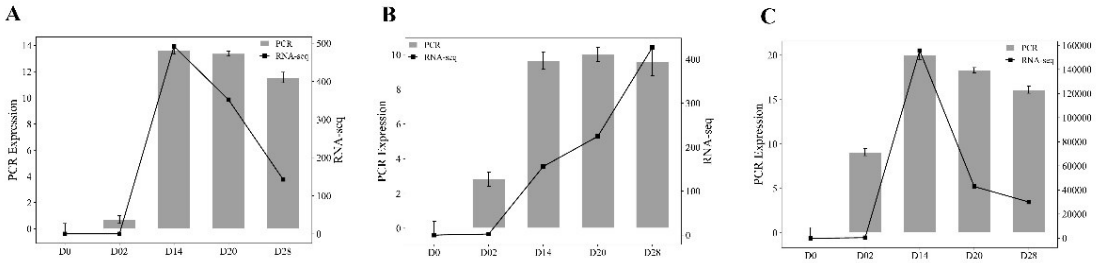

Figure 20. Validation by qPCR of UCP1 (**A**), PPARGC1A (**B**) and ADIPOQ (**C**). Figures were plotted by http://www.bioinformatics.com.cn/srplot.

20.7 Differentiated SGBS cells acquire BAT phenotype.

A bar graph of the expression of the markers BAT and WAT was constructed by analysing the normalized read counts of SGBS cells using PROFAT tool. The results showed an increase in the estimated percentage of BAT phenotype peaking at D14 of differentiation and decreased to 62% at D28 when a higher percentage of WAT markers was observed. (**Fig. 21**).

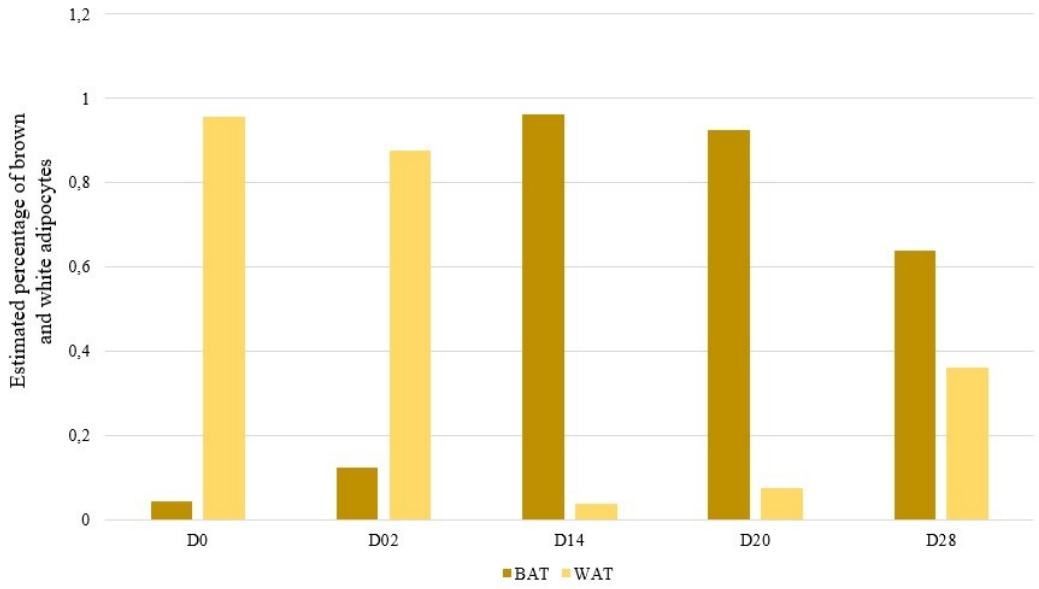

Figure 21. PROFAT prediction percentage of brown and white at each stage of differentiation.

Conclusively, the current data from SGBS cells RNA sequencing analysis provides an important insight into the changes in the gene expression at different days of differentiation. Importantly, SGBS cells showed an increase in the expression of thermogenic related genes in mature differentiated adipocytes demonstrating a shift towards a BAT phenotype compared to the WAT phenotype at D0 or early differentiated cells (D02). However, further studies are required to investigate the shift towards the white phenotype after the peak expression of BAT genes in mature adipocytes. It could be used as a useful source in future studies to further investigate the molecular mechanism underlying adipogenesis and thermogenesis.

21. Browning effect of allicin on SGBS cells

BAT and the formation of beige adipocytes represent potential therapeutic options to counteract obesity[252]. Studies have identified various browning agents, such as capsaicin, resveratrol, caffeine, and fucoxanthin, that can increase energy expenditure[253], *Allium sativum* L., commonly known as garlic, is a species known for its abundance in organosulfur compounds, which have beneficial properties for medicinal use. Allicin is known to suppress cholesterol biosynthesis by inhibiting squalene monooxygenase and acetyl-CoA synthetase [254].

Alliin is released from garlic when it is chopped or crushed, and allicinase subsequently hydrolyzes it into allicin. *In vitro*, allicin breaks down into several fat soluble organosulfur compounds, including diallyl trisulfide (DATS), diallyl disulphide (DADS), and diallyl sulphide (DAS)[255,256]. Studies have shown that allicin can upregulate the expression of genes related to adipokines, lipolysis, and fatty acid oxidation in adipose tissue[257]. Moreover, allicin can promote browning in adipocytes and white inguinal adipose tissue of mice through the ERK1/2 and KLF15 pathways, which stimulate the expression of UCP1[258]. The Sirt1-PGC1α-Tfam pathway may also play a role in promoting allicin-mediated BAT activity. In conclusion, allicin may represent a potential therapeutic option to counteract obesity by promoting energy expenditure and BAT activity[259].

The present research aimed to assess the browning effect of allicin (ALLI) *in vitro* using the SGBS cell strain as a human adipocyte model, by utilizing RNAseq and quantifying the dynamics of LDs and mitochondrial morphology. The control group, and cells treated with di butyryl cAMP sodium salt were negative and positive controls, respectively. Additionally, a network pharmacology approach was employed to identify potential targets and further elucidate the browning effect of allicin.

For this experimental study SGBS cells were cultured in medium reported in Table 5. The allicin treatment started at day 0 of differentiation (D0) and lasted until the analysis at day six (D06) of differentiation. As positive control, SGBS cells received treatment with 500µM dibutyryl cAMP sodium salt, a cyclic nucleotide derivative that mimics endogenous cAMP, for 24 hours before the sixth day of differentiation (**Fig. 22**).

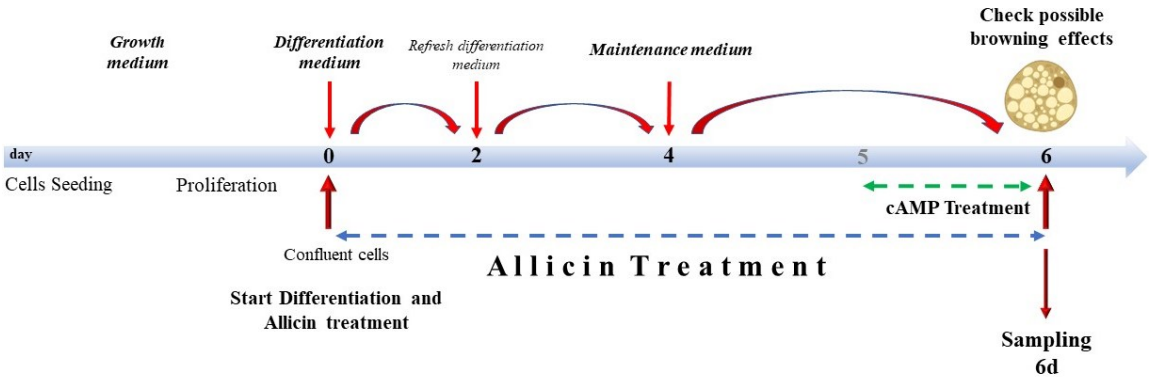

Figure 22. Cell culture treatment protocol. Cells were grown to 90% confluence. Differentiation lasted 6 days supplemented with allicin treatment. From day 4, cells were incubated with allicin in maintenance medium. Cells were incubated with cAMP for 24 hours (from day 5 to day 6 of differentiation). Sampling and analyses were performed on day 6.

Allicin was shown to promote the transition from white to beige adipocytes in SGBS after 6 days of differentiation, before the complete phenotype transition, as evidenced by changes in the size of LDs and shape of mitochondria.

The results of the research have been published in Cellular Endocrinology, a section of the journal Frontiers in Endocrinology, in 2023[260].

Lipolysis is considered essential for thermogenesis in brown and beige adipocytes[261], and allicin lipolytic activity may lead to the formation of multilocular adipocytes, a feature of WAT browning. The expression of genes related to lipolysis such as DFFA, MGLL, PLIN1, LIPE, LPL, and PNPLA2 increased with allicin treatment. Previously, allicin was found to reduce lipid accumulation in HepG2 cells and induces PPARA and FABP6 gene expression[262]

Treatment with allicin resulted in an increase in the number and area of mitochondria and a change in morphology. This was confirmed by the decrease in elongation (mean aspect ratio) and the change in shape of mitochondria from a round to a filamentous shape (mean form factor) of treated cells compared with control cells. This is consistent with the notion that mitochondria acquire spheroidal shape due to fission during cold exposure and thermogenesis[263]. Classical thermogenesis is activated by adreno receptors that promote cAMP synthesis for PKA activation and expression of downstream targets[264]. Allicin is known to increase intracellular cAMP by inhibiting phosphodiesterase activity or increasing adenylate cyclase activity[265]. PDE3 inhibitor increase intracellular cAMP level, which enhances lipolysis[266]. Allicin and cAMP treatments upregulated PDE3B in comparison to control that resulted in an increase in

intracellular cAMP level and in higher expression of LIPE, PLIN1, TBX, and UCP1. The BP GO terms enrichment, such as cellular respiration and cellular lipid metabolic process, and CC GO terms related to mitochondria were significantly upregulated in ALLI and cAMP treated cells compared to CTRL cells. The MF GO terms, such as oxidoreductase activity, were upregulated in allicin and cAMP treated cells. However, the positive browning effect of allicin treatment was only evident in comparison with control cells, not in comparison with cAMP-treated cells. Both allicin and cAMP treatment shared upregulated hub genes related to fatty acid metabolism, oxidation, while downregulated hub genes were enriched in ECM receptor interactions, integrin cell surface interactions, and focal adhesion, as previously demonstrated[267]. These findings suggest that SGBS cells can adjust cytoskeletal reorganization according to their size, LDs dynamics, and thermogenesis.

In fact, ALLI treatment shows statistically significant differences in area of LD/cell, MFD/cell, and IOD/cell as illustrated by BODIPY™ staining in SGBS cells after 6 days of treatment. The area of LDs/cell was significantly lower in cells treated with cAMP and ALLI compared with cells from CTRL ($p < 0.0001$). No significant differences were observed between cAMP and ALLI treated cells. A significant ($p < 0.0001$) decrease in MDF/cell was observed in cells treated with cAMP and ALLI compared with CTRL ($p < 0.0001$), while IOD/cell was significantly lower in cells treated with cAMP compared with cells treated with ALLI ($p = 0.016$) and CTRL ($p = 0.0001$). A significant increase in the number of LDs/cell ($p = 0.015$) was observed between ALLI treated cells and CTRL cells (**Fig. 23**).

The KEGG pathway enrichment analysis validated the upregulation of oxidative phosphorylation and thermogenesis in the ALLI_CTRL and cAMP_CTRL comparisons as they shared common DEGs enriched in these pathways. DEGs in PPAR signalling pathway was only upregulated in cAMP treated cells. Moreover, in ALLI_cAMP comparison, DEGs were significantly downregulated within the PPAR pathway, fatty acid metabolism, elongation, and degradation, and in TCA cycle. Importantly, DEGs were significantly upregulated in cAMP signaling pathway, calcium signaling pathway, and CGMP-PKG signaling pathway in ALLI_cAMP comparison.

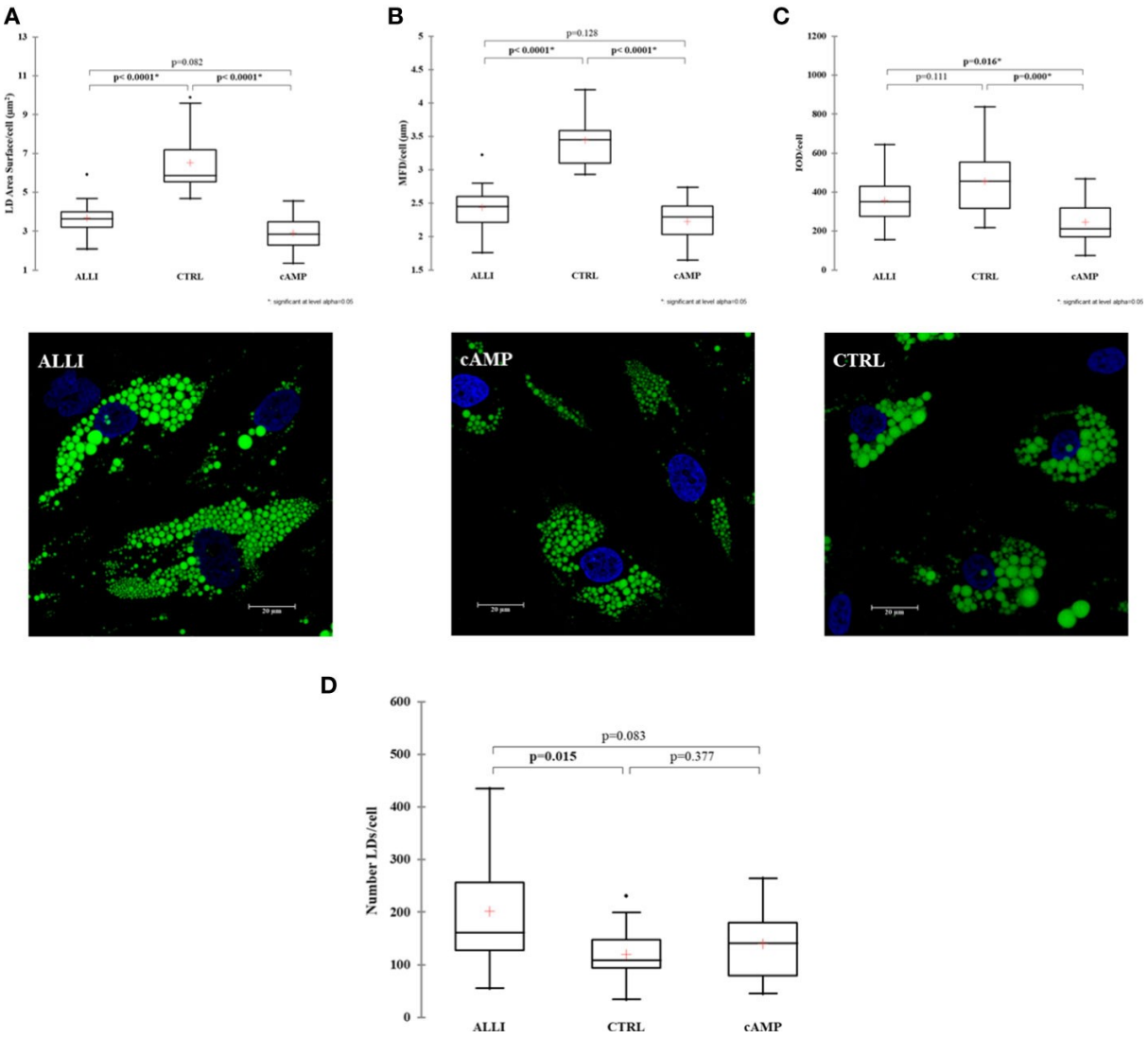

Figure 23. Results of lipid droplet analysis performed on SGBS cells. Boxplots show the median (horizontal lines), the first to third quartiles (box), and the most extreme values with the inter-quartile range (vertical lines). For all comparisons, differences between treatments on SGBS cells were statistically significant using the Kruskal-Wallis's test and Bonferroni correction. **(A)** LD area per cell; **(B)** MFD per cell; **(C)** IOD per cell; **(D)** number of lipid droplets per cell in treated and CTRL cells. Representative confocal images of SGBS cells treated with allicin (ALLI), cAMP, or control (CTRL) 6 days after differentiation and stained with BODIPY™. Nuclear staining, DAPI. Images are representative of n. 15 biological replicates. ALLI, 12.5µM allicin-treated cells; CTRL, control cells; cAMP, 500µM dibutyryl cAMP-treated cells.

Furthermore, the potential targets of allicin and its related organosulfur compounds by using computational resources such as PharmMapper, STITCH, Swish Target Prediction and Gene Card database was also investigated. The analysis identified 26 common targets that were used to construct a GeneMania network linking 46 genes, with 33.99% physical interactions and 23.56% predicted functional relationships (**Fig. 24A**).

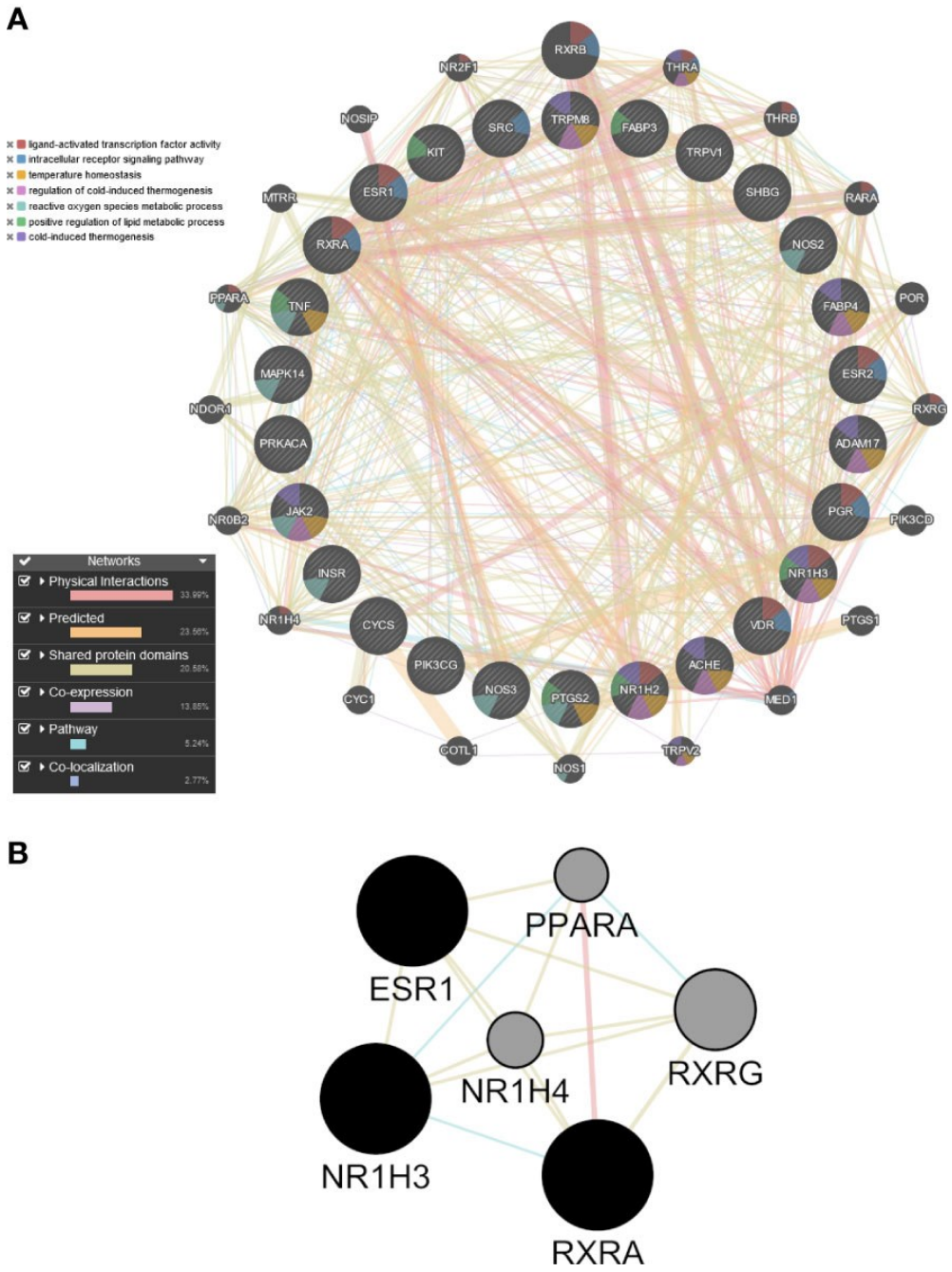

Figure 24. Using GeneMANIA, PPI network was constructed, and adipocyte-browning, related fat-soluble organosulfur compounds, and allicin were assigned 26 common targets based on the query gene. Functional related networks that were filtered based on FDR score connected the genes. The nodes used to represent the query targets were black, with larger nodes denoting a greater degree of the node and thicker, deeper-colored edges denoting stronger interactions. By combining PPI subnetworks based on their computed degree, betweenness, proximity, eigenvector, LAC, and network average values, a core PPI subnetwork was created. PPARA, NR1H3 NR1H4, RXRA, and RXRG were among the genes in the subnetwork.

The ranked targets were involved in categories such as 'ligand-activated transcription factor activity', intracellular receptor signaling pathway,' temperature homeostasis,' 'regulation of cold induced thermogenesis', 'reactive oxygen species metabolic process', 'positive regulation of lipid metabolic process', and 'cold-induced thermogenesis. A core PPI subnetwork was created using in Cytoscape that contain 6 key nodes and 15 edges. In ALLI_cAMP comparison PPAR and nuclear receptor subfamily 1 group H member (NR1H4) were significantly upregulated; while estrogen receptor 1 (ESR1), NR1H4, and retinoid X receptor alpha (RXRA) are the common targets of allicin and its derivative compounds (**Fig. 24B**).

Moreover, treatment with allicin and cAMP significantly increased the estimated BAT phenotype percentage ($p < 0.0001$) compared to control cells (**Fig. 25**). On the other hand, the WAT phenotype significantly ($p < 0.0001$) decreased in ALLI, and cAMP treated cells ($p < 0.0001$) compared to CTRL cells (**Fig. 25**).

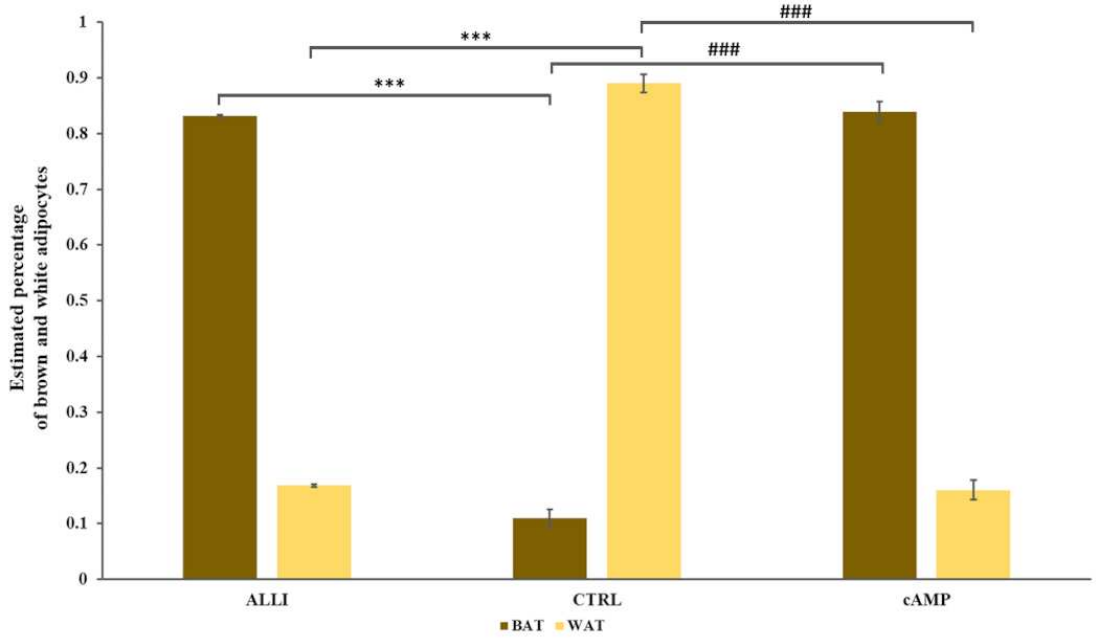

Figure 25. To ascertain the statistical significance of the PROFAT prediction % of brown and white adipocytes, the normalized gene expression data were examined using Euclidean distance and full linkage. A statistical t-test was used to examine the data; significant differences in the estimated percentages of brown and white cells were indicated by *** = p 0.0001 and ### = p 0.0001, respectively. The cells were divided into three groups: control cells (CTRL), cells treated with 500µM dibutyryl cAMP (cAMP), and cells treated with 12.5µM allicin (ALLI).

To verify the expression of UCP1 protein resulting from allicin treatment, a Western blot was conducted.

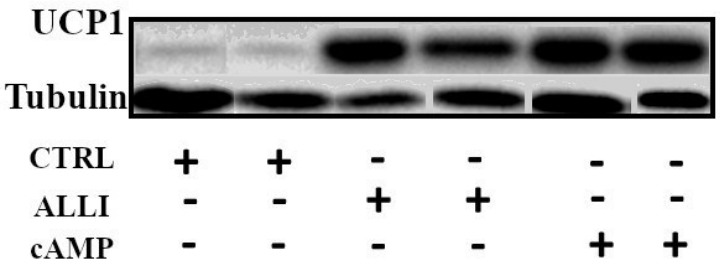

Figure 26. UCP1 protein expression in SGBS cells treated with 12.5μM allicin and 500μM cAMP compared to untreated cells. Proteins from SGBS cells were loaded as 20μg in total.

The UCP1 protein was detected at the expected size (32kDa) in cells treated with both ALLI and cAMP, in comparison to control (**Fig. 26**).

This research provides evidence that allicin has a regulatory effect on the brown phenotype of SGBS cells, leading to an increase in mitochondrial biogenesis and lipid catabolism. The mechanism underlying this process appears to involve an interaction of allicin with the cAMP and PPARA signaling pathways.

22. Effect of allicin on primary inguinal white adipocytes

A significant effect of allicin on the morphology and function of SGBS adipocytes, leading to the formation of multilocular adipocytes and the reduction in the surface area and size of lipid droplets was observed. Allicin treatment significantly upregulated BAT markers such as UCP1, PPARC1A, and OXPHOS-related genes, such as mitochondrially encoded cytochrome B (MT-CYB), mitochondrially encoded NADH: ubiquinone oxidoreductase core subunit 1 (MT-ND1), mitochondrially encoded ATP synthase membrane subunit 6 (ATP6), coenzyme Q2 (COQ2), and COQ3[268].

In line with the above study, a brief experiment was designed aimed to examine the browning effect of allicin on primary iWAT cells isolated from mice. The iWAT was isolated and cultured as mentioned in Table 6. After a few days visible lipid droplets were appear in iWAT cells (**Fig. 27**). The cells were treated by adding allicin directly into the differentiation medium (**Fig. 28**). Two different doses of allicin were used by diluting the stock solution in absolute ethanol. Rosiglitazone a PPARγ agonist was used as a positive control in a concentration of 2μM.

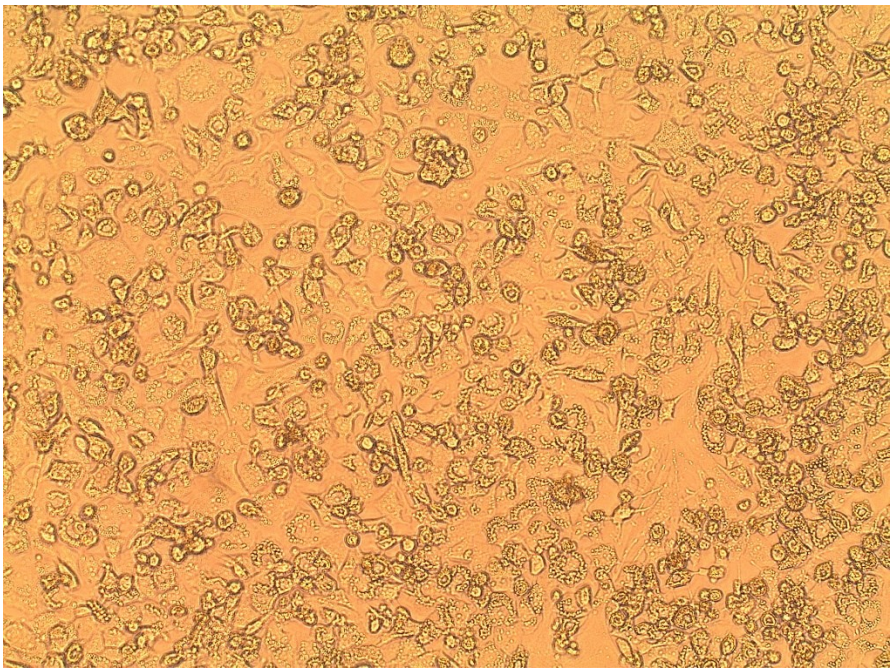

Figure 27. iWAT cells under inverted microscope (Leica DM 4000B). Magnification 10x

To investigate the potential browning effect of allicin on iWAT cells qPCR was performed for a few selected browning specific markers i.e., *Ucp1, Pgc1A, Elove3,* and *Cidea*.

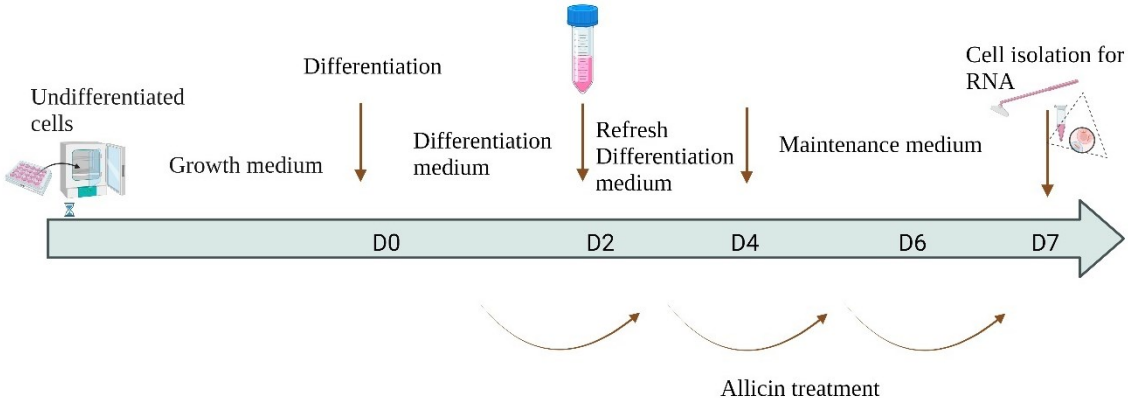

Figure 28. Primary iWAT cells treatment protocol with allicin. Cells were grown in DMEM F12/High Glucose. A differentiation medium was added to the confluent cells. Cells were maintained in a maintenance medium till D7. Allicin was added directly into the medium to treat the cells. Cells were isolated in TRIzol for RNA extraction.

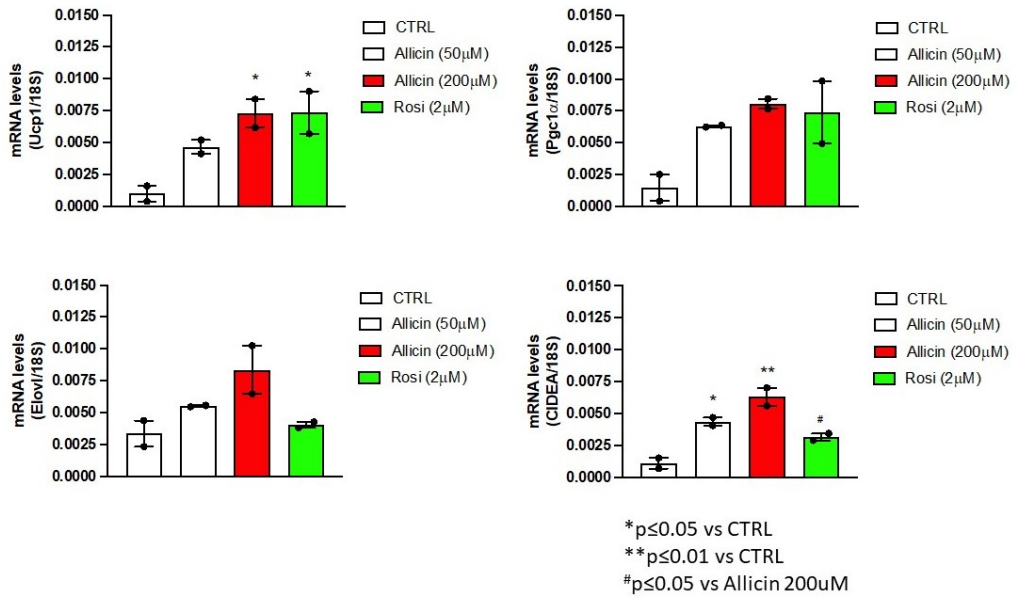

Figure 29. Analysis of Real-time PCR performed for selection browning marker genes on iWAT cells.

The browning markers *Ucp1* and *Cidea* were significantly upregulated in allicin treated cells (**Fig. 29**). *Ucp1* mRNA level was significantly upregulated ($p < 0.05$) at 200μM dose. Allicin has been reported to enhance succinylation levels of Ucp1 in BAT by inhibiting Sirt5[269]. Expression of mRNA level of *Cidea* was significantly upregulated in a dose dependent manner. Treatment of iWAT cells with 50μM allicin significantly ($p < 0.05$) increase *Cidea* expression. Likewise, treatment with 200μM allicin resulted in a more substantial ($p < 0.01$) increase in *Cidea* mRNA level. Rosiglitazone is well known to induce the expression of *Ucp1* through the activation of *Pparγ*[270]. In the current experiment a dose of 2μM rosiglitazone significantly increased the expression of both *Ucp1* and *Cidea* ($p < 0.05$). The highest levels of *Ucp1* and mitochondrial uncoupling were found treating iWAT cells with rosiglitazone and a 3-adrenoceptor agonist together[271]. Combining a browning agent such as rosiglitazone and a thermogenic agent (3-adrenoceptor agonist) is necessary to activate brite adipocytes. For instance, acute rosiglitazone treatment promotes strong β3-adrenoceptor signaling in iWAT cells while prolong exposure to rosiglitazone partially inhibit the effect of β3-adrenoceptor signaling[272]. The current results agree with the previously reported study by Chung et al.[273] who demonstrated the browning effect of allicin on iWAT cells *via* the expression of KLF15 and the phosphorylation of ERK1/2. However, in the current experiment, the expression of KLF15 or other proteins was not investigated.

23. Conclusion

High-throughput RNA sequencing confirmed the versatility of SGBS cells as an *in vitro* human adipocyte model to study the underlying mechanisms and pathways involved in adipogenesis and adipocyte browning. Therefore, the cell strain can be used as a human white or brown adipocyte model under control conditions to study various metabolic diseases. Moreover, allicin treatment showed a browning effect by inducing mitochondrial biogenesis, lipid catabolism, and upregulation of BAT marker genes such as UCP1 in SGBS and iWAT cells. The results have increased our knowledge of potential therapeutic strategies to treat obesity and its associated metabolic disorders using natural products.

IV. References

[1] Ghaben, A. L., & Scherer, P. E. (2019). Adipogenesis and metabolic health. Nature reviews Molecular cell biology, 20(4), 242-258.

[2] Hill, J. O., & Peters, J. C. (1998). Environmental contributions to the obesity epidemic. Science, 280(5368), 1371-1374.

[3] Caro, J. F., Sinha, M. K., Kolaczynski, J. W., Zhang, P. L., & Considine, R. V. (1996). Leptin: the tale of an obesity gene. Diabetes, 45(11), 1455-1463.

[4] Vázquez-Vela, M. E. F., Torres, N., & Tovar, A. R. (2008). White adipose tissue as endocrine organ and its role in obesity. Archives of medical research, 39(8), 715-728.

[5] Coelho, M., Oliveira, T., & Fernandes, R. (2013). State of the art paper Biochemistry of adipose tissue: an endocrine organ. Archives of medical science, 9(2), 191-200.

[6] Spalding, K. L., Arner, E., Westermark, P. O., Bernard, S., Buchholz, B. A., Bergmann, O. et.al (2008). Dynamics of fat cell turnover in humans. Nature, 453(7196), 783-787.

[7] Vishvanath, L., MacPherson, K. A., Hepler, C., Wang, Q. A., Shao, M., Spurgin, S. B et al. (2016). Pdgfrβ+ mural preadipocytes contribute to adipocyte hyperplasia induced by high-fat-diet feeding and prolonged cold exposure in adult mice. Cell metabolism, 23(2), 350-359.

[8] Trayhurn, P., & Beattie, J. H. (2001). Physiological role of adipose tissue: white adipose tissue as an endocrine and secretory organ. Proceedings of the Nutrition Society, 60(3), 329-339.

[9] Gregor, M. F., & Hotamisligil, G. S. (2011). Inflammatory mechanisms in obesity. Annual review of immunology, 29, 415-445.

[10] Driskell, R. R., Jahoda, C. A., Chuong, C. M., Watt, F. M., & Horsley, V. (2014). Defining dermal adipose tissue. Experimental dermatology, 23(9), 629-631.

[11] Suganami, T., Tanaka, M., & Ogawa, Y. (2012). Adipose tissue inflammation and ectopic lipid accumulation. Endocrine journal, 59(10), 849-857.

[12] Huang doran et al., 2010. Endocrinology, 207.3: 245-255.

[13] Ghaben, A. L., & Scherer, P. E. (2019). Adipogenesis and metabolic health. Nature reviews Molecular cell biology, 20(4), 242-258.

[14] Nedergaard, J., Petrovic, N., Lindgren, E. M., Jacobsson, A., & Cannon, B. (2005). PPARγ in the control of brown adipocyte differentiation. Biochimica et Biophysica Acta (BBA)-Molecular Basis of Disease, 1740(2), 293-304.

[15] Rosen, E. D., & Spiegelman, B. M. (2000). Molecular regulation of adipogenesis. Annual review of cell and developmental biology, 16(1), 145-171.

[16] Lowe, C. E., O'Rahilly, S., & Rochford, J. J. (2011). Adipogenesis at a glance. Journal of cell science, 124(16), 2681-2686.

[17] Cinti, S. (2009). Transdifferentiation properties of adipocytes in the adipose organ. American Journal of Physiology-Endocrinology and Metabolism, 297(5), E977-E986.

[18] Arbuthnott, E. (1989). Brown adipose tissue: structure and function. Proceedings of the Nutrition Society, 48(2), 177-182.

[19] Himms-Hagen, J. (1984). Thermogenesis in brown adipose tissue as an energy buffer: implications for obesity. New England Journal of Medicine, 311(24), 1549-1558.

[20] Cannon, B., & Nedergaard, J. A. N. (2004). Brown adipose tissue: function and physiological significance. Physiological reviews.

[21] Sanchez-Gurmaches, J., Hung, C. M., Sparks, C. A., Tang, Y., Li, H., & Guertin, D. A. (2012). PTEN loss in the Myf5 lineage redistributes body fat and reveals subsets of white adipocytes that arise from Myf5 precursors. Cell metabolism, 16(3), 348-362.

[22] Puigserver, P., Wu, Z., Park, C. W., Graves, R., Wright, M., & Spiegelman, B. M. (1998). A cold-inducible coactivator of nuclear receptors linked to adaptive thermogenesis. Cell, 92(6), 829-839.

[23] Rodríguez, A., Becerril, S., Hernández-Pardos, A. W., & Frühbeck, G. (2020). Adipose tissue depot differences in adipokines and effects on skeletal and cardiac muscle. Current opinion in pharmacology, 52, 1-8.

[24] Harms, M., & Seale, P. (2013). Brown and beige fat: development, function and therapeutic potential. Nature medicine, 19(10), 1252-1263.

[25] Wang, Q. A., Tao, C., Gupta, R. K., & Scherer, P. E. (2013). Tracking adipogenesis during white adipose tissue development, expansion and regeneration. Nature medicine, 19(10), 1338-1344.

[26] Jeremic, N., Chaturvedi, P., & Tyagi, S. C. (2017). Browning of white fat: novel insight into factors, mechanisms, and therapeutics. Journal of cellular physiology, 232(1), 61-68.

[27] Wu, J., Boström, P., Sparks, L. M., Ye, L., Choi, J. H., Giang, A. H. et al. (2012). Beige adipocytes are a distinct type of thermogenic fat cell in mouse and human. Cell, 150(2), 366-376.

[28] Garcia, R. A., Roemmich, J. N., & Claycombe, K. J. (2016). Evaluation of markers of beige adipocytes in white adipose tissue of the mouse. Nutrition & metabolism, 13(1), 1-14.

[29] Ma, L., Gilani, A., Yi, Q., & Tang, L. (2022). MicroRNAs as Mediators of Adipose Thermogenesis and Potential Therapeutic Targets for Obesity. Biology, 11(11), 1657.

[30] Ikeda, K., & Yamada, T. (2020). UCP1 dependent and independent thermogenesis in brown and beige adipocytes. Frontiers in endocrinology, 11, 498.

[31] Park, G., Horie, T., Kanayama, T., Fukasawa, K., Iezaki, T., Onishi, et al. (2017). The transcriptional modulator Ifrd1 controls PGC-1α expression under short-term adrenergic stimulation in brown adipocytes. The FEBS journal, 284(5), 784-795.

[32] Qian, S. W., Tang, Y., Li, X., Liu, Y., Zhang, Y. Y., Huang, et al. (2013). BMP4-mediated brown fat-like changes in white adipose tissue alter glucose and energy homeostasis. Proceedings of the National Academy of Sciences, 110(9), E798-E807.

[33] Fernandez-Marcos, P. J., & Auwerx, J. (2011). Regulation of PGC-1α, a nodal regulator of mitochondrial biogenesis. The American journal of clinical nutrition, 93(4), 884S-890S.

[34] Seale, P., Bjork, B., Yang, W., Kajimura, S., Chin, S., Kuang, S., et al. (2008). PRDM16 controls a brown fat/skeletal muscle switch. Nature, 454(7207), 961-967.

[35] Harms, M. J., Ishibashi, J., Wang, W., Lim, H. W., Goyama, S., Sato, et al. (2014). Prdm16 is required for the maintenance of brown adipocyte identity and function in adult mice. Cell metabolism, 19(4), 593-604.

[36] Qiang, L., Wang, L., Kon, N., Zhao, W., Lee, S., Zhang, Y et al. (2012). Brown remodeling of white adipose tissue by SirT1-dependent deacetylation of Pparγ. Cell, 150(3), 620-632.

[37] Qiang, L., Wang, L., Kon, N., Zhao, W., Lee, S., Zhang, et al. (2012). Brown remodeling of white adipose tissue by SirT1-dependent deacetylation of Pparγ. Cell, 150(3), 620-632.

[38] Dempersmier, J., Sambeat, A., Gulyaeva, O., Paul, S. M., Hudak, C. S., et al. (2015). Cold-inducible Zfp516 activates UCP1 transcription to promote browning of white fat and development of brown fat. Molecular cell, 57(2), 235-246.

[39] Sambeat, A., Gulyaeva, O., Dempersmier, J., Tharp, K. M., Stahl, A., Paul, S. M et al. (2016). LSD1 interacts with Zfp516 to promote UCP1 transcription and brown fat program. Cell reports, 15(11), 2536-2549.

[40] Seale, P. (2015). Transcriptional regulatory circuits controlling brown fat development and activation. Diabetes, 64(7), 2369-2375.

[41] Wu, L., Zhang, L., Li, B., Jiang, H., Duan, Y., Xie, Z et al. (2018). AMP-activated protein kinase (AMPK) regulates energy metabolism through modulating thermogenesis in adipose tissue. Frontiers in physiology, 122.

[42] Liu, P., Huang, S., Ling, S., Xu, S., Wang, F., Zhang, W et al. (2019). Foxp1 controls brown/beige adipocyte differentiation and thermogenesis through regulating β3-AR desensitization. Nature communications, 10(1), 5070.

[43] Tong, Q., Ye, C. P., Jones, J. E., Elmquist, J. K., & Lowell, B. B. (2008). Synaptic release of GABA by AgRP neurons is required for normal regulation of energy balance. Nature neuroscience, 11(9), 998-1000.

[44] Kimura, H., Nagoshi, T., Yoshii, A., Kashiwagi, Y., Tanaka, Y., Ito, K et al. (2017). The thermogenic actions of natriuretic peptide in brown adipocytes: The direct measurement of the intracellular temperature using a fluorescent thermoprobe. Scientific Reports, 7(1), 12978.

[45] Liu, D., Ceddia, R. P., & Collins, S. (2018). Cardiac natriuretic peptides promote adipose 'browning'through mTOR complex-1. Molecular metabolism, 9, 192-198.

[46] Bordicchia, M., Liu, D., Amri, E. Z., Ailhaud, G., Dessì Fulgheri, P., Zhang, C et al. (2012). Cardiac natriuretic peptides act via p38 MAPK to induce the brown fat thermogenic program in mouse and human adipocytes. The Journal of clinical investigation, 122(3), 1022-1036.

[47] Okoshi, M. P., Capalbo, R. V., Romeiro, F. G., & Okoshi, K. (2016). Cardiac cachexia: perspectives for prevention and treatment. Arquivos Brasileiros de Cardiologia, 108, 74-80.

[48] de Oliveira Leal, V., & Mafra, D. (2013). Adipokines in obesity. Clinica Chimica Acta, 419, 87-94.

[49] Cammisotto, P. G., & Bukowiecki, L. J. (2002). Mechanisms of leptin secretion from white adipocytes. American Journal of Physiology-Cell Physiology, 283(1), C244-C250.

[50] Park, H. K., & Ahima, R. S. (2015). Physiology of leptin: energy homeostasis, neuroendocrine function and metabolism. Metabolism, 64(1), 24-34.

[51] Van Harmelen, V., Reynisdottir, S., Eriksson, P., Thörne, A., Hoffstedt, J., Lönnqvist, F., et al. (1998). Leptin secretion from subcutaneous and visceral adipose tissue in women. Diabetes, 47(6), 913-917.

[52] Kadowaki, T., Yamauchi, T., & Kubota, N. (2008). The physiological and pathophysiological role of adiponectin and adiponectin receptors in the peripheral tissues and CNS. FEBS letters, 582(1), 74-80.

[53] Huypens, P. R. (2007). Leptin and adiponectin regulate compensatory beta cell growth in accordance to overweight. Medical hypotheses, 68(5), 1134-1137.

[54] McTernan, P. G., Kusminski, C. M., & Kumar, S. (2006). Resistin. Current opinion in lipidology, 17(2), 170-175.

[55] Muse, E. D., Obici, S., Bhanot, S., Monia, B. P., McKay, R. A., Rajala, M. W., et al. (2004). Role of resistin in diet-induced hepatic insulin resistance. The Journal of clinical investigation, 114(2), 232-239.

[56] Jung, H. S., Youn, B. S., Cho, Y. M., Yu, K. Y., Park, H. J., Shin, C. S., et al. (2005). The effects of rosiglitazone and metformin on the plasma concentrations of resistin in patients with type 2 diabetes mellitus. Metabolism, 54(3), 314-320.

[57] Steppan, C. M., Bailey, S. T., Bhat, S., Brown, E. J., Banerjee, R. R., Wright, C. M., et al. (2001). The hormone resistin links obesity to diabetes. Nature, 409(6818), 307-312.

[58] Tripathi, D., Kant, S., Pandey, S., & Ehtesham, N. Z. (2020). Resistin in metabolism, inflammation, and disease. The FEBS journal, 287(15), 3141-3149.

[59] Brychta, R. J., & Chen, K. Y. (2017). Cold-induced thermogenesis in humans. European journal of clinical nutrition, 71(3), 345-352.

[60] Ricquier, D. (2006). Fundamental mechanisms of thermogenesis. Comptes Rendus Biologies, 329(8), 578-586.

[61] Blaxter, K. (1989). Energy metabolism in animals and man. CUP Archive.

[62] Himms-Hagen, J. (1989). Role of thermogenesis in the regulation of energy balance in relation to obesity. Canadian Journal of Physiology and Pharmacology, 67(4), 394-401.

[63] Chouchani, E. T., Kazak, L., & Spiegelman, B. M. (2019). New advances in adaptive thermogenesis: UCP1 and beyond. *Cell metabolism*, *29*(1), 27-37.

[64] Chen, K. Y., Brychta, R. J., Sater, Z. A., Cassimatis, T. M., Cero, C., Fletcher, L. A., et al. (2020). Opportunities and challenges in the therapeutic activation of human energy expenditure and thermogenesis to manage obesity. Journal of biological chemistry, 295(7), 1926-1942.

[65] Nedergaard, J., Golozoubova, V., Matthias, A., Asadi, A., Jacobsson, A., & Cannon, B. (2001). UCP1: the only protein able to mediate adaptive non-shivering thermogenesis and metabolic inefficiency. Biochimica et Biophysica Acta (BBA)-Bioenergetics, 1504(1), 82-106.

[66] Ueno, N., Inui, A., Kalra, P. S., & Kalra, S. P. (2006). Leptin transgene expression in the hypothalamus enforces euglycemia in diabetic, insulin-deficient nonobese Akita mice and leptin-deficient obese ob/ob mice. Peptides, 27(9), 2332-2342.

[67] Gordon, K., Blondin, D. P., Friesen, B. J., Tingelstad, H. C., Kenny, G. P., & Haman, F. (2019). Seven days of cold acclimation substantially reduces shivering intensity and increases nonshivering thermogenesis in adult humans. Journal of Applied Physiology, 126(6), 1598-1606.

[68] Cannon, B., & Nedergaard, J. (2011). Nonshivering thermogenesis and its adequate measurement in metabolic studies. Journal of Experimental Biology, 214(2), 242-253.

[69] Kajimura, S., Spiegelman, B. M., & Seale, P. (2015). Brown and beige fat: physiological roles beyond heat generation. Cell metabolism, 22(4), 546-559.

[70] Nedergaard, J., Bengtsson, T., & Cannon, B. (2007). Unexpected evidence for active brown adipose tissue in adult humans. American Journal of Physiology-Endocrinology and Metabolism.

[71] Nedergaard, J., Bengtsson, T., & Cannon, B. (2007). Unexpected evidence for active brown adipose tissue in adult humans. American Journal of Physiology-Endocrinology and Metabolism.

[72] Blondin, D. P., Nielsen, S., Kuipers, E. N., Severinsen, M. C., Jensen, V. H., Miard, S., et al. (2020). Human brown adipocyte thermogenesis is driven by β2-AR stimulation. Cell metabolism, 32(2), 287-300.

[73] McNeill, B. T., Suchacki, K. J., & Stimson, R. H. (2021). Mechanisms in endocrinology: Human brown adipose tissue as a therapeutic target: warming up or cooling down. European Journal of Endocrinology, 184(6), R243-R259.

[74] Ruiz-Ojeda, F. J., Rupérez, A. I., Gomez-Llorente, C., Gil, A., & Aguilera, C. M. (2016). Cell models and their application for studying adipogenic differentiation in relation to obesity: a review. International journal of molecular sciences, 17(7), 1040.

[75] Rosen, E. D., Sarraf, P., Troy, A. E., Bradwin, G., Moore, K., Milstone, D. S.,et al(1999). PPARγ is required for the differentiation of adipose tissue in vivo and in vitro. Molecular cell, 4(4), 611-617.

[76] Chilliard, Y. (1993). Dietary fat and adipose tissue metabolism in ruminants, pigs, and rodents: a review. Journal of Dairy Science, 76(12), 3897-3931.

[77] Ruiz-Ojeda, F. J., Rupérez, A. I., Gomez-Llorente, C., Gil, A., & Aguilera, C. M. (2016). Cell models and their application for studying adipogenic differentiation in relation to obesity: a review. International journal of molecular sciences, 17(7), 1040.

[78] Ruiz-Ojeda, F. J., Rupérez, A. I., Gomez-Llorente, C., Gil, A., & Aguilera, C. M. (2016). Cell models and their application for studying adipogenic differentiation in relation to obesity: a review. International journal of molecular sciences, 17(7), 1040.

[79] Desarzens, S., Liao, W. H., Mammi, C., Caprio, M., & Faresse, N. (2014). Hsp90 blockers inhibit adipocyte differentiation and fat mass accumulation. PloS one, 9(4), e94127.

[80] Hernández-Mosqueira, C., Velez-delValle, C., & Kuri-Harcuch, W. (2015). Tissue alkaline phosphatase is involved in lipid metabolism and gene expression and secretion of adipokines in adipocytes. Biochimica et Biophysica Acta (BBA)-General Subjects, 1850(12), 2485-2496.

[81] Wolins, N. E., Quaynor, B. K., Skinner, J. R., Tzekov, A., Park, C., Choi, K., et al. (2006). OP9 mouse stromal cells rapidly differentiate into adipocytes: characterization of a useful new model of adipogenesis. Journal of lipid research, 47(2), 450-460.

[82] Rahman, F., Al Frouh, F., Bordignon, B., Fraterno, M., Landrier, J. F., Peiretti, F., et al. (2014). Ascorbic acid is a dose-dependent inhibitor of adipocyte differentiation, probably by reducing cAMP pool. Frontiers in cell and developmental biology, 2, 29.

[83] Seo, Y. S., Kang, O. H., Kim, S. B., Mun, S. H., Kang, D. H., Yang, D. W., .et al. (2015). Quercetin prevents adipogenesis by regulation of transcriptional factors and lipases in OP9 cells. International journal of molecular medicine, 35(6), 1779-1785.

[84] Xiao, L., Aoshima, H., Saitoh, Y., & Miwa, N. (2011). Highly hydroxylated fullerene localizes at the cytoskeleton and inhibits oxidative stress in adipocytes and a subcutaneous adipose-tissue equivalent. Free Radical Biology and Medicine, 51(7), 1376-1389.

[85] Armani, A., Mammi, C., Marzolla, V., Calanchini, M., Antelmi, A., Rosano, G. M., et al. (2010). Cellular models for understanding adipogenesis, adipose dysfunction, and obesity. Journal of cellular biochemistry, 110(3), 564-572.

[86] Jeong, M. Y., Kim, H. L., Park, J., Jung, Y., Youn, D. H., Lee, J. H., et al. (2015). Rubi Fructus (Rubus coreanus) activates the expression of thermogenic genes in vivo and in vitro. International Journal of Obesity, 39(3), 456-464.

[87] Cawthorn, W. P., Scheller, E. L., & MacDougald, O. A. (2012). Adipose tissue stem cells meet preadipocyte commitment: going back to the future [S]. Journal of lipid research, 53(2), 227-246.

[88] Bunnell, B. A., Flaat, M., Gagliardi, C., Patel, B., & Ripoll, C. (2008). Adipose-derived stem cells: isolation, expansion and differentiation. Methods, 45(2), 115-120.

[89] Tews, D., Brenner, R. E., Siebert, R., Debatin, K. M., Fischer-Posovszky, P., & Wabitsch, M. (2022). 20 Years with SGBS cells-a versatile in vitro model of human adipocyte biology. International Journal of Obesity, 46(11), 1939-1947.

[90] Wabitsch, M., Brenner, R. E., Melzner, I., Braun, M., Möller, P., Heinze, E et al. (2001). Characterization of a human preadipocyte cell strain with high capacity for adipose differentiation. International journal of obesity, 25(1), 8-15.

[91] DeBaun, M. R., Ess, J., & Saunders, S. (2001). Simpson Golabi Behmel syndrome: progress toward understanding the molecular basis for overgrowth, malformation, and cancer predisposition. Molecular genetics and metabolism, 72(4), 279-286.

[92] Fischer-Posovszky, P., Newell, F. S., Wabitsch, M., & Tornqvist, H. E. (2008). Human SGBS cells–a unique tool for studies of human fat cell biology. Obesity facts, 1(4), 184-189.

[93] Ruiz-Ojeda, F. J., Rupérez, A. I., Gomez-Llorente, C., Gil, A., & Aguilera, C. M. (2016). Cell models and their application for studying adipogenic differentiation in relation to obesity: a review. International journal of molecular sciences, 17(7), 1040.

[94] Allott, E. H., Oliver, E., Lysaght, J., Gray, S. G., Reynolds, J. V., Roche, H. M et al. (2012). The SGBS cell strain as a model for the in vitro study of obesity and cancer. Clinical and Translational Oncology, 14, 774-782.

[95] Guennoun, A., Kazantzis, M., Thomas, R., Wabitsch, M., Tews, D., Seetharama Sastry, et al. (2015). Comprehensive molecular characterization of human adipocytes reveals a transient brown phenotype. Journal of translational medicine, 13, 1-18.

[96] Montanari, T., & Colitti, M. (2018). Simpson–Golabi–Behmel syndrome human adipocytes reveal a changing phenotype throughout differentiation. Histochemistry and Cell Biology, 149, 593-605.

[97] Halbgebauer, D., Dahlhaus, M., Wabitsch, M., Fischer-Posovszky, P., & Tews, D. (2020). Browning capabilities of human primary adipose-derived stromal cells compared to SGBS cells. Scientific reports, 10(1), 9632.

[98] Montanari, T., & Colitti, M. (2018). Simpson–Golabi–Behmel syndrome human adipocytes reveal a changing phenotype throughout differentiation. Histochemistry and Cell Biology, 149, 593-605.

[99] Klusóczki, Á., Veréb, Z., Vámos, A., Fischer-Posovszky, P., Wabitsch, M., Bacso, et al. (2019). Differentiating SGBS adipocytes respond to PPARγ stimulation, irisin and BMP7 by functional browning and beige characteristics. Scientific Reports, 9(1), 1-12.

[100] Klusóczki, Á., Veréb, Z., Vámos, A., Fischer-Posovszky, P., Wabitsch, M., Bacso, et al. (2019). Differentiating SGBS adipocytes respond to PPARγ stimulation, irisin and BMP7 by functional browning and beige characteristics. Scientific Reports, 9(1), 1-12.

[101] Waldén, T. B., Hansen, I. R., Timmons, J. A., Cannon, B., & Nedergaard, J. (2012). Recruited vs. nonrecruited molecular signatures of brown, "brite," and white adipose tissues. American journal of physiology-endocrinology and metabolism, 302(1), E19-E31.

[102] Krause, K. (2020). Novel aspects of white adipose tissue browning by thyroid hormones. Experimental and Clinical Endocrinology & Diabetes, 128(06/07), 446-449.

[103] Peppler, W. T., Townsend, L. K., Knuth, C. M., Foster, M. T., & Wright, D. C. (2018). Subcutaneous inguinal white adipose tissue is responsive to, but dispensable for, the metabolic health benefits of exercise. American Journal of Physiology-Endocrinology and Metabolism, 314(1), E66-E77.

[104] Zhang, F., Hao, G., Shao, M., Nham, K., An, Y., Wang, Q et al. (2018). An adipose tissue atlas: an image-guided identification of human-like BAT and beige depots in rodents. Cell metabolism, 27(1), 252-262.

[105] Lim, S., Honek, J., Xue, Y., Seki, T., Cao, Z., Andersson, P., et al. (2012). Cold-induced activation of brown adipose tissue and adipose angiogenesis in mice. Nature protocols, 7(3), 606-615.

[106] Contreras, G. A., Lee, Y. H., Mottillo, E. P., & Granneman, J. G. (2014). Inducible brown adipocytes in subcutaneous inguinal white fat: the role of continuous sympathetic stimulation. American Journal of Physiology-Endocrinology and Metabolism, 307(9), E793-E799.

[107] Kim, S. N., Jung, Y. S., Kwon, H. J., Seong, J. K., Granneman, J. G., et al. (2016). Sex differences in sympathetic innervation and browning of white adipose tissue of mice. Biology of sex differences, 7(1), 1-13.

[108] Li, H., Matheny, M., Nicolson, M., Türner, N., & Scarpace, P. J. (1997). Leptin gene expression increases with age independent of increasing adiposity in rats. Diabetes, 46(12), 2035-2039.

[109] Abu-Odeh, M., Zhang, Y., Reilly, S. M., Ebadat, N., Keinan, O., Valentine, J. M,. et al. (2021). FGF21 promotes thermogenic gene expression as an autocrine factor in adipocytes. Cell reports, 35(13), 109331.

[110] Abu-Odeh, M., Zhang, Y., Reilly, S. M., Ebadat, N., Keinan, O., Valentine, J. M., et al. (2021). FGF21 promotes thermogenic gene expression as an autocrine factor in adipocytes. Cell reports, 35(13), 109331.

[111] Giralt, M., & Villarroya, F. (2013). White, brown, beige/brite: different adipose cells for different functions?. Endocrinology, 154(9), 2992-3000.

[112] Yoneshiro, T., Aita, S., Matsushita, M., Kayahara, T., Kameya, T., Kawai, Y.,et al. (2013). Recruited brown adipose tissue as an antiobesity agent in humans. The Journal of clinical investigation, 123(8), 3404-3408.

[113] Thyagarajan, B., & Foster, M. T. (2017). Beiging of white adipose tissue as a therapeutic strategy for weight loss in humans. Hormone molecular biology and clinical investigation, 31(2).

[114] Bartelt, A., Weigelt, C., Cherradi, M. L., Niemeier, A., Tödter, K., Heeren, J., et al. (2013). Effects of adipocyte lipoprotein lipase on de novo lipogenesis and white adipose tissue browning. Biochimica Et Biophysica Acta (BBA)-Molecular and Cell Biology of Lipids, 1831(5), 934-942.

[115] Kim, S. H., & Plutzky, J. (2016). Brown fat and browning for the treatment of obesity and related metabolic disorders. Diabetes & metabolism journal, 40(1), 12-21.

[116] Barberá, M. J., Schluter, A., Pedraza, N., Iglesias, R., Villarroya, F., & Giralt, M. (2001). Peroxisome proliferator-activated receptor α activates transcription of the brown fat uncoupling protein-1 gene: a link between regulation of the thermogenic and lipid oxidation pathways in the brown fat cell. Journal of Biological Chemistry, 276(2), 1486-1493.

[117] Hondares, E., Rosell, M., Díaz-Delfín, J., Olmos, Y., Monsalve, M., Iglesias, R., et al. (2011). Peroxisome proliferator-activated receptor α (PPARα) induces PPARγ coactivator 1α (PGC-1α) gene expression and contributes to thermogenic activation of brown fat: involvement of PRDM16. Journal of Biological Chemistry, 286(50), 43112-43122.

[118] Trajkovski, M., & Lodish, H. (2013). MicroRNA networks regulate development of brown adipocytes. Trends in Endocrinology & Metabolism, 24(9), 442-450.

[119] Colitti, M., & Grasso, S. (2014). Nutraceuticals and regulation of adipocyte life: premises or promises. Biofactors, 40(4), 398-418.

[120] Armani, A., Feraco, A., Camajani, E., Gorini, S., Lombardo, M., & Caprio, M. (2022). Nutraceuticals in Brown Adipose Tissue Activation. Cells, 11(24), 3996.

[121] Zhao, Y., Chen, B., Shen, J., Wan, L., Zhu, Y., Yi, T., & Xiao, Z. (2017). The beneficial effects of quercetin, curcumin, and resveratrol in obesity. Oxidative medicine and cellular longevity, 2017.

[122] Aggarwal, B. B. (2010). Targeting inflammation-induced obesity and metabolic diseases by curcumin and other nutraceuticals. Annual review of nutrition, 30, 173-199.

[123] Colitti, M., & Stefanon, B. (2016). Different anti-adipogenic effects of bio-compounds on primary visceral pre-adipocytes and adipocytes. EXCLI journal, 15, 362.

[124] Colitti, M., & Stefanon, B. (2016). Different anti-adipogenic effects of bio-compounds on primary visceral pre-adipocytes and adipocytes. EXCLI journal, 15, 362.

[125] Montanari, T., Pošćić, N., & Colitti, M. (2017). Factors involved in white-to-brown adipose tissue conversion and in thermogenesis: a review. Obesity Reviews, 18(5), 495-513.

[126] Azhar, Y., Parmar, A., Miller, C. N., Samuels, J. S., & Rayalam, S. (2016). Phytochemicals as novel agents for the induction of browning in white adipose tissue. Nutrition & metabolism, 13(1), 89.

[127] Wang, S., Wang, X., Ye, Z., Xu, C., Zhang, M., Ruan, B., ... & Lu, Z. (2015). Curcumin promotes browning of white adipose tissue in a norepinephrine-dependent way. Biochemical and Biophysical Research Communications, 466(2), 247-253.

[128] Wang, S., Wang, X., Ye, Z., Xu, C., Zhang, M., Ruan, B., ... & Lu, Z. (2015). Curcumin promotes browning of white adipose tissue in a norepinephrine-dependent way. Biochemical and Biophysical Research Communications, 466(2), 247-253.

[129] Lone, J., Choi, J. H., Kim, S. W., & Yun, J. W. (2016). Curcumin induces brown fat-like phenotype in 3T3-L1 and primary white adipocytes. The journal of nutritional biochemistry, 27, 193-202.

[130] Andrade, J. M. O., Frade, A. C. M., Guimaraes, J. B., Freitas, K. M., Lopes, M. T. P., Guimarães, A. L. S., et al. (2014). Resveratrol increases brown adipose tissue thermogenesis markers by increasing SIRT1 and energy expenditure and decreasing fat accumulation in adipose tissue of mice fed a standard diet. European journal of nutrition, 53, 1503-1510.

[131] Wang, S., Liang, X., Yang, Q., Fu, X., Rogers, C. J., Zhu, M., et al. (2015). Resveratrol induces brown-like adipocyte formation in white fat through activation of AMP-activated protein kinase (AMPK) α1. International journal of obesity, 39(6), 967-976.

[132] Zou, T., Chen, D., Yang, Q., Wang, B., Zhu, M. J., Nathanielsz, P. W., et al. (2017). Resveratrol supplementation of high-fat diet-fed pregnant mice promotes brown and beige adipocyte development and prevents obesity in male offspring. The Journal of physiology, 595(5), 1547-1562.

[133] Baskaran, P., Krishnan, V., Ren, J., & Thyagarajan, B. (2016). Capsaicin induces browning of white adipose tissue and counters obesity by activating TRPV1 channel-dependent mechanisms. British journal of pharmacology, 173(15), 2369-2389.

[134] Montanari, T., Boschi, F., & Colitti, M. (2019). Comparison of the effects of browning-inducing capsaicin on two murine adipocyte models. *Frontiers in physiology*, *10*, 1380.

[135] Montanari, T., Boschi, F., & Colitti, M. (2019). Comparison of the effects of browning-inducing capsaicin on two murine adipocyte models. Frontiers in physiology, 10, 1380.

[136] Baskaran, P., Krishnan, V., Ren, J., & Thyagarajan, B. (2016). Capsaicin induces browning of white adipose tissue and counters obesity by activating TRPV1 channel-dependent mechanisms. British journal of pharmacology, 173(15), 2369-2389.

[137] Arias, N., Picó, C., Teresa Macarulla, M., Oliver, P., Miranda, J., Palou, A., & Portillo, M. P. (2017). A combination of resveratrol and quercetin induces browning in white adipose tissue of rats fed an obesogenic diet. Obesity, 25(1), 111-121.

[138] Pei, Y., Otieno, D., Gu, I., Lee, S. O., Parks, J. S., Schimmel, K., et al. (2021). Effect of quercetin on nonshivering thermogenesis of brown adipose tissue in high-fat diet-induced obese mice. The Journal of Nutritional Biochemistry, 88, 108532.

[139] Pei, Y., Otieno, D., Gu, I., Lee, S. O., Parks, J. S., Schimmel, K., et al. (2021). Effect of quercetin on nonshivering thermogenesis of brown adipose tissue in high-fat diet-induced obese mice. The Journal of Nutritional Biochemistry, 88, 108532.

[140] Wein, S., Behm, N., Petersen, R. K., Kristiansen, K., & Wolffram, S. (2010). Quercetin enhances adiponectin secretion by a PPAR-γ independent mechanism. European Journal of Pharmaceutical Sciences, 41(1), 16-22.

[141] Tews, D., Brenner, R. E., Siebert, R., Debatin, K. M., Fischer-Posovszky, P., & Wabitsch, M. (2022). 20 Years with SGBS cells-a versatile in vitro model of human adipocyte biology. International Journal of Obesity, 46(11), 1939-1947.

[142] Fuggetta, M. P., Zonfrillo, M., Villivà, C., Bonmassar, E., & Ravagnan, G. (2019). Inflammatory microenvironment and adipogenic differentiation in obesity: the inhibitory effect of theobromine in a model of human obesity in vitro. Mediators of inflammation, 2019.

[143] Mitani, T., Watanabe, S., Yoshioka, Y., Katayama, S., Nakamura, S., & Ashida, H. (2017). Theobromine suppresses adipogenesis through enhancement of CCAAT-enhancer-binding protein β degradation by adenosine receptor A1. Biochimica et Biophysica Acta (BBA)-Molecular Cell Research, 1864(12), 2438-2448.

[144] Tanaka, E., Mitani, T., Nakashima, M., Yonemoto, E., Fujii, H., & Ashida, H. (2022). Theobromine enhances the conversion of white adipocytes into beige adipocytes in a PPARγ activation-dependent manner. The Journal of Nutritional Biochemistry, 100, 108898.

[145] Tanaka, E., Mitani, T., Nakashima, M., Yonemoto, E., Fujii, H., & Ashida, H. (2022). Theobromine enhances the conversion of white adipocytes into beige adipocytes in a PPARγ activation-dependent manner. The Journal of Nutritional Biochemistry, 100, 108898.

[146] Stote, K. S., Clevidence, B. A., Novotny, J. A., Henderson, T., Radecki, S. V., & Baer, D. J. (2012). Effect of cocoa and green tea on biomarkers of glucose regulation, oxidative stress, inflammation and hemostasis in obese adults at risk for insulin resistance. European Journal of Clinical Nutrition, 66(10), 1153-1159.

[147] Li, K. K., Liu, C. L., Shiu, H. T., Wong, H. L., Siu, W. S., Zhang, C., et al. (2016). Cocoa tea (Camellia ptilophylla) water extract inhibits adipocyte differentiation in mouse 3T3-L1 preadipocytes. Scientific reports, 6(1), 1-11.

[148] Min, S. Y., Yang, H., Seo, S. G., Shin, S. H., Chung, M. Y., Kim, J., et al. (2013). Cocoa polyphenols suppress adipogenesis in vitro and obesity in vivo by targeting insulin receptor. International journal of obesity, 37(4), 584-592.

[149] Drira, R., Chen, S., & Sakamoto, K. (2011). Oleuropein and hydroxytyrosol inhibit adipocyte differentiation in 3 T3-L1 cells. Life sciences, 89(19-20), 708-716.

[150] Hadrich, F., Mahmoudi, A., Chamkha, M., Isoda, H., & Sayadi, S. (2023). Olive Leaves Extract and Oleuropein Improve Insulin Sensitivity in 3T3-L1 Cells and in High-Fat Diet-Treated Rats via PI3K/AkT Signaling Pathway. Oxidative Medicine and Cellular Longevity, 2023.

[151] Fromme, T., & Klingenspor, M. (2011). Uncoupling protein 1 expression and high-fat diets. American Journal of Physiology-Regulatory, Integrative and Comparative Physiology, 300(1), R1-R8.

[152] Bayan, L., Koulivand, P. H., & Gorji, A. (2014). Garlic: a review of potential therapeutic effects. Avicenna journal of phytomedicine, 4(1), 1.

[153] Ding, G., Zhao, J., & Jiang, D. (2016). Allicin inhibits oxidative stress-induced mitochondrial dysfunction and apoptosis by promoting PI3K/AKT and CREB/ERK signaling in osteoblast cells. Experimental and therapeutic medicine, 11(6), 2553-2560.

[154] El-Sheakh, A. R., Ghoneim, H. A., Suddek, G. M., & Ammar, E. S. M. (2016). Attenuation of oxidative stress, inflammation, and endothelial dysfunction in hypercholesterolemic rabbits by allicin. Canadian journal of physiology and pharmacology, 94(2), 216-224.

[155] Zhang, C., He, X., Sheng, Y., Xu, J., Yang, C., Zheng, S., et al. (2020). Allicin regulates energy homeostasis through brown adipose tissue. IScience, 23(5), 101113.

[156] Zhang, C., He, X., Sheng, Y., Xu, J., Yang, C., Zheng, S., et al. (2020). Allicin regulates energy homeostasis through brown adipose tissue. IScience, 23(5), 101113.

[157] Lee, C. G., Rhee, D. K., Kim, B. O., Um, S. H., & Pyo, S. (2019). Allicin induces beige-like adipocytes via KLF15 signal cascade. The Journal of nutritional biochemistry, 64, 13-24.

[158] Guo, Y. Y., Li, B. Y., Peng, W. Q., Guo, L., & Tang, Q. Q. (2019). Taurine-mediated browning of white adipose tissue is involved in its anti-obesity effect in mice. Journal of Biological Chemistry, 294(41), 15014-15024.

[159] Guo, Y. Y., Li, B. Y., Peng, W. Q., Guo, L., & Tang, Q. Q. (2019). Taurine-mediated browning of white adipose tissue is involved in its anti-obesity effect in mice. Journal of Biological Chemistry, 294(41), 15014-15024.

[160] Zhang, P., He, Y., Wu, S., Li, X., Lin, X., Gan, M., et al. (2022). Factors Associated with White Fat Browning: New Regulators of Lipid Metabolism. International Journal of Molecular Sciences, 23(14), 7641.

[161] Li, Y., Schnabl, K., Gabler, S. M., Willershäuser, M., Reber, J., Karlas, A., et al. (2018). Secretin-activated brown fat mediates prandial thermogenesis to induce satiation. Cell, 175(6), 1561-1574.

[162] Li, Y., Schnabl, K., Gabler, S. M., Willershäuser, M., Reber, J., Karlas, A., et al. (2018). Secretin-activated brown fat mediates prandial thermogenesis to induce satiation. Cell, 175(6), 1561-1574.

[163] Li, L., Li, B., Li, M., & Speakman, J. R. (2019). Switching on the furnace: regulation of heat production in brown adipose tissue. Molecular aspects of medicine, 68, 60-73.

[164] Kibble, M., Saarinen, N., Tang, J., Wennerberg, K., Mäkelä, S., & Aittokallio, T. (2015). Network pharmacology applications to map the unexplored target space and therapeutic potential of natural products. Natural product reports, 32(8), 1249-1266.

[165] Hopkins, A. L. (2007). Network pharmacology. Nature biotechnology, 25(10), 1110-1111.

[166] Kim, S., Thiessen, P. A., Bolton, E. E., Chen, J., Fu, G., Gindulyte, A., ... & Bryant, S. H. (2016). PubChem substance and compound databases. *Nucleic acids research*, *44*(D1), D1202-D1213.

[167] Liu, X., Ouyang, S., Yu, B., Liu, Y., Huang, K., Gong, J., ... & Jiang, H. (2010). PharmMapper server: a web server for potential drug target identification using pharmacophore mapping approach. *Nucleic acids research*, *38*(suppl_2), W609-W614.

[168] Chen, Y. Z., & Zhi, D. G. (2001). Ligand–protein inverse docking and its potential use in the computer search of protein targets of a small molecule. *Proteins: Structure, Function, and Bioinformatics*, *43*(2), 217-226.

[169] Keiser, M. J., Roth, B. L., Armbruster, B. N., Ernsberger, P., Irwin, J. J., & Shoichet, B. K. (2007). Relating protein pharmacology by ligand chemistry. *Nature biotechnology*, *25*(2), 197-206.

[170] Szklarczyk, D., Santos, A., Von Mering, C., Jensen, L. J., Bork, P., & Kuhn, M. (2016). STITCH 5: augmenting protein–chemical interaction networks with tissue and affinity data. *Nucleic acids research*, *44*(D1), D380-D384.

[171] Safran, M., Dalah, I., Alexander, J., Rosen, N., Iny Stein, T., Shmoish, M., ... & Lancet, D. (2010). GeneCards Version 3: the human gene integrator. *Database*, *2010*.

[172] Schaller, D., Šribar, D., Noonan, T., Deng, L., Nguyen, T. N., Pach, S., et al. (2020). Next generation 3D pharmacophore modeling. Wiley Interdisciplinary Reviews: Computational Molecular Science, 10(4), e1468.

[173] Liu, X., Ouyang, S., Yu, B., Liu, Y., Huang, K., Gong, J., et al. (2010). PharmMapper server: a web server for potential drug target identification using a pharmacophore mapping approach. *Nucleic acids research*, *38*(suppl_2), W609-W614.

[174] Wang, Z., Liang, L., Yin, Z., & Lin, J. (2016). Improving chemical similarity ensemble approach in target prediction. *Journal of cheminformatics*, *8*, 1-10.

[175] Szklarczyk, D., Santos, A., Von Mering, C., Jensen, L. J., Bork, P., & Kuhn, M. (2016). STITCH 5: augmenting protein–chemical interaction networks with tissue and affinity data. *Nucleic acids research*, *44*(D1), D380-D384.

[176] Daina, A., Michielin, O., & Zoete, V. (2019). SwissTargetPrediction: updated data and new features for efficient prediction of protein targets of small molecules. *Nucleic acids research*, *47*(W1), W357-W364.

[177] Warde-Farley, D., Donaldson, S. L., Comes, O., Zuberi, K., Badrawi, R., Chao, P., et al. (2010). The GeneMANIA prediction server: biological network integration for gene prioritization and predicting gene function. *Nucleic acids research*, *38*(suppl_2), W214-W220.

[178] Wabitsch, M., Brenner, R. E., Melzner, I., Braun, M., Möller, P., Heinze, E., ... et al. (2001). Characterization of a human preadipocyte cell strain with high capacity for adipose differentiation. *International journal of obesity*, *25*(1), 8-15.

[179] Wabitsch, M., Brenner, R. E., Melzner, I., Braun, M., Möller, P., Heinze, E., et al. (2001). Characterization of a human preadipocyte cell strain with high capacity for adipose differentiation. International journal of obesity, 25(1), 8-15.

[180] Guo, Y. Y., Li, B. Y., Peng, W. Q., Guo, L., & Tang, Q. Q. (2019). Taurine-mediated browning of white adipose tissue is involved in its anti-obesity effect in mice. Journal of Biological Chemistry, 294(41), 15014-15024.

[181] Cannon, B., & Nedergaard, J. (2001). Cultures of adipose precursor cells from brown adipose tissue and of clonal brown-adipocyte-like cell lines. Adipose Tissue Protocols, 213-224.

[182] Baecker, V. (2012, October). ImageJ macro tool sets for biological image analysis. In Proceedings of the ImageJ User and Developer Conference, Luxembourg (Vol. 24, p. 26).

[183] Boschi, F., Rizzatti, V., Zoico, E., Montanari, T., Zamboni, M., Sbarbati, A., et al. (2019). Relationship between lipid droplets size and integrated optical density. European Journal of Histochemistry: EJH, 63(1).

[184] Boschi, F., Rizzatti, V., Zoico, E., Montanari, T., Zamboni, M., Sbarbati, A., et al. (2019). Relationship between lipid droplets size and integrated optical density. European Journal of Histochemistry: EJH, 63(1).

[185] Chazotte, B. (2011). Labeling mitochondria with MitoTracker dyes. Cold Spring Harbor Protocols, 2011(8), pdb-prot5648.

[186] Buckman, J. F., Hernández, H., Kress, G. J., Votyakova, T. V., Pal, S., & Reynolds, I. J. (2001). MitoTracker labeling in primary neuronal and astrocytic cultures: influence of mitochondrial membrane potential and oxidants. Journal of neuroscience methods, 104(2), 165-176.

[187] Chaudhry, A., Shi, R., & Luciani, D. S. (2020). A pipeline for multidimensional confocal analysis of mitochondrial morphology, function, and dynamics in pancreatic β-cells. American Journal of Physiology-Endocrinology and Metabolism, 318(2), E87-E101.

[188] Valente, A. J., Maddalena, L. A., Robb, E. L., Moradi, F., & Stuart, J. A. (2017). A simple ImageJ macro tool for analyzing mitochondrial network morphology in mammalian cell culture. Acta histochemica, 119(3), 315-326.

[189] Peng, J. Y., Lin, C. C., Chen, Y. J., Kao, L. S., Liu, Y. C., Chou, C. C., et al. (2011). Automatic morphological subtyping reveals new roles of caspases in mitochondrial dynamics. PLoS computational biology, 7(10), e1002212.

[190] Peng, J. Y., Lin, C. C., Chen, Y. J., Kao, L. S., Liu, Y. C., Chou, C. C., ... et al. (2011). Automatic morphological subtyping reveals new roles of caspases in mitochondrial dynamics. PLoS computational biology, 7(10), e1002212.

[191] Mosmann, T. (1983). Rapid colorimetric assay for cellular growth and survival: application to proliferation and cytotoxicity assays. Journal of immunological methods, 65(1-2), 55-63.

[192] Berridge, M. V., Herst, P. M., & Tan, A. S. (2005). Tetrazolium dyes as tools in cell biology: new insights into their cellular reduction. Biotechnology annual review, 11, 127-152.

[193] Rozen, S., & Skaletsky, H. (1999). Primer3 on the WWW for general users and for biologist programmers. Bioinformatics methods and protocols, 365-386.

[194] Schmittgen, T. D., & Livak, K. J. (2008). Analyzing real-time PCR data by the comparative CT method. Nature protocols, 3(6), 1101-1108.

[195]Gene Ontology Consortium. (2006). The gene ontology (GO) project in 2006. Nucleic acids research, 34(suppl_1), D322-D326.

[196] Ge, X. (2021). iDEP web application for RNA-Seq data analysis. RNA Bioinformatics, 417-443.

[197] Jiang, C., Xuan, Z., Zhao, F., & Zhang, M. Q. (2007). TRED: a transcriptional regulatory element database, new entries and other development. Nucleic acids research, 35(suppl_1), D137-D140.

[198] Waterborg, J. H. (2009). The Lowry method for protein quantitation. The protein protocols handbook, 7-10.

[199] Cheng, Y., Jiang, L., Keipert, S., Zhang, S., Hauser, A., Graf, E., et al. (2018). Prediction of adipose browning capacity by systematic integration of transcriptional profiles. Cell reports, 23(10), 3112-3125.

[200] Perdikari, A., Leparc, G. G., Balaz, M., Pires, N. D., Lidell, M. E., Sun, W., ... & Wolfrum, C. (2018). BATLAS: deconvoluting brown adipose tissue. *Cell reports*, *25*(3), 784-797.

[201] Cheng, Y., Jiang, L., Keipert, S., Zhang, S., Hauser, A., Graf, E., ... & Perocchi, F. (2018). Prediction of adipose browning capacity by systematic integration of transcriptional profiles. *Cell reports*, *23*(10), 3112-3125.

[202] Warde-Farley, D., Donaldson, S. L., Comes, O., Zuberi, K., Badrawi, R., Chao, P., et al. (2010). The GeneMANIA prediction server: biological network integration for gene

prioritization and predicting gene function. Nucleic acids research, 38(suppl_2), W214-W220.

[203] Tang, Y., Li, M., Wang, J., Pan, Y., & Wu, F. X. (2015). CytoNCA: a cytoscape plugin for centrality analysis and evaluation of protein interaction networks. Biosystems, 127, 67-72.

[204] Stelzer, G., Plaschkes, I., Oz-Levi, D., Alkelai, A., Olender, T., Zimmerman, S., et al. (2016). VarElect: the phenotype-based variation prioritizer of the GeneCards Suite. BMC genomics, 17(2), 195-206.

[205] Huang, J., Cheung, F., Tan, H. Y., Hong, M., Wang, N., Yang, J., et al. (2017). Identification of the active compounds and significant pathways of yinchenhao decoction based on network pharmacology. Molecular Medicine Reports, 16(4), 4583-4592.

[207] Ohno, H., Shinoda, K., Spiegelman, B. M., & Kajimura, S. (2012). PPARγ agonists induce a white-to-brown fat conversion through stabilization of PRDM16 protein. Cell metabolism, 15(3), 395-404.

[208] Wu, J., Cohen, P., & Spiegelman, B. M. (2013). Adaptive thermogenesis in adipocytes: is beige the new brown?. Genes & development, 27(3), 234-250.

[209] Christian, M., & Parker, M. G. (2010). The engineering of brown fat. Journal of molecular cell biology, 2(1), 23-25.

[210] Montanari, T., Pošćić, N., & Colitti, M. (2017). Factors involved in white-to-brown adipose tissue conversion and in thermogenesis: a review. Obesity Reviews, 18(5), 495-513.

[211] Kajimura, S., Seale, P., Kubota, K., Lunsford, E., Frangioni, J. V., Gygi, S. P., et al. (2009). Initiation of myoblast to brown fat switch by a PRDM16–C/EBP-β transcriptional complex. Nature, 460(7259), 1154-1158.

[212] Montanari, T., & Colitti, M. (2018). Simpson–Golabi–Behmel syndrome human adipocytes reveal a changing phenotype throughout differentiation. Histochemistry and Cell Biology, 149, 593-605.

[213] Galhardo, M., Sinkkonen, L., Berninger, P., Lin, J., Sauter, T., & Heinäniemi, M. (2014). Integrated analysis of transcript-level regulation of metabolism reveals disease-relevant nodes of the human metabolic network. Nucleic acids research, 42(3), 1474-1496.

[214] Hansson, B., Morén, B., Fryklund, C., Vliex, L., Wasserstrom, S., Albinsson, S., et al. (2019). Adipose cell size changes are associated with a drastic actin remodeling. Scientific Reports, 9(1), 1-14.

[215] Montanari, T., & Colitti, M. (2018). Simpson–Golabi–Behmel syndrome human adipocytes reveal a changing phenotype throughout differentiation. Histochemistry and Cell Biology, 149, 593-605.

[216] Nakajima, I., Muroya, S., Tanabe, R. I., & Chikuni, K. (2002). Extracellular matrix development during differentiation into adipocytes with a unique increase in type V and VI collagen. Biology of the Cell, 94(3), 197-203.

[217] Tharp, K. M., Kang, M. S., Timblin, G. A., Dempersmier, J., Dempsey, G. E., Zushin, P. J. H., et al. (2018). Actomyosin-mediated tension orchestrates uncoupled respiration in adipose tissues. Cell metabolism, 27(3), 602-615.

[218] Green, C. R., Wallace, M., Divakaruni, A. S., Phillips, S. A., Murphy, A. N., Ciaraldi, T. P., et al. (2016). Branched-chain amino acid catabolism fuels adipocyte differentiation and lipogenesis. Nature chemical biology, 12(1), 15-21.

[219] Fajas, L., Landsberg, R. L., Huss-Garcia, Y., Sardet, C., Lees, J. A., & Auwerx, J. (2002). E2Fs regulate adipocyte differentiation. Developmental cell, 3(1), 39-49.

[220] Vernochet, C., Peres, S. B., Davis, K. E., McDonald, M. E., Qiang, L., Wang, H., et al. (2009). C/EBPalpha and the corepressors CtBP1 and CtBP2 regulate repression of select visceral white adipose genes during induction of the brown phenotype in white adipocytes by peroxisome proliferator-activated receptor gamma agonists.. Mol Cell Biol, 29. (17): 4714-4728.

[221] Klusóczki, Á., Veréb, Z., Vámos, A., Fischer-Posovszky, P., Wabitsch, M., Bacso, Z., & Kristóf, E. (2019). Differentiating SGBS adipocytes respond to PPARγ stimulation, irisin and BMP7 by functional browning and beige characteristics. Scientific Reports, 9(1), 1-12.

[222] Petrovie, N., Walden, T. B., & Shabalina, I. G. (2010). Chronic peroxisome proliferator-activated receptor gamma (PPARgamma) activation of epididymally derived white adipocyte cultures reveals a population of thermogenically competent, UCP1-containing adipocytes molecularly distinct from classic brown adipocytes. J Biol Chem, 285(10), 7153-7164.

[223] Beaudoin, M. S., Snook, L. A., Arkell, A. M., Stefanson, A., Wan, Z., Simpson, J. A., et al. (2014). Novel effects of rosiglitazone on SMAD2 and SMAD3 signaling in white adipose tissue of diabetic rats. Obesity, 22(7), 1632-1642.

[224] Yadav, H., Quijano, C., Kamaraju, A. K., Gavrilova, O., Malek, R., Chen, W., et al. (2011). Protection from obesity and diabetes by blockade of TGF-β/Smad3 signaling. Cell metabolism, 14(1), 67-79.

[225] Reggio, S., Rouault, C., Poitou, C., Bichet, J. C., Prifti, E., Bouillot, J. L., et al. (2016). Increased basement membrane components in adipose tissue during obesity: links with TGFβ and metabolic phenotypes. The Journal of Clinical Endocrinology & Metabolism, 101(6), 2578-2587.

[226] Perdikari, A., Leparc, G. G., Balaz, M., Pires, N. D., Lidell, M. E., Sun, W., ... & Wolfrum, C. (2018). BATLAS: deconvoluting brown adipose tissue. *Cell reports*, *25*(3), 784-797.

[227] Yeo, C. R., Agrawal, M., Hoon, S., Shabbir, A., Shrivastava, M. K., Huang, S., et al. (2017). SGBS cells as a model of human adipocyte browning: A comprehensive comparative study with primary human white subcutaneous adipocytes. Scientific reports, 7(1), 4031.

[228] Raza, S. H. A., Sameer, D. P., Wani, A. K., Mohamed, H. H., Khalifa, N. E., Almohaimeed, H. M., et al. (2022). Krüppel-like factors family regulation of adipogenic markers genes in bovine cattle adipogenesis. Molecular and Cellular Probes, 101850.

[229] Li, H., Rafie, A. R., Hamama, A., & Siddiqui, R. A. (2023). Immature ginger reduces triglyceride accumulation by downregulating Acyl CoA carboxylase and phosphoenolpyruvate carboxykinase-1 genes in 3T3-L1 adipocytes. Food & Nutrition Research.

[230] Park, U. H., Jeong, J. C., Jang, J. S., Sung, M. R., Youn, H., Lee, S. J., et al. (2012). Negative regulation of adipogenesis by kaempferol, a component of Rhizoma Polygonati falcatum in 3T3-L1 cells. Biological and Pharmaceutical Bulletin, 35(9), 1525-1533.

[231] Rossato, M., Granzotto, M., Macchi, V., Porzionato, A., Petrelli, L., Calcagno, A., et al. (2014). Human white adipocytes express the cold receptor TRPM8 which activation induces UCP1 expression, mitochondrial activation and heat production. Molecular and cellular endocrinology, 383(1-2), 137-146.

[232] Goralczyk, A., van Vijven, M., Koch, M., Badowski, C., Yassin, M. S., Toh, S. A., et al. (2017). TRP channels in brown and white adipogenesis from human progenitors: new therapeutic targets and the caveats associated with the common antibiotic, streptomycin. The FASEB Journal, 31(8), 3251-3266.

[233] Bargut, T. C. L., Souza-Mello, V., Aguila, M. B., & Mandarim-de-Lacerda, C. A. (2017). Browning of white adipose tissue: lessons from experimental models. Hormone molecular biology and clinical investigation, 31(1).

[234] Anderson, C. M., & Stahl, A. (2013). SLC27 fatty acid transport proteins. Molecular aspects of medicine, 34(2-3), 516-528.

[235] Campbell, C. T., Kolesar, J. E., & Kaufman, B. A. (2012). Mitochondrial transcription factor A regulates mitochondrial transcription initiation, DNA packaging, and genome copy number. Biochimica et Biophysica Acta (BBA)-Gene Regulatory Mechanisms, 1819(9-10), 921-929.

[236] Moreno-Lastres, D., Fontanesi, F., García-Consuegra, I., Martín, M. A., Arenas, J., Barrientos, A., et al. (2012). Mitochondrial complex I plays an essential role in human respirasome assembly. Cell metabolism, 15(3), 324-335.

[237] Subramani, M., & Yun, J. W. (2021). Loss of lymphocyte cytosolic protein 1 (LCP1) induces browning in 3T3-L1 adipocytes via β3-AR and the ERK-independent signaling pathway. The International Journal of Biochemistry & Cell Biology, 138, 106053.

[238] Zimmermann, R., Strauss, J. G., Haemmerle, G., Schoiswohl, G., Birner-Gruenberger, R., Riederer, M., et al. (2004). Fat mobilization in adipose tissue is promoted by adipose triglyceride lipase. Science, 306(5700), 1383-1386.

[239] Chitraju, C., Walther, T. C., & Farese, R. V. (2019). The triglyceride synthesis enzymes DGAT1 and DGAT2 have distinct and overlapping functions in adipocytes. Journal of lipid research, 60(6), 1112-1120.

[240] van Eenige, R., van der Stelt, M., Rensen, P. C., & Kooijman, S. (2018). Regulation of adipose tissue metabolism by the endocannabinoid system. Trends in Endocrinology & Metabolism, 29(5), 326-337.

[241] Sadana, R., & Dessauer, C. W. (2009). Physiological roles for G protein-regulated adenylyl cyclase isoforms: insights from knockout and overexpression studies. Neurosignals, 17(1), 5-22.

[242] Chaves, V. E., Frasson, D., & Kawashita, N. H. (2011). Several agents and pathways regulate lipolysis in adipocytes. *Biochimie*, *93*(10), 1631-1640.

[243] Scalise, M., Pochini, L., Galluccio, M., & Indiveri, C. (2016). Glutamine transport. From energy supply to sensing and beyond. Biochimica et Biophysica Acta (BBA)-Bioenergetics, 1857(8), 1147-1157.

[244] Cheng, S., Qian, K., Wang, Y., Wang, G., Liu, X., Xiao, Y.,et al. (2019). PPARγ inhibition regulates the cell cycle, proliferation and motility of bladder cancer cells. Journal of Cellular and Molecular Medicine, 23(5), 3724-3736.

[245] Audano, M., Pedretti, S., Caruso, D., Crestani, M., De Fabiani, E., & Mitro, N. (2022). Regulatory mechanisms of the early phase of white adipocyte differentiation: An overview. *Cellular and Molecular Life Sciences*, *79*(3), 139.

[246] Guennoun, A., Kazantzis, M., Thomas, R., Wabitsch, M., Tews, D., Seetharama Sastry, K., et al. (2015). Comprehensive molecular characterization of human adipocytes reveals a transient brown phenotype. Journal of translational medicine, 13, 1-18.

[247] Montanari, T., & Colitti, M. (2018). Simpson–Golabi–Behmel syndrome human adipocytes reveal a changing phenotype throughout differentiation. Histochemistry and Cell Biology, 149, 593-605.

[248] Guennoun, A., Kazantzis, M., Thomas, R., Wabitsch, M., Tews, D., Seetharama Sastry, et al. (2015). Comprehensive molecular characterization of human adipocytes reveals a transient brown phenotype. Journal of translational medicine, 13, 1-18.

[249] Jeong, M. Y., Park, J., Youn, D. H., Jung, Y., Kang, J., Lim, S., et al. (2017). Albiflorin ameliorates obesity by inducing thermogenic genes via AMPK and PI3K/AKT in vivo and in vitro. Metabolism, 73, 85-99.

[250] Huang, X., Liu, G., Guo, J., & Su, Z. (2018). The PI3K/AKT pathway in obesity and type 2 diabetes. International journal of biological sciences, 14(11), 1483.

[251] Morrison, S. F., Madden, C. J., & Tupone, D. (2014). Central neural regulation of brown adipose tissue thermogenesis and energy expenditure. Cell metabolism, 19(5), 741-756.

[252] Oliver, P., Lombardi, A., & De Matteis, R. (2020). insights into brown adipose tissue functions and browning phenomenon. Frontiers in Physiology, 11, 219.

[253] Montanari, T., Pošćić, N., & Colitti, M. (2017). Factors involved in white-to-brown adipose tissue conversion and in thermogenesis: a review. Obesity Reviews, 18(5), 495-513.

[254] Manríquez-Núñez, J., & Ramos-Gómez, M. (2022). Bioactive compounds and adipocyte browning phenomenon. Current Issues in Molecular Biology, 44(7), 3039-3052.

[255] Amagase, H. (2006). Clarifying the real bioactive constituents of garlic. The Journal of nutrition, 136(3), 716S-725S.

[256] Hu, Y., Xu, J., Gao, R., Xu, Y., Huangfu, B., Asakiya, C., et al. (2022). Diallyl Trisulfide Prevents Adipogenesis and Lipogenesis by Regulating the Transcriptional Activation Function of KLF15 on PPARγ to Ameliorate Obesity. Molecular Nutrition & Food Research, 66(22), 2200173.

[257] Chen, Y. C., Kao, T. H., Tseng, C. Y., Chang, W. T., & Hsu, C. L. (2014). Methanolic extract of black garlic ameliorates diet-induced obesity via regulating adipogenesis, adipokine biosynthesis, and lipolysis. Journal of Functional Foods, 9, 98-108.

[258] Lee, C. G., Rhee, D. K., Kim, B. O., Um, S. H., & Pyo, S. (2019). Allicin induces beige-like adipocytes via KLF15 signal cascade. The Journal of nutritional biochemistry, 64, 13-24.

[259] Zhang, C., He, X., Sheng, Y., Xu, J., Yang, C., Zheng, S., et al. (2020). Allicin regulates energy homeostasis through brown adipose tissue. IScience, 23(5), 101113.

[260] Ali, U., Wabitsch, M., Tews, D., & Colitti, M. (2023). Effects of allicin on human Simpson-Golabi-Behmel syndrome cells in mediating browning phenotype. Frontiers in Endocrinology, 14.

[261] Braun, K., Oeckl, J., Westermeier, J., Li, Y., & Klingenspor, M. (2018). Non-adrenergic control of lipolysis and thermogenesis in adipose tissues. Journal of Experimental Biology, 221(Suppl_1), jeb165381.

[262] Cheng, B., Li, T., & Li, F. (2021). Use of network pharmacology to investigate the mechanism by which allicin ameliorates lipid metabolism disorder in HepG2 cells. *Evidence-Based Complementary and Alternative Medicine*, *2021*.

[263] Lin, X. L., Hu, H. J., Liu, Y. B., Hu, X. M., Fan, X. J., Zou, W. W., et al. (2017). Allicin induces the upregulation of ABCA1 expression via PPARγ/LXRα signaling in THP-1 macrophage-derived foam cells. International Journal of Molecular Medicine, 39(6), 1452-1460.

[264] Tabuchi, C., & Sul, H. S. (2021). Signaling pathways regulating thermogenesis. Frontiers in Endocrinology, 12, 595020.

[265] Allison, G. L., Lowe, G. M., & Rahman, K. (2012). Aged garlic extract inhibits platelet activation by increasing intracellular cAMP and reducing the interaction of GPIIb/IIIa receptor with fibrinogen. Life sciences, 91(25-26), 1275-1280.

[266] Chaves, V. E., Frasson, D., & Kawashita, N. H. (2011). Several agents and pathways regulate lipolysis in adipocytes. Biochimie, 93(10), 1631-1640.

[267] Colitti, M., Ali, U., Wabitsch, M., & Tews, D. (2022). Transcriptomic analysis of Simpson Golabi Behmel syndrome cells during differentiation exhibit BAT-like function. *Tissue and Cell*, *77*, 101822.

[268]

[269] Zhang, C., He, X., Sheng, Y., Xu, J., Yang, C., Zheng, S., et al. (2020). Allicin regulates energy homeostasis through brown adipose tissue. IScience, 23(5), 101113.

[270] Lu, M., Sarruf, D. A., Talukdar, S., Sharma, S., Li, P., Bandyopadhyay, G., et al. (2011). Brain PPAR-γ promotes obesity and is required for the insulin–sensitizing effect of thiazolidinediones. Nature medicine, 17(5), 618-622.

[271] Merlin, J., Sato, M., Chia, L. Y., Fahey, R., Pakzad, M., Nowell, C. J., et al. (2018). Rosiglitazone and a β3-adrenoceptor agonist are both required for functional browning of white adipocytes in culture. Frontiers in endocrinology, 9, 249.

[272] Merlin, J., Sato, M., Chia, L. Y., Fahey, R., Pakzad, M., Nowell, C. J., et al. (2018). Rosiglitazone and a β3-adrenoceptor agonist are both required for functional browning of white adipocytes in culture. Frontiers in endocrinology, 9, 249.

[273] Lee, C. G., Rhee, D. K., Kim, B. O., Um, S. H., & Pyo, S. (2019). Allicin induces beige-like adipocytes via KLF15 signal cascade. *The Journal of nutritional biochemistry*, *64*, 13-24.

Stockholm University
Department of Molecular Biosciences, The Wenner-Gren Institute (MBW)

V. Appendix

Summary report of the research period abroad

Title: *In vitro* expression analysis of CpG-depleted CGT2-plasmids

Studies conducted by Uzair Ali

Principal Investigators: Barbara Cannon and Jan Nedergaard

Period of study: April 2022 – December 2022

Study location: Stockholm University

Sponsor: CombiGene AB, Agavägen 52A, SE-181 55 Lidingö, Sweden

Table of contents

I. Background

Long-term expression by an adeno-associated virus (AAV) vector is the main goal of the CGT2 project for lipodystrophy. However, immunotoxicity towards CpG motifs in the DNA of the AAV genome has been described which can quickly eliminate the expression. Toll-like receptors (TLRs) are the most studied pattern recognition receptors (PRRs) and are strategically located on the cell surface or intracellularly in the endosome for early detection of invading pathogens[274]. A cytosine nucleotide is followed by a guanine nucleotide in a straight line in the 5′ 3′ direction of a DNA segment known as a CpG motif. When unmethylated, CpG sites are recognized by TLR9 which can lead to immunogenicity response[275]. To overcome this barrier and ensure long-term expression of an AAV vector, depletion of CpG sequences has become industry standard for vector development in gene therapy.

In this study, three different CpG-depleted CGT2 plasmids (developed by NexGen) were compared with the original non-CpG-depleted plasmid based on expression of UCP1. CpG depletion in the CGT2 plasmid was performed only in the UCP1 intron and coding sequence of the expression cassette and not in the promoter, enhancer, and ITR sequences. Importantly the amino acid sequence was not altered. Plasmid 1 was the "original" plasmid from vector CGT2-14 that contained the codon optimized UCP1 sequence. In plasmid 2 and 3, all CpG sequences were removed and in plasmid 4, one CpG sequence was retained. After evaluation of the CpG depleted expression cassettes *in vitro* based on UCP1 expression levels, AAV vectors will be prepared and evaluation of CpG depletion *in-vivo* will be continue.

1. HepG2 cells

Human liver hepatocellular carcinoma cells (HepG2) cells are liver cell lines that are commonly used as an *in vitro* model in medical research[276]. These cells are a valuable tool for scientists studying various diseases, especially liver disorders, because they can mimic many of the physiological processes that occur in human liver cells[277]. Their abundant availability, easy of handling, almost unlimited life span, and stable phenotype gave them an advantage over other available liver cell lines e.g., Hep3b, HuH7, and HepaRG[278]. These cells were obtained from the liver biopsy of a fifteen-year-old patient with hepatocellular carcinoma. These cells are highly proliferative and have been successfully grown in large-scale culture systems[279].

Transfection can modulate UCP1 expression in these cells. Again, plasmid DNA encoding UCP1 can be transfected into HepG2 cells by electroporation, lipofection, or other methods. After transfection, UCP1 expression can be examined using techniques such as Western blotting, qPCR, or immunofluorescence. It may provide insights into the molecular mechanisms of adipocyte browning and the potential therapeutic applications of promoting browning in the treatment of metabolic disorders.

2. AIM

The aim of this study was to investigate whether UCP1 expression of three different CpG-depleted CGT2-plasmids changes compared with the original non-CpG-depleted CGT2-plasmid when transfected into HepG2 cells. Based on these results, two of the CpG depleted constructs will be selected to produce AAV vectors.

3. MATERIALS

3.1 Plasmids

Plasmids were manufactured and shipped by the vendor Vector builder.

Plasmid 1: VB210218-1403gpt at 3.1µg/µl of DNA (Lot 20220210HTZ105-M).

Plasmid 2: VB220121-1236bck at 3µg/µl of DNA (Lot 20220225HTZ51-M).

Plasmid 3: VB220121-1237rkt at 1.9µg/µl of DNA (Lot 20220314HTZ47-M).

Plasmid 4: VB220121-1239cxb at 2.9µg/µl of DNA (Lot 20220403HTZ28-M).

DNA concentration was received in a total volume of 1 ml in 1xTE buffer for each one of the four plasmids. The plasmids were tested for inverted terminal repeats (ITR) integrity, identity, endotoxin, and sterility.

3.2 UCP1 primer sequences

hCGT2 codon optimized gene.

Forward primer sequence: AAGCCTGGGTAGCAAGATTC;

Reverse Primer sequence: AGATGGGACTGTGCTTGGAG;

DNA Probe bind sequence: TTGCTGGACTGACAACTGG.

Table 1. List of Media, chemical reagents, and antibodies

Product	Identifier	Source
HepG2 cell line	HB-8065	ATCC
DMEM low glucose	D6046	Sigma Aldrich
Fetal Bovise Serum (FBS;	F7524	Sigma Aldrich
MEM Non Essential Amino Acids (MEM NEAA)	1140035	Gibco/ThermoFisher Scientific
Gentamicin	15750060	Gibco/ThermoFisher Scientific
Trypsin	25200056	Gibco/ThermoFisher Scientific
Plasmid Transfection		
Opti-MEM™ I Reduced Serum Medium	31985062	Gibco/ThermoFisher Scientific
Lipofectamine™ 3000	. 2413604	Invitrogen™
6-well cell culture plate, TC-treated		353046, Falcon
RNA Preparation and cDNA synthesis		
TRIzol Reagent™	15596018	Invitrogen
cDNA Reverse Transcription Kit	4368814	Applied Biosystems
Gene Expression assay		
TaqManTM Gene Expression Assays (FAM)	4331182	Applied Biosystems
TaqManTM Gene Expression Assays, FAM	4331348	Applied Biosystems
Eukaryotic 18S ribosomal RNA	4333760F	Applied Biosystems
hCGT2opt (Human UCP1 codon optimized) - Assay ID	APKA7YP	Applied Biosystems
Western blotting		
Tween 20	P1379	Sigma
Bovine Serum Albumine (BSA)	A7906	Sigma
ECL detection reagent	RPN2232	Millipore Corpo- ration
Antibodies		
anti UCP1 antibody	AB10983	Abcam
anti-rabbit IgG	7074	Cell Signaling

4. METHODS

4.1 Cell culture and transfection

HepG2 cells were cultured in DMEM containing 1 g/L glucose supplemented with 10% heat inactivated FBS, 1 mM MEM NEAA, and 25 μg/ml gentamicin. Cells were incubated in a humidified atmosphere of 95% air and 5% CO_2 at 37°C and seeded in 6-well plates (9.6 cm^2 /well) at a density of $5x10^5$ cells/well. The plates were cultured overnight in complete DMEM.

Transfection was performed according to the Transfection protocol provided by Transfection reagent supplier. The plasmid DNA (5 μg/well) was mixed with Lipofectamine (3.75 μl/well) and added to the cells approximately 24 hours after seeding. For mRNA expression each plasmid was transfected in biological triplicates and for western blotting the plasmids were transfected in duplicates.

4.2 RNA preparation

Freshly harvested cells were homogenized in TriReagent after 48h of plasmid transfection. Total RNA was extracted on ice using the chloroform-isopropanol method according to the instructions of the manufacturer and homogenized using a T25 digital ULTRA-TURRAX® High-performance dispersing instrument. RNA samples were purified according to manufacturer's instructions and eluted in RNase-free H_2O. RNA concentration and quality were determined using NanoDrop 2000 Spectrophotometer. The total RNA was stored at -80°C until cDNA synthesis.

4.3 cDNA synthesis

Total RNA (500 ng) was reverse transcribed according to the manufacturer instructions, using the High Capacity cDNA Kit in a total volume of 20 μl using random hexamer primers, deoxynucleotide triphosphates, Multiscript Reverse Transcriptase, and RNase inhibitor.

4.4 qPCR

Aliquots of 2 μl of the cDNA sample were mixed with Maxima Probe/ROX qPCR Master Mix (2X), primers, and diethylpyrocarbonate-treated water and measured in triplicate for each sample. The Comparative, ΔΔCt method was used to quantify gene expression of UCP1 and expression of Eucaryotic 18S ribosomal RNA was used to normalize expression levels.

4.5 Western blotting

Cells were harvested 48 hours after transfection. The media was removed, and wells were rinsed PBS, and thereafter cells were lysed directly in 200 μl ice cold RIPA buffer containing Protease Inhibitor Cocktail (Complete Mini, Roche). Cell lysates were transferred into 2 ml epp tubes and homogenized at 30hz, 30 seconds using a

tissue lyser. Lysates were centrifuged for 2 minutes at 14 000 rpm and supernatant collected on ice. Protein concentration was determined using the method of Lowry.

Equal volume of sample buffer was added to each sample to boil, and proteins were separated by SDS-PAGE in a 12% polyacrylamide gel at 80V for 2h. After, proteins were transferred to a PVDF membrane in a transfer buffer using a semi-dry Trans-Blot Turbo^{TM} transfer system (Bio-Rad) at 2.5A, 25V for 10min. The membrane was blocked with 4% non-fat milk powder in Tris-buffered saline with 0.1% Tween 20 (TBS/T) for one hour at room temperature and then incubated overnight at 4°C with the specific antibodies diluted in TBS-T containing 5% BSA. Subsequently, the membranes were washed 3 x 15 minutes in TBS/T followed by incubation with horseradish peroxidase-conjugated secondary antibody diluted in 2.5% non-fat milk powder in TBS/T for one hour at room temperature. The membranes were washed 3 x 15 minutes in TBS/T before adding detection reagents (ECL Plus Kit, Amersham Biosciences). The chemiluminescence signal was detected with a ChemiDoc XRS+ Imaging System with Image Lab Software (Model No. Universal Hood II, Serial no. 721BR03341, BioRad).

HEK 293 cells transfected with human UCP1 coding sequence (cloned into a pcDNA3.1+vector and amplified before transfection) (Keipert and Jastroch, 2014) as a positive control and empty HEK 293 cells as negative control. Another positive control used was brown adipose tissue protein extract from C57Bl/6 mice living under standard animal house condition.

5. RESULTS

After transfection of the four different plasmids, expression analysis was performed to check the expression level of both UCP1 mRNA and protein. As shown in Figures 1A and B, the UCP1 mRNA was significantly lower in all three plasmids (here named as plasmids 2, 3, and 4) constructs that had CpG-depletion in their sequences compared to non-CpG depleted plasmid (plasmid 1), used as control.

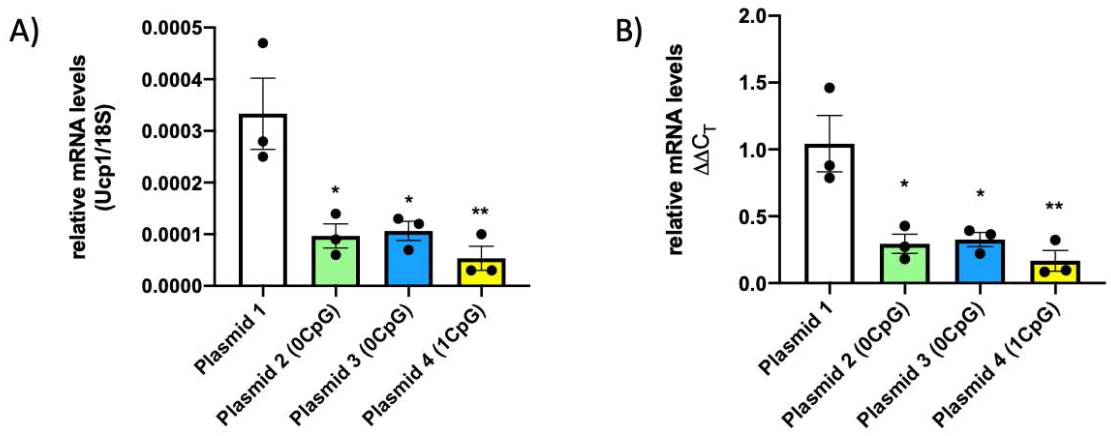

Figure 1. mRNA levels of UCP1 in HepG2 cells transfected with CpG-depleted CGT2 plasmid constructs for 48h. **A)** Absolute values of Ucp1 related to the 18S reference gene levels. **B)** relative mRNA values to the non-CpG-depleted plasmid used as control, settled as 1. Results are expressed as Mean ± SEM (n=3). Reactions were performed in triplicates. $^{*}p \leq 0.05$; $^{**}p \leq 0.01$ compared with plasmid 1. Data analyzed by ANOVA one-way and GraphPad Prism software.

The UCP1 protein was expressed at the correct size (32 kDa) from all plasmids P1-P4, when compared to the positive controls, such as human UCP1 from stable transfected HEK293 cells and mouse UCP1 from brown adipose tissue (BAT). Although all plasmid constructs showed the ability to be translated into protein, all CpG-depleted plasmids expressed a lower amount of UCP1 compared with the non-CpG-depleted plasmid (plasmid 1) (**Fig. 2A, 2B**) similar to the mRNA level shown above (**Fig. 1**).

A)

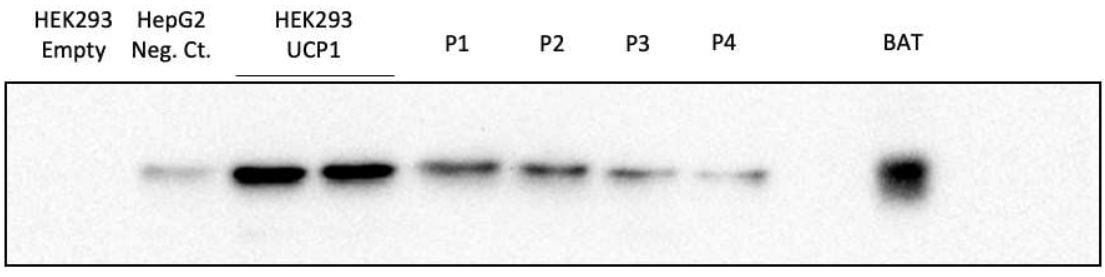

B)

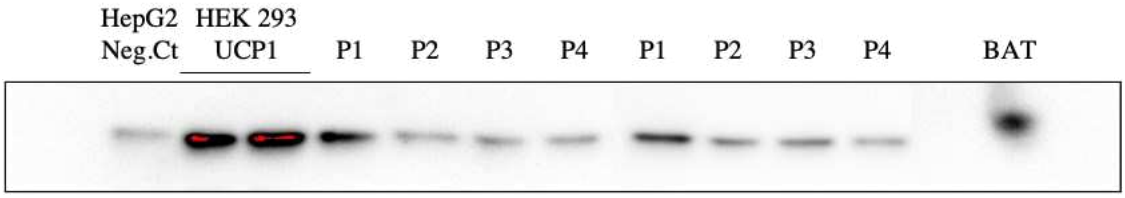

C)

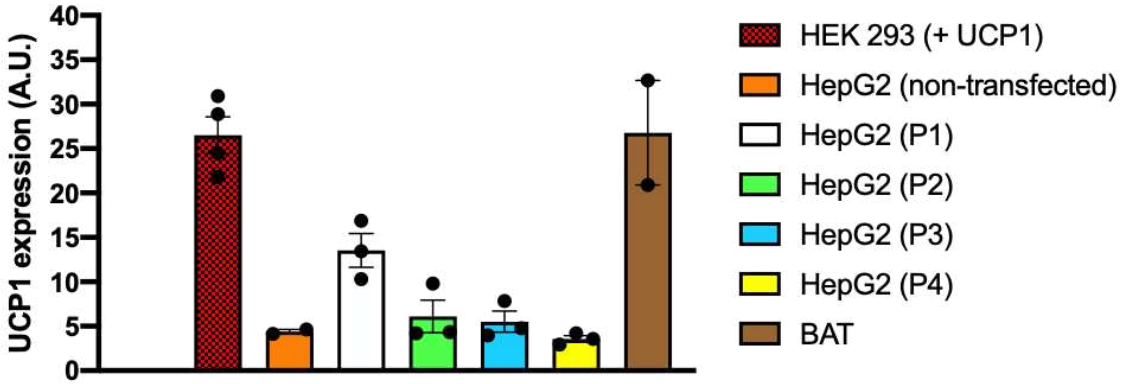

Figure 2. UCP1 protein expression in HepG2 cells transfected with CpG-depleted CGT2 plasmids for 48h. **A** and **B** were performed with HepG2 samples from two different independent experiments with exactly same experimental design. HEK293 empty cell and HepG2 non-transfected cells (HepG2 Neg. Ct) were used as negative control and loaded as 15µg total and 30µg total, respectively. Human UCP1 from HEK 293 cells and mouse UCP1 from BAT were used as positive controls and loaded as 15µg and 2 µg, respectively. HepG2 cells transfected with the four plasmid constructs (plasmid 1 – P1; plasmid 2 – P2; plasmid 3 – P3 and plasmid 4 – P4) were loaded as 30ug total. C) Quantification from membranes A and B in arbitrary units.

6. Conclusion

All three CpG-depleted CGT2 plasmids transfected into HepG2 cells expressed UCP1 at a lower level than the non-CpG depleted plasmid, both at the mRNA and protein levels. From these data it is not possible to determine which CpG-depleted construct should be further used to produce AAV vectors. However, the successful transfection of UCP1 variants demonstrate a promising gene therapy strategy for fatty liver disease.

7. References

[274] Verdera, H. C., Kuranda, K., & Mingozzi, F. (2020). AAV vector immunogenicity in humans: a long journey to successful gene transfer. *Molecular Therapy*, *28*(3), 723-746.

[275] Verdera, H. C., Kuranda, K., & Mingozzi, F. (2020). AAV vector immunogenicity in humans: a long journey to successful gene transfer. *Molecular Therapy*, *28*(3), 723-746.

[276] Nagarajan, S. R., Paul-Heng, M., Krycer, J. R., Fazakerley, D. J., Sharland, A. F., & Hoy, A. J. (2019). Lipid and glucose metabolism in hepatocyte cell lines and primary mouse hepatocytes: a comprehensive resource for in vitro studies of hepatic metabolism. *American Journal of Physiology-Endocrinology and Metabolism*, *316*(4), E578-E589.

[277] Costantini, S., Di Bernardo, G., Cammarota, M., Castello, G., & Colonna, G. (2013). Gene expression signature of human HepG2 cell line. *Gene*, *518*(2), 335-345.

[278] Bort, A., Sánchez, B. G., Mateos-Gómez, P. A., Díaz-Laviada, I., & Rodríguez-Henche, N. (2019). Capsaicin targets lipogenesis in HepG2 cells through AMPK activation, AKT inhibition and PPARs regulation. *International journal of molecular sciences*, *20*(7), 1660.

[279] Barberá, M. J., Schluter, A., Pedraza, N., Iglesias, R., Villarroya, F., & Giralt, M. (2001). Peroxisome proliferator-activated receptor α activates transcription of the brown fat uncoupling protein-1 gene: a link between regulation of the thermogenic and lipid oxidation pathways in the brown fat cell. *Journal of Biological Chemistry*, *276*(2), 1486-1493.

Tissue and Cell 77 (2022) 101822

Contents lists available at ScienceDirect

Tissue and Cell

journal homepage: www.elsevier.com/locate/tice

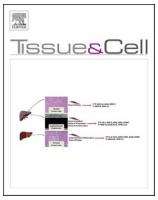

Transcriptomic analysis of Simpson Golabi Behmel syndrome cells during differentiation exhibit BAT-like function

M. Colitti [a,*,1], U. Ali [a], M. Wabitsch [b,2], D. Tews [b,3]

[a] Department of Agricultural, Food, Environmental and Animal Sciences, University of Udine, Italy
[b] Division of Pediatric Endocrinology and Diabetes, Department of Pediatrics and Adolescent Medicine, University Medical Center Ulm, Germany

ARTICLE INFO

Keywords:
SGBS cells
Gene expression
Browning
Extracellular matrix organization
Oxidative stress

ABSTRACT

High-throughput RNA sequencing of human Simpson-Golabi-Behmel syndrome cells (SGBS) was performed during the time-course of adipogenic differentiation at day 4 (D04), 6 (D06), 8 (D08), and 10 (D10) to characterize transcriptomic changes and to identify key patterns involved in adipogenesis and browning. In the comparisons, 932 and 384 overlapping transcripts were consistently up- and down-regulated, respectively. Combining the results of protein-protein interaction network analysis MCODE and CytoHubba, 55 up-regulated hub genes from four clusters and 9 down-regulated genes were identified. The up-regulated hub genes were mainly enriched in brown adipocyte differentiation, extracellular matrix organization, and valine, leucine, and isoleucine degradation. The enrichment of downregulated hub genes was related to NRF2 signalling and glutathione metabolism, indicating that oxidative stress also plays a role. Analysis of overlapping down-regulated genes, targets of transcription factors, revealed enrichment in the IL-18 signalling pathway, which is involved in browning process and extracellular matrix organization *via* actomyosin mechanics and integrin-extracellular matrix interactions. Finally, the comparison transcriptomic analysis with the gene signature reported by BATLAS and PROFAT web-based tools showed an increased percentage of the brown phenotype, confirming that differentiated SGBS cells at D06, D08, and D10 gradually acquire BAT-like function.

1. Introduction

In the last decade, adaptive thermogenesis has been recognized as a potential therapy for the treatment of obesity and its associated diseases due to its ability to increase energy expenditure and modulate circulating lipid and glucose levels (Wu et al., 2013). While brown adipocytes originate from the Myf^{5+} precursors, like striated muscle cells, and respond to cAMP for increasing UCP1 expression, other molecules strongly up-regulate UCP1 at transcriptional level, such as C/EBPs, RAR, ATF2, PPARγ and PPARα (Christian and Parker, 2010). Thus, activation of PPARγ using thiazolidinediones (*e.g.* rosiglitazone) is usually required to induce UCP1 expression in adipocytes differentiated in primary culture from subcutaneous adipose tissue (Ohno et al., 2012). Further, adipose tissue responds dynamically to many triggers such as cold exposure, hormones, and natural substances to recruit more brown adipose cells or to convert white cells into beige cells (Montanari et al., 2017, 2019). To understand the cellular and molecular events that maintain adipogenesis and the process of browning, different murine cell lines, such as 3T3-L1, have been frequently used. Although 3T3-L1 cells have made important contributions to the understanding of adipogenesis and adipocyte metabolism, they are unable to develop a beige adipocyte phenotype (Morrison and McGee, 2015).

Simpson-Golabi-Behmel syndrome (SGBS) cells have been recognized as a representative *in vitro* model more suitable than mouse models for studying the biology of human white subcutaneous preadipocytes. Indeed, the SGBS model has been frequently used to analyse key signalling pathways, networks and regulators. This strain was established in 2001 by Wabitsch and colleagues, who isolated preadipocytes from the subcutaneous adipose tissue of a paediatric patient suffering from SGBS (Wabitsch et al., 2001). Although SGBS cells are neither immortalized nor transformed, they retain the ability to expand and differentiate into mature adipocytes over a high number of generations, but this

* Correspondence to: Department of Agricultural, Food, Environmental and Animal Sciences, via delle Scienze, 206, 33100 Udine, Italy.
E-mail address: monica.colitti@uniud.it (M. Colitti).
[1] orcid.org/0000-0002-1775-3880
[2] orcid.org/0000-0001-6795-8430
[3] orcid.org/0000-0003-3300-3446

https://doi.org/10.1016/j.tice.2022.101822
Received 18 March 2022; Received in revised form 13 May 2022; Accepted 13 May 2022
Available online 18 May 2022

capability has not been demonstrated to be related to mutations of the X-linked gene Glypican 3 (GPC3) (Huber et al., 1998; Capurro et al., 2008). Moreover, SGBS cells are the only fully inducible human pre-adipocyte cell line (Ruiz-Ojeda et al., 2016). For these reasons, these cells are an excellent model for obesity research and have been used extensively in the last years (Allott et al., 2012). During differentiation, these adipocytes show a transient brown phenotype (Guennoun et al., 2015; Yeo et al., 2017), since around the 14th day of differentiation, the expression of canonical BAT markers, such as UCP1, sharply increases. However, as reported by Halbgebauer et al., (2020), this feature is due to the action of rosiglitazone. At later time points in adipogenesis, morphological changes in lipid droplets and mitochondria and a decrease in the expression of BAT markers indicate the induction of a white adipocyte differentiation program.Morphological dynamics of lipid droplets and mitochondria, that agreed with the regulation of nutrient utilization and energy expenditure, have been observed in SGBS cells during 21 days of differentiation (Montanari and Colitti, 2018). Using RNAseq we sought to address transcriptomic changes during differentiation of SGBS cells to identify key patterns involved in adipogenesis and browning.

2. Materials and methods

2.1. Chemicals and culture media

Dulbecco's modified Eagle medium (DMEM)/F-12 medium (1:1) enriched with L-glutamine and 15 mM 4-(2-hydroxyethyl)− 1-piperazineethanesulfonic acid (HEPES), fetal bovine serum (FBS) and penicillin streptomycin solution were purchased from Gibco by Life Technologies (Thermo Fisher Scientific Inc., Waltham, Massachusetts). TRIzol reagent, PureLink™ RNA Mini Kit and SuperScript™ III one-step RT-PCR system with Platinum™ *Taq* DNA polymerase were purchased from Invitrogen (Thermo Fisher Scientific Inc., Waltham, Massachusetts). Rosiglitazone was purchased from Cayman Chemical (Ann Arbor, Michigan).

All other chemicals used in the experiment and not listed above were purchased from Sigma-Aldrich (Darmstadt, Germany).

2.2. Cell culture

Human SGBS cells were kindly provided by prof. M. Wabitsch (University of Ulm, Germany). Cells were grown in DMEM/F-12 supplemented with 10% FBS, 3.3 mM biotin, 1.7 mM pantothenate and 1% penicillin/streptomycin solution, at 37 °C with 5% CO_2 and 95% relative humidity. Differentiation was induced on confluent cells with serum-free growth medium supplemented with 10 μg/ml transferrin, 0.2 nM triiodothyronine (T_3), 250 nM hydroxycortisone, 20 nM human insulin, 25 nM dexamethasone, 250 μM 3-isobutyl-1-methylxanthine (IBMX) and 2 μM rosiglitazone (day 0 of differentiation). After 4 days, the differentiation medium was replaced with a maintenance medium composed by serum-free growth medium supplemented with 10 μg/ml transferrin, 0.2 nM T_3, 250 nM hydroxycortisone and 20 nM human insulin. Fresh maintenance medium was added every 4 days.

Cells were analyzed during differentiation at day 4 (D4) and at day 6 (D6), at day 8 (D8) and at day 10 (D10).

2.3. RNA extraction and sequencing

The experiment was designed with 2 biological replicates for the 4 different days of cell differentiation.

After culture medium removal from Petri dishes, 1 ml/10 cm^2 of TRIzol reagent was added in each plate and repeatedly pipetted to induce a severe breakdown of cell structures. These samples were immediately proceeded with the PureLink™ RNA Mini Kit following the manufacturer's instructions.

The concentration of the extracted total RNA was quantified using a spectrophotometer (NanoDrop 1000 Spectrophotometer, Thermo-Scientific, Wilmington, Delaware) and the purity of RNA samples ranged between 1.8 and 1.9. RNA integrity was evaluated through the observation of 18 S and 28 S ribosomal bands after electrophoresis on 1% agarose gel, in the presence of GelRed. β-actin expression was used as internal control, confirming thorough integrity of the RNA.

Purified total RNA was subjected to deep sequencing analysis. Initially, isolated RNA was quantified using Agilent Bioanalyzer 2100 with the RNA integrity number (RIN) greater than 8.0 before Illumina Genome Analyzer (GA) sequencing. RNA sequencing (RNAseq) was performed using the Illumina Genome Analyzer to measure mRNA expression levels from eight human cell line samples. Typically, 2–4 ug total RNA were used in library construction. Total RNA was reverse transcribed to double-stranded cDNA, digested with *Nla*III and ligated to an Illumina specific adapter containing a recognition site of MmeI. Following MmeI digestion, a second Illumina adapter, containing a 2-bp degenerate 3′ overhang was ligated. The obtained sequences were aligned on GRCh38 human genome (https://www.ncbi.nlm.nih.gov/assembly/GCF_000001405.39) using STAR software (Dobin et al., 2013). Data were uploaded in the NCBI Sequence Read Archive (SRA), bioproject ID PRJNA783150.

2.4. Data processing

Raw counts were uploaded in Differential Expression and Pathway analysis (iDEP93) R package (v0.92) that is a web-based tool available at http://ge-lab.org/idep/ (Ge et al., 2018; Ge, 2021). In the pre-processing step, genes expressed at very low level across samples were filtered out and genes expressed with a minimum of 0.2 counts per millions (CPM) in one library were further analyzed. To reduce the variability and normalized count data EdgeR log2(CPM+c), with pseudocount c = 8 transformation, was chosen. Next, DESeq2 package in R language was used to identify differentially expressed genes (DEG) at day 6, 8 and 10 of differentiation *vs* day 4, using a threshold of false discovery rate (FDR) < 0.05 and $\log_2$fold-change $> |1.0|$. The heatmaps, principal component analysis (PCA), k-means cluster and enrichment analyses were also performed in iDEP93.

Gene set enrichment analysis to determine the shared biological functions of differentially regulated genes based on significant GO terms (Ashburner et al., 2000), Kyoto Encyclopedia of Genes and Genomes (KEGG) pathway (Kanehisa and Goto, 2000) and TF. target.TRED analyses were completed (Jiang et al., 2007).

Venn diagrams were created by web tool available at http://bioinformatics.psb.ugent.be/webtools/Venn/.

2.5. Protein protein interaction (PPI) network construction and module analysis

Based on the Search Tool for the Retrieval of Interacting Genes (STRING; https://string-db.org/) online tool, PPI of the 932 up-regulated and 384 down-regulated overlapping DEGs were constructed with a confidence of ≥ 0.4 and the PPI network was visualized by Cytoscape software (version 3.9.0, https://cytoscape.org/) Unique DEGs of the different comparisons were also analysed. Additionally, the plug-in of Molecular Complex Detection (MCODE) (Bader and Hogue, 2003) in Cytoscape suite was applied to explore the significant modules in PPI network. The options set as degree cuttoff = 6, K-core = 2 and node Score Cutoff = 0.2. Subsequently, the enrichment analysis of DEGs in modules with a score ≥ 5 was performed. Cytoscape cytoHubba plugin was used to select the top 15 hub nodes according to Maximal Clique Centrality (MCC) algorithm (Chin et al., 2014).

In order to deeper understand the difference between DEGs target of TF networks, specific subnetworks for the overlapping genes between comparisons were constructed using the Maximal Clique Centrality (MCC) algorithm in cytoHubba and enrichment analysis of the 10 most important genes according with MCC was performed.

2.6. BATLAS and PROFAT webtool analysis

Two computational tools that quantify the thermogenic potential (BAT content) of adipose tissue were used. The BATLAS webtool uses a Digital Sorting Algorithm from the CellMix package in combination with the brown and white markers to estimate the percentage of brown adipocytes in human or mouse tissues using RNA-seq data (Perdikari et al., 2018). The estimation of the fraction of brown adipocytes per each sample at different days of differentiation was analysed on normalized read counts. The PROFAT is another tool that automatically performs hierarchical clustering analysis to predict browning capacity from mouse and human RNA-seq datasets (Cheng et al., 2018).

2.7. BODIPY staining and confocal imaging

Cells for BODIPY™ staining and subsequent confocal imaging were cultured on ibiTreat 8-well μ-Slides (Ibidi GmbH, Planegg/Martinsried, Germany). Cells were fixed in a 2% formalin solution diluted in PBS 1X at room temperature (RT) for 15 min. Subsequently, after three washes in PBS 1X, cells were incubated in a solution of BODIPY™ 493/503 in PBS 1X to fluorescently label lipid droplets. Incubation was performed at RT in the dark for 45 min. The slides were then washed three times in PBS 1X. Fluorescent images were obtained using a Leica SP8 confocal microscope (Leica Microsystems Srl, Milan, Italy) equipped with LAS X 3.1.5.16308 software. Slides were observed with HC PL APO CS2 40X/1.10 WATER objective lens. BODIPY™ fluorescence was detected by white light laser (503/588 nm). The images were acquired by a photomultiplier tube (PMT), which allowed point-by-point scanning of the region of interest (ROI) with the selected laser and produced 1024 × 1024 px images.

2.8. Validation data by Real-time PCR analysis (qPCR)

cDNA from the same purified RNA samples was synthesized and amplified using an MJ thermal cycler (PT-100; MJ Research, Inc., Waltham, MA, USA), according to ImProm-II™ Reverse Transcription System (Promega, Milan, Italy).

Primer3 Input software (Rozen and Skaletsky, 2000) was used to design the primer sequences encoding for (**Table A.9**): β-actin (ACTB), Ribosomal Protein Lateral Stalk Subunit P0 (RP0L0), PPARG Coactivator 1 Alpha (PPARCG1A), uncoupling protein 1 (UCP1), PR domain containing 16 (PRDM16), Peroxisome Proliferator Activated Receptor Gamma (PPARG), NFE2 Like BZIP Transcription Factor 2 (NFE2L2) and Nuclear Factor Kappa B Subunit 1(NFKB1).

The qPCR was performed in triplicate with the Platinum SYBR® Green qPCR SuperMix-UDG w/ROX (Invitrogen, Milan, Italy) on CFX96 Real-Time PCR Detection System (Bio-Rad). Mastermix reactions were prepared as the manufacturer's instructions with each primer pair and the cDNA added last. The expression of target genes was normalized using ACTB and RPL0 and ΔCts were calculated by the difference between Ct of genes target and the geometric mean of the two housekeeping genes. Differences between samples (D06, D08, D10) and D04 were calculated using the $2^{(-\Delta\Delta Ct)}$ method (Livak and Schmittgen, 2001; Bustin et al., 2009), where D04 was equal to 1.

2.9. Statistical analysis

Real-time and RNA seq gene expression data were compared through Kolmogorov-Smirnov statistical test that enables the similarity of the distributions to be tested at the same time as their shape and position, using XLSTAT (Addinsoft, 2022).

3. Results

3.1. Data sets are clustered according to the day of differentiation

After removal of low-quantity reads, the final mapping rate of filtered transcript reads was 34.5%. At the initial analysis of the RNAseq results, hierarchical clustering was performed indicating the difference of genes and showing that the transcriptome data was well-clustered depending on the day of differentiation (Fig. 1a).

Furthermore, PCA showed the overall variability in the expression profile of the samples and treatments. Overall, there was a clear difference between the D04 and D06, D08 and D10 along the first principal component that explained 73% of the variance, with less differences 8% along the second component. Moreover, the ANOVA analysis, performed by iDEP, on these projections detected significant correlation of each PCs with treatments, being the first principal component significantly correlated with day of development for $p = 1.26^{-03}$ (Fig. 1b). Fig. 1**c** shows the lipid droplets (LDs) enlargement at day 6 (A) and day 10 (B) of differentiation.

3.2. The number of transcripts increases with the day of differentiation

Analysis of DEGs was performed between D06, D08 and D10 in comparison to D04, based on a $\log_2$fold change of ≥ 1 and FDR adjusted p value of ≤ 0.05.

iDEP93 expression analysis identified significantly ($p < 0.05$) 3512 up-regulated genes between D06 *vs* D04, 3992 between D08 *vs* D04 and 4165 between D10 *Vs* D04 (Fig. 2a). Significantly ($p < 0.05$) down-regulated genes were 2876 between D06 *Vs* D04, 3542 genes between D08 *vs* D04 and 3763 between D10 *vs* D04 (Fig. 2a).

Three Venn diagrams were composed displaying the highest and lowest expression at each day of differentiation *vs* D04 for adjusted p-value ≤ 0.05 and $\log_2$fold change ≥ 1 and identified 932 and 384 overlapping DEGs consistently up- and down-regulated (Fig. 2b). For each of the three differentiation days in comparison to D04, an increasing number of genes displayed unique expression: 46 at D06, 107 at D08, 275 at D10 for up-regulated genes and 42 at D06, 118 at D08, 253 at D10 for down-regulated genes, with the greatest number of transcripts, induced or suppressed, between D10 and D04. The results of this analyses were also presented in the form of volcano plots in Fig. 2c and in Table A.2.

3.3. Construction of PPI networks and module analysis of DEGs suggest brown adipocyte differentiation without up-regulation of PRDM16 and an increase in oxidative stress through down-regulation of antioxidant genes

PPI analysis of the 932 up-regulated overlapping DEGs revealed 821 nodes and 2937 edges. Further analysis through MCODE with a score ≥ 5 filtered four significant clusters. To gain further insight into the potential functions of genes in each module, the enrichment analysis was performed and results were displayed in Fig. 3. The most significant pathways in cluster 1 (Fig. 3a) were enriched, among others, in 'Regulation of cold-induced thermogenesis' (FDR 1.18^{-17}) 'PPAR signalling pathway' (FDR 9.39^{-13}) and 'Brown fat cell differentiation' (FDR 4.00^{-04}). Cluster 2 was enriched in 'Cholesterol biosynthetic process' (FDR 3.09^{-17}) 'Acyl-CoA metabolic process' (FDR 1.61^{-12}) and in 'Cellular respiration' (FDR 5.42^{-11}) (Fig. 3b). The most significant pathways in cluster 3 were 'Extracellular matrix organization' (FDR 2.48^{-16}) and 'Muscle contraction' (FDR 9.93^{-08}) (Fig. 3c) and in cluster 4 'Fatty acid degradation' (FDR 1.33^{-08}), 'Valine, leucine and isoleucine degradation' (FDR 1.33^{-08}) and 'Mitochondrial matrix' (FDR 2.34^{-04}) were found (Fig. 3d). The top 15 hub genes, selected from the four clusters using MCC algorithm of CytoHubba plugin, are listed in Table 1.

The analysis of down-regulated overlapping DEGs showed 317 nodes and 425 edges. Only one cluster with a score ≥ 5 was identify by MCODE analysis (Fig. 4). Significant down-regulated pathways were 'NRF2

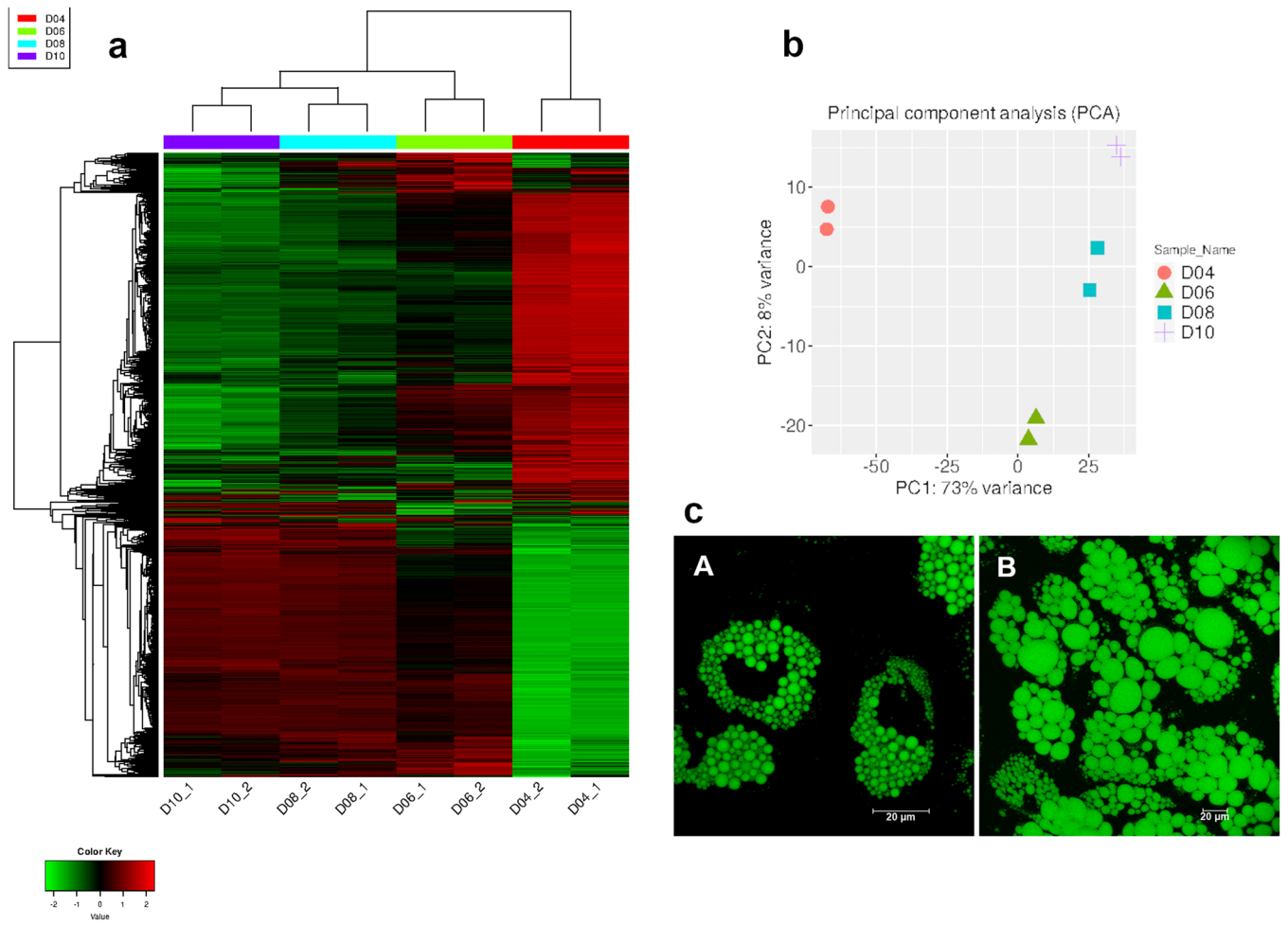

Fig. 1. (a) Hierarchical clustering heatmap of 2000 genes expressed in SGBS cells at different days of differentiation. The coloured bars above the heatmap indicate the differentiation stage. The colour key indicates z-score and displays the relative expression levels: green, lowest expression; black, intermediate expression; red, highest expression. (b) Principal component analysis of SGBS samples at different days of differentiation. The results indicate that the transcriptome data are of high quality, as the duplicate samples are clustered together according to differentiation; early differentiated cells (D04) were significantly separated on the first component ($p = 1.26^{-03}$) in agreement with the unsupervised hierarchical clustering. (c) Detection of lipid droplets by BODIPY of SGBS adipocytes at day 6 (A) and 10 of differentiation (B). Scale bar = 20 µm. (For interpretation of the references to colour in this figure legend, the reader is referred to the web version of this article.)

pathway' (FDR 1.63^{-13}), 'Glutathione metabolism' (FDR 3.65^{-06}). The top ten hub genes with a high degree of connectivity between the nodes, according to the degree in the module are listed in Table 2.

3.4. GO term analysis enriches genes in mitochondrial organization and oxidoreductase activity

To further investigate the function of the DEGs, GO term enrichment analysis was conducted. The DEGs were significantly enriched in biological processes (BP), molecular function (MF) and cellular component (CC). Among the differentially regulated BP, 'Macromolecule localization', 'Protein localization to endoplasmic reticulum', 'Protein targeting to ER', 'SRP-dependent cotranslational protein targeting to membrane' and 'Translational initiation' were significantly down- regulated in all comparisons, while 'Carboxylic acid metabolic process', 'Cellular respiration', 'Energy derivation by oxidation of organic compounds', 'Generation of precursor metabolites and energy', 'Mitochondrion organization', 'Oxidation-reduction process' and 'Oxidative phosphorylation' were significantly up-regulated (Table A.3). Down-regulated DEGs, among all comparison, were significantly enriched in MF, including 'RNA binding', 'Catalytic activity acting on a protein' and 'Transferase activity'; among the up-regulated MF, 'Adenyl nucleotide binding ', 'Oxidoreductase activity', were found (Table A.4). The DEGs that specifically down-regulated CC within the comparisons D06 *vs* D04, D08 *vs* D04 and D10 *vs* D04 were related to 'Cell junction' and 'Cytosolic ribosome' and 'Focal adhesion', the up-regulated CC was significantly related to mitochondria matrix, membrane, and protein (Table A.5).

3.5. KEGG pathway analysis confirms BAT-like phenotype during differentiation

A total of 36 significantly enriched pathways were identified in KEGG, 21 down-regulated and 15 up-regulated in all the comparison *vs* D04 (Table A.6). Fig. 5 illustrated the results of the KEGG analysis as a graphical representation of the scatter plots. Each figure represents KEGG enrichment of 10 identified pathways for each of the time differentiation points with corresponding GeneRatio, adjusted p-value, and the number of the enriched genes in the corresponding pathways. The GeneRatio is defined as the number of the enriched candidate genes *vs* the total number of the annotated genes (number of enriched genes/ number of total annotated genes) that are considered by the KEGG analysis in the corresponding pathway. Therefore, a higher GeneRatio suggests a more significant enrichment of the candidate genes in the corresponding pathway and adjusted p-value indicates the FDR for

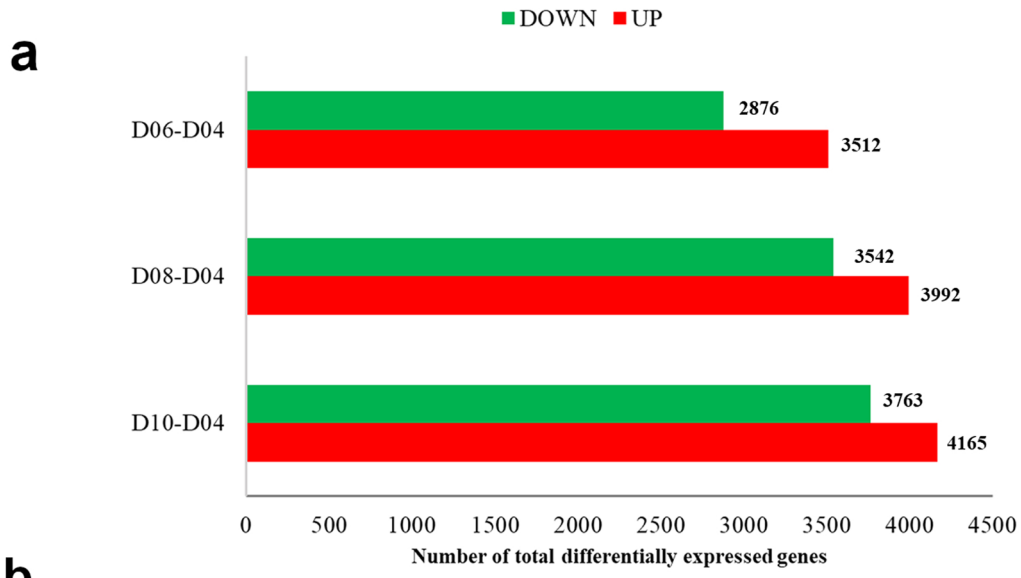

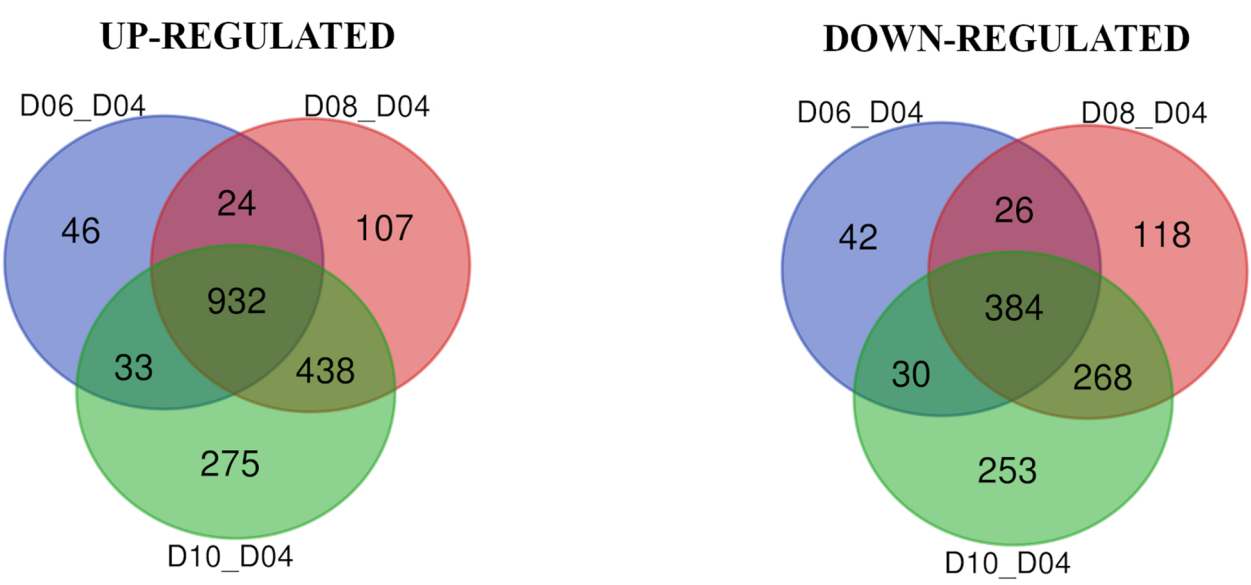

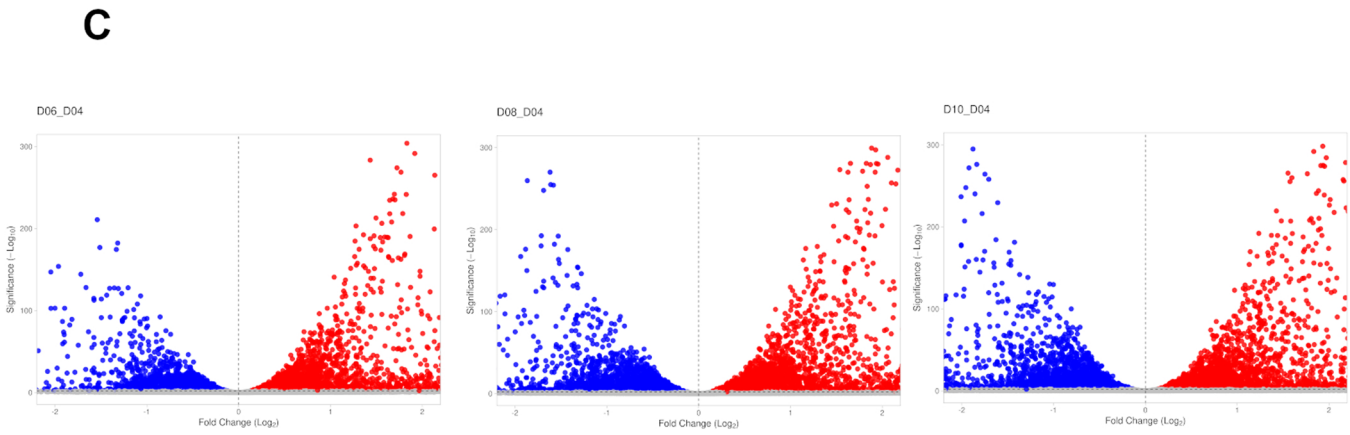

Fig. 2. Number of gene differentially expressed for adjusted $p < 0.05$. Gene expressions were measured in SGBS cells at different days of differentiation and the comparisons were related to immature adipocytes (D04). (a) Numbers of differentially expressed genes for each comparison. (b) Three-way Venn diagram illustrating DEGs up- and down-regulated for $p < 0.05$ and with $\log_2$ fold change higher than 1 and lower than -1. The findings indicate that 932 and 384 overlapping transcripts were consistently up- and down-regulated (FDR ≤ 0.05 and $|\log_2$fold change$| \geq 1$), among comparisons. (c) Volcano plots representing the composition of the analysed differentiation days, as well as the proportion and distribution of differentially expressed genes. (a) D06 *vs* D04; (b) D08 *vs* D04; (c) D10 *vs* D04.

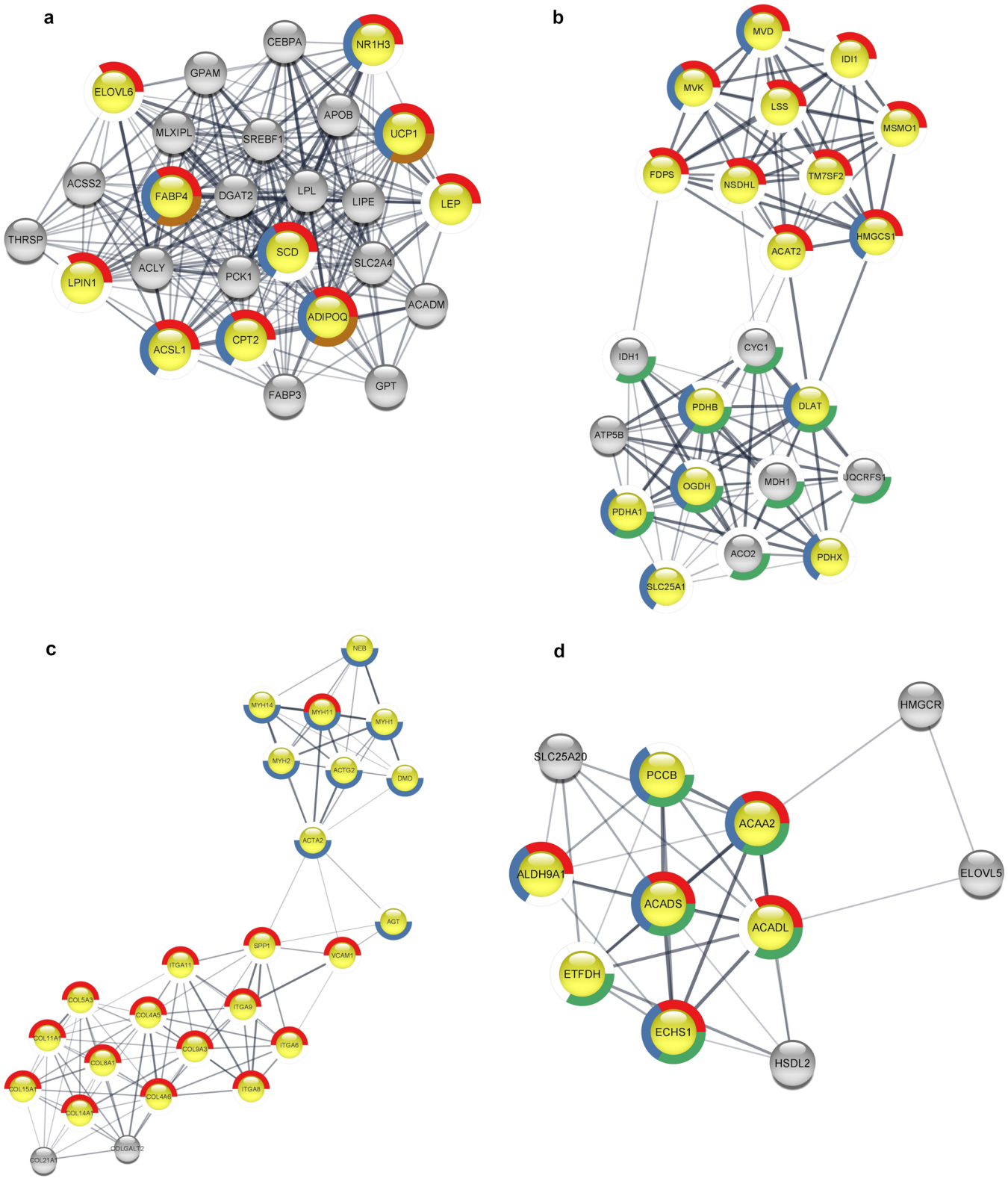

(caption on next page)

measuring variables of a large data set, such as for the level of gene expression of RNA-sequencing data. DEGs were highly clustered in several signalling pathways, such as 'Fatty acid metabolism', 'Metabolic pathways', 'Oxidative phosphorylation', 'PPAR signaling pathway' 'Thermogenesis' and 'Valine, leucine and isoleucine degradation'. Of note, the 'Ras signaling pathway' and 'TNF signaling pathway' were down-regulated and 'AMPK signalling' up-regulated pathway only at D06 in comparison to D04, while the up-regulated pathways were the same in all comparisons (Table A.6).

Fig. 3. Four significant modules identified from the PPI network constructed with up-regulated DEGs overlapping to all the comparisons *vs* D04. The enriched pathways are marked in different colours. (a) Cluster 1 with a MCODE score of 17.93. Red: genes enriched in 'Regulation of cold-induced thermogenesis' blue: 'PPAR signalling pathway' and brown: 'Brown fat cell differentiation'. (b) Cluster 2 with a MCODE score of 9.48. Red genes enriched in: 'Cholesterol biosynthetic process'; blue: 'Acyl-CoA metabolic process' and green: 'Cellular respiration'. (c) Cluster 3 with a MCODE score of 7.85. Red: 'Extracellular matrix organization' and blue 'Muscle contraction'. (d) Cluster 4 with a MCODE score of 5.5. Red: genes enriched in 'Fatty acid degradation'; blue: 'Valine, leucine and isoleucine degradation' and green 'Mitochondrial matrix'. Yellow nodes indicate genes involved in pathways obtained by enriched analysis. Edges represent the protein-protein associations, Abbreviations: (a) ACSL1, Acyl-CoA Synthetase Long Chain Family Member 1; ADIPOQ, adiponectin, C1Q and collagen domain containing; CPT2, Carnitine Palmitoyltransferase 2; ELOVL6, ELOVL fatty acid elongase 6; FABP4, fatty acid binding protein 4; LEP, leptin; SCD, stearoyl-CoA desaturase; LPIN1, lipin 1; NR1H3, nuclear receptor subfamily 1 group H member 3; UCP1, uncoupling protein 1. (b) ACAT2, acetyl-CoA acetyltransferase 2; ACO2, aconitase 2; CYC1, cytochrome c1; DLAT, dihydrolipoamide S-acetyltransferase; FDPS, farnesyl diphosphate synthase; HMGCS1, 3-hydroxy-3-methylglutaryl-CoA synthase 1; IDH1, isocitrate dehydrogenase (NADP(+)) 1; IDI1, sopentenyl-diphosphate delta isomerase 1; LSS, lanosterol synthase; MDH1, malate dehydrogenase 1; MSMO1, methylsterol monooxygenase 1; MVD, mevalonate diphosphate decarboxylase; MVK, mevalonate kinase; NSDHL, NAD(P) dependent steroid dehydrogenase-like; OGDH, oxoglutarate dehydrogenase; PDHA1,pyruvate dehydrogenase E1 subunit alpha 1; PDHB, pyruvate dehydrogenase E1 subunit beta; PDHX, pyruvate dehydrogenase complex component X; SLC25A1, solute carrier family 25 member 1; TM7SF2transmembrane 7 superfamily member 2; UQCRFS1, ubiquinol-cytochrome c reductase, Rieske iron-sulfur polypeptide 1. (c) ACTA2, actin alpha 2, smooth muscle; ACTG2, actin gamma 2, smooth;AGT, angiotensinogen; COL11A1, collagen type XI alpha 1 chain; COL14A1, collagen type XIV alpha 1 chain; COL15A1, collagen type XV alpha 1 chain; COL4A5, collagen type IV alpha 5 chain; COL4A6, collagen type IV alpha 6 chain; COL9A3, collagen type IX alpha 3 chain; DMD, dystrophin; ITGA11, integrin subunit alpha 11; ITGA6, integrin subunit alpha 6; ITGA8, integrin subunit alpha 8; MYH1, myosin heavy chain; MYH11, myosin heavy chain 11; MYH14, myosin heavy chain 14; MYH2, myosin heavy chain 2; NEB, nebulin; SPP1, secreted phosphoprotein 1; VCAM1, vascular cell adhesion molecule. (d) ACADL, acyl-CoA dehydrogenase long chain; ACADS, acyl-CoA dehydrogenase short chain; ACAA2, acetyl-CoA acyltransferase 2; ALDH9A1, aldehyde dehydrogenase 9 family member A1; ECHS1, enoyl-CoA hydratase, short chain 1; ETFDH, electron transfer flavoprotein dehydrogenase; PCCB,propionyl-CoA carboxylase subunit. (For interpretation of the references to colour in this figure legend, the reader is referred to the web version of this article.)

Table 1
Top 15 hub genes from four clusters of up-regulated genes.

Cluster 1			Cluster 2			Cluster 3			Cluster 4		
Rank	Gene	Score	Rank	Gene	Score	Rank	Gene	Score	Rank	Gene	Score
1	SREBF1	1946568960	1	ACAT2	362884	1	COL4A6	15864	1	ACAA2	409
1	SCD	1946568960	2	NSDHL	362882	2	COL11A1	15144	1	ACADL	409
1	DGAT2	1946568960	2	TM7SF2	362882	3	COLGALT2	15120	3	ACADS	408
4	LPL	1935682560	2	HMGCS1	362882	3	COL5A3	15120	4	ECHS1	360
5	PCK1	1934876160	5	FDPS	362881	3	COL14A1	15120	5	ETFDH	264
6	LIPE	1931610240	6	IDI1	362880	3	COL8A1	15120	6	PCCB	240
7	FABP4	1826012160	6	LSS	362880	7	COL4A5	11544	7	ALDH9A1	144
8	SLC2A4	1789361280	6	MVK	362880	8	COL15A1	10080	8	HSDL2	120
9	MLXIPL	1698641280	6	MVD	362880	9	COL9A3	6504	9	SLC25A20	48
10	ADIPOQ	1647475200	6	MSMO1	362880	10	COL21A1	5040	10	ELOVL5	2
11	LEP	1520467200	11	DLAT	90724	11	ITGA11	1464			
12	UCP1	1045094400	12	PDHB	90722	12	ITGA9	1446			
13	CEBPA	997920000	13	OGDH	90720	12	ITGA6	1446			
14	ACLY	878532480	13	PDHA1	90720	14	MYH1	1440			
15	NR1H3	522910080	13	MDH1	90720	14	MYH11	1440			

Abbreviations: ACAA2, acetyl-CoA acyltransferase 2; ACADL, acyl-CoA dehydrogenase long chain; ACADSacyl-CoA, dehydrogenase short chain; ACAT2, acetyl-CoA acetyltransferase 2; ACLY, ATP citrate lyase; ADIPOQ, adiponectin, C1Q and collagen domain containing; ALDH9A1,aldehyde dehydrogenase 9 family member A1; CEBPA, CCAAT enhancer binding protein alpha; COL11A1, collagen type XI alpha 1 chain; COL14A1, collagen type XIV alpha 1 chain; COL15A1, collagen type XV alpha 1 chain; COL21A1, collagen type XXI alpha 1 chain; COL4A5, collagen type IV alpha 5 chain; COL4A6, collagen type IV alpha 6 chain; COL5A3, collagen type V alpha 3 chain; COL8A1, collagen type VIII alpha 1 chain; COL9A3, Collagen Type IX Alpha 3 Chain; COLGALT2, collagen beta(1-O)galactosyltransferase 2; DGAT2, diacylglycerol O-acyltransferase 2; DLAT, dihydrolipoamide S-acetyltransferase; ECHS1, enoyl-CoA hydratase, short chain 1; ELOVL5, ELOVL fatty acid elongase 5; ETFDH, electron transfer flavoprotein dehydrogenase; FABP4, fatty acid binding protein 4; FDPS, farnesyl diphosphate synthase; HMGCS1, 3-hydroxy-3-methylglutaryl-CoA synthase 1; HSDL2, hydroxysteroid dehydrogenase like 2; IDI1, isopentenyl-diphosphate delta isomerase 1; ITGA11, integrin subunit alpha 11; ITGA6, integrin subunit alpha 6; ITGA9, integrin subunit alpha 9; LIPE, lipase E, hormone sensitive type; LPL, lipoprotein lipase; LSS, lanosterol synthase; MDH1, malate dehydrogenase 1; MLXIPL, MLX interacting protein like; MSMO1, methylsterol monooxygenase 1; MVD, mevalonate diphosphate decarboxylase; MVK, mevalonate kinase; MYH1, myosin heavy chain 1; MYH11, myosin heavy chain 11; NR1H3, nuclear receptor subfamily 1 group H member 3; NSDHL, NAD(P) dependent steroid dehydrogenase-like; OGDH, oxoglutarate dehydrogenase; PCCB, propionyl-CoA carboxylase subunit beta; PCK1, phosphoenolpyruvate carboxykinase 1; PDHA1, pyruvate dehydrogenase E1 subunit alpha 1; PDHB, pyruvate dehydrogenase E1 subunit beta; SCD, stearoyl-CoA desaturase; SLC25A20, solute carrier family 25 member 20; SLC2A4, solute carrier family 2 member 4; SREBF1, sterol regulatory element binding transcription factor 1, TM7SF2, transmembrane 7 superfamily member 2; UCP1, uncoupling protein 1.

3.6. Genes enriched in target of E2F4, cMYC and SMAD are involved in acetylation and extracellular matrix organization

TRED (http://rulai.cshl.edu/TRED) was designed as a resource for gene regulation and function studies and allow to know interaction data between transcription factors (TFs) and the promoters of their target genes, including binding motifs (Jiang et al., 2007). Selecting database TF. target.TRED in iDEP93, in the comparison D06_D04, significantly target genes of 10 TF were down-regulated and 9 up-regulated; in D08_D04 comparison 15 TF were down- regulated and 10 up-regulated; in D10_D04, 11 were down-regulated and 14 up-regulated (Table A.7).

The up-regulated genes enriched with target of AR, CEBPA, cMYC, E2F1, E2F4, PPARA, PPARG and TFAP2A were found in all the comparison *vs* D04. The down-regulated genes are enriched with target genes again of cMYC and E2F4, but also with JUN, JUND, NFKB1, SMAD3, SP1 and TP53 in all comparison (Table A.7).

PPI networks among the overlapped DEGs target of TFs were constructed and representative subnetworks using the MCC algorithm of CytoHubba plugin and enrichment analysis on the top ten highest-score genes up and down-regulated were shown in Figs. 6 and 7. Top ten with overlapped genes up-regulated and target of E2F1 in 'The citric acid (TCA) cycle and respiratory electron transport' (FDR 4.02^{-11}), in

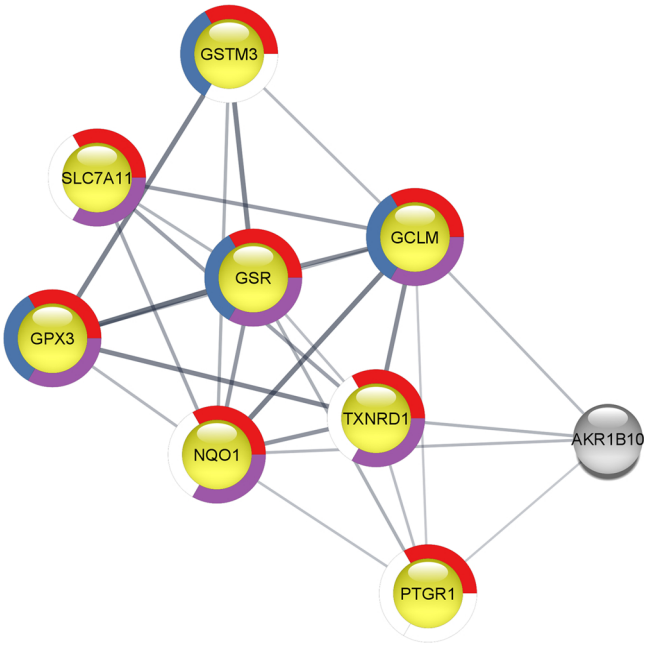

Fig. 4. Cluster with a MCODE score of 5.2 identified from the PPI network constructed with down-regulated DEGs overlapping to all the comparison *vs* D04. The enriched pathways are marked in different colours. Red: 'NRF2 pathway'; blue: 'Glutathione metabolism'; purple: 'Response to oxidative stress'. Yellow nodes indicate genes involved in pathways obtained by enriched analysis. Edges represent the protein-protein associations, Abbreviations: GCLM, glutamate-cysteine ligase modifier subunit; GPX3, glutathione peroxidase; GSR, glutathione-disulfide reductase; GSTM3, glutathione S-transferase mu 3; NQO1, NAD(P)H quinone dehydrogenase 1; PTGR1, prostaglandin reductase 1; SLC7A11, solute carrier family 7 member 11; TXNRD1, thioredoxin reductase 1. (For interpretation of the references to colour in this figure legend, the reader is referred to the web version of this article.)

Table 2
Top 10 hub genes from the cluster of down-regulated overlapping genes.

Cluster 1		
Rank	Gene	Score
1	GCLM	120
1	NQO1	120
3	TXNRD1	96
3	GSR	96
5	PTGR1	48
5	GPX3	48
7	SLC7A11	24
7	GSTM3	24
7	AKR1B10	24

Abbreviations: AKR1B10, aldo-keto reductase family 1 member B10; GCLM, glutamate-cysteine ligase modifier subunit; GPX3, glutathione peroxidase 3; GSR, glutathione-disulfide reductase; GSTM3, glutathione S-transferase mu 3; NQO1, NAD(P)H quinone dehydrogenase 1; PTGR1, prostaglandin reductase 1; SLC7A11, solute carrier family 7 member 11; TXNRD1, thioredoxin reductase 1.

'Oxidative phosphorylation' (FDR 3.78^{-10}) and 'Thermogenesis' (FDR 1.29^{-07}) (Fig. 6a), genes target of cMYC were enriched, among others, in 'cellular respiration' (FDR 1.75^{-11}) and in 'Oxidation-reduction process' (FDR 3.00^{-10}) (Fig. 6b), The overlapped genes with the highest score target of E2F4 were enriched in 'Acetylation' (FDR 9.80^{-04}) (Fig. 6c).

Fig. 7 showed the down-regulated overlapped genes target of E2F4, JUN, NFKB1 and SMAD3. The top ten gens with the highest score target of E2F4 were significantly related to 'Retinoblastoma gene in cancer' (FDR 3.53^{-09}) and in 'Cell cycle' (FDR 5.89^{-09}) (Fig. 7a), those target of JUN were enriched in 'Proteoglycan in cancer' (FDR 1.03^{-07}), in 'Interleukin-4 and Interleukin-13 signalling' (FDR 2.40^{-05}) and in 'Extracellular matrix organization'(FDR 9.77^{-05}) (Fig. 7b). The enrichment analysis of hub genes target of NFKB1 revealed that these genes were mainly involved in 'PI3K-Akt signalling pathway' (FDR 3.29^{-08}) and 'IL-18 signalling pathway' (FDR 8.68^{-07}) (Fig. 7c), those target of SMAD3 again in 'Extracellular matrix organization' (FDR 6.72^{-09}) (Fig. 7d).

Hub overlapped up- or down-regulated genes and target of all TFs were screened. Target genes of AR, CEBPA, PPARA and PPARG were related to adipogenesis, AMPK signaling pathway, regulation of lipid metabolic process, positive regulation of cold-induced thermogenesis and fatty acid metabolic process. Down-regulated hub genes target of cMYC, SP1 and RELA were significantly enriched in cytosolic ribosome, AGE-RAGE signalling pathway in diabetic complications, extracellular matrix organization and apoptosis (data not shown).

3.7. *The estimated percentage of brown-like adipocytes increases with the day of differentiation*

Starting from normalized reads counts of SGBS cells at all day of differentiation, D04, D06, D08 and D10, the BATLAS webtool estimated an increasing percentage of brown phenotype (Fig. 8). The estimate percentage at D04 was 36.7%, 50.2% at D06, 54.5% at D08 and 57.6% at D10. Inversely the estimated percentages of white adipocytes were 63.35% at D04, 49.7% at D06, 45.5% at D08 and 42.4% at D10. Of the 98 candidate genes used to classify the proportion of brown adipocytes, 87 were found from our DEGs (Table A.8). Eighteen DEGs were found among the 21 genes associated with white adipocytes (Table A.9).

Using PROFAT tool (Cheng et al., 2018) the estimation of BAT phenotype at D04 was 7.60%, at D06 16.44%, at D08 75.50% at D10 95.96% (data not shown) and the heatmap of marker expression was constructed (Fig. 9). These results indicate that during differentiation SGBS cells displayed a gene expression pattern similar to "beige" or "brown" cells.

3.8. *Validation of gene expression with Real-time PCR*

In order to validate the results obtained from the RNAseq analysis, the mean values of $2^{\hat{}(-\Delta\Delta Cts)}$ of PPARG, PPARGC1A, UCP1, PRDM16, NFKB1 and NFE2L2 genes was measured and compared (Fig. 10). No statistical differences were found between the expression level distribution.

4. Discussion

In recent years, ample interest has grown in the potential that white adipose tissue (WAT) acquires features of brown adipose tissue (BAT) in nonclassical BAT regions of the body, in order to develop strategies to counteract obesity and metabolic disorders. *In vitro* experimental models of white and brown adipocytes are a key resource for researching the biological features of BAT. Characteristics, functions and molecular signatures of BAT are mainly based on rodent models (Wang et al., 2018), while researches in human BAT are consistently less advanced. Among human cellular models, SGBS cells have been frequently used to study human adipocyte biology for their metabolic changes during the differentiation (Galhardo et al., 2014) and also to study obesity (Allott et al., 2012) and adaptive thermogenesis (Klusóczki et al., 2019). To gain further insight into the tanscriptional program of human adipogensis and browning, we performed RNAseq of SGBS cells at different stages of adipogenesis, in particular at early differentiation (D04), mid-differentiation (D06, D08), and mature adipocytes (D10).

PCA analysis based on reads clearly clustered the data set on the first component between D04 and D06, D08, D10. Moreover, biological replicates of same time point were very close each other indicating a robust data reproducibility (Fig. 1b).

A group of 932 up-regulated overlapping DEGs were identified at 6, 8 and 10 days of differentiation. According to GO-terms, these DEGs were

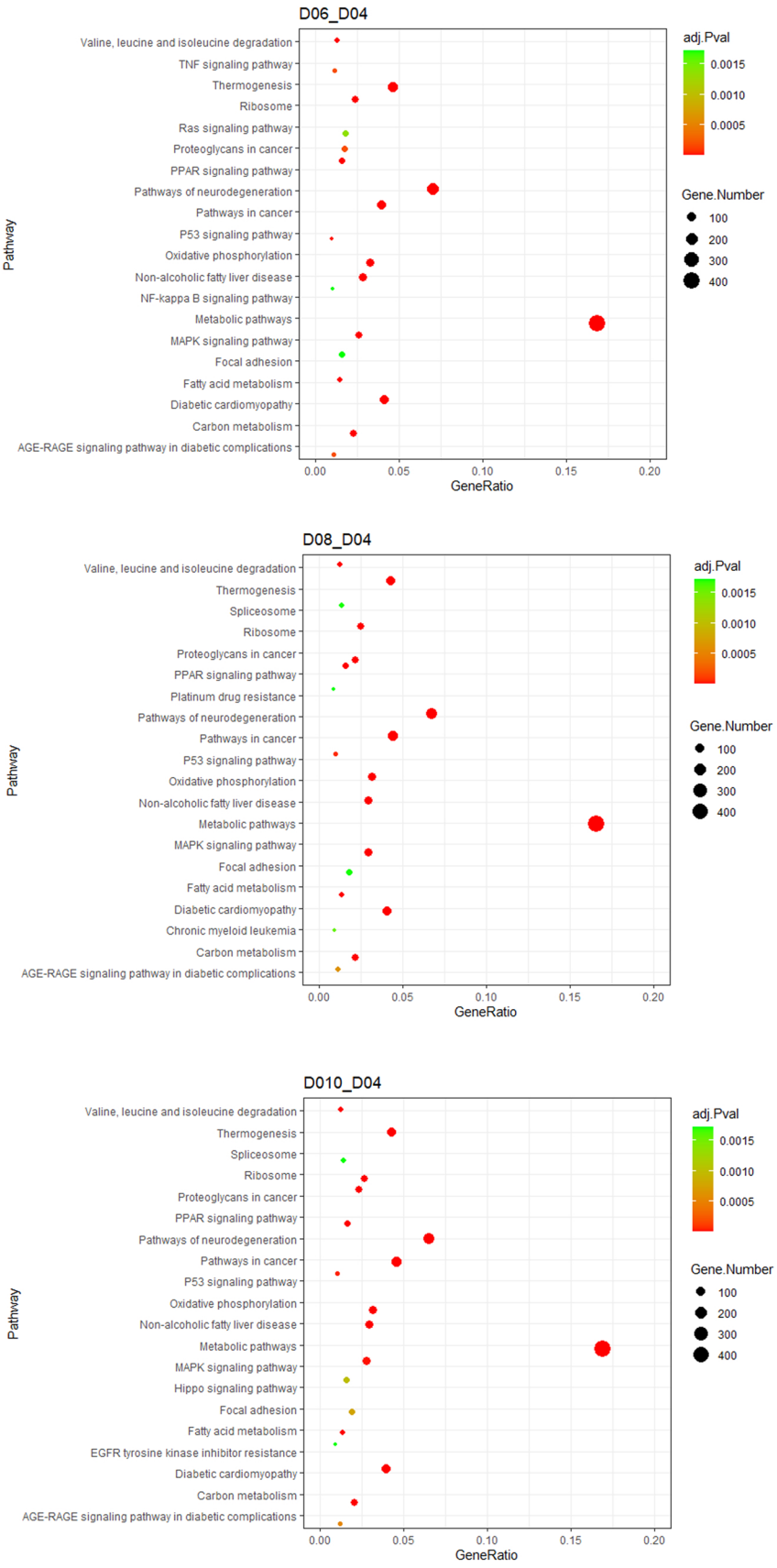

Fig. 5. KEGG pathway enrichment analysis. Dot size represents the number of genes in each KEGG pathway; adj.Pval (adjusted *p*-value): Red < orange < green. (For interpretation of the references to colour in this figure legend, the reader is referred to the web version of this article.)

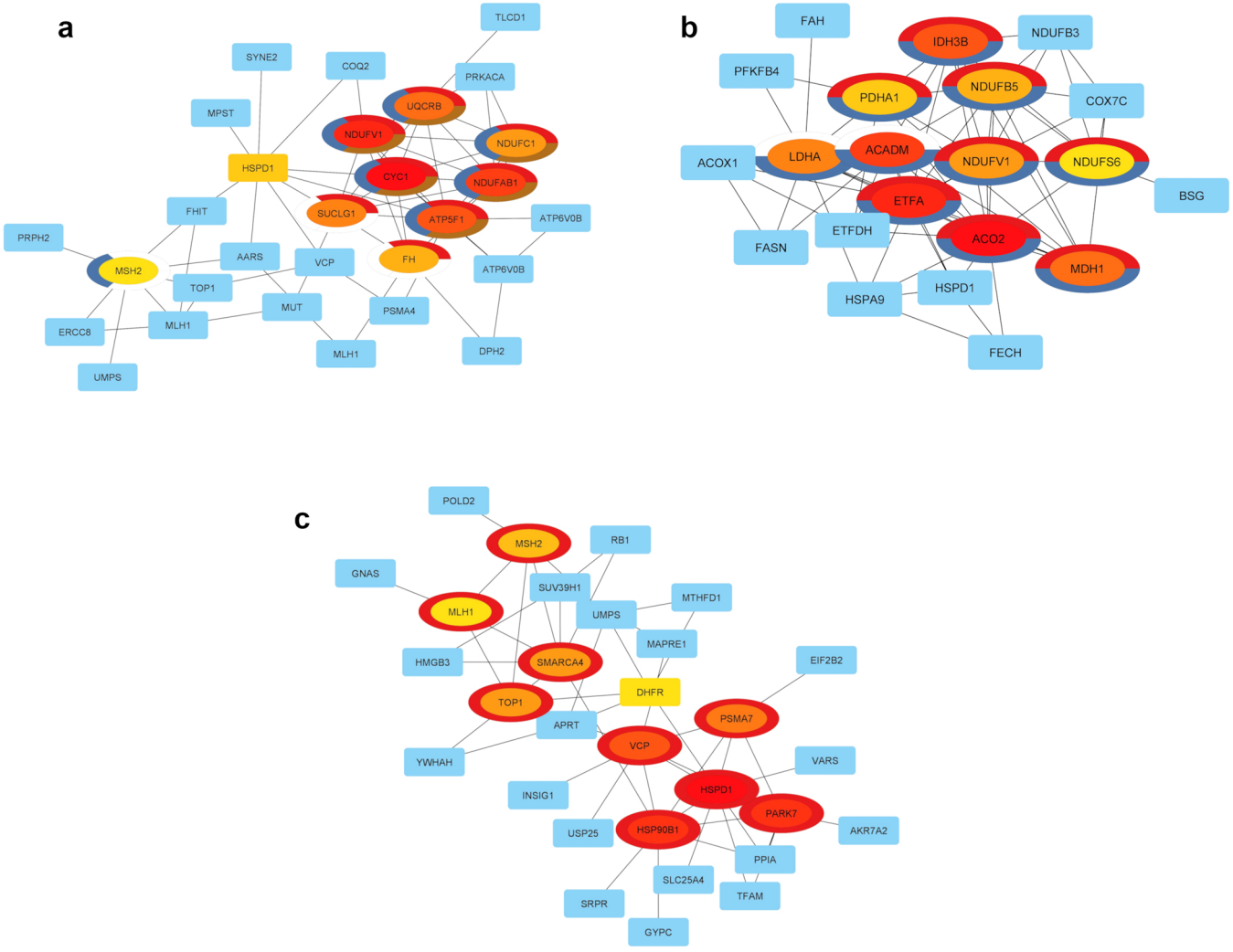

Fig. 6. Top ten hub genes identified by MCC algorithm from the PPI networks of overlapped up-regulated genes target of TFs. The enriched analysis was performed for genes with highest score and are marked in different colours. (a) Top ten hub up-regulated genes target of E2F1 were enriched in the 'Citric acid (TCA) cycle and respiratory electron transport' (red), in 'Oxidative phosphorylation' (blue) and 'Thermogenesis' (brown). (b) Top ten hub up-regulated genes target of cMYC were enriched in 'Cellular respiration' (red) and in 'Oxidation reduction process' (blue). (c) Top ten hub up-regulated genes target of E2F4 were enriched in 'Acetylation' (red). Hub genes in the PPI pathways with the highest MCC score are marked from red, with the lowest in yellow. Edges represent the protein-protein associations. Abbreviations: (a) ATP5PB, ATP synthase peripheral stalk-membrane subunit b; CYC1, cytochrome c1; FH, fumarate hydratase; MSH2, mutS homolog 2; HSPD1, heat shock protein family D (Hsp60) member 1; NDUFAB1, NADH:ubiquinone oxidoreductase subunit AB1; NDUFC1, NADH:ubiquinone oxidoreductase subunit C1; NDUFV1, NADH:ubiquinone oxidoreductase core subunit V1; SUCLG1, succinate-CoA ligase GDP/ADP-forming subunit alpha; UQCRB, ubiquinol-cytochrome c reductase binding protein. (b) ACADM, acyl-CoA dehydrogenase medium chain; ACO2, aconitase 2, ETFA, electron transfer flavoprotein subunit alpha; IDH3B, isocitrate dehydrogenase (NAD(+)) 3 non-catalytic subunit beta; LDHA, lactate dehydrogenase A; MDH1, malate dehydrogenase 1; NDUFB5,NADH:ubiquinone oxidoreductase subunit B5; NDUFS6, NADH:ubiquinone oxidoreductase subunit S6; NDUFV1, NADH:ubiquinone oxidoreductase core subunit V1; PDHA1, pyruvate dehydrogenase E1 subunit alpha 1. (c) HSP90B1, heat shock protein 90 beta family member 1; HSPD1, heat shock protein family D (Hsp60) member 1, MLH1, mutL homolog 1; MSH2 mutS homolog 2; PARK7, Parkinsonism associated deglycase; PSMA7, proteasome 20 S subunit alpha 7; SMARCA4, SWI/SNF related, matrix associated, actin dependent regulator of chromatin, subfamily a, member 4; TOP1, DNA topoisomerase I; VCP, valosin containing protein. (For interpretation of the references to colour in this figure legend, the reader is referred to the web version of this article.)

enriched in pathways related to energy production by oxidation of organic compounds, oxidoreductase activity, and mitochondrial organisation (Table A.2), this can be related to the continuous increase of UCP1 expression from D04 to D10, a feature of browning (Rosell et al., 2014). KEGG pathways enrichment confirmed that oxidative phosphorylation, PPARG signalling, thermogenesis, and amino acid metabolism were the most significantly up-regulated pathways in all the three comparisons (Fig. 5; Table A.5) corroborating that differentiated SGBS cells at D06, D08 and D10 progressibly acquire a BAT-like function. These results are in partial agreement with those of Kalkhof et al. (2020) and provide evidence that SGBS cells exhibit a molecular signature for the induction of thermogenesis in the early phase of differentiation. The mechanism of nonshivering thermogenesis in BAT is mitochondrial uncoupling, mediated by the catabolism of energy substrates without the release of chemical energy. This process is achieved through the action of UCP1, which is a mitochondrial proton transporter (Collins et al., 2010). PRDM16 is recognised as a brown fat switch that leads to the expression of key regulators of the brown fat, PPARG and PPARGC1A, by forming a transcriptional complex with C/EBPβ (Kajimura et al., 2009). However, among the clustered and hub up-regulated genes enriched in 'Brown fat cell differentiation' or 'Cold induced thermogenesis' (Fig. 3; Table 1) PRDM16 is not listed and its expression decreased from D06 to D10 SGBS cells, suggesting that PRDM16 is an early trancription marker needed for early determination of differentiation (Table A.2), as already observed in previous studies (Galhardo et al., 2014; Yeo et al., 2017; Montanari and Colitti, 2018). Interestingly,

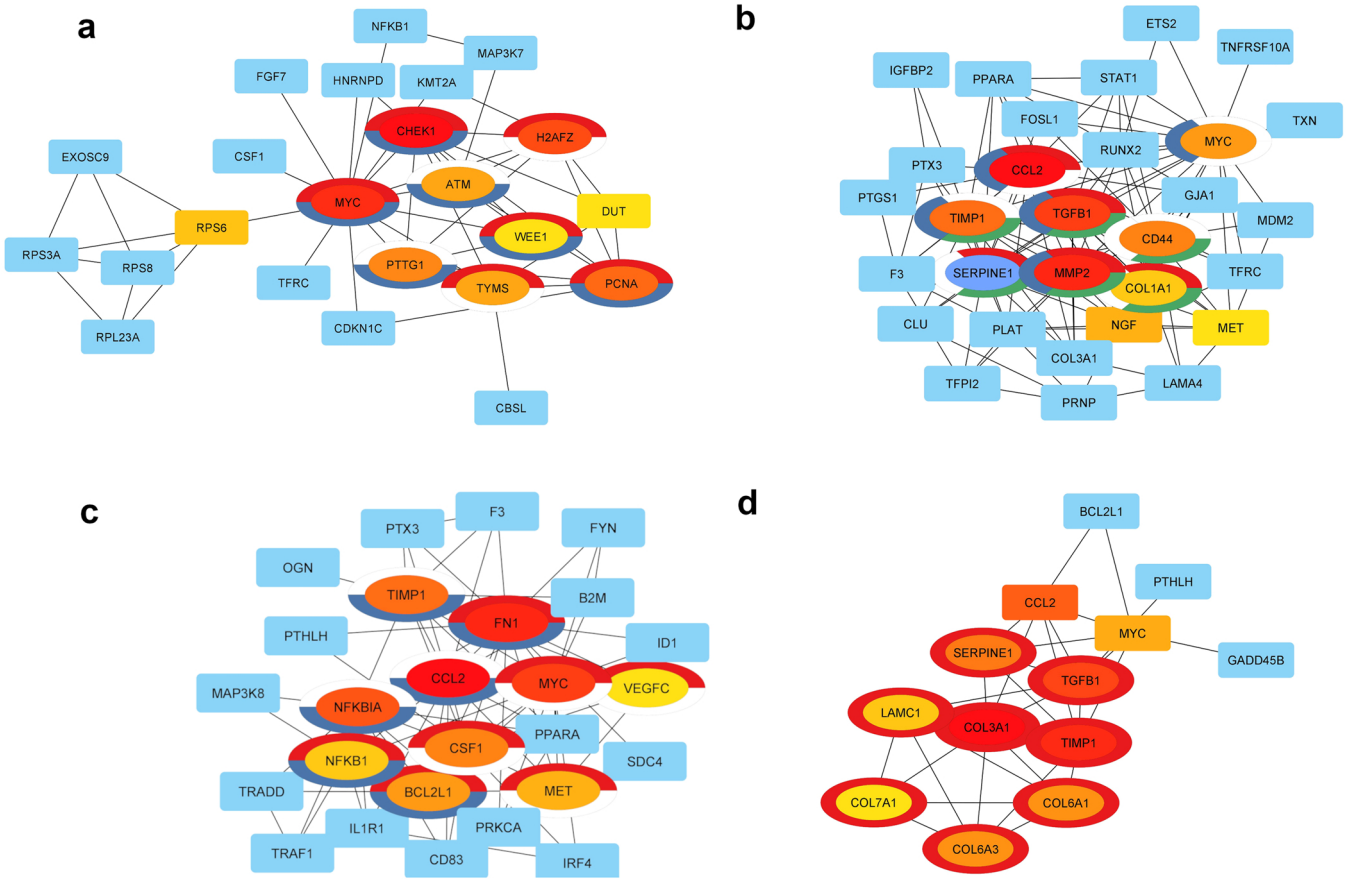

Fig. 7. Top ten hub genes identified by MCC algorithm from the PPI networks of overlapped down-regulated genes target of TFs. The enriched analysis was performed for genes with highest score and are marked in different colours. (a) Top ten hub down-regulated genes target of E2F4 were enriched in 'Retinoblastoma gene in cancer' (red) and in 'Cell cycle' (blue). (b) Top ten hub down-regulated genes target of JUN were enriched in 'Proteoglycan in cancer' (red), in 'Interleukin-4 and Interleukin-13 signalling' (blue) and in 'Extracellular matrix organization' (green). (c) Top ten hub down-regulated genes target of NFKB1 were enriched in 'PI3K-Akt signaling pathway' (red) and 'IL-18 signalling pathway' (blue). (d) Top ten hub down-regulated genes target of SMAD3 were enriched in 'Extracellular matrix organization' (red). Hub genes in the PPI pathways with the highest MCC score are marked from red, with the lowest in yellow. Edges represent the protein-protein associations, Abbreviations: (a) ATM, ATM serine/threonine kinase; CHECK1, Checkpoint Kinase 1; H2AFZ, H2A.Z Variant Histone 1; MYC, MYC proto-oncogene, bHLH transcription factor; PCNA, proliferating cell nuclear antigen; PTTG1, PTTG1 regulator of sister chromatid separation, securing; TYMS, thymidylate synthetase; WEE1, WEE1 G2 checkpoint kinase. (b) CCL2, C-C motif chemokine ligand 2; CD44, CD44 molecule (Indian blood group); COL1A1, collagen type I alpha 1 chain; MET, MET proto-oncogene, receptor tyrosine kinase; MMP2, matrix metallopeptidase 2; MYC, MYC proto-oncogene, bHLH transcription factor; SERPINE1, serpin family E member 1; TGFB1, transforming growth factor beta 1; TIMP1, TIMP metallopeptidase inhibitor 1. (c) BCL2L1, BCL2 like 1; CCL2, C-C motif chemokine ligand 2; CSF1, colony stimulating factor 1; FN1, fibronectin 1; MET, MET proto-oncogene, receptor tyrosine kinase; MYC, MYC proto-oncogene, bHLH transcription factor; NFKB1, nuclear factor kappa B subunit 1; NFKBIA, NFKB inhibitor alpha; TIMP1, TIMP metallopeptidase inhibitor 1, VEGFC, vascular endothelial growth factor C. (d) COL3A1, collagen type III alpha 1 chain; COL6A1, collagen type VI alpha 1 chain; COL6A3, collagen type VI alpha 3 chain; COL7A1, collagen type VII alpha 1 chain; LAMC1, laminin subunit gamma 1; SERPINE1, serpin family E member 1; TGFB1, transforming growth factor beta 1; TIMP1, TIMP metallopeptidase inhibitor 1. (For interpretation of the references to colour in this figure legend, the reader is referred to the web version of this article.)

released factor such as BMP7 and transcription factor as EBF2, essential for PRDM16 activation and brown cells formation, are not expressed or significantly down-regulated in D06, D08 and D10 cells in comparison to D04 (Table A.2). In fact, these factors are blocked by the nuclear protein ZNF423 (Shao et al., 2016a,2016b), which is up-regulated in all the comparisons and whose expression increased from D06 to D10 (Table A.2), although organic substance catabolic process and cellular respiration, oxido-reductase activity and oxidative phosphorilation are the most significantly biological and molecular process identified (Tables A.3, A.4, A.5). Further, moderate BAT developed in *Prdm*16$^{-/-}$ mice at embryonic day 17 and ablation of *Prdm*16 into adipocytes only impairs differentiation of beige fat, leaving the classic BAT intact (Cohen et al., 2014).

The 384 down-regulated overlapping DEGs were associated with protein translation, cellular connectivity, and focal adhesion (Table A.2). Again, focal adhesion and ribosome-related genes were the most down-regulated ones in KEGG enrichement (Fig. 5; Table A.5). It is known that adipocytes have a great capacity to adjust their size depending on substrate availability, and that during adipocyte differentiation and enlargement of lipid droplets (LDs), there is cytoskeletal restructuring and actin reorganisation (Hansson et al., 2019; Kim et al., 2019). This agrees with our previous study on SGBS cells that showed, during differentiation and without any external stimulation, a constant and significant increase of LDs surface without any variation of the number of LDs per cell (Montanari and Colitti, 2018) (Fig. 1c). In primary brown adipocytes exposed to thermoneutral condition, a uniilocular LDs organization and an increase of cell size were observed, together with a down-regulation of F-actin (Kim et al., 2019). In the present study, the deeper investigation with the molecular complex detection (MCODE) and with MCC scores from the CytoHubba plugin in Cytoscape, identified, among others, a clusters of up-regulated genes (COL4A6, COL11A1, COLGALT2, COL5A3, COL14A1, COL8A1, COL4A5 COL15A1, COL9A3, COL21A1, ITGA11, ITGA9, ITGA6, MYH1, MYH11) associated to ECM organization. Adipocytes are surrounded by a

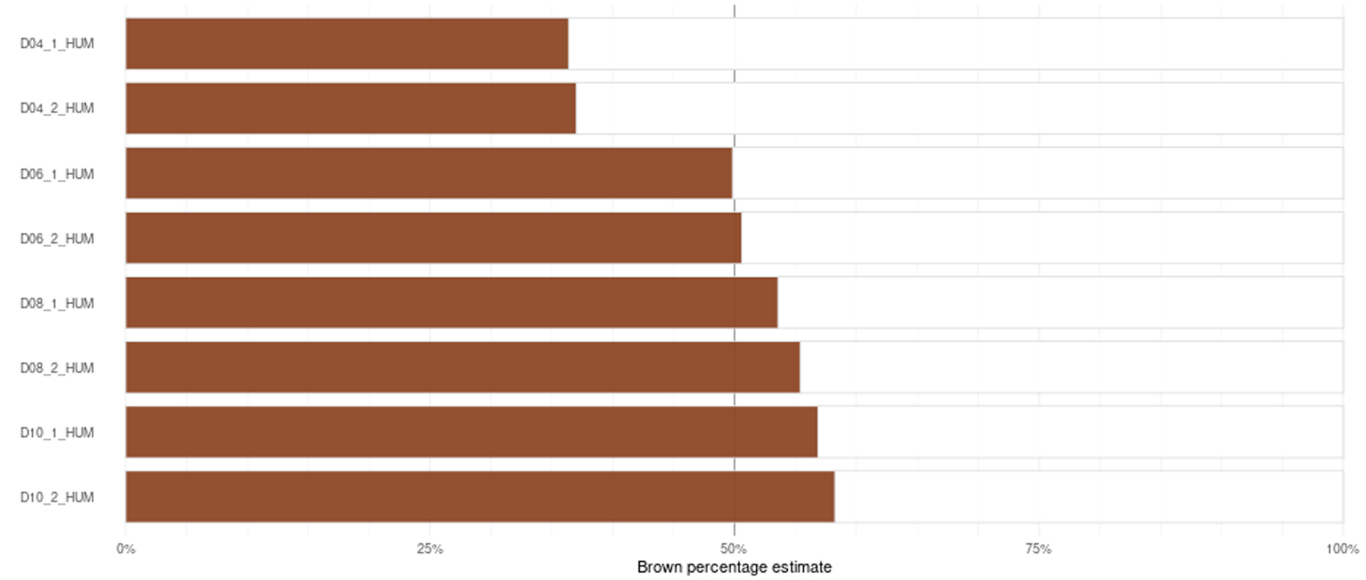

Fig. 8. The BATLAS estimation of the percentage of brown phenotype at different days of differentiation in SGBS cells. By the comparison of up and down-regulated hub DEGs and gene signature that classifies brown and white adipocytes reported by BATLAS (Perdikari et al., 2018), 6 genes PCK1 (phosphoenolpyruvate carboxykinase 1), UCP1 (uncoupling protein 1), OGDH (oxoglutarate dehydrogenase), PDHA1 (pyruvate dehydrogenase E1 subunit alpha 1), ACADS (acyl-CoA dehydrogenase short chain) and ECHS1 (enoyl-CoA hydratase, short chain 1) were associated to brown fat and one LEP (leptin) to the white phenotype. (For interpretation of the references to colour in this figure legend, the reader is referred to the web version of this article.)

basement membrane mainly composed by collagen IV and VI (Nakajima et al., 2002). This structure allows anchorage to the basement membrane and survival of adipocytes, as well as the transduction of signals across the plasma membrane by integrins that are critical for adipocyte expansion (Mariman and Wang, 2010). More recently, the interaction of ECM with adipocytes has been found related to brown adipose formation and function through actomyosin mechanics and integrin-extracellular matrix interactions (Tharp et al., 2018; Gonzalez Porras et al., 2021). Of note, in the cluster the expression of muscle-specific type II myosin heavy chains such as MYH1 and MYH11, which promote intrinsic physical forces in cells, are listed.

Interconnected genes in cluster 4 were related to fatty acid degradation and to valine, leucine and isoleucine degradation (Fig. 3, Table 1) and both processes have been widely recognised in WAT and BAT adipocytes. Branched-chain amino acids (BCAA; valine, leucine, and isoleucine) are strongly up-regulated in mature white adipocytes during adipogenesis (Halama et al., 2015) and are an important source of *de novo* lipogenesis (Green et al., 2016). Interestingly SLC25A44 gene coding for the mitochondrial transporter for BCAA catabolism in BAT was significantly up-regulated in D08 and D10 SGBS cells. The intermediates of BCAA catabolism, produced in mitochondria, can then be exported in cytoplasm and elongated through carnitine acyl transferase (CPT2), which was significantly up-regulated in D06, D08 and D10 cells, to be stored or mobilized as monomethyl branched-chain fatty acid (mmBCFA) (Green et al., 2016). BAT, after cold exposure, actively employs BCAA for thermogenesis thus promoting systemic BCAA clearance in mice and humans (Yoneshiro et al., 2019), even if intracellular triglycerides are likely the primary energy source of BAT upon activation (Carpentier et al., 2018).

Reactive oxygen species ROS plays a controversial role in adipogenesis (Schneider and Chan, 2013), while its role has been ascertained during thermogenesis (Han et al., 2016; Mills et al., 2018). Pathway of nuclear factor erythroid 2-related factor 2 (NRF2), a main regulator of antioxidants genes (Ma, 2013; Colitti et al., 2019) was associated to overlapping down-regulated DEGs in SGBS cells and the NRF2 gene was significantly down-regulated in comparison to D04 (Table A.2). Of note, in *Nrf2* deficient mice an increased UCP1 expression was found due to an increased oxidative stress (Schneider et al., 2016; Chang et al., 2021), therefore related to a decreased glutathione peroxidases (GPxs) expression, regulated by NRF2. In fact, level of glutathione (GSH), is negatively correlated with activation of the thermogenic program (Lettieri Barbato et al. 2015). GPX3 and NQO1 are included among the hub down-regulated genes both involved in the protection from oxidative stress and in adipogenesis (Schneider and Chan, 2013). Accordingly, it has been demonstrated that the enhancement of oxidative stress increases the expression of Pgc1α in mice (Matsuzawa-Nagata et al., 2008), which boosts mitochondrial biogenesis and the UCP1 expression (Rius-Pérez et al., 2020).

Target genes of AR, CEBPA, cMYC, E2F1, E2F4, PPARA, PPARG and TFAP2A obtained by transcription factors enrichment analysis were overrepresented in the up-regulated genes. AR, CEBPA, PPARG and PPARA are known to be involved in adipogenesis and lipid metabolism with a clearly defined role (Colitti and Grasso, 2014), others, like the E2F family of transcription factors, are cell-cycle proteins that regulates adipogenesis with their pocket proteins (Fajas et al., 2002). While E2F1 induces transcription of PPARG, promoting adipogenesis, on the contrary E2F4 through the association of pocket protein RBL1 (p107) or RBL2 (p130) represses PPARG trascription (Farmer, 2006). More recently Han et al. (2016) showed that in muscle progenitors cells of mice repression of *Prdm16* is mediated through E2F4/pocket proteins and that switching on transcription repressor complex promotes BAT formation.

Our data demonstrate that hub genes, target of E2F1, such as CYC1, NDUFV1, NDUFC1, NDUFAB1, ATP5F1 and UQCRB are shared genes between the citric acid (TCA) cycle and respiratory electron transport, oxidative phosphorilation and thermogenesis (Fig. 6a). Overlapping genes up-regulated by cMyc showed that hub genes ACO2, NDUFB5, NDUFS6, NDUFV1, PDHA1, IDH3B, MDH1 and ETFA were also related to the citric acid (TCA) cycle and cellular respiration (Fig. 6b), while the down-regulated ones were enriched in cytosol ribosomal proteins. However, transcriptional repressors of WAT, such as CTBP1 and CTBP2, which promote WAT browning (Vernochet et al., 2009), were significantly down-regulated in all the differentiation days examined in comparison to D04. Moreover, EBF2 and ZNF516 brown adipocyte lineage-specific transcription factors (Jung et al., 2019), were down-regulated at D06, D08 and D10 and no enrichment for their target

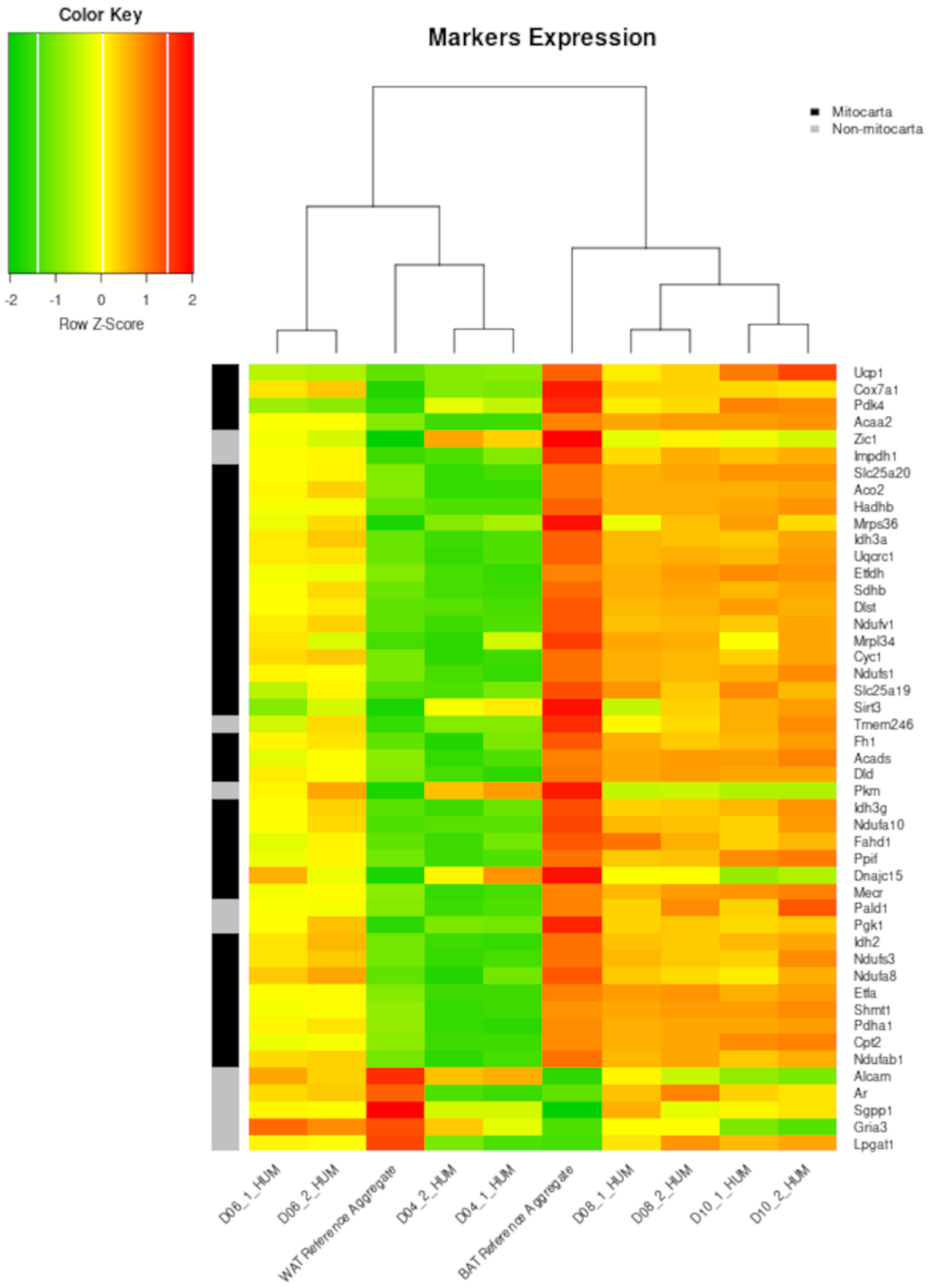

Fig. 9. Hierarchical clustering obtained by PROFAT web tool performed using Euclidean distance and complete linkage based on normalized gene expression values. DEGs were defined based on an adjusted *p*-values < 0.01 and a mean $\log_2$ fold-change threshold > 1.5. WAT reference aggregate = white adipose tissue predicted marker gene set, BAT reference aggregate = brown adipose tissue predicted marker gene set.

genes were found. On the contrary, ZNF423, identified as anti-thermogenic transcription factor, was up-regulated in comparison to D04 probably leading to a repression of PRDM16, as already reported (Shao et al., 2016a,2016b).

The up-regulated genes target of E2F4 (Fig. 6**c**) and cMYC were enriched in 'Acetylation', a process that is widely involved in adipocyte

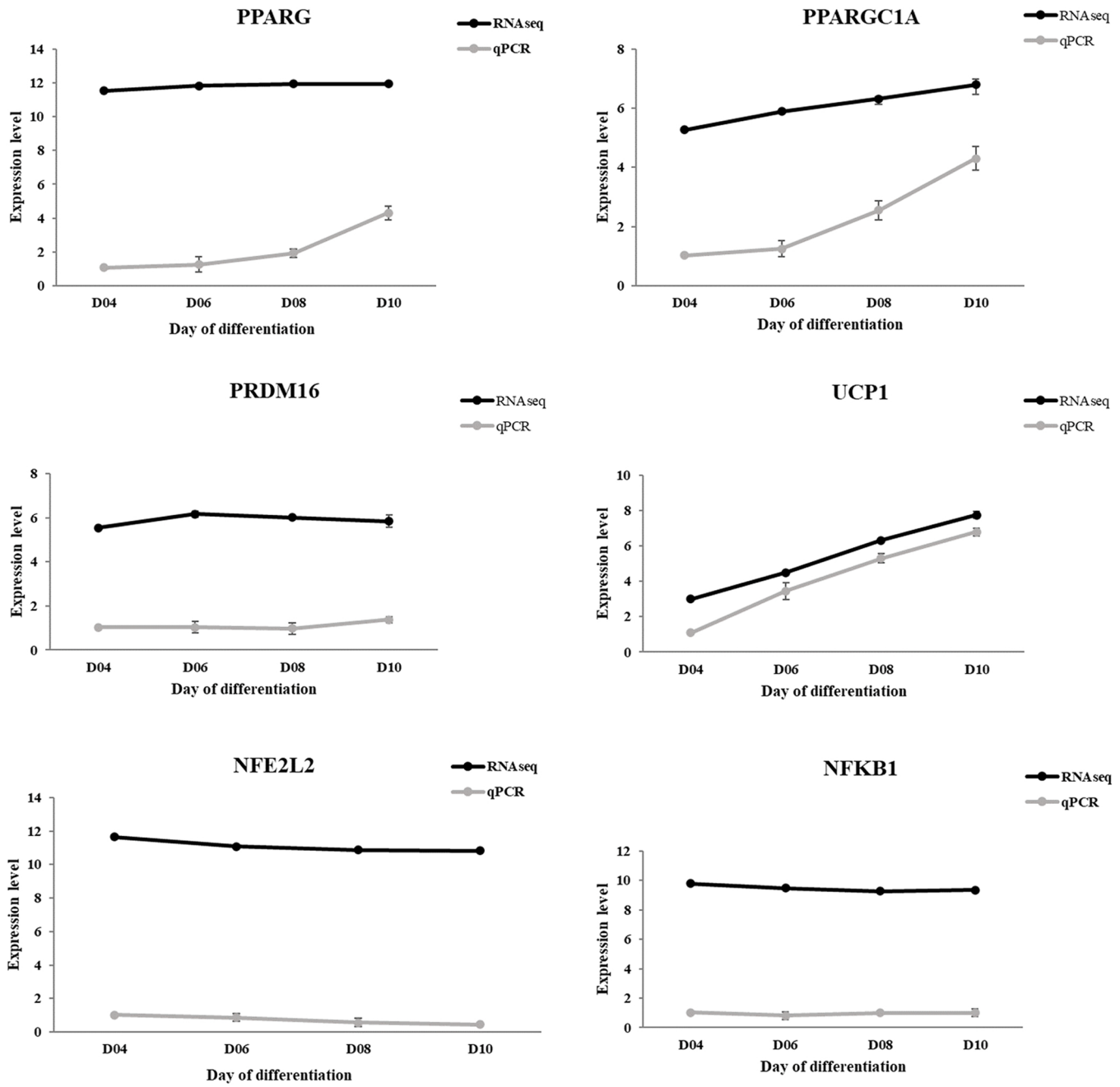

Fig. 10. qPCR validation of of the DEGs from RNA sequencing. Expression level of qPCR were normalized against the geometric mean of housekeeping genes and reported as $2^{(-\Delta\Delta Ct)}$ mean values relative to D04 (equal to 1). PPARCG1A, PPARG Coactivator 1 Alpha; UCP1, uncoupling protein 1; PRDM16, PR domain containing 16; PPARG, Peroxisome Proliferator Activated Receptor Gamma, NFE2L2, NFE2 Like BZIP Transcription Factor 2; NFKB1, Nuclear Factor Kappa B Subunit 1.

thermogenic differentiation and adaptive thermogenesis or browning through the down-regulation HDAC1, HDAC3 and HDAC11 and the up-regulation of SIRT1 and HADC6 (Ong et al., 2020). Interestingly, HDAC9 is known to inhibit HDAC1, HDAC3 promoting an oxidative metabolism (Galmozzi et al., 2013), suppressing adipogenic differentiation in 3T3-L1 preadipocytes (Chatterjee et al., 2011). Accordingly, compared with D04, SGBS cells showed significant down-regulation of HDAC1, HDAC3, but not HDAC11 along with significant up-regulation of HDAC9, HDAC6, and SIRT1 (Table A.2).

Hub genes target of selected down-regulated TFs were significantly enriched, among others, in 'Retinoblastoma gene in cancer', 'Proteoglycan in cancer, 'Extracellular matrix organization' and 'IL-18 signalling pathway' (Fig. 7), that confirmed previous data obtained by down-regulated overlapping DEGs. In particular, the retinoblastoma pathway could be related to a down-regulation of RBL1 and RBL2 that, if deleted, have an important role in browning process (Hansen et al., 2004). Proteoglycans are a subset of glycoproteins found at the cell surface and in the extracellular matrix and were connected to metabolic homeostasis and adipocytes differentiation (Pessentheiner et al., 2020). Moreover, it has been known that ablation of specific proteoglycans, such as NG2, impaired brown fat development through a reduced transcription of PRDM16 (Chang et al., 2012) and that metalloproteinase such as MMP-2 and CD44 are involved in obesity and insuline resistance (Lin et al., 2016). Interestingly, down-regulated hub gene targets of NFKB1 are involved in IL-18 signalling pathway whose deletion promoted a brown phenotype in brown tissue and cells of *Il18*$^{-/-}$ mice (Yamanishi et al., 2018).

It has been observed previously that SGBS cells induce a beige

adipocyte differentiation program upon rosiglitazone and T3 treatment (Klusóczki et al., 2019), as previously observed in adipocytes derived from epididymal depot (Petrovic et al., 2010). Of note, rosiglitazone was also found to inhibit SMAD signalling in white adipose tissue *in vivo* (Beaudoin et al., 2014), supporting the notion that in $SMAD^{-/-}$ mice WAT exhibited an increased number of brown adipocytes and mitochondrial biogenesis (Yadav et al., 2011). Among the down-regulated genes SMAD, TGFB1, COL3A1, COL6A1 are highly connected and their expression decreased from D06 compared to D10 comparsion (Table A.2). Elevated collagen VI, the major ECM protein in adipose tissues, together TGFβ are responsible factors for excessive accumulation of the ECM in adipose tissue of human with obesity (Reggio et al., 2016).

Finally, the comparison of DEGs with candidate genes of brown and white cell molecular signature indicated an increase in percentage of genes related to brown phenotype according to SGBS cells differentiation.

5. Conclusions

This is a detailed study comparing the DEGs of SGBS cells up to the tenth day of differentiation. RNA-Seq analysis identified genes involved in ECM organization and oxidative stress that may regulate thermogenesis. The present study provided useful resources and sequencing information of considerable value for further research on the browning process. Functional characterization of several unigenes, involved in the identified biological processes, could stimulate research to further unravel the molecular basis of adipose tissue browning and also provide a reference base to promote experimental research.

Funding

Not applicable.

CRediT authorship contribution statement

CM designed research, performed bioinformatic statistical analysis and interpretation, written and polished the manuscript; AU performed experimental analyses; WM and TD involved in the discussion and revision the paper. All authors read and approved the manuscript.

Conflict of interest

The authors declare no competing interests.

Data Availability

Raw sequence data were deposited in SRA accession number: PRJNA783150 at https://www.ncbi.nlm.nih.gov/sra/PRJNA783150.

Appendix A. Supporting information

Supplementary data associated with this article can be found in the online version at doi:10.1016/j.tice.2022.101822.

References

Addinsoft (2022) XLSTAT statistical and data analysis solution. New York, USA.

Allott, E.H., Oliver, E., Lysaght, J., Gray, S.G., Reynolds, J.V., Roche, H.M., Pidgeon, G.P., 2012. The SGBS cell strain as a model for the in vitro study of obesity and cancer. Clin. Transl. Oncol. 14 (10), 774–782. https://doi.org/10.1007/s12094-012-0863-6.

Ashburner, M., Ball, C.A., Blake, J.A., Botstein, D., Butler, H., Cherry, J.M., Davis, A.P., Dolinski, K., Dwight, S.S., Eppig, J.T., Harris, M.A., Hill, D.P., Issel-Tarver, L., Kasarskis, A., Lewis, S., Matese, J.C., Richardson, J.E., Ringwald, M., Rubin, G.M., Sherlock, G., 2000. Gene ontology: tool for the unification of biology. Nat. Genet. 25 (1), 25–29. https://doi.org/10.1038/75556.

Bader, G.D., Hogue, C.W., 2003. An automated method for finding molecular complexes in large protein interaction networks. BMC Bioinform. 4, 2. https://doi.org/10.1186/1471-2105-4-2.

Beaudoin, M.S., Snook, L.A., Arkell, A.M., Stefanson, A., Wan, Z., Simpson, J.A., Holloway, G.P., Wright, D.C., 2014. Novel effects of rosiglitazone on SMAD2 and SMAD3 signaling in white adipose tissue of diabetic rats. Obesity 22 (7), 1632–1642. https://doi.org/10.1002/oby.20717.

Bustin, S.A., Benes, V., Garson, J.A., Hellemans, J., Huggett, J., Kubista, M., Mueller, R., Nolan, T., Pfaffl, M.W., Shipley, G.L., Vandesompele, J., Wittwer, C.T., 2009. The MIQE guidelines: minimum information for publication of quantitative real-time PCR experiments. Clin. Chem. 55 (4), 611–622. https://doi.org/10.1373/clinchem.2008.112797.

Capurro, M.I., Xu, P., Shi, W., Li, F., Jia, A., Filmus, J., 2008. Glypican-3 inhibits Hedgehog signaling during development by competing with patched for Hedgehog binding. Dev. Cell. 14 (5), 700–711. https://doi.org/10.1016/j.devcel.2008.03.006.

Carpentier, A.C., Blondin, D.P., Virtanen, K.A., Richard, D., Haman, F., Turcotte, E.E., 2018. Brown adipose tissue energy metabolism in humans. Front. Endocrinol. 9, 447. https://doi.org/10.3389/fendo.2018.00447.

Chang, S.H., Lee, J.S., Yun, U.J., Park, K.W., 2021. A role of stress sensor NRF2 in stimulating thermogenesis and energy expenditure. Biomedicines 9 (9), 1196. https://doi.org/10.3390/biomedicines9091196.

Chang, Y., She, Z.G., Sakimura, K., Roberts, A., Kucharova, K., Rowitch, D.H., Stallcup, W.B., 2012. Ablation of NG2 proteoglycan leads to deficits in brown fat function and to adult onset obesity. PLoS One 7 (1), e30637. https://doi.org/10.1371/journal.pone.0030637.

Chatterjee, T.K., Idelman, G., Blanco, V., Blomkalns, A.L., Piegore, M.G., Weintraub, D.S., Kumar, S., Rajsheker, S., Manka, D., Rudich, S.M., Tang, Y., Hui, D.Y., Bassel-Duby, R., Olson, E.N., Lingrel, J.B., Ho, S.M., Weintraub, N.L., 2011. Histone deacetylase 9 is a negative regulator of adipogenic differentiation. J. Biol. Chem. 286 (31), 27836–27847. https://doi.org/10.1074/jbc.M111.262964.

Cheng, Y., Jiang, L., Keipert, S., Zhang, S., Hauser, A., Graf, E., Strom, T., Tschöp, M., Jastroch, M., Perocchi, F., 2018. Prediction of adipose browning capacity by systematic integration of transcriptional profiles. Cell. Rep. 23 (10), 3112–3125. https://doi.org/10.1016/j.celrep.2018.05.021.

Chin, C.H., Chen, S.H., Wu, H.H., Ho, C.W., Ko, M.T., Lin, C.Y., 2014. CytoHubba: identifying hub objects and sub-networks from complex interactome. BMC Syst. Biol. 8 (4), S11. https://doi.org/10.1186/1752-0509-8-S4-S11.

Christian, M., Parker, M.G., 2010. The engineering of brown fat. J. Mol. Cell. Biol. 2 (1), 23–25. https://doi.org/10.1093/jmcb/mjp035.

Cohen, P., Levy, J.D., Zhang, Y., Frontini, A., Kolodin, D.P., Svensson, K.J., Lo, J.C., Zeng, X., Ye, L., Khandekar, M.J., Wu, J., Gunawardana, S.C., Banks, A.S., Camporez, J.P., Jurczak, M.J., Kajimura, S., Piston, D.W., Mathis, D., Cinti, S., Shulman, G.I., Seale, P., Spiegelman, B.M., 2014. Ablation of PRDM16 and beige adipose causes metabolic dysfunction and a subcutaneous to visceral fat switch. Cell 156 (1–2), 304–316. https://doi.org/10.1016/j.cell.2013.12.021.

Colitti, M., Grasso, S., 2014. Nutraceuticals and regulation of adipocyte life: premises or promises. Biofactors 40 (4), 398–418. https://doi.org/10.1002/biof.1164.

Colitti, M., Stefanon, B., Gabai, G., Gelain, M.E., Bonsembiante, F., 2019. Oxidative stress and nutraceuticals in the modulation of the immune function: Current knowledge in animals of veterinary interest. Antioxidants 28. https://doi.org/10.3390/antiox8010028.

Collins, S., Yehuda-Shnaidman, E., Wang, H., 2010. Positive and negative control of Ucp1 gene transcription and the role of β-adrenergic signaling networks. Int. J. Obes. 34 (1), S28–S33. https://doi.org/10.1038/ijo.2010.180.

Dobin, A., Davis, C.A., Schlesinger, F., Drenkow, J., Zaleski, C., Jha, S., Batut, P., Chaisson, M., Gingeras, T.R., 2013. STAR: ultrafast universal RNA-seq aligner. Bioinformatics 29 (1), 15–21. https://doi.org/10.1093/bioinformatics/bts635.

Fajas, L., Landsberg, R.L., Huss-Garcia, Y., Sardet, C., Lees, J.A., Auwerx, J., 2002. E2Fs regulate adipocyte differentiation. Dev. Cell 3 (1), 39–49. https://doi.org/10.1016/s1534-5807(02)00190-9.

Galhardo, M., Sinkkonen, L., Berninger, P., Lin, J., Sauter, T., Heinäniemi, M., 2014. Integrated analysis of transcript-level regulation of metabolism reveals disease-relevant nodes of the human metabolic network. Nucleic Acids Res. 42 (3), 1474–1496. https://doi.org/10.1093/nar/gkt989.

Ge, S.X., Son, E.W., Yao, R., 2018. iDEP: an integrated web application for differential expression and pathway analysis of RNA-Seq data. BMC Bioinform. 19 (1), 534. https://doi.org/10.1186/s12859-018-2486-6.

Ge, X., 2021. iDEP web application for RNA-Seq data analysis. Methods Mol. Biol. 2284, 417–443. https://doi.org/10.1007/978-1-0716-1307-8_22.

Galmozzi, A., Mitro, N., Ferrari, A., Gers, E., Gilardi, F., Godio, C., Gualerzi, A., Donetti, E., Rotili, D., Valente, S., Guerrini, U., Caruso, D., Mai, A., Saez, E., De Fabiani, E., Crestani, M., 2013. Inhibition of class I histone deacetylases unveils a mitochondrial signature and enhances oxidative metabolism in skeletal muscle and adipose tissue. Diabetes 62, 732–742. https://doi.org/10.2337/db12-0548.

Gonzalez Porras, M.A., Stojkova, K., Vaicik, M.K., Pelowe, A., Goddi, A., Carmona, A., Long, B., Qutub, A.A., Gonzalez, A., Cohen, R.N., Brey, E.M., 2021. Integrins and extracellular matrix proteins modulate adipocyte thermogenic capacity. Sci. Rep. 11 (1), 1–14. https://doi.org/10.1038/s41598-021-84828-z.

Green, C.R., Wallace, M., Divakaruni, A.S., Phillips, S.A., Murphy, A.N., Ciaraldi, T.P., Metallo, C.M., 2016. Branched-chain amino acid catabolism fuels adipocyte differentiation and lipogenesis. Nat. Chem. Biol. 12 (1), 15–21. https://doi.org/10.1038/nchembio.1961.

Guennoun, A., Kazantzis, M., Thomas, R., Wabitsch, M., Tews, D., Seetharama Sastry, K., Abdelkarim, M., Zilberfarb, V., Strosberg, A.D., Chouchane, L., 2015. Comprehensive molecular characterization of human adipocytes reveals a transient brown phenotype. J. Transl. Med. 13 (135) doi.org/10.1186/s12967-015-0480-6.

Halbgebauer, D., Dahlhaus, M., Wabitsch, M., Fischer-Posovszky, P., Tews, D., 2020. Browning capabilities of human primary adipose-derived stromal cells compared to SGBS cells. Sci. Rep. 10 (9632) https://doi.org/10.1038/s41598-020-64369-7.

Halama, A., Horsch, M., Kastenmüller, G., Möller, G., Kumar, P., Prehn, C., Laumen, H., Hauner, H., Hrabě, de., Angelis, M., Beckers, J., Suhre, K., Adamski, J., 2015. Metabolic switch during adipogenesis: From branched chain amino acid catabolism to lipid synthesis. Arch. Biochem. Biophys. 589, 93–107. https://doi.org/10.1016/j.abb.2015.09.013.

Han, Y.H., Buffolo, M., Pires, K.M., Pei, S., Scherer, P.E., Boudina, S., 2016. Adipocyte-specific deletion of manganese superoxide dismutase protects from diet-induced obesity through increased mitochondrial uncoupling and biogenesis. Diabetes 65 (9), 2639–2651. https://doi.org/10.2337/db16-0283.

Hansen, J.B., te Riele, H., Kristiansen, K., 2004. Novel function of the retinoblastoma protein in fat: regulation of white versus brown adipocyte differentiation. Cell Cycle 3 (6), 774–778. https://doi.org/10.4161/cc.3.6.908.

Hansson, B., Morén, B., Fryklund, C., Vliex, L., Wasserstrom, S., Albinsson, S., Berger, K., Stenkula, K.G., 2019. Adipose cell size changes are associated with a drastic actin remodeling. Sci. Rep. 9 (1), 12941. https://doi.org/10.1038/s41598-019-49418-0.

Huber, R., Mazzarella, R., Chen, C.N., Chen, E., Ireland, M., Lindsay, S., Pilia, G., Crisponi, L., 1998. Glypican 3 and glypican 4 are juxtaposed in Xq26.1. Gene 225 (1–2), 9–16. https://doi.org/10.1016/s0378-1119(98)00549-6.

Jiang, C., Xuan, Z., Zhao, F., Zhang, M.Q., 2007. TRED: a transcriptional regulatory element database, new entries and other development. Nucleic Acids Res. 35, 137–140. https://doi.org/10.1093/nar/gkl1041.

Jung, S.M., Sanchez-Gurmaches, J., Guertin, D.A., 2019. Brown adipose tissue development and metabolism. Handb. Exp. Pharmacol. 251, 3–36. https://doi.org/10.1007/164_2018_168.

Kajimura, S., Seale, P., Kubota, K., Lunsford, E., Frangioni, J.V., Gygi, S.P., Spiegelman, B.M., 2009. Initiation of myoblast to brown fat switch by a PRDM16-C/EBP-beta transcriptional complex. Nature 460 (7259), 1154–1158. https://doi.org/10.1038/nature08262.

Kalkhof, S., Krieg, L., Büttner, P., Wabitsch, M., Küntzel, C., Friebe, D., Landgraf, K., Hanschkow, M., Schubert, K., Kiess, W., Krohn, K., Blüher, M., von Bergen, M., Körner, A., 2020. In depth quantitative proteomic and transcriptomic characterization of human adipocyte differentiation using the SGBS cell line. Proteomics, e1900405. https://doi.org/10.1002/pmic.201900405.

Kanehisa, M., Goto, S., 2000. KEGG: kyoto encyclopedia of genes and genomes. Nucleic Acids Res. 28 (1), 27–30. https://doi.org/10.1093/nar/28.1.27.

Kim, J.I., Park, J., Ji, Y., Jo, K., Han, S.M., Sohn, J.H., Shin, K.C., Han, J.S., Jeon, Y.G., Nahmgoong, H., Han, K.H., 2019. During adipocyte remodeling, lipid droplet configurations regulate insulin sensitivity through F-actin and G-actin reorganization. Mol. Cell. Biol. 39 (20), e00210–e00219 doi.org/10.1128/MCB.00210-19.

Klusóczki, Á., Veréb, Z., Vámos, A., Fischer-Posovszky, P., Wabitsch, M., Bacso, Z., Fésüs, L., Kristóf, E., 2019. Differentiating SGBS adipocytes respond to PPARγ stimulation, irisin and BMP7 by functional browning and beige characteristics. Sci. Rep. 9 (1), 5823. https://doi.org/10.1038/s41598-019-42256-0.

Lettieri Barbato, D., Tatulli, G., Maria Cannata, S., Bernardini, S., Aquilano, K., Ciriolo, M.R., 2015. Glutathione decrement drives thermogenic program in adipose cells. Sci. Rep. 5, 13091. https://doi.org/10.1038/srep13091.

Lin, D., Chun, T.H., Kang, L., 2016. Adipose extracellular matrix remodelling in obesity and insulin resistance. Biochem. Pharmacol. 19, 8–16. https://doi.org/10.1016/j.bcp.2016.05.005.

Livak, K.J., Schmittgen, T.D., 2001. Analysis of relative gene expression data using real-time quantitative PCR and the 2(-Delta Delta C(T)) Method. Methods 25 (4), 402–408. https://doi.org/10.1006/meth.2001.1262.

Ma, Q., 2013. Role of Nrf2 in oxidative stress and toxicity. Annu. Rev. Pharmacol. Toxicol. 53, 401–426. https://doi.org/10.1146/annurev-pharmtox-011112-140320.

Mariman, E.C., Wang, P., 2010. Adipocyte extracellular matrix composition, dynamics and role in obesity. Cell. Mol. Life Sci. 67 (8), 1277–1292. https://doi.org/10.1007/s00018-010-0263-4.

Matsuzawa-Nagata, N., Takamura, T., Ando, H., Nakamura, S., Kurita, S., Misu, H., Ota, T., Yokoyama, M., Honda, M., Miyamoto, K., Kaneko, S., 2008. Increased oxidative stress precedes the onset of high-fat diet-induced insulin resistance and obesity. Metabolism 57 (8), 1071–1077. https://doi.org/10.1016/j.metabol.2008.03.010.

Mills, E.L., Pierce, K.A., Jedrychowski, M.P., Garrity, R., Winther, S., Vidoni, S., Yoneshiro, T., Spinelli, J.B., Lu, G.Z., Kazak, L., Banks, A.S., Haigis, M.C., Kajimura, S., Murphy, M.P., Gygi, S.P., Clish, C.B., Chouchani, E.T., 2018. Accumulation of succinate controls activation of adipose tissue thermogenesis. Nature 560 (7716), 102–106. https://doi.org/10.1038/s41586-018-0353-2.

Montanari, T., Colitti, M., 2018. Simpson-Golabi-Behmel syndrome human adipocytes reveal a changing phenotype throughout differentiation. Histochem. Cell Biol. 149 (6), 593–605. https://doi.org/10.1007/s00418-018-1663-z.

Montanari, T., Pošćić, N., Colitti, M., 2017. Factors involved in white-to-brown adipose tissue conversion and in thermogenesis: a review. Obes. Rev. 18 (5), 495–513. https://doi.org/10.1111/obr.12520.

Montanari, T., Boschi, F., Colitti, M., 2019. Comparison of the effects of browning-inducing capsaicin on two murine adipocyte models. Front. Physiol. 10, 1380. https://doi.org/10.3389/fphys.2019.01380.

Morrison, S., McGee, S.L., 2015. 3T3-L1 adipocytes display phenotypic characteristics of multiple adipocyte lineages. Adipocyte 4 (4), 295–302. https://doi.org/10.1080/21623945.2015.1040612.

Nakajima, I., Muroya, S., Tanabe, R., Chikuni, K., 2002. Extracellular matrix development during differentiation into adipocytes with a unique increase in type V and VI collagen. Biol. Cell. 94 (3), 197–203. https://doi.org/10.1016/s0248-4900(02)01189-9.

Ohno, H., Shinoda, K., Spiegelman, B.M., Kajimura, S., 2012. PPARγ agonists induce a white-to-brown fat conversion through stabilization of PRDM16 protein. Cell Metab. 15 (3), 395–404. https://doi.org/10.1016/j.cmet.2012.01.019.

Ong, B.X., Brunmeir, R., Zhang, Q., Peng, X., Idris, M., Liu, C., Xu, F., 2020. Regulation of thermogenic adipocyte differentiation and adaptive thermogenesis through histone acetylation. Front. Endocrinol. 11, 95. https://doi.org/10.3389/fendo.2020.00095.

Perdikari, A., Leparc, G.G., Balaz, M., Pires, N.D., Lidell, M.E., Sun, W., Fernandez-Albert, F., Müller, S., Akchiche, N., Dong, H., Balazova, L., Opitz, L., Röder, E., Klein, H., Stefanicka, P., Varga, L., Nuutila, P., Virtanen, K.A., Niemi, T., Taittonen, M., Rudofsky, G., Ukropec, J., Enerbäck, S., Stupka, E., Neubauer, H., Wolfrum, C., 2018. BATLAS: Deconvoluting brown adipose tissue. e4 Cell Rep. 25 (3), 784–797. https://doi.org/10.1016/j.celrep.2018.09.044.

Pessentheiner, A.R., Ducasa, G.M., Gordts, P.L.S.M., 2020. Proteoglycans in obesity-associated metabolic dysfunction and meta-inflammation. Front. Immunol. 11, 769. https://doi.org/10.3389/fimmu.2020.00769.

Petrovic, N., Walden, T.B., Shabalina, I.G., Timmons, J.A., Cannon, B., Nedergaard, J., 2010. Chronic peroxisome proliferator-activated receptor gamma (PPARgamma) activation of epididymally derived white adipocyte cultures reveals a population of thermogenically competent, UCP1-containing adipocytes molecularly distinct from classic brown adipocytes. J. Biol. Chem. 285, 7153–7164. https://doi.org/10.1074/jbc/M109.053942.

Reggio, S., Rouault, C., Poitou, C., Bichet, J.C., Prifti, E., Bouillot, J.L., Rizkalla, S., Lacasa, D., Tordjman, J., Clement, K., 2016. Increased basement membrane components in adipose tissue during obesity: links with TGFbeta and metabolic phenotypes. J. Clin. Endocrinol. Metab. 101, 2578–2587. https://doi.org/10.1210/jc.2015-4304.

Rius-Pérez, S., Isabel Torres-Cuevas, I., Millán, I., Ortega, A.L., Pérez, S., 2020. PGC-1 α, inflammation, and oxidative stress: an integrative view in metabolism. Oxid. Med. Cell. Longev. 2020, 1452696 https://doi.org/10.1155/2020/1452696.

Rosell, M., Kaforou, M., Frontini, A., Okolo, A., Chan, Y.W., Nikolopoulou, E., Millership, S., Fenech, M.E., MacIntyre, D., Turner, J.O., Moore, J.D., Blackburn, E., Gullick, W.J., Cinti, S., Montana, G., Parker, M.G., Christian, M., 2014. Brown and white adipose tissues: intrinsic differences in gene expression and response to cold exposure in mice. Am. J. Physiol. Endocrinol. Metab. 306 (8), E945–E964. https://doi.org/10.1152/ajpendo.00473.2013.

Rozen, S., Skaletsky, H., 2000. Primer3 on the WWW for general users and for biologist programmers. Methods Mol. Biol. 132, 365–386. https://doi.org/10.1385/1-59259-192-2:365.

Ruiz-Ojeda, F.J., Rupérez, A.I., Gomez-Llorente, C., Gil, A., Aguilera, C.M., 2016. Cell models and their application for studying adipogenic differentiation in relation to obesity: a review. Int. J. Mol. Sci. 17 (7), 1040. https://doi.org/10.3390/ijms17071040.

Schneider, K., Valdez, J., Nguyen, J., Vawter, M., Galke, B., Kurtz, T.W., Chan, J.Y., 2016. Increased energy expenditure, Ucp1 expression, and resistance to diet-induced obesity in mice lacking nuclear factor-erythroid-2-related transcription factor-2 (Nrf2). J. Biol. Chem. 291 (14), 7754–7766. https://doi.org/10.1074/jbc.M115.673756.

Schneider, K.S., Chan, J.Y., 2013. Emerging role of Nrf2 in adipocytes and adipose biology. Adv. Nutr. 4 (1), 62–66. https://doi.org/10.3945/an.112.003103.

Shao, M., Ishibashi, J., Kusminski, C.M., Wang, Q.A., Hepler, C., Vishvanath, L., MacPherson, K.A., Spurgin, S.B., Sun, K., Holland, W.L., Seale, P., Gupta, R.K., 2016a. Zfp423 maintains white adipocyte identity through suppression of the beige cell thermogenic gene program. Cell Metab. 23 (6), 1167–1184. https://doi.org/10.1016/j.cmet.2016.04.023.

Shao, M., Ishibashi, J., Kusminski, C.M., Wang, Q.A., Hepler, C., Vishvanath, L., MacPherson, K.A., Spurgin, S.B., Sun, K., Holland, W.L., Seale, P., Gupta, R.K., 2016b. Zfp423 maintains white adipocyte identity through suppression of the beige cell thermogenic gene program. Cell Metab. 23 (6), 1167–1184. https://doi.org/10.1016/j.cmet.2016.04.023.

Tharp, K.M., Kang, M.S., Timblin, G.A., Dempersmier, J., Dempsey, G.E., Zushin, P.H., Benavides, J., Choi, C., Li, C.X., Jha, A.K., Kajimura, S., Healy, K.E., Sul, H.S., Saijo, K., Kumar, S., Stahl, A., 2018. Actomyosin-mediated tension orchestrates uncoupled respiration in adipose tissues. e4 Cell Metab. 27 (3), 602–615. https://doi.org/10.1016/j.cmet.2018.02.005.

Vernochet, C., Peres, S.B., Davis, K.E., McDonald, M.E., Qiang, L., Wang, H., Scherer, P.E., Farmer, S.R., 2009. C/EBPalpha and the corepressors CtBP1 and CtBP2 regulate repression of select visceral white adipose genes during induction of the brown phenotype in white adipocytes by peroxisome proliferator-activated receptor gamma agonists. Mol. Cell Biol. 29 (17), 4714–4728. https://doi.org/10.1128/MCB.01899-08.

Wabitsch, M., Brenner, R.E., Melzner, I., Braun, M., Möller, P., Heinze, E., Debatin, K.M., Hauner, H., 2001. Characterization of a human preadipocyte cell strain with high capacity for adipose differentiation. Int. J. Obes. Relat. Metab. Disord. 25 (1), 8–15. https://doi.org/10.1038/sj.ijo.0801520.

Wang, X.Y., You, L.H., Cui, X.W., Li, Y., Wang, X., Xu, P.F., Zhu, L.J., Wen, J., Pang, L.X., Guo, X.R., JI, C.B., 2018. Evaluation and optimization of differentiation conditions for human primary brown adipocytes. Sci. Rep. 8 (1), 5304. https://doi.org/10.1038/s41598-018-23700-z.

Wu, J., Cohen, P., Spiegelman, B.M., 2013. Adaptive thermogenesis in adipocytes: is beige the new brown? Genes Dev. 27 (3), 234–250. https://doi.org/10.1101/gad.211649.112.

Yadav, H., Quijano, C., Kamaraju, A.K., Gavrilova, O., Malek, R., Chen, W., Zerfas, P., Zhigang, D., Wright, E.C., Stuelten, C., Sun, P., 2011. Protection from obesity and diabetes by blockade of TGF-β/Smad3 signaling. Cell Metab. 14 (1), 67–79 doi.org/10.1016/j.cmet.2011.04.013.

Yamanishi, K., Maeda, S., Kuwahara-Otani, S., Hashimoto, T., Ikubo, K., Mukai, K., Nakasho, K., Gamachi, N., El-Darawish, Y., Li, W., Okuzaki, D., Watanabe, Y., Yamanishi, H., Okamura, H., Matsunaga, H., 2018. Deficiency in interleukin-18 promotes differentiation of brown adipose tissue resulting in fat accumulation despite dyslipidemia. J. Transl. Med. 16 (1), 314. https://doi.org/10.1186/s12967-018-1684-3.

Yeo, C.R., Agrawal, M., Hoon, S., Shabbir, A., Shrivastava, M.K., Huang, S., Khoo, C.M., Chhay, V., Yassin, M.S., Tai, E.S., Vidal-Puig, A., Toh, S.A., 2017. SGBS cells as a model of human adipocyte browning: a comprehensive comparative study with primary human white subcutaneous adipocytes. Sci. Rep. 7 (1), 4031. https://doi.org/10.1038/s41598-017-04369-2.

Yoneshiro, T., Wang, Q., Tajima, K., Matsushita, M., Maki, H., Igarashi, K., Dai, Z., White, P.J., McGarrah, R.W., Ilkayeva, O.R., Deleye, Y., Oguri, Y., Kuroda, M., Ikeda, K., Li, H., Ueno, A., Ohishi, M., Ishikawa, T., Kim, K., Chen, Y., Sponton, C.H., Pradhan, R.N., Majd, H., Greiner, V.J., Yoneshiro, M., Brown, Z., Chondronikola, M., Takahashi, H., Goto, T., Kawada, T., Sidossis, L., Szoka, F.C., McManus, M.T., Saito, M., Soga, T., Kajimura, S., 2019. BCAA catabolism in brown fat controls energy homeostasis through SLC25A44. Nature 572 (7771), 614–619. https://doi.org/10.1038/s41586-019-1503-x.

frontiers | Frontiers in Endocrinology

TYPE Original Research
PUBLISHED 01 March 2023
DOI 10.3389/fendo.2023.1141303

OPEN ACCESS

EDITED BY
Endre Károly Kristóf,
University of Debrecen, Hungary

REVIEWED BY
Stefania Carobbio,
Principe Felipe Research Center (CIPF), Spain
Rosalba Senese,
University of Campania Luigi Vanvitelli, Italy

*CORRESPONDENCE
Monica Colitti
monica.colitti@uniud.it

SPECIALTY SECTION
This article was submitted to Cellular Endocrinology, a section of the journal Frontiers in Endocrinology

RECEIVED 10 January 2023
ACCEPTED 17 February 2023
PUBLISHED 01 March 2023

CITATION
Ali U, Wabitsch M, Tews D and Colitti M (2023) Effects of allicin on human Simpson-Golabi-Behmel syndrome cells in mediating browning phenotype. *Front. Endocrinol.* 14:1141303. doi: 10.3389/fendo.2023.1141303

Effects of allicin on human Simpson-Golabi-Behmel syndrome cells in mediating browning phenotype

Uzair Ali[1], Martin Wabitsch[2], Daniel Tews[2] and Monica Colitti[1]*

[1]Department of Agricultural, Food, Environmental and Animal Sciences, University of Udine, Udine, Italy, [2]Division of Pediatric Endocrinology and Diabetes, Department of Pediatrics and Adolescent Medicine, Ulm University Medical Center, Ulm, Germany

Introduction: Obesity is a major health problem because it is associated with increased risk of cardiovascular disease, diabetes, hypertension, and some cancers. Strategies to prevent or reduce obesity focus mainly on the possible effects of natural compounds that can induce a phenotype of browning adipocytes capable of releasing energy in the form of heat. Allicin, a bioactive component of garlic with numerous pharmacological functions, is known to stimulate energy metabolism.

Methods: In the present study, the effects of allicin on human Simpson-Golabi-Behmel Syndrome (SGBS) cells were investigated by quantifying the dynamics of lipid droplets (LDs) and mitochondria, as well as transcriptomic changes after six days of differentiation.

Results: Allicin significantly promoted the reduction in the surface area and size of LDs, leading to the formation of multilocular adipocytes, which was confirmed by the upregulation of genes related to lipolysis. The increase in the number and decrease in the mean aspect ratio of mitochondria in allicin-treated cells indicate a shift in mitochondrial dynamics toward fission. The structural results are confirmed by transcriptomic analysis showing a significant arrangement of gene expression associated with beige adipocytes, in particular increased expression of T-box transcription factor 1 (TBX1), uncoupling protein 1 (UCP1), PPARG coactivator 1 alpha (PPARGC1A), peroxisome proliferator-activated receptor alpha (PPARA), and OXPHOS-related genes. The most promising targets are nuclear genes such as retinoid X receptor alpha (RXRA), retinoid X receptor gamma (RXRG), nuclear receptor subfamily 1 group H member 3 (NR1H3), nuclear receptor subfamily 1 group H member 4 (NR1H4), PPARA, and oestrogen receptor 1 (ESR1).

Discussion: Transcriptomic data and the network pharmacology-based approach revealed that genes and potential targets of allicin are involved in ligand-activated transcription factor activity, intracellular receptor signalling, regulation of cold-induced thermogenesis, and positive regulation of lipid metabolism. The present study highlights the potential role of allicin in triggering browning in human SGBS cells by affecting the LD dynamics, mitochondrial morphology, and expression of brown marker genes. Understanding the potential targets through which allicin promotes this effect may reveal the underlying signalling pathways and support these findings.

KEYWORDS

SGBS cells, allicin, lipid droplets, mitochondria, thermogenesis

Introduction

Obesity is a complex multifactorial disease that presents a risk of death as it is associated with many noncommunicable diseases such as cardiovascular diseases, type 2 diabetes, and cancer. Since the discovery of brown adipose tissue (BAT) in the adult human body and its ability to dissipate energy, it has been of particular interest to exploit the activity of BAT as a therapeutic option to counteract obesity. In addition, the formation of thermogenic or beige adipocytes in white adipose tissue (e.g., adipocyte browning) may represent another option to increase energy expenditure (1). In both brown and beige adipocytes oxidative phosphorylation is uncoupled from ATP production, which is due to up-regulation of uncoupling protein-1 (UCP1) (2). To date, *in vitro* and *in vivo* studies have identified a considerable number of browning agents, such as capsaicin, resveratrol, caffeine, and fucoxanthin (3, 4). Garlic (*Allium sativum* L.) is a popular species rich in organosulfur compounds that are useful for medicinal purposes. When garlic is chopped or crushed, alliin is released and then hydrolyzed into allicin by allicinase. Allicin *in vitro* breaks down into a variety of fat-soluble organosulfur compounds, including diallyl trisulfide (DATS), diallyl disulfide (DADS), and diallyl sulfide (DAS) (5–7). The high permeability of allicin through cell membranes and rapid reaction with free thiol groups promote its diverse biological and therapeutic functions (8). Allicin is known for its antibacterial, antifungal, and antiparasitic activities (9), as well as its anticarcinogenic (10, 11) and anti-inflammatory functions (12, 13). Allicin has also been shown to suppress cholesterol biosynthesis by inhibiting squalene monooxygenase and acetyl-CoA synthetase (14). Methanolic extract of black garlic containing alliin, upregulated the expression of genes related to adipokines, lipolysis, and fatty acid oxidation in adipose tissue of rats fed a high-fat diet (15).

Recently, allicin was reported to promote browning in differentiated 3T3-L1 adipocytes and white inguinal adipose tissue of mice through extracellular signal regulated kinase 1/2 (ERK1/2) and KLF Transcription Factor 15 (KLF15) pathways, which stimulates the expression of UCP1 through interaction with its promoter (16). It has also been suggested that the Sirt1-PGC1α-Tfam pathway plays a role in promoting allicin-mediated BAT activity (17).

Although several mouse cell lines are available to understand the adipogenic and thermogenic regulatory networks *in vitro*, human cell lines are of interest to explore the molecular mechanism of browning and to identify potential dietary supplements and nutraceuticals that could induce browning. The Simpson-Golabi-Behmel Syndrome (SGBS) cell strain is commonly used as a model for the differentiation of human white adipocytes (18). These cells retain their differentiation ability up to several generations when provided with the appropriate adipogenic differentiation medium. Based on the effect of rosiglitazone (19), a browning phenotype was observed in SGBS cells during differentiation, and RNA sequencing revealed an increase in genes involved in extracellular matrix organization and oxidative stress that may regulate adaptive thermogenesis, with an increased percentage of brown phenotype, confirming that differentiated SGBS cells gradually acquire BAT-like function from day 4 to day 10 (20).

After stimulation of browning, the formation of micro lipid droplets (LDs) has been demonstrated in response to lipolytic release of fatty acids (21). This enables efficient intracellular lipolysis from the LD surface and subsequent promotion of free fatty acid transport to mitochondria for β-oxidation in BAT (22). Consistent with this property, both cold exposure and adrenergic stimulation induce rapid mitochondrial fragmentation, which synergistically promote uncoupling and thus heat production (23).

Using RNAseq and quantifying the dynamics of LDs and mitochondrial morphology, the current study aims to evaluate the browning effect of allicin *in vitro* using the SGBS cell strain as a human primary adipocyte model in comparison to the control and cells treated with dibutyryl cAMP sodium salt (cAMP) as a positive control. To clarify the potential browning effect of allicin, a network pharmacology strategy was also performed based on the identification of potential targets.

Materials and methods

Chemicals and culture media

Dulbecco's modified Eagle medium (DMEM)/F-12 medium (1:1) enriched with L-glutamine and 15 mM 4-(2-hydroxyethyl)-1-piperazineethanesulfonic acid (HEPES), fetal bovine serum (FBS) and penicillin streptomycin solution were purchased from Gibco by Life Technologies (Thermo Fisher Scientific Inc., Waltham, Massachusetts). TRIzol reagent, PureLink™ RNA Mini Kit and SuperScript™ III one-step RT-PCR system with Platinum™ *Taq* DNA polymerase were purchased from Invitrogen (Thermo Fisher Scientific Inc., Waltham, Massachusetts). Rosiglitazone was purchased from Cayman Chemical (Ann Arbor, Michigan). Allicin was purchased from Solarbio Life Sciences® (Beijing, China).

All other chemicals used in the experiment and not listed above were purchased from Sigma-Aldrich (Darmstadt, Germany).

Cell culture and treatments

Human SGBS cells were grown Dulbecco's Modified Eagle Medium Nutrient Mixture F-12 (DMEM/F-12) supplemented with 10% fetal bovine serum (FBS), 3.3 mM biotin, 1.7 mM panthotenate and 1% penicillin/streptomycin solution, at 37°C, 5% CO_2 and 95% relative humidity. Cells were platted in Petri dishes (100mm) in duplicate. Once the cells reached approximately 90% confluence, differentiation was induced by feeding the cells with serum-free growth medium supplemented with 10 µg/ml transferrin, 0.2 nM triiodothyronine (T_3), 250 nM hydroxycortisone, 20 nM human insulin, 25 nM dexamethasone, 250 µM 3-isobutyl-1-methylxanthine (IBMX) and 2 µM rosiglitazone (day 0 of differentiation). After 4 days, the

differentiation medium was replaced with maintenance medium composed by serum-free growth medium supplemented with 10 µg/ml transferrin, 0.2 nM T_3, 250 nM hydroxycortisone and 20 nM human insulin. Fresh maintenance medium was added every 2 days.

Treatment with allicin began on day 0 of differentiation (D0), and continued until analysis on day six (D06) of differentiation (Figure 1). Allicin concentrations of 5, 12.5, 25, and 50 µM were tested. Prior to treatment, allicin was diluted in dimethyl sulfoxide (DMSO) and a stock solution was prepared. Stock solutions were prepared so that the volume of DMSO in the treatment medium did not exceed 0.5%. Control cells (CTRL) were incubated with the same volume of 0.5% DMSO in the differentiation medium for 6 days. As a positive control (cAMP), SGBS cells were treated with 500 µM dibutyryl cAMP sodium salt (a cyclic nucleotide derivative that mimics endogenous cAMP) for 24 hours before the sixth day of differentiation (24) (Figure 1).

Cell viability assay

Cell viability was determined using the 3-(4,5-dimethylthiazol-2-yl)-2,5-diphenyltetrazolium bromide (MTT) assay. Cells were plated in a 96-well plate and treated with 5.0, 12.5, 25.0, and 50 µM allicin (25). Before incubation with 5 mg/mL MTT in HBSS, cells were rinsed with 1X phosphate buffer saline (PBS) 1X. Incubation with the MTT solution was performed at 37°C for 4 hours. The resulting formazan was dissolved in dimethyl sulfoxide (DMSO) and incubated overnight (O/N) at 37°C. Optical density was used as an indicator of cell viability and was measured at 590 nm.

BODIPY staining and confocal imaging

Cells for BODIPY™ staining and subsequent confocal imaging were cultured on ibiTreat 8-well µ-slides (Ibidi GmbH, Planegg/Martinsried, Germany). Cells were fixed in a 2% formalin solution diluted in PBS 1X at room temperature (RT) for 15 minutes. Subsequently, after washing three times in PBS 1X, the cells were incubated in a solution of BODIPY™ 493/503 in PBS 1X to fluorescently label the lipid droplets. Incubation was performed for 45 minutes in the dark at RT. The slides were then washed three times in PBS 1X.

Fluorescence images were acquired using a Leica SP8 confocal microscope (Leica Microsystems Srl, Milan, Italy) and LAS X 3.1.5.16308 software. Slides were viewed with the HCX PL APO lambda blue 63x/1.40 OIL objective. DAPI fluorescence was detected with a 405 diode laser (410/480 nm), while BODIPY fluorescence was detected with a white light laser (503/588 nm). Images were acquired using a photomultiplier tube (PMT) that allowed point scanning of the region of interest (ROI) with the selected laser and produced 1024 × 1024 px images.

Morphology of LDs

The MRI_Lipid Droplets Tool (http://dev.mri.cnrs.fr/projects/imagej-macros/wiki/LipidDroplets_Tool), a macro in the ImageJ 1.50b software (http://rsb.info.nih.gov/ij/), was used to measure LD area (26). Individual cells were defined by regions of interest (ROIs) and images were analyzed as previously described (27). For each cell, the LD area (in μm^2), maximum Feret diameter (MFD, in µm), and integrated optical density (IOD, dimensionless) were measured. The MDF is used as a measure of the diameter of irregularly shaped objects, whereas the IOD is related to both triglyceride accumulation and the size of LDs (28).

MitoTracker® staining

SGBS cells cultured on ibiTreat 8-well µ-slides (Ibidi GmbH, Germany) were incubated at 37°C with 100 nM MitoTracker® Orange CMTMRos (Thermo Fisher Scientific, USA) for 30 minutes. The stained cells were washed with PBS 1X and fixed with 2% formalin at RT for 15 minutes. After fixation, cells were rinsed three times with PBS 1X, mounted in DAPI-containing mounting medium (Cayman Chemical Company, USA), and imaged using a Leica SP8 confocal microscope (Leica Microsystems, Germany) and LAS X 3.1.5.16308 software. Slides were viewed with the HCX PL APO lambda blue 63x/1.40 OIL objective. DAPI fluorescence was detected with a 405 diode laser (410/480 nm), while MitoTracker® fluorescence was detected with a white light laser (550/605 nm). Images were acquired using a photomultiplier tube (PMT) that allowed point-by-point scanning of the region of interest (ROI) with the selected laser and produced images with a resolution of 1024 x 1024 px.

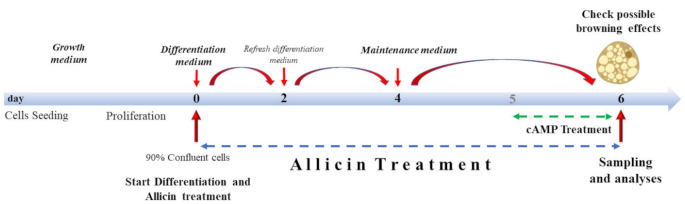

FIGURE 1
Cell culture treatment protocol. Cells were grown to 90% confluence. Differentiation lasted 6 days supplemented with allicin treatment. From day 4, cells were incubated with allicin in maintenance medium. Cells were incubated with cAMP for 24 hours (from day 5 to day 6 of differentiation). Sampling and analyses were performed on day 6.

Mitochondrial morphology analyses

To quantify mitochondrial morphology on standard confocal fluorescence microscopy images of CTRL, ALLI, and cAMP-treated cells, the Mitochondrial Analyzer based on adaptive thresholding and the ImageJ/Fiji open-source image analysis platform were used (29). Scale was set for magnification and the global check box in the Set Scale dialog box was selected. After 2D threshold optimization, the images were thresholded with a block size of 1,350µm and a C-value of 5. Subsequently, the images were also processed using the MiNa (30) and Micro2P (31) tools.

The Mitochondria Analyzer tool was used to measure counts (number of mitochondria in the image), total area (sum of the area of all mitochondria in the image), mean area (total area/mitochondria number), total perimeter (sum of perimeter of all mitochondria in the image), mean perimeter (total perimeter/mitochondria number), mean aspect ratio (shape descriptor measuring elongation), and mean form factor (shape descriptor measuring round to filamentous shape). In addition, parameters describing the connectivity of the mitochondrial network were calculated, including the number of branches, the total length of branches, the mean length of branches, the branch junctions, the end points of branches, and the mean diameter of branches. The branches consist of point-shaped objects without branching junctions and minimal length, long single tubular objects without branching junctions, but the highest branch length and complex objects with multiple branches and junctions. The number of branches, total branch length, branch junctions and branch end points were also expressed as normalization to either the number of mitochondria or total area (29).

The MiNa tool, a macro of the ImageJ1.53o software (http://rsb.info.nih.gov/ij/), was also used to quantify mitochondrial morphology (30). Threshold images were processed using the Tophat option (32), as was the MiNa interface. The macro detected 'individual' mitochondrial structures in a skeletonized image, such as punctate, rod-shaped, and large/round structures without branching, and 'networks' identified as mitochondrial structures with a single node and three branches. All parameters were used in the discriminant analysis. Among the nine parameters calculated by MiNa, the number of individuals (punctate, rod-shaped, and large/round mitochondria), the number of networks (objects with at least one branch), and the mean rod/branch length, which refers to the average length of all mitochondrial rods/branches, were considered for statistical comparisons. Other parameters such as the mean number of branches per network, i.e., the mean number of mitochondrial branches per network, the mean length of branches, and the mitochondrial footprint, which refers to the total area of mitochondria, were included in the discriminant analysis.

Mitochondria were also analyzed and classified using MicroP software, a useful tool validated in CHO-K1 cells (31). The software classifies six morphological types of mitochondria, such as small globules, round-shaped mitochondria, that may have arisen by fission; large globules with a larger area; simple tubules, i.e. straight, elongated mitochondria without branches; twisted tubules, elongated tubular mitochondria with a non-linear development; donuts, like elongated tubules mitochondria but with fused ends; branched tubules, complex interconnected mitochondria with a network-like structure. On each image, the total number of mitochondria and their area were calculated as the ratio of mitochondria and area for each subtype in the different SGBS cells treated. These data with the number of objects and total area were used for discriminant analysis.

RNA extraction and sequencing

The experiment was set up with 2 biological replicates for the 3 experimental conditions.

After removing the culture medium from the Petri dishes, 1ml/10cm^2 of TRIzol reagent was added to each plate and repeatedly pipetted to induce a severe breakdown of the cell structures. These samples were immediately processed further using the PureLink™ RNA Mini Kit according to the manufacturer's instructions.

The concentration of extracted total RNA was quantified using a spectrophotometer (NanoDrop 1000 Spectrophotometer, ThermoScientific, Wilmington, Delaware), and the purity of the RNA samples ranged from 1.8 to 1.9. RNA integrity was assessed by observing the 18S and 28S ribosomal bands after electrophoresis on 1% agarose gel, in the presence of GelRed. β-actin expression was used as an internal control, and confirmed the complete integrity of the RNA.

The purified total RNA was subjected to deep sequencing analysis. First, the isolated RNA was quantified using Agilent Bioanalyzer 2100 with the RNA integrity number (RIN) greater than 8.0 before sequencing using Illumina Genome Analyzer (GA). Generally, 2-4 ug of the total RNA was used for library construction. Total RNA was reverse transcribed into double-stranded cDNA, digested with NlaIII and ligated to an Illumina specific adapter containing a recognition site of MmeI. After MmeI digestion, a second Illumina adapter, containing a 2-bp degenerate 3' overhang was ligated. The obtained sequences were aligned on GRCh38 human genome (https://www.ncbi.nlm.nih.gov/assembly/GCF_000001405.39) using STAR software (33).

Data processing

Raw data were uploaded to the R package (v0.92) Differential Expression and Pathway analysis (iDEP951) that is a web-based tool available at http://bioinformatics.sdstate.edu/idep/(34, 35). In the pre-processing step, genes expressed at very low levels across samples were filtered out, and genes expressed at a minimum of 0.5 counts per million (CPM) in a library were further analyzed. To reduce variability and normalizecount data, EdgeR log2(CPM+c) was chosen with pseudocount c = 4 transformation,. Next, the DESeq2 package in the R language was used to identify differentially expressed genes (DEG) between ALLI_ cAMP, ALLI_CTRL and cAMP_CTRL using a of false discovery rate (FDR) threshold ≤ 0.05 and fold-change > |1.0|. Heatmaps, principal component analysis

(PCA), k-means cluster and enrichment analyses were also performed in iDEP951.

Gene set enrichment analysis to determine the shared biological functions of differentially regulated genes based on significant GO terms (36), Kyoto Encyclopedia of Genes and Genomes (KEGG) pathway (37) and TF. target.TRED analyses were performed (38).

Venn diagrams were created by web tool available at http://bioinformatics.psb.ugent.be/webtools/Venn/.

Protein-protein interaction Network construction and hub genes analysis

On the basis of the online tool Search Tool for the Retrieval of Interacting Genes (STRING; https://string-db.org/), PPI networks of the up regulated and the down regulated DEGs in each comparison were generated with a confidence level of ≥ 0.4, and the PPI network was visualized using Cytoscape software (version 3.9.1, https://cytoscape.org/). Then, the PPI networks of DEGs in each comparison were analyzed using the Cytoscape CytoHubba plugin to select the top 10 hub nodes according to the Degree algorithm (39). The Molecular Complex Detection (MCODE) plug-in (40) in the Cytoscape suite was used to examine the significant modules in the PPI network of overlapping DEGs that are the target ofshared TF networks between comparisons. Degree cutoff = 2, K-core = 2, and node score cutoff = 0.2 were set as options. Enrichment analysis of DEGs in modules with a score ≥ 5 was then performed.

PROFAT webtool analysis

Estimation of the proportion of brown adipocytes in each sample was analyzed based on read counts using the PROFAT tool, which automatically performs hierarchical cluster analysis to predict the browning capacity of mouse and human RNA-seq datasets (41).

Targets prediction of allicin, DAS, DADS, DATS

To identify a larger number of potential targets, PharmMapper (http://www.lilab-ecust.cn/pharmmapper/; 42, 43), the similarity ensemble approach (SEA, https://sea.bkslab.org/), the STITCH database (http://stitch.embl.de/; 44), Swiss Target Prediction (http://www.swisstargetprediction.ch/; 45), and GeneCard (https://www.genecards.org/) were used. The 2D structure and canonical SMILES of allicin (CID_65036), diallyl sulphide (CID_11617), diallyl disulfide (CID_16590), and diallyl trisulfide (CID_16315) were obtained from the PubChem database (https://pubchem.ncbi.nlm.nih.gov/). The sdf files were uploaded to the PharmMapper server, and the search was started using the maximum generated conformations of 300 by selecting the option 'Human Protein Targets Only (v2010, 2241)' and the default value of 300 for the number of reserved matching targets. for the other parameters, the 'default mode' was selected. Canonical SMILES were uploaded to the other tools. The predicted targets were entered into the UniProt database (https://www.uniprot.org/) with the species set to *Homo sapiens* to determine their gene IDs. A Venn diagram was used to find common targets among the allicin compounds. Genes related to 'adipocyte', 'browning', 'non shivering thermogenesis', 'cold-induced thermogenesis', 'brown adipose thermogenesis,' and 'adaptive thermogenesis' were downloaded from GeneCard, and the intersection of the targets was determined using the Venn tool. The resulting common genes associated with browning and adipocytes were then crossed with common putative targets of allicin, and a Venn diagram was generated. Subsequently, the overlapping targets were uploaded to GeneMANIA (https://genemania.org/) (46) to perform functional gene analysis and generate a PPI network.

CytoNCA, another Cytoscape plugin, was applied to the network to perform topological analysis evaluating the centrality measures of the network (47). Then, the Cytoscape intersectional merge function was used to isolate the PPI subnetworks. Key node functions were determined by analyzing GO terms, KEGG and Reactome pathways.

By entering the screened key nodes into the online tool VarElect (48), the correlation between nodes and 'cold induced thermogenesis' was investigated.

Statistical analysis

All measurement results are given as means ± SD and were analyzed with XLSTAT (49). Measurements of LD area surface/cell, MFD/cell, and IOD/cell obtained from 15 biological replicates were compared along with Mitochondrial Analyzer, MiNa, and Micro2P results using the Kruskal-Wallis statistical test, followed by pairwise comparisons using the Mann-Whitney approach with Bonferroni correction ($p < 0.0167$).

All Mitochondrial Analyzer and MiNa parameters, as well as ratios of parameters obtained with the Micro2P tool, were calculated together to perform a canonical discriminant analysis (DA) that integrates morphological mitochondrial parameters into a single multivariate model with the aim of maximizing differences between treatments and calculating the best discriminant components between treatments (49).

Results

Cell viability

To investigate possible adverse effects of allicin, a viability assay was used to investigate possible adverse effects of ALLI extract on SGBS cells treated with doses of 5, 12.5, 25, and 50 µM. In particular, the analysis showed that the viability of cells treated with ALLI extract decreased significantly ($p < 0.001$) in a dose-dependent manner (Figure S1), with the 50 µM dose always significantly different from the other doses. Nevertheless, viability remained above 85% up to 25 µM and 12.5 µM ALLI and did not

10.3389/fendo.2023.1141303

differ from 5 and 25 μM. Based on these findings, 12.5 μM ALLI was selected for further experiments.

Allicin treatment affects the number of lipid droplets and their maximum diameter

Next, We investigated whether allicin has an effect on early adipogenic differentiation. Thus, we performed LD analysis in SGBS cells after ALLI treatment during the induction of adipogenesis. Figure 1 shows statistically significant differences in area of LDs/cell, MFD/cell, and IOD/cell between treatments and illustrates Bodipy staining in SGBS cells after 6 days of treatment with allicin (ALLI), CTRL, and dibutyryl cAMP (cAMP). The area of LDs/cell was significantly lower in cells treated with cAMP and ALLI compared with cells from CTRL ($p < 0.0001$). No significant differences were observed between cAMP- and ALLI-treated cells (Figure 2A). A significant ($p < 0.0001$) decrease in MDF/cell was observed in cells treated with cAMP and ALLI compared with CTRL ($p < 0.0001$) (Figure 2B), while IOD/cell was significantly lower in cells treated with cAMP compared with cells treated with ALLI ($p = 0.016$) and CTRL ($p = 0.0001$) (Figure 2C). A significant increase in the number of LDs/cell ($p = 0.015$) was observed between ALLI treated cells and CTRL cells (Figure 2D).

Allicin increases the number and area of small round mitochondria

Accurate analysis of mitochondria is critical for determining mitochondrial dynamics, so three different tools were used to characterize mitochondrial morphology. Figure S2 shows the identification and classification of objects using adaptive thresholding (radius = 1.350 μm, C = 5) on images of ALLI- and cAMP-treated cells and CTRL. Figures S2A, B show the effects of the different treatments measured with the three tools, on the total number and area of mitochondria in SGBS cells. No statistical differences in mitochondrial distribution patterns were detected between treatments, although treatments with allicin and cAMP caused a shift toward a greater number of mitochondria (Figure S2A) and a greater total area of mitochondria compared with cells from CTRL (Figure S2B). These results suggest that ALLI treatment increases the number of mitochondria by inducing mitochondrial fission or biogenesis and thus also increases the total area of mitochondria.

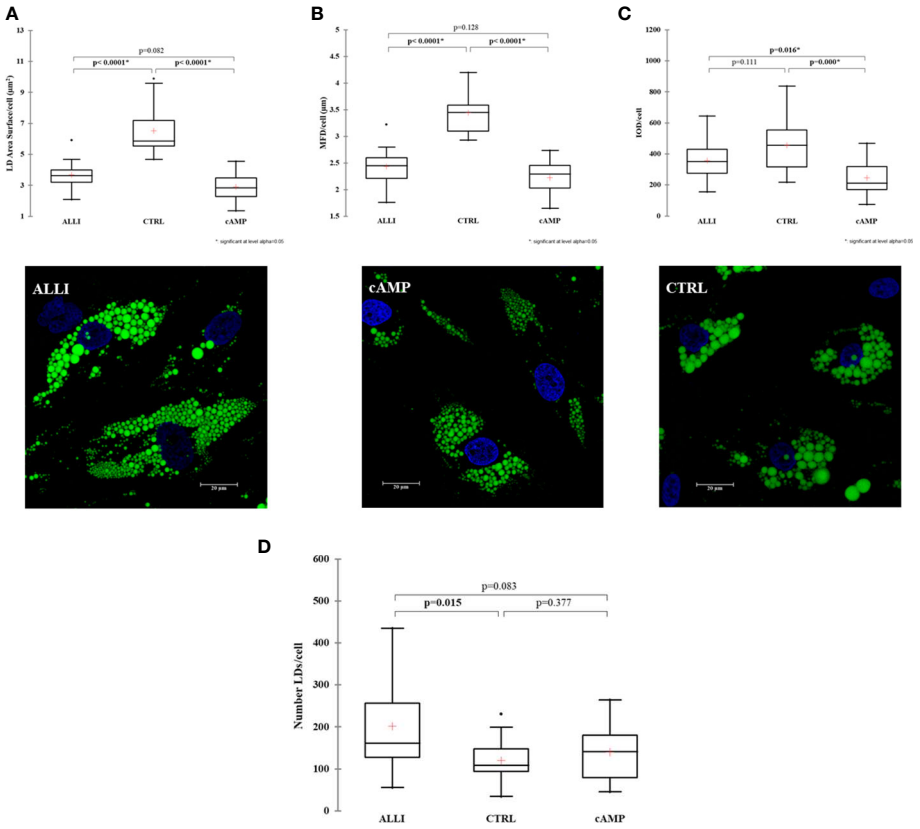

FIGURE 2
Results of lipid droplet analysis performed on SGBS cells. Boxplots show the median (horizontal lines), the first to third quartiles (box), and the most extreme values with the interquartile range (vertical lines). For all comparisons, differences between treatments on SGBS cells were statistically significant using the Kruskal-Wallis test and Bonferroni correction. **(A)** LD area per cell; **(B)** Maximum Feret Diameter (MFD) per cell; **(C)** Optical Density Intensity (IOD) per cell; **(D)** number of lipid droplets per cell in treated and CTRL cells.Representative confocal images of SGBS cells treated with allicin (ALLI), dibutyryl cAMP (cAMP), or control (CTRL) 6 days after differentiation and stained with BODIPY. Nuclear staining, DAPI. Images are representative of n. 15 biological replicates. ALLI, 12.5 μg/mL allicin-treated cells; CTRL, control cells; cAMP, 500 μM dibutyryl cAMP-treated cells.

10.3389/fendo.2023.1141303

Therefore, more than 26000 mitochondria were analysed using Micro2P software to classify six morphological subtypes and calculate the average proportion of mitochondrial subtypes within each treatment (Figure 3A, B). ALLI and cAMP treatments resulted in 13.6% ($p < 0.01$) and 11.5% ($p < 0.05$) more small globules, respectively, compared with CTRL. ALLI treatment reduced the percentage of mitochondria with large globules to 32.5% and that of the simple tube subtype to 19.5% compared with CTRL ($p < 0.01$) (Figure 3A). Accordingly, the ratio of surface area was significantly higher ($p < 0.05$) in ALLI- and cAMP-treated cells compared with CTRL at 30.3 and 31.7%, respectively, whereas the area of large globules in ALLI-treated cells decreased significantly ($p < 0.05$) (Figure 3B).

Specifically, the average ratio of mitochondrial amount in the different treatments was 53.4% in ALLI-treated cells, 28.6% in cAMP-treated cells, and 18.02% in CTRL. The relative percent area of total mitochondrial content between treatments was 51.9% in ALLI-treated cells, 27.8% in cAMP-treated cells, and 20.3% in cells from CTRL. Considering all treatments together, small globules (65.7%) and simple tubules (23.3%) were the most representative subtypes, followed by branched tubules (5.42%), large globules (2.3%), donuts (1.7%), and twisting tubules (1.6%). Accordingly, the percentage area of mitochondrial subtypes was 34.9% for small globules, 33.9.8% for simple tubules, 16.67% in branching tubules, 7.4% for donuts, 3.6% for large globules, and 3.5% for twisting tubules.

Mitochondrial Analyzer detected significantly higher numbers of mitochondria in ALLI-treated cells (Figure 3C), whereas the mean perimeter and area (Figure 3D) were significantly lower compared with cells from CTRL. No statistical differences were observed in the cells treated with cAMP. The shape of mitochondria, characterized by aspect ratio and form factor, decreased significantly under ALLI and cAMP compared with cells from CTRL (Figures 3E, F). Mitochondria Analyser tool was also used to quantify the morphological complexity of mitochondria. The mean length of branches and the total number of branches per mitochondrion were lowest in cells treated with ALLI and showed a significant difference in cells treated with cAMP (data not shown).

Network parameters calculated with MiNa confirmed a significant ($p < 0.05$) increase in the number of individuals (puncta, rods and large) in ALLI-treated cells compared with CTRL cells (Figure 4A). The number of networks showed no significant differences between treatments (Figure 4B), but the mean value of rod/branch length significantly decreased in cells treated with ALLI ($p < 0.05$) and cAMP ($p < 0.05$) (Figure 4C).

Mitochondrial analysis results classify treatments into non-overlapping groups

To determine the extent of treatment-specific variation in an unbiased manner, all Mitochondrial Analyzer measurements, six MiNa measurements from, and the percentage of the number and area of each mitochondrial subtype, number of objects, and total area calculated by Micro2P were integrated into a single

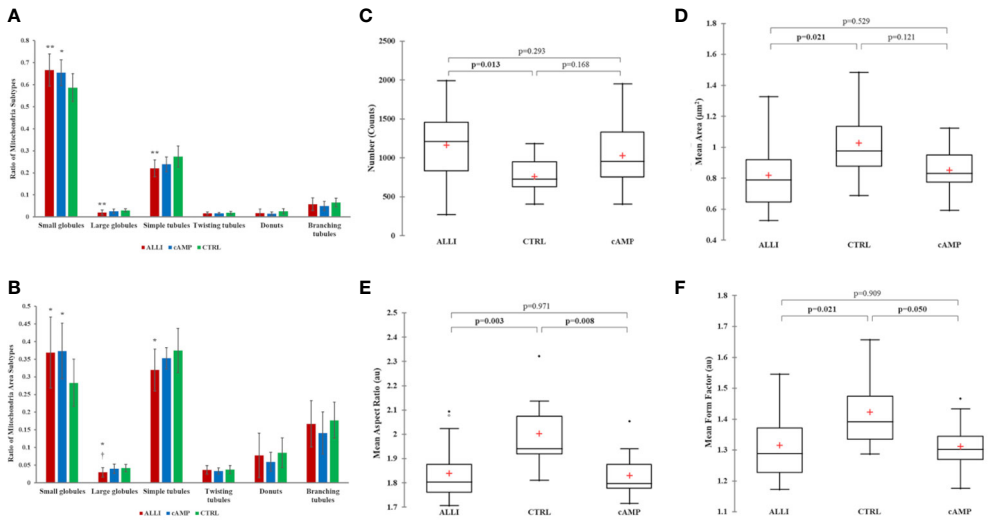

FIGURE 3
Mitochondrial analyses. Differences in the distribution of mitochondrial morphological characteristics were analysed between cells incubated with ALLI and cAMP compared with cells from CTRL. **(A)** Average ratio of mitochondrial subtypes within each treatment. The Kruskal-Wallis test was performed between ALLI-treated cells compared with CTRL (**$p < 0.01$) and cAMP-treated cells compared with CTRL (*$p < 0.05$). Differences between ALLI-treated cells and cAMP were also detected († $p < 0.05$). **(B)** The ratio of the surface area was significantly higher in ALLI- and cAMP-treated cells compared with CTRL by 30.3 and 31.7%, respectively ($p < 0.05$). The average ratio surface area of large globules showed a significant (* † $p < 0.05$) decrease in ALLI-treated cells by 24.9 and 28.6% compared with cAMP-treated and CTRL cells, respectively. Mitochondria features determined using the Mitochondria Analyser tool. **(C)** Number of mitochondria. **(D)** Mitochondrial size measured by mean area. **(E, F)** Mitochondrial shape measured by mean aspect ratio and mean form factor. Boxplots showed the difference between medians (horizontal lines), first to third quartiles (box), and the most extreme values within the interquartile range (vertical lines) between treatments. Statistical significance in the boxplots was determined by the Kruskal-Wallis statistical test with Bonferroni correction ($p < 0.0167$). ALLI, 12.5 µg/mL allicin-treated cells; CTRL, control cells; cAMP, 500 µM dibutyryl cAMP-treated cells.

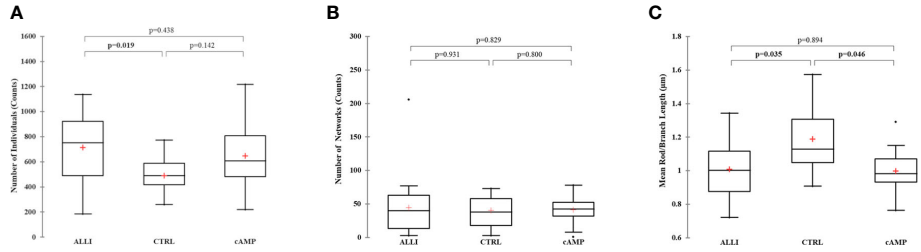

FIGURE 4
Summary statistics of mitochondrial network analysis performed with the MiNa tool on SGBS cells for each treatment. **(A)** Number of individual mitochondria. **(B)** Number of networks. **(C)** Mean value of rod/branch length. Boxplots show the median (horizontal lines), first through third quartiles (box), and the most extreme values with the interquartile range (vertical lines). The number of individual counts was statistically different in ALLI-treated SGBS cells from CTRL cells, using the Kruskal-Wallis test and Bonferroni correction ($p < 0.0167$). The number of networks showed no statistical difference. The mean length of rod/branch mitochondria significantly decreased in ALLI- ($p = 0.035$) and cAMP-treated cells ($p < 0.046$) compared with CTRL. ALLI, 12.5 µg/mL allicin-treated cells; CTRL, control cells; cAMP, 500 µM dibutyryl cAMP-treated cells.

multivariate model (DA) that maximized differences between treatments (Figure 5).

The model achieved clear separation of samples. With few exceptions, the treatments were grouped and divided into 3 clusters. Mitochondrial values of ALLI-treated cells were projected in the quadrant with a positive value for the F1 and F2 components, CTRL was projected in the quadrant with a negative value for F1 and a positive value for the F2 component. The projection of cAMP-treated cells was observed in the quadrant with negative value for F1 and positive value for F2. The significant morphological characteristics that distinguished the different experimental groups are shown in Table 1. This analysis showed that most of the variance between treatments in mitochondrial dynamics was based on elongation index, area of small globes, solidity of simple tubes, number of punctate and rod-shaped mitochondria (individuals), and number of simple tubes (Table 1). Discriminant functions were used to classify the treatments into the correct groups. To check the functionality and robustness of the classification model, a cross-validation test was performed, in which the success rate of correctly classified samples was 88.6%.

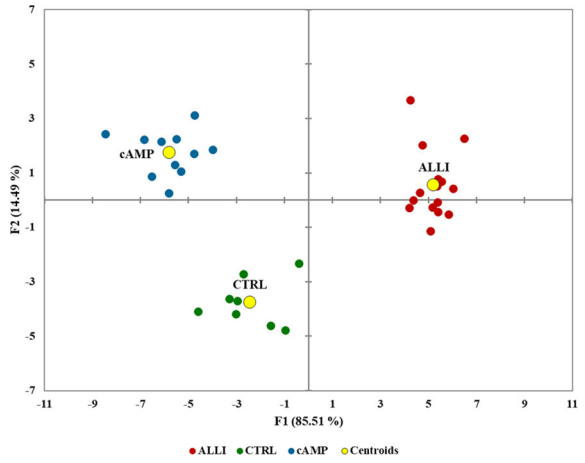

FIGURE 5
Biplot of canonical discriminant analysis to visualize the information of the whole mitochondrial dataset in the treatments and controls. F1 and F2 are canonical discriminant functions, and the two-component model separated the treatments. Centroids are shown as yellow circles. ALLI, 12.5 µg/mL allicin-treated cells; CTRL, control cells; cAMP, 500 µM dibutyryl cAMP-treated cells.

RNAseq analysis

After removal of low abundance reads, the final mapping rate of the filtered transcript reads was 71.2%. Hierarchical clustering was performed on the initial analysis of the RNAseq results, that showed that the transcriptomic data was well-clustered according to the treatment. In addition, PCA showed the overall variability in the expression profile of the samples and treatments. Overall, there was a significant difference between CTRL and the treatments with cAMP and ALLI along the first principal component, which explained 61% of the variance, with smaller differences 28% along the second component (Figure S3).

Analysis of DEGs was performed between cells treated with allicin and cAMP compared to control cells and between allicin and cAMP treatments, based on a $\log_2$fold change of $|1|$ and an FDR adjusted p value of ≤ 0.05.

iDEP951 expression analysis significantly identified ($p < 0.05$) 820 up regulated genes between cells treated with ALLI *vs* cAMP, 1417 up regulated genes between cells treated with ALLI *vs* CTRL and 1647 between cells treated with cAMP *vs* CTRL cells. Significantly down regulated ($p < 0.05$) genes were 640 between cells treated with ALLI compared with cAMP, 1085 genes between cells treated with ALLI *vs* CTRL and 1521 between cells treated with cAMP compared with CTRL cells (Supplementary Table 1).

GO term and KEGG analysis enriches genes of treated cells in cellular respiration, mitochondrial organization, and thermogenesis

To further investigate the function of the DEGs, GO term enrichment analysis was performed. The up- and down regulated DEGs were significantly enriched in biological processes (BP), molecular functions (MF) and cellular components (CC).

TABLE 1 Unidimensional test of equality of the means of the classes illustrating the contribution of different morphological features to the separation of differentially treated cells.

Variable	Wilk's Lambda	F	p-value
Mean Aspect Ratio (au)	0.746	5.795	0.007
Simple tubules (%)	0.765	5.224	0.011
Mean Branch Length (µm)	0.779	4.817	0.014
Total Branch Length/area	0.789	4.533	0.018
Median Branch Length (µm)	0.802	4.205	0.023
Mean Network Size (Branches) (µm)	0.805	4.115	0.025
Mean Branch Length (µm)	0.808	4.050	0.026
Mean Form Factor (au)	0.815	3.863	0.031
Area_Large globules (%)	0.834	3.392	0.045
Mean Perimeter (µm)	0.834	3.381	0.046

The most discriminant parameters have a low Wilk's lambda and a high F.

In all comparisons, 30 BP, CC and MF GO terms were found to be significantly enriched (Supplementary Tables 2–4). Notably, BP terms such as 'Oxoacid metabolic process', 'Small molecule metabolic process', 'Fatty acid metabolic process', 'Cellular respiration', 'Cellular lipid metabolic process', 'Energy derivation by oxidation of organic compounds', 'Monocarboxylic acid metabolic process' were down regulated in the ALLI_cAMP comparison, but up regulated in the ALLI_CTRL and cAMP_ CTRL comparisons (Supplementary Table 2). Interestingly 'Mitochondrion', 'Mitochondrial matrix', 'Mitochondrial inner membrane', 'Mitochondrial membrane', 'Mitochondrial envelope', 'Mitochondrial protein-containing complex' CC terms were down regulated in ALLI_cAMP comparison, but up regulated in ALLI_CTRL and in cAMP_ CTRL comparisons (Supplementary Table 3).

In contrast, significantly enriched MF terms such as 'Calcium ion binding', 'Cell adhesion molecule binding', 'Collagen binding', 'Extracellular matrix structural constituent', 'Glycosaminoglycan binding', 'Growth factor binding', 'Heparin binding', 'Integrin binding' and 'Signalling receptor binding' were up regulated in the ALLI_cAMP comparison, but down regulated in the ALLI_CTRL and in the cAMP_CTRL comparisons (Supplementary Table 4). Interestingly, significantly enriched MF terms such as 'Active transmembrane transporter activity', 'Electron transfer activity', 'Oxidoreductase activity' and 'Transmembrane transporter activity' were up regulated in the ALLI_CTRL and in the cAMP_CTRL comparisons (Supplementary Table 4).

Figure 6 shows the results of the KEGG analysis in the form of a graphical representation of the scatter plots. Each figure shows the KEGG enrichment of 15 identified pathways for each treatment comparison with the corresponding GeneRatio, adjusted *p*-value, and number of enriched genes in the corresponding pathways. The GeneRatio is defined as the number of enriched candidate genes compared with the total number of annotated genes included in the corresponding pathway in the KEGG analysis. Therefore, a higher GeneRatio indicates a higher enrichment of candidate genes in the corresponding pathway. KEGG analysis showed that DEGs were significantly down regulated within the 'PPAR pathway,' Fatty acid metabolism, elongation and degradation, and in 'Citrate cycle (TCA cycle)' in ALLI_cAMP comparison. Of note, DEGs were over-expressed in pathways such as 'cAMP signalling pathway,' 'Calcium signalling pathway,' and 'CGMP-PKG signalling pathway' in ALLI_cAMP comparison (Figure 6). ALLI_CTRL and cAMP_CTRL had common DEGs significantly enriched in 'Oxidative phosphorylation' and 'Thermogenesis', whereas DEGs within the 'PPAR signalling pathway' were down regulated in ALLI *vs* cAMP and up regulated only in cells under cAMP treatment (Figure 6).

These results suggest that the browning effect of ALLI is only evident when compared with CTRL cells, so the ALLI-cAMP contrast was not discussed further.

Construction of PPI networks and module analysis of DEGs in cells treated with allicin and positive control indicate brown adipocyte differentiation associated with an increase in AMPK and PPARA signalling through downregulation of extracellular matrix organization

The PPIs of all up regulated and down regulated DEGs with combined scores greater than 0.4 were constructed from the three comparisons, and each entire PPI network was analysed using Cytohubba. The ten most highly regulated hub genes with a high degree of connectivity between nodes are listed in Table 2. The highly regulated hub genes in the ALLI_CTRL and cAMP_CTRL comparisons shared 6 genes such as PPARG, FASN, SREBF1, SCD, PPARGC1A, and ACLY. Both comparisons, referring to CTRL, were similarly enriched in 'Fatty acid synthase complex,' 'acetyl-CoA carboxylase complex,' 'AMPK signalling pathway,' 'PPARA activates gene

FIGURE 6
KEGG pathway enrichment analysis. Dot size represents the number of genes in each KEGG pathway; p.val (adjusted p-value): Red < orange < green. ALLI_cAMP = 12.5 μg/mL allicin-treated cells *vs* cAMP = 500 μM dibutyryl cAMP-treated cells; ALLI_CTRL = 12.5 μg/mL allicin-treated cells *vs* control cells; cAMP_CTRL =500 μM dibutyryl cAMP-treated cells *vs* control cells. Scatter plot was drawn by http://www.bioinformatics.com.cn/srplot.

expression,' 'Regulation of small molecule metabolic process,' and 'Thermogenesis'.

Four down regulated hub genes, such as FN1, THBS1, COL1A2, and CCN2, are common between ALLI- and cAMP-treated cells compared with CTRL cells (Table 3). Enrichment of both comparisons included 'AGE-RAGE signalling pathway in diabetic complications', 'PI3K-Akt signalling pathway', 'Focal adhesion', 'ECM-receptor interaction', and 'TGF-beta signalling pathway'.

TABLE 2 Top 10 hub genes from up regulated DEGs calculated by Degree topological algorithm of Cytohubba plugin.

ALLI_CTRL			cAMP_CTRL		
ank	Gene	Score	Rank	Gene	Score
1	PPARG	100	1	FASN	100
2	IL1B	87	2	PPARG	97
3	FASN	86	3	CS	96
4	SREBF1	84	3	ACLY	96
5	EGF	78	5	SREBF1	94
5	SCD	78	6	SCD	89
7	APOE	74	7	PPARGC1A	87
7	PPARGC1A	74	8	ACADM	86
9	CD4	73	9	ACACA	79
10	ACLY	69	9	ACO2	79

ALLI_CTRL, 12.5 μg/mL allicin-treated cells vs control cells; cAMP_CTRL, 500 μM dibutyryl cAMP-treated cells vs control cells.

TABLE 3 Top 10 hub genes from down regulated DEGs calculated by Degree topological algorithm of Cytohubba plugin.

ALLI_CTRL			cAMP_CTRL		
Rank	Gene	Score	Rank	Gene	Score
1	FN1	96	1	FN1	179
2	MYC	61	2	IL6	130
3	CD34	45	3	CD44	104
4	THBS1	39	4	COL1A1	103
5	COL1A2	38	5	MMP2	99
5	THY1	38	6	ERBB2	83
5	HGF	38	7	THBS1	82
8	LOX	36	7	CCN2	82
8	DCN	36	7	CCND1	82
8	CCN2	36	10	COL1A2	79

ALLI_CTRL, 12.5 μg/mL allicin-treated cells vs control cells; cAMP_CTRL, 500 μM dibutyryl cAMP-treated cells vs control cells.

Genes upregulated by allicin and cAMP are enriched in the target genes of AR and PPARG, which are involved in the positive regulation of cold-induced thermogenesis and fatty acid metabolism

TRED analysis (http://rulai.cshl.edu/TRED) allows to know interaction data between transcription factors (TFs) and the promoters of their target genes, including binding motifs (38). In the ALLI_cAMP comparison, the target genes of only 1 TF (c-MYC) were down regulated and 15 were up regulated; in the ALLI_CTRL comparison, 4 TFs were down regulated and 3 (AR, PPARA, PPAG) were up regulated; in the cAMP_CTRL, 15 were down regulated and the same 3 of the ALLI_CTRL comparison were up regulated (Supplementary Table 5).

The up regulated genes were enriched in the target of AR in all comparisons (14 genes), whereas genes enriched in the target of PPARG (37 genes) and PPARA (18 genes) were enriched only in the ALLI_CTRL and cAMP_ CTRL comparisons (Supplementary Table 5). The target genes of JUN, SP1, and TP53 were significantly down regulated in the ALLI_CTRL and cAMP_CTRL comparisons but up regulated in the ALLI_cAMP comparison (Supplementary Table 5). Down regulated DEGs were enriched in target genes of EGR1, ETS1, SMAD1, SMAD3, SMAD4, and TFAP2A in the cAMP_CTRL comparison, but up regulated in ALLI_cAMP (Supplementary Table 5).

Enrichment analysis of the 14 genes targeting to AR and common to all comparisons showed significant up-regulation of 'Response to hormone, 'Regulation of lipid metabolic process', 'Regulation of small molecule metabolic process', 'Cellular response to hormone stimulus', 'Zinc finger nuclear hormone receptor-type' and 'PPARA activates gene expression'. The MCODE plugin cluster analysis did not filter any cluster with a score ≥ 5 for these genes.

The 37 DEGs targeting AR that were common only between ALLI and cAMP treatments compared with CTRL cells and the 51 common DEGs targeting PPARG resulted in only one MCODE cluster. No cluster with a score ≥ 5 was found for common DEGs targeting PPARA.

Enrichment analysis revealed the potential function of genes in each module. Shared DEGs targeted by AR and PPARG and over-expressed in ALLI_CTRL and cAMP_CTRL were enriched, among others, in 'PPARG signalling pathway' (Figures 7A, B red), 'Positive regulation of cold-induced thermogenesis' (Figures 7A, B, brown), 'Fatty acid metabolic process', 'AMPK signalling pathway' (Figures 7A, B, green), 'AMPK signalling pathway' (Figure 7A, blue) and 'PPARA activates gene expression' (Figure 7B, blue).

DEGs targeted by TP53, JUN and SP1 were down regulated in both ALLI_CTRL and cAMP_CTRL comparisons, but up regulated in ALLI_cAMP comparison. Shared DEGs targeted by SP1 and down-expressed in ALLI_CTRL and cAMP_CTRL were enriched in 'Interleukin-4 and Interleukin-13 signalling' (Figure 7C, red), and in 'Extracellular matrix organization' (Figure 7C, red). Interestingly, DEGs targeted by SP1 were found over-expressed in ALLI_cAMP comparison. Down regulated DEGs targeted by TP53 and JUN common to ALLI_CTRL and cAMP_CTRL were enriched in 'Interleukin-4 and Interleukin-13 signalling' and 'IL-18 signalling pathway' (data not shown).

Allicin stimulation favors the differentiation into brown adipocyte

Allicin stimulation favors the differentiation into beige adipocyte The PROFAT tool (41) generated the heatmap of marker expression starting from normalized reads counts of SGBS cells. The estimation of BAT phenotype in ALLI- and cAMP-treated cells increased significantly ($p < 0.0001$) in comparison to CTRL cells. In contrast, WAT phenotype decreased significantly ($p < 0.0001$) in ALLI- and cAMP-treated cells compared with CTRL (Figure 8). These results evidenced that SGBS cells exhibit a gene expression pattern

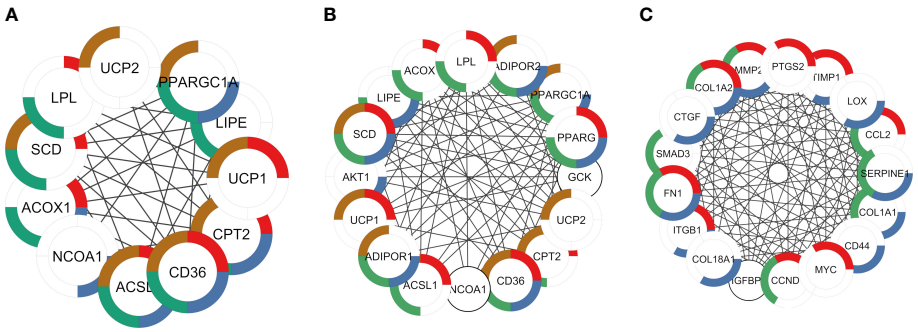

FIGURE 7
PPI networks identified by cluster functional analysis constructed with up- and down regulated DEG targets to TFs and overlapping to ALLI and cAMP treatments *vs* CTRL. The enriched pathways are marked in different colors. **(A)** Cluster 1 with a MCODE score of 7.83 achieved from up regulated genes target of AR. Red: genes enriched in 'PPARG signalling pathway' (FDR 1.82^{-12}); brown: 'Positive regulation of cold-induced thermogenesis' (FDR 4.05^{-10}); green: 'Fatty acid metabolic process' (FDR 3.08^{-09}); and blue: 'PPARA activates gene expression (FDR 4.59^{-08}). **(B)** Cluster 1 with a MCODE score of 10.47 achieved from up regulated genes target of PPARG. Red: genes enriched in 'PPARG signalling pathway' (FDR 3.10^{-13}); brown: 'Positive regulation of cold-induced thermogenesis' (FDR 4.02^{-13}); green: 'Fatty acid metabolic process' (FDR 5.23^{-13}); and blue: 'AMPK signalling pathway' (FDR 5.53^{-12}). **(C)** Cluster 1 with a MCODE score of 13.67 achieved from down regulated genes target of SP1. Red: genes enriched in 'Interleukin-4 and Interleukin-13 signalling (FDR 3.32^{-13}); green: AGE-RAGE signalling pathway in diabetic complications (FDR 4.42^{-12}); blue: 'Extracellular matrix organization' (FDR 7.12^{-12}).

similar to that of brown cells during 6 days of differentiation under allicin treatment.

Identification of common candidate targets among allicin, their organosulfur compounds and browning target genes

Because allicin is rapidly converted *in vitro* to its related fat-soluble organosulfur compounds such as DATS, DADS and DAS, the potential targets of these compounds and of allicin were screened by computational target fishing from the PharmMapper, STITCH, Swiss Target Prediction and GeneCard databases. By overlapping the highest ranked common targets of allicin and related organosulfur compounds with the 315 overlapped 'adipocyte-browning' genes, 26 common targets between allicin compounds and adipocyte-browning were used to create a GeneMania network (Supplementary Table 5). The results of the analysis showed that these 26 targets correlated with 20 others and a total of 407 different links were predicted to construct a network linking these 46 genes (Figure 9A). The constructed network had 33.99% physical interactions and 23.56% predicted functional relationships between genes. In addiction 20.58% shared the same protein domain and 13.85% shared similar co-expression characteristics, other results were pathways (5.24%) and colocalization (2.77%) as shown in Figure 9A. The molecular functions of the top ranked targets, filtered by their FDR score, were reported as GO categories. The preliminary network illustrated that the genes, depicted by different colours in Figure 9A, were involved in 'ligand-activated transcription factor activity', 'intracellular receptor signalling pathway', 'temperature homeostasis', 'regulation of cold induced thermogenesis', 'reactive

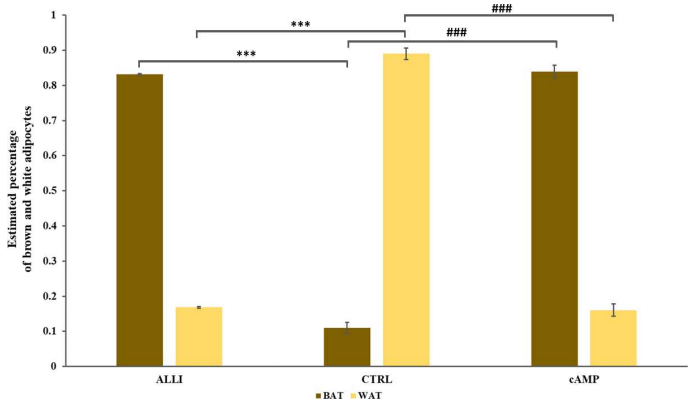

FIGURE 8
Statistical significance of PROFAT prediction percentage of brown and white adipocytes was determined using Euclidean distance and complete linkage on normalized gene expression values and analyzed by statistical test-t. *** = $p < 0.0001$ between estimated percentage of brown cells; ### = $p < 0.0001$ between estimated percentage of white cells. ALLI, 12.5 µg/mL allicin-treated cells; cAMP, 500 µM dibutyryl cAMP-treated cells; CTRL, control cells.

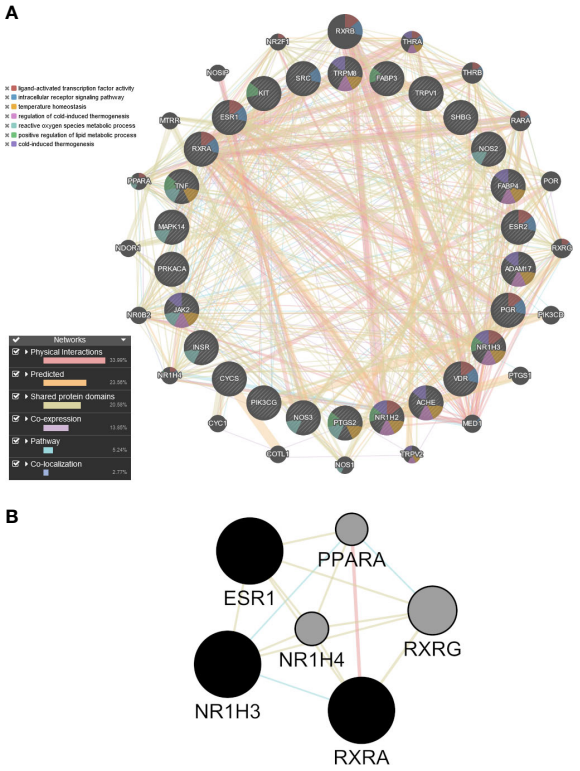

FIGURE 9
Preliminary PPI network constructed with GeneMANIA. **(A)** Twenty-six common targets between allicin, related fat-soluble organosulfur compounds and adipocytes-browning were built as assigned based on query gene. Genes are linked by functional associated networks filtered on their FDR score. Black nodes are the query targets and the larger the node, the higher degree of the node. The stronger interaction between node, the ticker and deeper colour of the edge. **(B)** Core PPI subnetwork generated by intersectional merge of PPI subnetworks according to the calculated degree, betweenness, closeness, eigenvector, LAC and network average values. ESR1, Estrogen Receptor 1; PPARA,Peroxisome Proliferator Activated Receptor Alpha; NR1H3, Nuclear Receptor Subfamily 1 Group H Member 3; NR1H4, Nuclear Receptor Subfamily 1 Group H Member 4; RXRA, Retinoid X Receptor Alpha; RXRG, Retinoid X Receptor Gamma.

oxygen species metabolic process', 'positive regulation of lipid metabolic process', and 'cold-induced thermogenesis'.

PPI subnetwork construction and identification of core targets

A topological analysis of the preliminary network was performed using the CytoNCA plugin in Cytoscape to find the core proteins that form the preliminary network. The mean the degree (17.70), betweenness (48.96), closeness (0.49), eigenvector (0.106), LAC (12.40), network (10.95) values of the preliminary network was calculated, and the nodes of the preliminary PPI network that were above this mean were sorted out to build the corresponding subnetworks. Using the intersectional merge function in Cytoscape a core PPI subnetwork was extracted (Figure 9B) containing 6 key nodes (ESR1, NR1H3, NR1H4, PPARA, RXRA, RXRG) and 15 edges. Among these genes, Nuclear Receptor Subfamily 1 Group H Member 4 (NR1H4) and PPARA were significantly up regulated in the ALLI_CTRL comparison of SGBS cells (Supplementary Table 1), whereas estrogen receptor 1 (ESR1), Nuclear Receptor Subfamily 1 Group H Member 3 (NR1H3) and Retinoid X receptor alpha (RXRA) are common targets of allicin and related fat-soluble organosulfur compounds.

The effects of allicin are related to mitochondrial biogenesis and lipid catabolism through the activation of core targets transcription factors

GO terms from biological process, cellular component, and molecular functions were examinedand the most enriched GO terms from biological process were 'intracellular receptor signalling pathway', 'cellular response to lipid', 'hormone-mediated signalling pathway', 'response to steroid hormone', 'response to lipid', whereas the most enriched GO terms from cellular component and molecular functions were 'transcription regulator complex', 'nuclear receptor activity', and ligand-activated transcription factor activity, respectively (data not shown).

KEGG pathways were analysed with a redundancy cut-off of 0.7, 17 pathways were statistically significant (FDR < 0.05) 'PPAR signalling pathway', 'Adipocytokine signalling pathway', 'Thyroid hormone signalling pathway', 'Non-alcoholic fatty liver disease, 'Insulin resistance' and 'Lipid and atherosclerosis'(data not shown).

The pathways enriched by Reactome analysis were 'Nuclear Receptor transcription pathway', 'PPARA activates gene expression', 'SUMOylation of intracellular receptors', Regulation of lipid metabolism by PPARalpha' and 'Mitochondrial biogenesis', which were shown as bubble plot combined with a Sankey diagram (Figure 10).

In addition, the score of the 6 key nodes identified by the topological analysis was scored using VarElect. The score indicates the strength of the association between the target and the 'cold induced thermogenesis' phenotype (Table 4). ESR1, PPARA, NR1H3, and NR1H4 scored > 6.

Discussion

As a thermogenic organ, BAT is known to enhance energy metabolism and weight loss (50), so promoting mass and activity of BAT is one of the most promising strategies against obesity. Treatment of white adipose cells with rosiglitazone or with other β-adrenergic agonists induces beige cells with similar properties as BAT (51). Induction of the beige/brown fat cell phenotype leads not only to thermogenesis, but also to lipolysis, which facilitates energy metabolism, and mitochondrial dynamics, which precede the depolarization associated with heat dissipation (23). A high rate of mitochondrial fragmentation and free fatty acid release promote mitochondrial uncoupling and energy expenditure (52). Knowledge of the signalling pathways that stimulate the transition from white

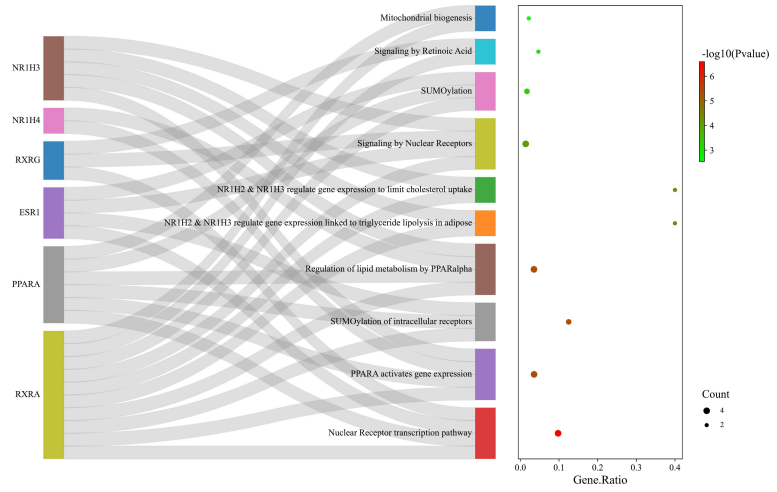

FIGURE 10
Bubble plot combined with Sankey diagram showing statistically significant Reactome pathways and the genes within each pathway. Figure was plotted by http://www.bioinformatics.com.cn/srplot.

to beige adipocytes, could help identify effective therapeutic strategies against obesity.

The discovery of functionally active BAT in adult humans and the possible recruitment of beige adipocytes by browning of WAT have introduced the way for new potential strategies for anti-obesity agents (53).

Previous studies have shown that SGBS cells gradually acquire BAT-like function in the absence of external stimulation during different days of differentiation, suggesting that lipid droplets t dynamics, and mitochondrial morphology (27) together with a differential expression of genes involved in extracellular matrix organization and oxidative stress are related to the brown fat phenotype (20). While it has been clearly demonstrated that the β3-adrenergic receptor (β3-AR) mediates thermogenesis in rodents (54), BAT is activated in humans by β2-AR signalling (55). Therefore, to bypass the ADRBs receptors dibutyryl-cAMP was chosen as a positive control.

The present study demonstrated that allicin supported the transition from white to beige adipocytes in SGBS after 6 days of differentiation and that the transformation of structural cell phenotype was evidenced by the dynamic changes in the size of LDs and the shape of mitochondria similar to those observed in the positive control.Lipolysis is generally considered an essential requirement for thermogenesis in brown and beige adipocytes, and any lipolytic compound could be a potential activator of thermogenesis (56). In HepG2 cells, allicin reduces lipid accumulation either by regulating AMPK-SREBPs and PKA-CREB signalling pathways (57) or by activating PPARA and FABP6 gene expression (58). The effect of allicin on lipid reduction argues for PPARγ/LXRα signalling in THP-1 macrophage foam cells (59). In the present work, ALLI and cAMP treatments decreased the area and diameter of LDs, but because the number of LDs/cell increased significantly with ALLI treatment, the lipolytic activity of allicin may have led to the formation of multilocular adipocytes, a feature of WAT browning. This is confirmed by the increased number of differentially expressed genes related to lipolysis, such as DNA fragmentation factor subunit alpha (DFFA), monoglyceride lipase (MGLL), perilipin 1 (PLIN1), patatin like phospholipase domain containing 2 (PNPLA2), lipoprotein lipase (LPL) and hormone-sensitive lipase (LIPE) in ALLI- and cAMP-treated cells (Supplementary Table 1). However, a thermogenic futile cycle of lipolysis/lipogenesis has been claimed to explain the unilocular to multilocular transformation during WAT browning (21). In 3T3-L1 cells exposed to β-adrenergic stimulation, remodelling of LDs involves first their reduction into small LDs and then their new

TABLE 4 Score of the six key nodes evaluated by VarElect.

Gene Symbol	Description	-Log10(*P*)	Score
ESR1	Estrogen Receptor 1	2.35	14.91
PPARA	Peroxisome Proliferator Activated Receptor Alpha	2.07	11.56
NR1H3	Nuclear Receptor Subfamily 1 Group H Member 3	1.49	6.30
NR1H4	Nuclear Receptor Subfamily 1 Group H Member 4	1.63	6.09
RXRA	Retinoid X Receptor Alpha	1.44	5.89
RXRG	Retinoid X Receptor Gamma	0.55	0.56

formation and subsequent enlargement (21). Indeed, significant expression of negative regulators of lipolysis such as G0/G1 switch gene 2 (G0S2) and patatin like phospholipase domain containing 3 (PNPLA3) were also found in ALLI-treated SBGS cells as well as the mRNA levels of the perilipin 4 (PLIN4), diacylglycerol o-acyltransferase 1 (DGAT1), diacylglycerol o-acyltransferase 2 (DGAT2) and adipocyte glycerol transporter aquaporin7 (AQP7), (Supplementary Table 1), indicating that the cells store and export metabolites released during lipolysis. Moreover, other studies have shown that triglyceride lipolysis catalysed by PNPLA2 in mice brown adipocytes is not required to maintain body temperature during cold exposure (60, 61) and that other sources such as circulating glucose and fatty acids can balance thermogenesis (62).

During cold exposure mitochondrial reorganization and free fatty acid release synergize to facilitate uncoupling and thereby heat production (23). Concomitantly, mitochondria acquire a spheroid morphology driven by increased fission (63). Present results show an increased in number and area of mitochondria in cells treated with allicin, and the data was also confirmed by the reduction of elongation (mean aspect ratio) and by the change from round to filamentous shape (mean form factor) in ALLI- and cAMP-treated cells. Network parameters obtained by MiNa also show a significant decrease in mean rod/branch length in both treatments compare to CTRL cells. According to the Micro2P plugin, six different subtypes of mitochondria with the highest proportion of small globules were classified in ALLI- and cAMP-treated cells. Canonical DA further evidenced that mitochondrial parameters specifically those related to mean aspect ratio, percentage of simple tubules, mean branch length, accurately clustered differentially treated cells and CTRL cells.

The high content of organosulfur compounds in garlic suggests that many of its active compounds may have anti-adipogenic effects by promoting the expression of genes specific for brown adipocytes (64). Recent data showed that allicin promotes browning of 3T3-L1 mouse adipocytes and iWAT by inducing the expression of brown marker genes through KLF15 signalling (16) or through the SIRT1-PGC1α-TFAM pathway (17).

PCA analysis based on reads clearly grouped the data set on the first component between CTRL cells and cells treated with ALLI or cAMP. On the second component, the treatments are separated, but the replicates of the same point were very close, indicating robust reproducibility of the data.

Classical thermogenesis is activated by adrenoreceptors that promote cAMP synthesis for PKA activation and expression of downstream targets (65). Intracellular cAMP levels are maintained by a balance between the rate of synthesis mediated by adenylate cyclase and the rate of degradation regulated by cAMP phosphodiesterase 3 (PDE3). Allicin is known to increase intracellular cAMP by inhibiting phosphodiesterase activity in isolated human platelets (66, 67) or by increasing adenylate cyclase activity in the human bronchial epithelial cell line (68). In adipose tissue, PDE3 inhibitors increase intracellular cAMP levels, thereby enhancing lipolysis (69). The present results showed a significant up-regulation of PDE3B in ALLI_CTRL and cAMP_CTRL (Supplementary Table 1), resulting in an increase in intracellular cAMP and downstream genes involved in lipolysis, such as LIPE and PLIN1, and in browning, such as TBX1 and UCP1 (Supplementary Table 1). This is consistent with the results obtained in adipose tissue of mice fed a high-fat diet when treated with cilostazol, a selective inhibitor of phosphodiesterase III with multiple effects on metabolism (70). In addition, cilostazol, which has antiplatelet, antithrombotic, and vasodilatory properties similar to allicin, increased the intracellular concentration of cAMP, which stimulated the expression of thermogenic and brown specific genes (70). The BP GO terms enrichment, such as cellular respiration and cellar lipid metabolic process as well as CC GO terms related to mitochondria were significantly up regulated in ALLI- and cAMP-treated cells compared with CTRL cells, suggesting similar activity in cells with different treatments, but was opposite when ALLI-treated cells were compared with cAMP-treated cells. MF GO terms, such as oxidoreductase activity, were up regulated in ALLI- and cAMP-treated cells compared with CTRL cells, but down regulated in ALLI-treated and cAMP-treated cells. Therefore, the positive browning effect of ALLI treatment was evident only in comparison with CTRL cells, but not in comparison with cAMP incubation. However, ALLI and cAMP treatments shared the most up regulated hub genes such as PPARG, FASN, SREBF1, SCD, PPARGC1A, and ACLY, which are related to fatty acid metabolic process, fatty acid oxidation and response to cold. The lowest down regulated hub genes common to ALLI and cAMP treatments FN1, THBS, COL1A2 and CCN2 were enriched in ECM receptor interactions, integrin cell surface interactions and focal adhesion. This is consistent with the down regulation of collagen, integrin and laminin genes (COL1A1, COL1A2, ITGA2, ITGA3, ITGA4, ITGA5, LAMA1, LAMA2, LAMA3; Supplementary Table 1) observed in SGBS cells during differentiation (20) demonstrating their ability to adjust cytoskeletal reorganization according to their size, LDs dynamics and thermogenesis (71).

KEGG pathway enrichment confirmed that oxidative phosphorylation, thermogenesis, and fatty acid metabolism were the most significantly up-regulated pathways in the ALLI_CTRL and cAMP_CTRL comparisons, whereas ECM-receptor interaction, PI3K-Akt signalling pathway and Focal adhesion were downregulated. In contrast, pathways related to PPAR and fatty acid metabolism were significantly downregulated in the ALLI_ cAMP comparison.

Interestingly, an *in vivo* study suggests that the allyl-containing sulphides of garlic significantly enhance thermogenesis and increase epinephrine and norepinephrine levels in rat plasma (72), which is why allicin may interact with the adrenergic receptor (AR), which is one of the most effective mechanisms to deplete excess energy through cAMP/PKA-dependent signal transduction (73). In the present study, up regulated DEGs common to ALLI_CTRL and cAMP_CTRL comparisons and the targets of transcription factor AR were significantly associated with 'PPARG signalling pathway', 'positive regulation of cold-induced thermogenesis', 'fatty acid metabolic process' and 'PPARA activates gene expression'. All of these metabolic pathways and processes share the genes for fatty acid translocase (FATP or CD36), acyl-coA synthetase long chain family member 1 (ACSL1) and carnitine palmitoyltransferase II (CPT2), each of which is involved in the storage and recycling of

fatty acids, their conversion to acyl-CoA and transport to mitochondria (74). Their co-expression is clearly part of the thermogenesis programme. In 3T3-L1 adipocytes, CD36 has been found to play an important lipolytic role (75) and its translocation from the cell membrane to lipid droplets mediates the release of long-chain fatty acids by exocytosis (76). In human macrophages aged garlic extract inhibits CD36 expression through modulation of the PPARγ pathway (77), but in SGBS cells, its over expression together with that of LPL, and aquaporin 7 (AQP7) (Supplementary Table 1) can lead to triglycerides uptake and then lipolysis associated with heat production (78). In addition, CD36 has been found to be a scavenger receptor required for coenzyme Q (CoQ10) uptake in BAT and therefore essential for adaptive thermogenesis and BAT morphology, (79). Of note, CoQ10 is up regulated in ALLI-treated SGBS cells (Supplementary Table 1).

ACSL1 and CPT2 have been shown to be required for fatty acid oxidation for cold-induced thermogenesis (80). Interestingly, all of these genes are downstream targets of the nuclear transcription factor PPARA, which is expressed in metabolically active tissues such as brown adipose tissue (81). In contrast, down regulated DEGs targets of SP1 and other TFs, such as TP53 and JUN, were involved in 'Interleukin-4 and Interleukin-13 signalling' and 'Extracellular matrix organization', 'Cytokine-mediated signalling pathways' and 'IL-18 signalling pathways', as previously described in SGBS cells (20). In particular, the down regulation of fibronectin (FN1), collagen type I alpha 1 chain (COL1A1), collagen type I alpha 2 chain (COL1A2) is associated with that of the zinc finger transcription factor early growth response-1 (EGR1) (Supplementary Table 1) and, in mice, with a concomitant increase of beige cells differentiation and a decrease in genes encoding the extracellular matrix proteins (82). The down regulations of cell-surface glycoprotein CD44 and its receptor ONP in SGBS cells treated with allicin and cAMP (Supplementary Table 1) further confirms the browning activity of the compounds present in garlic. CD44 was recently recognized as a major receptor for an extracellular matrix component that plays an essential role in promoting obesity and diabetes (83).

Brown features were also confirmed by PROFAT analysis, which revealed a significant increase in 80% of genes related to BAT phenotype.

Using open-source tools, computational target fishing facilitates the investigation of biological targets of bioactive molecules using the reverse pharmacophore mapping approach (84) (Supplementary Table 6). To understand potential targets involved in the browning process six major targets ESR1, NR1H3, RXRA, PPARA, NR1H4, and RXRG were extracted from the comparison of targets of allicin and related organosulfur compounds with browning genesafter topological analysis. The targets were strongly associated, and enrichment analysis confirmed the involvement of these genes in limiting cholesterol uptake, lipolysis and mitochondrial biogenesis, all processes in which allicin plays a role. The lipolytic role of allicin may be related to the activation of PPARA through the release of fatty acids. RXRA forms heterodimers with PPARA to regulate the expression of genes involved in fatty acid oxidation (ACOX1, ACADM, CYP4A1, HMGCS2), fatty acid transport (CD36, SLC27A1, CPT2), and lipid storage (PLIN) (85), that were over expressed by ALLI treatment (Supplementary Table 1). This is consistent with the activation of PPARA promoted by allicin in palmitic acid-loaded HepG2 cells (58). Again, garlic essential oil significantly up regulated PPARA expression level in the liver of HFD-fed mice compared with control mice (86). Moreover, PPARA was found to be associated with the expression of superoxide dismutase (CuZn-SOD) in human aortic endothelial cells (87), a scavenger of ROS, which is consistent with the antioxidant properties of allicin. Of note, ESR1 is known to induce a selective beiging in 3T3-L1 cells leading to ATGL-mediated lipolysis (88). Moreover, in human and mouse adipocytes ESR1 promotes mitochondrial remodelling and thermogenesis through uncoupled respiration by regulating the mitochondrial gene POLG1 (89). All of downstream genes of these metabolic pathways, such as SOD1, ATGL, and POLG were significantly expressed in SGBS cells (Supplementary Table 1).

Conclusion

Overall, this study supports the modulatory role of allicin in stimulating the brown phenotype of SGBS cells, which is associated with an increase in mitochondrial biogenesis and lipid catabolism. The possible mechanism of this interesting process may be based on the partial interaction of allicin within the regulatory steps of cAMP signalling and PPARA signalling.

However, the study has some limitations, because neither down-regulation of SIRT5 nor significant up-regulation of KLF15, as recently reported, was detected in SGBS cells. The mechanism by which allicin promotes browning and induces mitochondrial biogenesis is not yet fully elucidated, and functional studies could be performed to further investigate the browning effect.

Data availability statement

The original contributions presented in the study are included in the article/Supplementary Material. Further inquiries can be directed to the corresponding author.

Author contributions

UA and MC designed the study. UA performed the experiments and collected data. MC collected data measurements, performed statistical analyses prepared the figures and wrote the manuscript. MW and DT provided SGBS cells and were involved in the revision of the paper. All authors read and approved the manuscript. All authors contributed to the article and approved the submitted version.

Funding

This research did not receive any specific grant from funding agencies in the public, commercial, or not-for-profit sectors.

Conflict of interest

The authors declare that the research was conducted in the absence of any commercial or financial relationships that could be construed as a potential conflict of interest.

The handling editor EKK declared a past co-authorship with the author MW.

Publisher's note

All claims expressed in this article are solely those of the authors and do not necessarily represent those of their affiliated organizations, or those of the publisher, the editors and the reviewers. Any product that may be evaluated in this article, or claim that may be made by its manufacturer, is not guaranteed or endorsed by the publisher.

Supplementary material

The Supplementary Material for this article can be found online at: https://www.frontiersin.org/articles/10.3389/fendo.2023.1141303/full#supplementary-material

References

1. Oliver P, Lombardi A, De Matteis R. Editorial: Insights into brown adipose tissue functions and browning phenomenon. *Front Physiol* (2020) 11:219. doi: 10.3389/fphys.2020.00219

2. Wu J, Boström P, Sparks LM, Ye L, Choi JH, Giang AH, et al. Beige adipocytes are a distinct type of thermogenic fat cell in mouse and human. *Cell* (2012) 150:366–76. doi: 10.1016/j.cell.2012.05.016

3. Montanari T, Pošćić N, Colitti M. Factors involved in white-to-brown adipose tissue conversion and in thermogenesis: A review. *Obes Rev* (2017) 18:495–513. doi: 10.1111/obr.12520

4. Manríquez-Núñez J, Ramos-Gómez M. Bioactive compounds and adipocyte browning phenomenon. *Curr Issues Mol Biol* (2022) 44:3039–52. doi: 10.3390/cimb44070210

5. Amagase H. Clarifying the real bioactive constituents of garlic. *J Nutr* (2006) 136 (3 Suppl):716S–25S. doi: 10.1093/jn/136.3.716S

6. Borlinghaus J, , (Née Reiter) FJ, Kappler U, Antelmann H, Ulrike Noll U, Gruhlke MCH, et al. Allicin, the odor of freshly crushed garlic: A review of recent progress in understanding allicin's effects on cells. *Molecules* (2021) 26:1505. doi: 10.3390/molecules26061505

7. Hu Y, Xu J, Gao R, Xu Y, Huangfu B, Asakiya C, et al. Diallyl trisulfide prevents adipogenesis and lipogenesis by regulating the transcriptional activation function of KLF15 on PPARγ to ameliorate obesity. *Mol Nutr Food Res* (2022) 66:e2200173. doi: 10.1002/mnfr.202200173

8. Miron T, Listowsky I, Wilchek M. Reaction mechanisms of allicin and allyl-mixed disulfides with proteins and small thiol molecules. *Eur J Med Chem* (2010) 45:1912–8. doi: 10.1016/j.ejmech.2010.01.031

9. Ankri S, Mirelman D. Antimicrobial properties of allicin from garlic. *Microbes Infect* (1999) 1:125–9. doi: 10.1016/s1286-4579(99)80003-3

10. Oommen S, Anto RJ, Srinivas G, Karunagaran D. Allicin (from garlic) induces caspase-mediated apoptosis in cancer cells. *Eur J Pharmacol* (2004) 485:97–103. doi: 10.1016/j.ejphar.2003.11.059

11. Bat-Chen W, Golan T, Peri I, Ludmer Z, Schwartz B. Allicin purified from fresh garlic cloves induces apoptosis in colon cancer cells *via* Nrf2. *Nutr Cancer* (2010) 62:947–57. doi: 10.1080/01635581.2010.509837

12. Arreola R, Quintero-Fabián S, López-Roa RI, Flores-Gutiérrez EO, Reyes-Grajeda JP, Carrera-Quintanar L, et al. Immunomodulation and anti-inflammatory effects of garlic compounds. *J Immunol Res* (2015) 2015:401630. doi: 10.1155/2015/401630

13. Tedeschi P, Nigro M, Travagli A, Catani M, Cavazzini A, Merighi S, et al. Therapeutic potential of allicin and aged garlic extract in alzheimer's disease. *Int J Mol Sci* (2022) 23:6950. doi: 10.3390/ijms23136950

14. Gupta N, Porter TD. Garlic and garlic-derived compounds inhibit human squalene monooxygenase. *J Nutr* (2001) 131:1662–7. doi: 10.1093/jn/131.6.1662

15. Chen YC, Kao TH, Tseng CY, Chang WT, Hsu CL. Methanolic extract of black garlic ameliorates diet-induced obesity *via* regulating adipogenesis, adipokine biosynthesis, and lipolysis. *J Funct Food* (2014) 9:98–108. doi: 10.1016/j.jff.2014.02.019

16. Lee CG, Rheea DK, Kimb BO, Umc SH, Pyo S. Allicin induces beige-like adipocytes *via* KLF15 signal cascade. *J Nutr Biochem* (2019) 64:13–24. doi: 10.1016/j.jnutbio.2018.09.014

17. Zhang C, He X, Sheng Y, Xu J, Yang C, Zheng S, et al. Allicin regulates energy homeostasis through brown adipose tissue. *iScience* (2020) 23:101113. doi: 10.1016/j.isci.2020.101113

18. Wabitsch. M, Brenner. RE, Melzner. I, Braun. M, Möller. P, Heinze E, et al. Characterization of a human preadipocyte cell strain with high capacity for adipose differentiation. *Int J Obes Relat Metab Disord* (2001) 25:8–15. doi: 10.1038/sj.ijo.0801520

19. Halbgebauer D, Dahlhaus M, Wabitsch M, Fischer-Posovszky P, Tews. D. Browning capabilities of human primary adipose-derived stromal cells compared to SGBS cells. *Sci Rep* (2020) 10:9632. doi: 10.1038/s41598-020-64369-7

20. Colitti M, Ali U, Wabitsch M, Tews D. Transcriptomic analysis of Simpson golabi behmel syndrome cells during differentiation exhibit BAT-like function. *Tissue Cell* (2022) 77:101822. doi: 10.1016/j.tice.2022.101822

21. Barneda D, Frontini A, Cinti S, Christian M. Dynamic changes in lipid droplet-associated proteins in the "browning" of white adipose tissues. *Biochim Biophys Acta* (2013) 1831:924–33. doi: 10.1016/j.bbalip.2013.01.015

22. Nishimoto Y, Tamori YJ. CIDE family-mediated unique lipid droplet morphology in white adipose tissue and brown adipose tissue determines the adipocyte energy metabolism. *Atheroscler. Thromb* (2017) 24:989–98. doi: 10.5551/jat.RV17011

23. Wikstrom JD, Mahdaviani K, Liesa M, Sereda SB, Si Y, Las G, et al. Hormone-induced mitochondrial fission is utilized by brown adipocytes as an amplification pathway for energy expenditure. *EMBO J* (2014) 33:418–36. doi: 10.1002/embj.201385014

24. Klusóczki Á., Veréb Z, Vámos A, Fischer-Posovszky P, Wabitsch M, Bacso Z, et al. Differentiating SGBS adipocytes respond to PPARγ stimulation, irisin and BMP7 by functional browning and beige characteristics. *Sci Rep* (2019) 9:5823. doi: 10.1038/s41598-019-42256-0

25. Hirsch K, Danilenko M, Giat J, Miron T, Rabinkov A, Wilchek M, et al. Effect of purified allicin, the major ingredient of freshly crushed garlic, on cancer cell proliferation. *Nutr Canc.* (2009) 38:245–54. doi: 10.1207/S15327914NC382_14

26. Bäcker V. (2012). ImageJ macro tool sets for biological image analysis, in: *ImageJ User and Developer Conference 2012*, Luxembourg. doi: 10.13140/RG.2.1.2868.9446

27. Montanari T, Colitti M. Simpson-Golabi-Behmel syndrome human adipocytes reveal a changing phenotype throughout differentiation. *Histochem Cell Biol* (2018) 149:593–605. doi: 10.1007/s00418-018-1663-z

28. Boschi F, Rizzatti V, Zoico E, Montanari T, Zamboni M, Sbarbati A, et al. Relationship between lipid droplets size and integrated optical density. *Eur J Histochem* (2019) 63:3017. doi: 10.4081/ejh.2019.3017

29. Chaudhry A, Shi R, Luciani DS. A pipeline for multidimensional confocal analysis of mitochondrial morphology, function, and dynamics in pancreatic β-cells. *Am J Physiol Endocrinol Metab* (2020) 318:E87–E101. doi: 10.1152/ajpendo.00457.2019

30. Valente AJ, Maddalena LA, Robb WL, Moradi F, Stuart JA. A simple ImageJ macro tool for analyzing mitochondrial network morphology in mammalian cell culture. *Acta Histochem* (2017) 119:315–26. doi: 10.1016/j.acthis.2017.03.001

31. Peng JY, Lin CC, Chen YJ, Kao LS, Liu YC, Chou CC, et al. Automatic morphological subtyping reveals new roles of caspases in mitochondrial dynamics. *PloS Comput Biol* (2011) 7:e1002212. doi: 10.1371/journal.pcbi.1002212

32. Iannetti EF, Smeitink JAM, Beyrath J, Willems PHGM, Koopman WJH. Multiplexed high-content analysis of mitochondrial morphofunction using live-cell microscopy. *Nat Protoc* (2016) 11:1693–710. doi: 10.1038/nprot.2016.094

33. Dobin A, Davis CA, Schlesinger F, Drenkow J, Zaleski C, Jha S, et al. STAR: Ultrafast universal RNA-seq aligner. *Bioinformatics* (2013) 29:15–21. doi: 10.1093/bioinformatics/bts635

34. Ge SX, Son EW, Yao R. iDEP: an integrated web application for differential expression and pathway analysis of RNA-seq data. *BMC Bioinf* (2018) 19:534. doi: 10.1186/s12859-018-2486-6

35. Ge X. iDEP web application for RNA-seq data analysis. *Methods Mol Biol* (2021) 2284:417–43. doi: 10.1007/978-1-0716-1307-8_22

36. Ashburner M, Ball CA, Blake JA, Botstein D, Butler H, Cherry JM, et al. Gene ontology: Tool for the unification of biology. *Nat Genet* (2000) 25:25–9. doi: 10.1038/75556

37. Kanehisa M, Goto S. KEGG: Kyoto encyclopedia of genes and genomes. *Nucleic Acids Res* (2000) 28:27–30. doi: 10.1093/nar/28.1.27

38. Jiang C, Xuan Z, Zhao F, Zhang MQ. TRED: A transcriptional regulatory element database, new entries and other development. *Nucleic Acids Res* (2007) 35:137–40. doi: 10.1093/nar/gkl1041

39. Chin CH, Chen SH, Wu HH, Ho CW, Ko MT, Lin CY. CytoHubba: Identifying hub objects and sub-networks from complex interactome. *BMC Syst Biol* (2014) 8 (Suppl 4):S11. doi: 10.1186/1752-0509-8-S4-S11

40. Bader GD, Hogue CW. An automated method for finding molecular complexes in large protein interaction networks. *BMC Bioinf* (2003) 4:2. doi: 10.1186/1471-2105-4-2

41. Cheng Y, Jiang L, Keipert S, Zhang S, Hauser A, Graf E, et al. Prediction of adipose browning capacity by systematic integration of transcriptional profiles. *Cell Rep* (2018) 23:3112–25. doi: 10.1016/j.celrep.2018.05.021

42. Liu X, Ouyang S, Yu B, Huang K, Liu Y, Gong J, et al. PharmMapper server: A web server for potential drug target identification *via* pharmacophore mapping approach. *Nucleic Acids Res* (2010) 38:W609–14. doi: 10.1093/nar/gkq300

43. Wang X, Shen Y, Wang S, Li S, Zhang W, Liu X, et al. PharmMapper 2017 update: a web server for potential drug target identification with a comprehensive target pharmacophore database. *Nucleic Acids Res* (2017) 45:W356–60. doi: 10.1093/nar/gkx374

44. Szklarczyk D, Santos A, von Mering C, Jensen LJ, Bork P, Kuhn M. STITCH 5: augmenting protein-chemical interaction networks with tissue and affinity data. *Nucleic Acids Res* (2016) 44:D380–384. doi: 10.1093/nar/gkv1277

45. Daina A, Michielin O, Vincent Z. SwissTargetPrediction: Updated data and new features for efficient prediction of protein targets of small molecules. *Nucleic Acids Res* (2019) 47:W357–64. doi: 10.1093/nar/gkz382

46. Warde-Farley D, Donaldson SL, Comes O, Zuberi K, Badrawi R, Chao P, et al. The GeneMANIA prediction server: biological network integration for gene prioritization and predicting gene function. *Nucleic Acids Res* (2010) 38 Suppl: W214–220. doi: 10.1093/nar/gkq537

47. Tang Y, Li M, Wang J, Pan Y, Wu FX. CytoNCA: a cytoscape plugin for centrality analysis and evaluation of protein interaction networks. *Biosystems* (2015) 127:67–72. doi: 10.1016/j.biosystems.2014.11.005

48. Stelzer G, Plaschkes I, Oz-Levi D, Alkelai A, Olender T, Zimmerman S, et al. VarElect: the phenotype-based variation prioritizer of the GeneCards suite. *BMC Genomics* (2016) 17(Suppl 2):444. doi: 10.1186/s12864-016-2722-2

49. Addinsoft. *XLSTAT statistical and data analysis solution*. USA: New York (2022). Available at: https://www.xlstat.com/en.

50. Harms M, Seale P. Brown and beige fat: development, function and therapeutic potential. *Nat Med* (2013) 19:1252–63. doi: 10.1038/nm.3361

51. Cheng L, Wang J, Dai H, Duan Y, An Y, Shi L. Brown and beige adipose tissue: a novel therapeutic strategy for obesity and type 2 diabetes mellitus. *Adipocyte* (2021) 10:48–65. doi: 10.1080/21623945.2020.1870060

52. Gao AW, Houtkooper RH. Mitochondrial fission: Firing up mitochondria in brown adipose tissue. *EMBO J* (2014) 33:401–2. doi: 10.1002/embj.201487798

53. Murugan DD, Balan D, Wong PF. Adipogenesis and therapeutic potentials of antiobesogenic phytochemicals: Insights from preclinical studies. *Phytother Res* (2021) 35:5936–60. doi: 10.1002/ptr.7205

54. Cypess AM, Weiner LS, Roberts-Toler C, Franquet EE, Kessler SH, Kahn PA, et al. Activation of human brown adipose tissue by a β3-adrenergic receptor agonist. *Cell Metab* (2015) 21:33–8. doi: 10.1016/j.cmet.2014.12.009

55. Blondin DP, Nielsen S, Kuipers EN, Severinsen MC, Jensen VH, Miard S, et al. Human brown adipocyte thermogenesis is driven by β2-AR stimulation. *Cell Metab* (2020) 32:287–300. doi: 10.1016/j.cmet.2020.07.005

56. Braun K, Oeckl J, Westermeier J, Li Y, Klingenspor M. Non-adrenergic control of lipolysis and thermogenesis in adipose tissues. *J Exp Biol* (2018) 221(Pt Suppl 1): jeb165381. doi: 10.1242/jeb.165381

57. Lu J, Cheng C, Fang B, Meng Z, Zheng Y, Tian X, et al. Protective effects of allicin on 1,3-DCP-induced lipid metabolism disorder in HepG2 cells. *Biomed Pharmacother.* (2017) 96:1411–7. doi: 10.1016/j.biopha.2017.10.125

58. Cheng B, Li T, Li F. Use of network pharmacology to investigate the mechanism by which allicin ameliorates lipid metabolism disorder in HepG2 cells. *Evid. Based Complement. Alternat. Med* (2021) 12:3956504. doi: 10.1155/2021/3956504

59. Lin XL, Hu HJ, Liu YB, Hu XM, Fan XJ, Zou WW, et al. Allicin induces the upregulation of ABCA1 expression *via* PPARγ/LXRα signaling in THP-1 macrophage-derived foam cells. *Int J Mol Med* (2017) 39:1452–60. doi: 10.3892/ijmm.2017.2949

60. Schreiber R, Diwoky C, Schoiswohl G, Feiler U, Wongsiriroj N, Abdellatif M. Cold-induced thermogenesis depends on ATGL-mediated lipolysis in cardiac muscle, but not brown adipose tissue. *Cell Metab* (2017) 26:753–763.e7. doi: 10.1016/j.cmet.2017.09.004

61. Shin H, Ma Y, Chanturiya T, Cao Q, Wang Y, Kadegowda AKG, et al. Lipolysis in brown adipocytes is not essential for cold-induced thermogenesis in mice. *Cell Metab* (2017) 26:764–777.e5. doi: 10.1016/j.cmet.2017.09.002

62. Chitraju C, Fischer AW, Farese R, Walther. TC. Lipid droplets in brown adipose tissue are dispensable for cold-induced thermogenesis. *Cell Rep* (2020) 33:108348. doi: 10.1016/j.celrep.2020.108348

63. Von Bank H, Hurtado-Thiele M, Oshimura N, Simcox J. Mitochondrial lipid signaling and adaptive thermogenesis. *Metabolites* (2021) 11:124. doi: 10.3390/metabo11020124

64. Quesada I, de Paola M, Torres-Palazzolo C, Camargo A, Ferder L, Manucha W, et al. Effect of garlic's active constituents in inflammation, obesity and cardiovascular disease. *Curr Hypertens Rep* (2020) 22:6. doi: 10.1007/s11906-019-1009-9

65. Tabuchi C, Sul HS. Signaling pathways regulating thermogenesis. *Front Endocrinol* (2021) 12:595020. doi: 10.3389/fendo.2021.595020

66. Agarwal KC. Therapeutic actions of garlic constituents. *Med Res Rev* (1996) 16:111–24. doi: 10.1002/(SICI)1098-1128(199601)16:1<111::AID-MED4>3.0.CO;2-5

67. Allison GL, Lowe GM, Rahman K. Aged garlic extract inhibits platelet activation by increasing intracellular cAMP and reducing the interaction of GPIIb/IIIa receptor with fibrinogen. *Life Sci* (2012) 91:1275–80. doi: 10.1016/j.lfs.2012.09.019

68. Qiu ZR, Xu JB, Chen L, Huang ZX, Lei TL, Huang ZY. Allicin facilitates airway surface liquid hydration by activation of CFTR. *Front Pharmacol* (2022) 13:890284. doi: 10.3389/fphar.2022.890284

69. Chaves VE, Frasson D, Kawashita NH. Several agents and pathways regulate lipolysis in adipocytes. *Biochimie* (2011) 93:1631–40. doi: 10.1016/j.biochi.2011.05.018

70. Seo DH, Shin E, Lee YH, Park SE, Nam KT, Kim JW, et al. Effects of a phosphodiesterase inhibitor on the browning of adipose tissue in mice. *Biomedicines* (2022) 10:1852. doi: 10.3390/biomedicines10081852

71. Gonzalez Porras MA, Stojkova K, Vaicik MK, Pelowe A, Goddi A, Carmona A, et al. Integrins and extracellular matrix proteins modulate adipocyte thermogenic capacity. *Sci Rep* (2021) 11:5442. doi: 10.1038/s41598-021-84828-z

72. Oi Y, Kawada T, Shishido C, Wada K, Kominato Y, Nishimura S, et al. Allyl-containing sulfides in garlic increase uncoupling protein content in brown adipose tissue, and noradrenaline and adrenaline secretion in rats. *J Nutr* (1999) 129:336–42. doi: 10.1093/jn/129.2.336

73. Cannon B, Nedergaard JAN. Brown adipose tissue: Function and physiological significance. *Physiol Rev* (2004) 84:277–359. doi: 10.1152/physrev.00015.2003

74. Hankir MK, Klingenspor M. Brown adipocyte glucose metabolism: A heated subject. *EMBO Rep* (2018) 19:e46404. doi: 10.15252/embr.201846404

75. Zhou D, Samovski D, Okunade AL, Stahl PD, Abumrad NA, Su X. CD36 level and trafficking are determinants of lipolysis in adipocytes. *FASEB J* (2012) 26:4733–42. doi: 10.1096/fj.12-206862

76. Daquinag AC, Gao Z, Fussell C, Immaraj L, Pasqualini R, Arap W, et al. Fatty acid mobilization from adipose tissue is mediated by CD36 posttranslational modifications and intracellular trafficking. *JCI Insight* (2021) 6:e147057. doi: 10.1172/jci.insight.147057

77. Morihara N, Ide N, Weiss N. Aged garlic extract inhibits CD36 expression in human macrophages *via* modulation of the PPARgamma pathway. *Phytother Res* (2010) 24:602–8. doi: 10.1002/ptr.3008

78. van der Vaart JI, Boon MR, Houtkooper RH. The role of AMPK signaling in brown adipose tissue activation. *Cells* (2021) 10:1122. doi: 10.3390/cells10051122

79. Anderson CM, Kazantzis M, Wang J, Venkatraman S, Goncalves RL, Quinlan CL, et al. Dependence of brown adipose tissue function on CD36-mediated coenzyme q uptake. *Cell Rep* (2015) 10:505–15. doi: 10.1016/j.celrep.2014.12.048

80. Lee J, Ellis JM, Wolfgang MJ. Adipose fatty acid oxidation is required for thermogenesis and potentiates oxidative stress-induced inflammation. *Cell Rep* (2015) 10:266–79. doi: 10.1016/j.celrep.2014.12.023

81. Grygiel-Górniak B. Peroxisome proliferator-activated receptors and their ligands: nutritional and clinical implications – a review. *Nutr J* (2014) 13:17. doi: 10.1186/1475-2891-13-17

82. Milet C, Bléher M, Allbright K, Orgeur M, Coulpier F, Duprez D, et al. Egr1 deficiency induces browning of inguinal subcutaneous white adipose tissue in mice. *Sci Rep* (2017) 7:16153. doi: 10.1038/s41598-017-16543-7

83. Weng X, Maxwell-Warburton S, Hasib A, Ma L, Kang L. The membrane receptor CD44: Novel insights into metabolism. *Trends Endocrinol Metab* (2022) 33:318–32. doi: 10.1016/j.tem.2022.02.002

84. Forouzesh A, Samadi Foroushani S, Forouzesh F, Zand E. Reliable target prediction of bioactive molecules based on chemical similarity without employing statistical methods. *Front Pharmacol* (2019) 10:835. doi: 10.3389/fphar.2019.00835

85. Rakhshandehroo M, Knoch B, Müller M, Kersten S. Peroxisome proliferator-activated receptor alpha target genes. *PPAR Res* (2010) 2010:612089. doi: 10.1155/2010/612089

86. Lai YS, Chen WC, Ho CT, Lu KH, Lin SH, Tseng HC, et al. Garlic essential oil protects against obesity-triggered nonalcoholic fatty liver disease through modulation of lipid metabolism and oxidative stress. *J Agric Food Chem* (2014) 62:5897–906. doi: 10.1021/jf500803c

87. Inoue I, Goto S, Matsunaga T, Nakajima T, Awata T, Hokari S, et al. The ligands/activators for peroxisome proliferator-activated receptor alpha (PPARalpha) and PPARgamma increase Cu2+, Zn2+-superoxide dismutase and decrease p22phox message expressions in primary endothelial cells. *Metabolism* (2001) 50:3–11. doi: 10.1053/meta.2001.19415

88. Santos RS, Frank AP, Fatima LA, Palmer BF, Oz OK, Clegg DJ. Activation of estrogen receptor alpha induces beiging of adipocytes. *Mol Metab* (2018) 18:51–9. doi: 10.1016/j.molmet.2018.09.002

89. Zhou Z, Moore TM, Drew BG, Ribas V, Wanagat J, Civelek M, et al. Estrogen receptor α controls metabolism in white and brown adipocytes by regulating Polg1 and mitochondrial remodeling. *Sci Transl Med* (2020) 12:eaax8096. doi: 10.1126/scitranslmed.aax8096